An Experimental Study on the Liftoff of a Co-Flowing Non-Premixed Turbulent Methane Flame: Effect of the Fuel Nozzle Geometry

by

Mohsen Akbarzadeh

A Thesis submitted to the Faculty of Graduate Studies of
The University of Manitoba
in partial fulfillment of the requirements of the degree of

Doctor of Philosophy

Department of Mechanical and Manufacturing Engineering
University of Manitoba
Winnipeg, Manitoba
Canada

ABSTRACT

The effect of the fuel nozzle geometry on the liftoff phenomenon of turbulent methane diffusion flame with and without a co-airflow is investigated experimentally. This investigation consists of two parts. In the first part, the effect of the internal geometry of a circular nozzle is examined. This was accomplished via varying the nozzle diameter, orifice length to diameter ratio (L/D), and (3) the contraction angle. These geometrical parameters were aimed to create a wide range of test conditions of the ensuing jet flow. The strength of the co-airflow was also varied to evaluate its impact on the jet flame liftoff parameters. The second part consists of investigating the effect of the fuel nozzle exit orifice geometry on the flame liftoff. This was achieved by employing a rectangular nozzle with an exit aspect ratio of 2 and a circular nozzle.

Particle Image Velocimetry (PIV) technique was used to characterize the velocity field of the turbulent jets issuing from these nozzles. Also, a high speed imaging technique was employed to determine the flame liftoff height.

The flame results showed that the fuel nozzle having the greater L/D or smooth contraction has higher liftoff velocity. In addition, the results revealed that the rectangular nozzle has a lower liftoff velocity. The effect of the nozzle diameter on the liftoff, however, was found to depend on the co-airflow strength. The corresponding turbulent jet flow characteristics showed that higher levels of jet near-field turbulence results in a lower flame liftoff velocity regardless of the nozzle internal geometry. Moreover, the results showed that a nozzle with the lowest L/D or with smooth contraction has the lowest flame liftoff height.

The PIV results revealed that a circular jet, which spreads faster and generates higher near-field turbulence, generates a flame with its base sitting closer to the nozzle. The results revealed

also that the rectangular fuel nozzle, which, in general, has lower liftoff height, produces higher turbulence intensity in the jet near-field and faster spread along the minor axis of the nozzle which is an indication of the presence of relatively more turbulent flow structures (which is induced by the nozzle's exit asymmetry). The results confirmed that higher jet spread rate in the near-field in conjunction with higher turbulence level result in an increased flame propagation speed (in line with Kalghatgi's lifted diffusion flame stability theory), and hence make it possible for a flame to stabilize at a relatively lower height from the nozzle.

ACKNOWLEDGEMENTS

I would like to express my gratitude to my advisor, Dr. Birouk, for his continuous time and effort in supervising and guiding my research throughout the course of this study. The financial support from NSERC and Manitoba Hydro (Mr. N. Read, Project Manager) is gratefully acknowledged. My sincere thanks go also to the examination committee (Dr. Mark Tachie, Dr. Gregory Bridges and Dr. Alain Champlain), for their time and input in this thesis. I would like to thank the technicians of the Mechanical Engineering department (John Finken, Irvin Penner, Dan Rossong and Kim Majury) for their technical assistance. Finally, I would like to acknowledge my parents for their love and support throughout my life. My sisters deserve my wholehearted thanks, as well.

DEDICATION

I would like to dedicate this thesis to my parents for their love, support and encouragement throughout my life.

TABLE OF CONTENTS

LIST OF FIGURES

LIST OF TABLES

NOMENCLATURE

English symbols

A	area of a nozzle exit
a and b	half height and half width of a rectangular orifice exit
AR	aspect ratio of rectangular orifice exit
B_V	biased error
D	internal diameter of circular orifice exit
D_e	internal equivalent diameter of rectangular orifice exit
d_p	diameter of seeding particles
E	total error
g	gravity
H_l	flame liftoff height
M	magnification factor
N	number of samples
P_V	precision error
Re	Reynolds number
Δs	streamwise component of the particles displacement
t	time instance
t_r	time response of seeding particles
V and X	independent variables in error analysis equation
U_{jet}	jet exit mean velocity

U_{co}	coflow exit mean velocity
U_{cl}	axial mean-velocity on the centerline
U_l	flame liftoff velocity (axial mean velocity)
U_b	flame blowout velocity (axial mean velocity)
U_r	flame reattachment velocity (axial mean velocity)
U_{jet}/U_{cl}	axial mean-velocity decay
U_{max}	maximum velocity at jet exit
u	axial component of turbulent velocity
v	lateral component of turbulent velocity
v_s	settling velocity of seeding particles
u/U_{jet}	axial component of turbulence intensity
v/U_{jet}	lateral component of turbulence intensity
$(u^2 + v^2)/U_{jet}^2$	normalized turbulent kinetic energy
$\overline{uv}$	Reynolds shear stress
$\overline{uv}/U_{cl}^2$	normalized Reynolds shear stress
$Y_{1/2}$	half width of mean-velocity in radial direction for circular nozzle (or along major axis for rectangular nozzle)
$Z_{1/2}$	half width of mean-velocity in lateral direction along minor axis of rectangular nozzle
$Y_{1/2}/D$	non-dimensional radial spread of axial mean-velocity decay (spanwise spread along major axis of rectangular nozzle)
$Z_{1/2}/D$	non-dimensional lateral spread of rectangular jet along minor axis

x	streamwise direction in Cartesian coordinates system
y	radial coordinate axis (spanwise coordinate along major axis of rectangular nozzle)
z	lateral coordinate along minor axis of rectangular nozzle

Greek symbols

α	tan(α) is slope of decay or spread profile; also, sensitivity coefficient in error analysis equation
μ	molecular viscosity
ϑ	kinematic viscosity
ρ_{jet}	fuel density
ρ_{co}	coflowing air density
ρ_p	density of seeding particles
σ	standard deviation

Derivatives

$d\ (U_{jet}/U_{cl})\ /\ dx$	rate of velocity decay along nozzle centerline
$d(Y_{1/2}/D)\ /\ dx$	rate of spread along nozzle axis
$d(\overline{uv}/U_{cl}^2)\ /\ dy$ or dz	rate of change of normalized turbulent shear stress, respectively, along major and minor axes of rectangular nozzle

Subscripts and abbreviations

1/2	jet half-width

air	air properties
avg	averaged parameter
C	circular nozzle
R	rectangular nozzle
cl	nozzle centerline
co	coflow
e	equivalent diameter
jet	jet exit
MA	major plane of rectangular nozzle
MI	minor plane of rectangular nozzle
b	blowoff velocity
l	liftoff velocity/height
r	reattachment velocity
p	seeding particles

CHAPTER 1
INTRODUCTION AND OBJECTIVES

Jet diffusion flames (non-premixed combustion) are used in various engineering combustion power systems such as gas turbine engines and industrial burners. In these systems, the fuel is either discharged into a quiescent medium of oxidizer, or the fuel and oxidizer are separately supplied to the combustion chamber, often in the same direction, i.e. co-flowing, but with the oxidizer side having a much slower stream [1–3]. This preference for non-premixed flames (in comparison with premixed flames) is driven mainly by its safe operation because of the absence of flashback which is, in contrast, a common problem in premixed flames. The rate of mixing between the fuel and oxidizer, which is a determining factor in the combustion performance, however; is considerably lower in a diffusion flame than in a premixed flame. Nonetheless, it is proved that beyond a critical fuel velocity, an attached diffusion flame lifts off from its nozzle and stabilizes above it, which is the advent of a lifted diffusion flame [4–12]. This, therefore, provides the opportunity for the fuel and oxidizer to mix which consequently leads to an improvement in the combustion efficiency of a jet diffusion flame. In addition, a lifted flame helps to preserve the lifespan of a burner due to the absence of direct contact between the nozzle and the hot flame zones [2]. However, universal relationships, capable of predicting the limits within which a stable lifted flame can exist, are still unavailable.

The flame stability is an evident indication of combustion performance and efficiency. In understanding the flame stability, the flame liftoff height and velocity as well as blowout and reattachment velocities are important parameters. These parameters give the overall operation range of the reaction between fuel and oxidizer in a combustion power system.

Several parameters, such as fuel and oxidizer composition and their properties, the combustion chamber pressure and temperature, and burner aerodynamic arrangement can affect the stability of a turbulent diffusion flame. The present study is concerned with the effect of the burner geometry/aerodynamics. It has been reported that the burner geometry can influence the flame stability and pollutants emission such as NO_x and soot [13, 14]. Hence, a variety of fuel nozzle geometries have been designed and tested with the aim of enhancing stability ranges of a non-premixed flame [7, 15]. For instance, it has been shown that different constriction geometries, designed for a conventional axisymmetric circular nozzle, have an impact on the jet flame stability [5, 6, 16]. It has also been demonstrated that non-conventional, asymmetric fuel nozzle geometries (e.g., a rectangular nozzle) have an effect on the jet characteristics via inducing a wide range of turbulent structures as opposed to their counterparts' axisymmetric nozzles and consequently alter the flame stability range [15, 17, 18]. The production of such turbulent structures in the flow from asymmetric nozzles has shown to increase air entrainment and hence mixing between the (central) jet and its surrounding ambient (stagnant or co-flowing) which consequently improve the stability limits of the ensuing flame [13, 19].

The present research is a modest contribution to the research concerning the effect of a fuel nozzle geometry may have on the mixing and flow characteristics of the ensuing free shear turbulent jet and consequently the stability of a turbulent methane diffusion flame with and without a co-flow. To achieve this goal, several nozzles with different diameters, internal contraction profiles and exit orifice shapes were designed and tested using Particle Image Velocimetry (PIV). These geometrical parameters were aimed to create a wide range of conditions of the ensuing jet flow. The strength of the co-airflow was also varied to assess its impact, in conjunction with the fuel nozzle geometry, on the jet flame stability parameters. The stability limits of the corresponding diffusion flames (including liftoff height and velocity as well as blowout and reattachment velocities) influenced by nozzle geometry, jet characteristics and co-flow conditions, were determined using a high speed imaging technique. Finally, PIV results of non-reacting turbulent jets were utilized to help explain the stability parameters of the corresponding turbulent diffusion flames.

In this research, the effects of nozzle geometry, fuel jet and air co-flow conditions on non-premixed methane flame stability were experimentally investigated. In Chapter 2, a detailed survey of pertaining literature on reacting and non-reacting turbulent jets is presented. The literature review includes a discussion of flow characteristics of axisymmetric and asymmetric turbulent jets. Also, the existing flame stability theories are also briefly discussed to highlight the impact of the flow parameters on the stability of a turbulent non-premixed gaseous flame. In Chapter 3, details of the experimental test facility, measurement techniques and the test conditions studied are reported. In Chapter 4, the experimental results on the conventional circular nozzles with different internal geometries are presented and discussed. Similarly, in Chapter 5 the experimental results on the effect of changing the fuel nozzle exit orifice shape (i.e. circular versus rectangular) in conjunction with its internal geometry are presented. Finally, a summary of the conclusions along with some recommendations for future work are given in Chapter 6.

CHAPTER 2
LITERATURE SURVEY

In diffusion flames, the fuel (mostly in the form of a jet) is discharged into an oxidizer ambient (quiescent/moving) where combustion occurs [1, 2, 20]. Since there is not any premixing between the fuel jet and the ambient, the rate of mixing between the fuel jet and oxidizer is a considerably important factor in the combustion performance and stability of turbulent diffusion flames. Therefore, the literature review presented in this chapter is divided into two sections. In the first section, the literature on mixing and flow characteristics of non-reacting turbulent jets is reviewed with particular attention paid to turbulent axisymmetric jets with and without a co-flowing stream and also turbulent jets from asymmetric nozzles. In the second section, the up to date literature on the stability of turbulent diffusion flames (non-premixed combustion) is reviewed with particular interest in the liftoff phenomenon.

2.1. Turbulent jets

Turbulent jets are frequently used in industrial applications from aerodynamic systems to air-conditioning and more specifically in combustion power systems. For instance, in turbulent gaseous diffusion (non-premixed) flames, the fuel (often in the form of a gaseous jet, as mentioned earlier) is usually either discharged into a quiescent medium of oxidizer (well-known as free jets), or supplied to the combustion chamber with a co-flowing oxidizer-stream. The latter (well-known as coflowing jets) takes place in two separate streams with no prior mixing where the oxidizer side having a much slower stream. Hence, the level of mixing between a jet and its surrounding ambient (either quiescent or coflowing stream) can significantly influence the combustion performance and its stability [21]. It has been experimentally shown that mixing and velocity fields upstream of the flame base evolve consistently with the corresponding non-reacting jet characteristics [21].

Early investigations on the flow field of turbulent jets were performed in the 50s and 60s (e.g., [22, 23]). These studies investigated the mean-velocity field of a turbulent jet from an axisymmetric nozzle and demonstrated that, downstream a certain distance from the nozzle exit, the mean-velocity profiles of a turbulent axisymmetric jet become self-similar. Later studies also reported self-similarity of turbulence intensity at farther locations downstream of the nozzle [24]. Although many studies demonstrated the self-similarity of a turbulent axisymmetric jet [25], there are some studies which questioned the self-similarity of turbulent quantities of a jet (unlike its mean velocity) even at very far distances away from the nozzle. Nevertheless, it was commonly agreed that downstream development of a turbulent jet and its mixing with its surroundings can be described in two distinct regions: (*i*) a developing near-field region, and (*ii*) a downstream developed far-field region. In the near-field region, an initial mixing takes place between the jet and its ambient fluid which involves the entrainment of a relatively large amount of ambient fluid into the central jet. This region starts right from the nozzle exit (i.e., in the non-self-similar region of the jet), and continues up to the self-similar region of a turbulent axisymmetric jet where the jet exit mean-velocity profile (e.g., a top-hat profile for a jet emerging from a contoured nozzle or a fully-developed profile for a jet from a pipe) gradually changes to a rounded shape; i.e., the inception of far-field region (e.g. [18, 26, 27]). The distinction between the mixing mechanism in the near-field and far-field regions is important because, for instance in non-premixed combustion, though most of combustion occurs in the far-field region, it has been shown that the flame stability mechanism depends upon the properties of the mixture in the near-field region (e.g. [1, 13, 28–31]). In fact, it is stated that large-scale structures (resulted from the roll-up of the initial shear layer) and the subsequent strong stirring of the jet and its ambient is the dominant mechanism of mixing in the near-field region [32]. In the far-field region, where the mean-velocity profiles become self-similar, the secondary stage of mixing occurs. In this region, mixing is promoted by wider range of turbulent structures (i.e., both large- and small-scale vortical structures). The entrainment of ambient fluid into the central jet and its downstream spread, however, are dominated by large-scale coherent vortical structures [33, 34]. Nonetheless, the molecular mixing required for chemical reaction is dominated by small-scale structures. To estimate the rate of the entrainment and lateral spreading of a turbulent jet (in order to evaluate the mixing quality of it with the ambient), two parameters are introduced: (1) the centerline mean velocity decay (U_{jet}/U_{cl}), and (2) the half width of the mean-velocity of a jet normalized by the nozzle diameter, i.e., $Y_{1/2}/D$ [25, 35].

Most early studies used intrusive flow measurement techniques such as pitot tube and hot wire (e.g., [22]). However, recent studies used more advanced/non-intrusive measurement techniques (e.g., [36–38]). It was reported that the use of intrusive techniques to measure turbulent jets especially in reverse flow regions affect the results [32]. It is also reported that hot wire technique has a poor accuracy in capturing highly three dimensional flows and flow regions with high turbulence intensity such as the near-field of a turbulent jet [32, 39]. Advent of laser Doppler anemometry (LDA) as a non-intrusive velocity measurement tool significantly improved the experiments accuracy [25, 40]. However, as a single point technique, LDA cannot provide spatial correlations of the flow. By advent of particle image velocimetry (PIV), however, a unique ability was produced in capturing the instantaneous velocity field of a turbulent jet and its spatial resolution/structures. It was also reported that the accuracy of PIV, in contrast with that of hot wire, is not considerably reduced in highly turbulent flow regions. However, PIV typically has poorer spatial and temporal resolutions compared with LDA and hot wire [32]. Nonetheless, advent of PIV provided a chance to re-examine the previous studies in order to acquire more accurate results with great detail which helped researchers in advancing our understanding of the characteristics of turbulent jets [25, 32].

Up to the 90s, it was assumed that the initial conditions of an axisymmetric jet would not influence its development in the far-field region suggesting that all jets should asymptotically approach the same self-similar state regardless of the differences of initial conditions [25]. Later studies, however, demonstrated otherwise (e.g., [41]). Panchapakesan and Lumley [40] observed major differences between their results and others, yet they attributed the discrepancies to the different measurement techniques employed in different studies. However, Hussein *et al*., [25] stated that "the laboratory jets can never approximate the point-source of momentum jets of the earlier analysis, and that each class of laboratory jet is in principle asymptotically unique" (due to different source types such as a top-hat jet, a fully-developed pipe jet, etc), and therefore, retains forever a dependence on the source characteristics. These recent findings combined with the development of laser-based measurement diagnostics motivated investigating further turbulent jets. These studies questioned an earlier assumption which stated that the initial conditions of an axisymmetric jet would not influence its development in the far-field region suggesting that all jets should asymptotically approach the same self-similar state regardless of the differences of initial conditions. For instance, the studies of Mi *et al*., [42] and Xu and Antonia [43] observed that the initial conditions of a smoothly contracted nozzle and a pipe affect the jet characteristics differently. These differences, which were found to extend to the far-field of the jet, resulted in different mean-velocity decay and lateral spread and subsequently different mixing and entrainment rate between the two different jets. Later on, the studies of Langman *et al*., [16] and

Iyogun and Birouk [44] reported similar differences. However, the extent to which the influence of the initial conditions of an axisymmetric jet could permeate farther downstream and alter the jet development was reported differently by different studies. For instance, Antonia and Zhao [45] and Coats and Zhao [6] reported less significant qualitative difference between the flow of the two nozzles compared with other studies (e.g., [16, 42–44, 46]).

Most published studies on axisymmetric jets were limited to turbulent jets issuing from a long pipe or a smoothly contracted nozzle. In fact, the lack of detailed and extensive velocity or scalar measurements was attributed to the complexity of flows issuing from nozzles with different geometries [32]. However, Mi *et al*., [47] examined the development of the scalar-field of a turbulent jet from an orifice plate and found higher entrainment rate compared with the other two geometries (i.e., pipe or a smoothly contracted nozzle). This improvement was significant compared with that of the pipe, and only slightly different compared with that of the contoured nozzle. This behavior was attributed to the presence of "primary coherent" structures occurring in the near-field of the orifice plate and contracting jets which were typically distributed asymmetrically with reference to the nozzle axis (unlike that of the long pipe jet). By analogy, Mi *et al*., [42, 47] concluded that the momentum transfer rate within the jet from a sharp-edged orifice plate is expected to take place at a higher rate compared with that of a long pipe or a contoured nozzle. The velocity measurement of Xu and Antonia [43] agreed with the observations of Mi *et al*., [47] from temperature measurements. Later on, Mi *et al*., [32] employed PIV to investigate the velocity field in the near-field and transition region of the same flow; i.e., the turbulent jet from a round sharp-edged plate pipe and the contoured nozzle [32]. They found (from the velocity field) the highest entrainment for the sharp-edged orifice plate, followed by the contoured nozzle, and then the long pipe which has the least entrainment rate.

This was attributed to the presence of “coherent structures” in both, orifice plate and smooth contracting jet, due to the thin initial shear layer (recognized to results in the formation of “azimuthally coherent vortex rings in the jet”), as opposed to the pipe jet which has an initially thick boundary layer and less coherent structures [32]. The results revealed also that coherent structures occur in the near field of an orifice plate jet or contoured nozzle jet, and are commonly distributed more asymmetrically with reference to the axis of the orifice plate jet. This suggests that an orifice plate generates more complex three-dimensional structures compared with a smooth contracting jet. As a result, the length of the potential core (defined as the region of the jet in which the axial mean-velocity remains nearly equal to the jet exit velocity [48]) for the orifice-plate jet (~ 3 to $4D$) was found to be shorter than that of the smooth contracting nozzle (~ 5 to 6 D). The results of Mi *et al*., [32] agreed with that of Quinn [19].

2.1.1. Turbulent jets with co-flowing (coaxial) stream

Turbulent coflowing jets, i.e., jets flowing coaxially, are frequently used in many engineering applications such as pumps, mixing tanks, cooling systems and in premixed and non-premixed combustion power systems [49–51]. For instance, in non-premixed combustion, it has been reported that the use of co-flow stream can help in enhancing flame stability and combustion efficiency by shortening the flame and also reducing pollutants emission [52]. Coflowing jets are also found useful for studying the structure of jets in general because the coflow eliminates the possible “backflow” encountered in a confined jet which also prevents from the problems associated with measuring the nearly-zero velocities at the edge of the shear layer of a free jet [53]. It is also found that a coflowing jet configuration provides more stable flow conditions compared to free jets. Other studies demonstrated that presence of co-flow in general alters the stability of a diffusion flame significantly [30, 54, 55].

There have been numerous studies investigating the flow characteristics of coflowing turbulent jets [49–53, 56–63]. Forstall and Shapiro [56] concluded that the initial mean-velocity ratio of coflow to jet (i.e., U_{co}/U_{jet}) is the most important parameter in determining the flow configuration. Williams *et al*. [51] tested a coaxial jet with U_{co}/U_{jet} around unity and observed that while the potential core of the annular jet is inclined slightly inward, it does not coalesce with the potential core of the central jet. It was also shown that with increasing coflow rate, the length of the central jet core increased up to a certain limit. Nonetheless, it was shown that the length of the potential core of a coflowing jet is greater than that of a jet discharging into stationary air [51].

Up to the 70s, most of published studies investigating coaxial jets were limited to mean flow characteristics rather than turbulence. In 1971, however, Champagne and Wygnanski [57] examined the flow characteristics of a turbulent coflowing jet and demonstrated that the distribution of turbulence intensities is strongly affected by the shape of the mean velocity profile and hence by the nozzle geometry. They concluded that most of the mixing in turbulent coflowing jets occurs in the near-field region where the potential core of the jet and co-flow forms. The study of Ko and Kwan [58] on the initial region of coflowing jets demonstrated that the vortices created in the mixing layer between the jet and co-flow (inner mixing region) are at higher frequency and hence more dominant compared with the lower-frequency vortices generated in the mixing layer between the co-flow and the quiescent ambient (outer mixing region). They confirmed also the earlier conclusion that, in a coflowing jet, the length of the potential core depends on the co-flow strength (which is also confirmed by Warda *et al*., [62]), yet it is much longer than that of a free jet which results in a reduction in the radial spread of the co-flowing jet compared with that of a pure jet. This phenomenon was attributed to the fact that in a co-flowing flow the central jet acts similar to a jet discharging into a stream with uniform velocity in which the width of the inner mixing layer becomes smaller compared with that of a non-coflowing jet. It was also observed that reducing the co-flow strength results in the deflection of the annular jet toward the axis of the jet indicating that the inner central jet becomes relatively more dominant. Kwan and Ko [59] in another study further investigated the characteristics of the vortices and found that the inner high-frequency vortices are generated further upstream (~ 1 or 2 D) compared with the outer low-frequency vortices. They obtained also that the downstream convection velocity for the inner vortices is a function of both the jet and co-flow velocities (i.e., 0.6 ($U_{jet} - U_{co}$) + U_{co}), but only a function of the co-flow velocity for the outer vortices (i.e., 0.6 U_{co}). Finally, they concluded that there are two "trains of vortex rings" in the inner and outer mixing layers, and that these vertices in coflowing jets are characteristically similar to the vortical motions of a free (single) jet. Dahm *et al*. [60] implemented a broad flow visualization of the vortical motions and their dynamics patterns and interactions in the near field of a circular coflowing jet and concluded that a wide variety of dramatically differing near field vertex patterns can arise. Their results indicated that variations in the potential core length does not linearly depend on the co-flow to jet velocity ratio, but instead show a nonlinear dependence. In fact, such a phenomenon was attributed to the flow near-field vorticity dynamics, which depends not only on the co-flow to jet velocity ratio but also on the magnitude of velocities of the jet and co-flow. Buresti *et al*. [64] investigated the vertex characteristics of a co-flowing jet and concluded that overall the length of the potential core of the co-flowing jet is a fundamental parameter which affects the flow characteristics and its downstream development.

Up to now, most published studies of coflowing jets were limited to investigating the velocity ratio (U_{co}/U_{jet}) of coaxial jets with the coflow stream having a finite cross-sectional area in the same order with that of the central jet, but almost no studies on the effect of cross-sectional area of the co-flow or other geometrical parameters such as the lip thickness of the central nozzle. In 1996, however, Nickels and Perry [53] studied a turbulent jet issuing into a coflowing stream of infinite extent. It was concluded that the length of the jet potential core increases with the area ratio of the co-flow to the central jet (in comparison with previous studies, e.g., Williams *et al*., [51]), and therefore, it is the longest for the jet with an infinite co-flow. Buresti *et al*. [61] investigated the effect of wall thickness of the central jet of a co-flowing jet and concluded that increasing wall thickness might accelerate mixing between the central jet and its co-flowing stream due to the vortex shedding and generation of a wake behind it. They demonstrated that sharpening of the inner nozzle edge causes a reduction in the radial fluctuations and Reynolds stresses in the near field; however, the effect of lip thickness was found to rapidly decreases, and becomes negligible beyond the potential core. Recently, Warda *et al*. [63] varied both U_{jet} and U_{co} to further investigate the effect of magnitude of initial mean velocity. Their result showed that a reduction in the magnitude of the velocities of both jet and co-flow, while keeping the velocity ratio constant, made the co-flowing jet decays faster along the centerline and increased the spread rate. Their results demonstrated also that the development of turbulence intensity, u/U_{jet}, on the centerline was affected by varying the absolute initial velocity of the jet and co-flow. However, a coherent and consistent trend was not observed. Experimental study of Sadr and Klewicki [49] demonstrated that the magnitude of axial turbulence intensities on each side of the central jet edge is subject to the velocity magnitude of the corresponding jet which confirms earlier statement that, in addition to the initial mean-velocity ratio, the absolute velocity also affect the downstream development and flow characteristics of a co-flowing turbulent jet. Their results also indicated that the values of the integral and “Taylor length” scales in the shear region (between the central jet and co-flow) are linearly proportional to axial distance, x, (measured from the jet exit) which indicates that size of both the “energy-containing” eddies and eddies responsible for “small-scale stirring” grow at nearly the same rate. Their results reinforce the conclusion that the turbulent structures in the inner mixing region of a coflowing jet are highly anisotropic [49].

Overall, it was concluded that the parameters characterizing the configuration, and therefore potentially affecting the physical characteristics of the various regions of a coflowing jet flow, are many. These parameters include (but not limited to) the central jet and coflow velocity profiles at the nozzle exit, the jet and coflow exit area, the wall lip thickness of the central nozzle, the boundary layer momentum thickness at the nozzle exit, as well as weather the flow is in laminar or turbulent regime, and the turbulence level of both jet and coflow at the exits [49, 58].

2.1.2. Turbulent jets from asymmetric nozzles

Most studies in the literature, as discussed above, are limited to investigating the characteristics and development of turbulent jets issuing from axisymmetric nozzles and comparatively fewer studies dealt with jets issuing from asymmetric nozzles. However, there is still a considerable number of studies on non-reacting (isothermal) flows which demonstrated that non-symmetric (e.g., rectangular, elliptical, triangular, etc) fuel nozzles have the potential of inducing a wider range of turbulent structures as opposed to their counterparts’ axisymmetric nozzles [18, 65–69]. In fact, it was shown that asymmetric nozzles (especially the rectangular and elliptical nozzles) increase air entrainment and hence mixing between the (central) jet and its surrounding ambient (stagnant or co-flow) via increasing the jet axial mean-velocity decay and speeding its radial spread in comparison with that of axisymmetric nozzles which consequently can improve the stability limits of the ensuing flame (e.g., [65, 70–75]). This, in general, is attributed to the presence of "higher-order instability" modes and the "self-induction" process of the jet vortices occurring in the flow-field of the asymmetric jets which are more unstable than those in the rounded jet configurations. The reported improvement in the jet entrainment rate of asymmetric nozzles as opposed to their axisymmetric counterparts, specifically in the near-field region, also supports the earlier presumption that changes in the exit flow pattern of a jet through changes in the nozzle shape propagate downstream into the far-field [25]. For instance, Ho and Gutmark [76] investigated the jet characteristics from an elliptic nozzle with $AR = 2$ versus its corresponding axisymmetric jet and concluded that the ambient entrainment of the elliptical jet is noticeably higher than that of its circular counterpart. Later on, Gutmark *et al*. [77] observed a similar scenario for an elliptic and a rectangular nozzle with aspect ratio of three. They found that both the rectangular and elliptic jets significantly enhanced entrainment and mixing with the ambient fluid in comparison to a circular jet. Gutmark *et al*. [78, 79] investigated also the vortical structures just behind the corners as well as on the flat sides of triangular and rectangular nozzles and concluded that the interaction between the coherent structures shed from the flat sides of the nozzle with the smaller structures generated behind its corners create a wide range of turbulent structures and, therefore, are presumably responsible for better mixing and higher entrainment of a non-symmetric jet compared with the axisymmetric counterpart.

In general, a rectangular or elliptical jet has qualitatively common characteristics of a circular jet. That is, the flow field can be divided into (*i*) a near-field (developing) region, and (*ii*) a far-field region, in the same way the flow field of a conventional turbulent axisymmetric jet. Likewise, the exit velocity profile of an asymmetric jet gradually changes from a step-shape profile to a rounded shape in the near-field region while it maintains its rounded shape farther downstream in the far-field region in spite of the jet axial decay, which implies self-similar behaviour of the mean-velocity profile (e.g., [18, 27]). However, the inception of the self-similar region might be delayed due to the level of asymmetry of the jet. For instance, the study of Grandmaison *et al*. [27] on the scalar mixing field of a turbulent rectangular jet emerging from a sharp-edged orifice with an aspect ratio AR = 10 indicated that, in the near-field, the mean concentration axial decay is characterized by the dimension of the jet narrow side implying that a rectangular jet with a large aspect ratio behaves similarly to a plane jet. On the contrary, they found that in the far-field region, the axial mean-concentration decay rate is characterized by a length scale called "equivalent diameter" which is equal to the exit diameter of a round jet with the same cross-sectional area ($D_e = \sqrt{4A/\pi}$). The flow field of a low-aspect-ratio rectangular nozzle, on the contrary, is reported to be characterized by the equivalent diameter (D_e) both in the near-field and far-field regions. Nevertheless, Grandmaison *et al*. [27] found the centerline decay rate to be considerably higher for the rectangular nozzle compared with that of the round jet. It is believed that asymmetry, in general, induces different turbulence structures in the flow field which then leads to an increase in the jet decay and subsequently higher jet entrainment and spreading rates. The "vena contracta" previously seen in jets issuing from sharp-edged circular orifice [32] were also seen in non-symmetric nozzles. In fact, the presence of vena contracta in the flow was attributed to the existence of the edge of a sharp orifice (regardless of its exit shape) which generates an inward radial velocity component in the nozzle exit [32]. However, "axis-switching" phenomena associated mainly with rectangular and elliptical jets [80–85] is not observed in axisymmetric jets, and, therefore is only associated with asymmetric jets, especially turbulent jets issuing from elliptical and rectangular nozzles, as mentioned earlier. Axis-switching occurs when the jet width in the minor axis of an asymmetric nozzle (e.g., a rectangular or an elliptical nozzle) which is initially lower than that of the major axis catches up with the jet width in the major axis at a point called "axis-switching". To identify the axis-switching point location, however, instead of determining the jet width in the minor and major axes, the jet half width parameter (the radial location where the axial velocity component is half of the centerline velocity at the same axial distance from the nozzle exit) is used. That is, axis-switching point is where the half width of the jet in the minor axis becomes equal to that of in the major axis.

So far, no clear reason(s) has been found behind the occurrence of axis-switching phenomenon; however, it has been claimed by many researchers that axis-switching is the major reason for the higher entrainment and mixing associated with asymmetric jets compared with that of axisymmetric (Gutmark and colleagues. [66, 79, 86, 87] and Iyogun *et al.*, [88]). It was concluded that the axis-switching phenomenon enhances large-scale mixing due to self-induction of vortical structures originated from both, the flat sides and corners of asymmetric nozzles. These findings also demonstrated that axis-switching occurs mainly due to the exit asymmetry of an elliptical or rectangular nozzle irrespective of its aspect ratio or internal contracting geometry.

"Saddle-backed" velocity profile is another phenomenon observed in the flow-field of some asymmetric nozzles [26]. It has been reported that the occurrence of saddle-backed velocity profile, in general, is observed only within the near-field region along the major axis of a rectangular jet with aspect ratios (AR) not lower than 5 [27, 68, 89]. Therefore, the occurrence of saddle-backed and vena contracta phenomena might not be the major causes of higher entrainment associated with asymmetric nozzles compared with axisymmetric nozzles.

A common denominator of these studies reviewed above is that asymmetric nozzles enhance mixing between the jet and its ambient and consequently leads to higher entrainment compared with axisymmetric nozzles. However, there are still discrepancies in the literature on the extent of the increase in entrainment associated with these nozzles (i.e., asymmetric nozzles) compared with circular nozzles [65, 77–79, 90]. For instance, Gutmark *et al*. [77–79] reported substantial increase in the entrainment and spreading of the rectangular jets with AR = 2 compared to their circular (axisymmetric) jet counterpart; however, Zaman [90] observed only slight improvement. This discrepancy was attributed to the considerably higher exit velocity of Zaman's experiment which resulted in very different Reynolds numbers between the two studies [90]. In another study, Zaman [90, 91] reported that varying the exit orifice aspect ratio does not noticeably change the spreading and entrainment rates of a rectangular nozzle with AR < 10. This result, however, does not agree with the observations of Quinn [92] who reported a considerable improvement in jet entrainment of a rectangular nozzle whose aspect ratio was increased from 2 to 10. Numerical studies (e.g., Faghani *et al*., [93] and Akbarzadeh *et al*., [94]) also reported noticeable improvement in the near-field entrainment of a rectangular nozzle with AR = 4 compared with that of a nozzle with AR = 2. These contradictions were also attributed to different flow conditions between these studies. A similar scenario was presumed to be the reason for the difference in the results of Mi *et al*. [95] and Quinn [68]. The study of Riopelle *et al*. [96] on a two-dimensional plane and an axisymmetric jet, however, demonstrated that conditions other than flow conditions (e.g., velocity and Reynolds number) such as the ambient pressure can also cause discrepancies in the results. To the best knowledge of the present author, there is no published study on the effect of exit velocity or Reynolds number on the flow characteristics and development of asymmetric jets (issuing from rectangular or elliptical nozzles). However, as it was reviewed in the previous section, the study of Warda *et al*. [62] demonstrated that the exit velocity (and correspondingly Reynolds number) does have an effect on the development of a coflowing jet. Such a conclusion can presumably be extended to flow development of axisymmetric and asymmetric jets.

While there are considerable experimental studies on the jet flow characteristics of rectangular nozzles [67, 92, 95, 97–102], comparatively there are a few numerical simulations/studies conducted on this three-dimensional type of turbulent flows [80–85, 93, 103–105] which might be mainly due to the significant computational time and the required memory associated with these flow simulations. Numerical studies of these three dimensional turbulent flows can provide other details that might not be achievable experimentally. Akbarzadeh *et al*. [94] presented a fairly comprehensive summary of these studies and concluded that, to date, a comprehensive numerical study that can resolve reasonably all structures of a turbulent rectangular jet is lacking. This was attributed to the complex three-dimensional behavior of these flows and also the weakness of the available turbulence models, and also to the fact that LES and DNS are very costly at high Reynolds numbers pertaining to the flow regimes of turbulent rectangular jets.

There have been also several studies on free turbulent jets issuing from nozzles with more complex geometries such as lobbed nozzles and those with tabs [74, 80, 81, 91, 106–111]. Such nozzle geometries were aimed at enhancing ambient fluid entrainment via increasing the interface area of the jet and its ambient fluid, and also in producing more complex vortical structures that can persist farther downstream. Nathan *et al*. [13] presented a comprehensive review of jets from these types of nozzles.

2.2. Turbulent diffusion flames

Turbulent jet diffusion flames (non-premixed combustion) are used in various engineering combustion power systems owing to their safer operation mainly due to the absence of flashback. In understanding flame stability, the flame liftoff height and velocity as well as blowout and reattachment velocities are important parameters. The particular focus of this study is on the inception of liftoff of an attached flame and the liftoff height of a lifted flame. These parameters are introduced (in brief) later in this section but will be explained with more details in the results chapter.

In the last decades, numerous published studies were devoted to understanding these flame stability parameters and their governing mechanisms [8–11, 112–114]. These studies advanced our understanding of turbulent diffusion flames. In fact, it was unanimously agreed that by increasing the fuel velocity (U_{jet}) of an attached diffusion flame beyond a critical velocity (called "liftoff velocity"), the flame lifts off from the burner and stabilizes above it. The vertical distance between the lowest point of the lifted flame from its burner is called "liftoff height". Further increase in the fuel velocity results in an increase of the flame liftoff height (H_l) and eventually leads to the extinguishment of the flame above another critical velocity called "blowout velocity". It was also proved that by decreasing the fuel jet exit velocity, a lifted diffusion flame would stabilize closer to the burner (i.e., flame liftoff height continuously decreases) and abruptly attaches back to the burner at a velocity (i.e., "reattachment velocity", U_r) lower than the velocity at which it initially lifts off from the burner (liftoff velocity, U_l). This phenomenon (i.e., the reattachment velocity to be lower than the liftoff velocity) is referred to as "hysteresis phenomenon" in the literature [4–7, 55, 115, 116].

Several theories were proposed in terms of correlations between the flame stability parameters (e.g., liftoff height and blowout velocity) and fuel jet conditions (e.g., fuel jet diameter and bulk velocity). In particular, the liftoff height (H_l) has been studied extensively and several theories have been proposed to explain the stabilization mechanism of a lifted diffusion flame. In the following, a summary of existing stabilization theories/mechanisms of a lifted flame is presented.

The first theory called "premixed theory" was proposed by Vanquickenborne and Van Tiggelen [8] in 1966. It states that the fuel and oxidizer are completely mixed before the combustion (of a lifted flame) and the flame front propagates with the turbulent burning/propagating velocity of a premixed flame, which is maximum for the stabilization point on the stoichiometric contour. Expanding on this theory, several correlations between the liftoff height and fuel conditions were proposed, which will be explained later in this section.

The second major theory called "flamelet extinction theory" was first presented by Peters and Williams [10]. This theory suggests that the extinction of laminar "diffusion flamelets" by "flame stretching" determines the position of the flame base. In fact, no premixing prior to combustion is assumed, instead the flame is assumed to consist of several laminar diffusion flamelets. This assumption justifies the wrinkled-shape of the front edge of the flame. However, the flamelet extinction mechanism/theory does not address the existence of fluctuations in the location of flame base. In addition, the scalar dissipation rate, which is used to scale the liftoff height in this theory, was found to be considerably lower than its critical value for flame quenching at liftoff [21, 117, 118].

Other theories, for instance, "turbulence intensity theory", "large eddy theory" and "triple flame theory" either used the premixed theory or assumed a sort of partial premixing between fuel and oxidizer ahead of the flame base. For example, using the premixed theory, Kalghatgi [9] determined that turbulent burning velocity controls the propagation speed of the flame base, and it is proportional to the axial turbulence intensity. Kalghatgi [9] derived an equation that showed a linear relationship between the flame liftoff height and fuel jet velocity. Broadwell *et al*. [11], however, assumed that combustion takes place both in laminar-diffusion-type flamelets formed at the interface between the fuel and air, and also in the premixed patches of the flow. In fact, this theory stresses that re-entrainment of the flow structures that carry hot combustion products sustains a stable lifted flame [119]. That is, according to this theory, the flame quenches when the time required for re-entraining structures (which contain hot products) to mix with upcoming fresh mixture (toward the flame front) is less than a critical chemical time required for ignition. Finally, a more recent theory called "triple flame theory" argues that the leading edge of a lifted diffusion flame is partially premixed, and hence can propagate upstream [120, 121]. The triple flame consists of a "triple point" at the flame base followed by lean and rich branches downstream and the trailing "diffusion filament" at their interface. Although it is fairly accepted that the triple flame theory is the governing mechanism of a laminar diffusion lifted flame, the presence of this triple flame is not yet clearly observed in a turbulent diffusion lifted flame [1]. In the following, the existing studies on the stability parameters of turbulent diffusion flames (particularly for methane flame) are reviewed.

The Schlieren photographs of a lifted flame provided by Eickhoff *et al*. [5] showed that there is a fluctuating turbulence pattern upstream of the flame base, indicating the importance of turbulence intensity and the intermittent character of the fine scale structures which can support the concept of premixed combustion. Coats and Zhao [6], on the other hand, showed evidence of a "cellular-type" structure. They believed that lifted flame remains sensitive to the initial conditions of a fuel jet up to a considerable distance above the nozzle (~ 10 D), and concluded that models which assume flame propagation into fully developed turbulent flow are not necessarily adequate for lifted flames in the near-burner region. This may justify the non-linear character of flame liftoff height with respect to the fuel jet velocity in the proximity of flame liftoff event (e.g., [9]). Coats and Zhao [6] concluded that the reaction zone/layer is located away enough from the central jet's shear region, which does not seem to explain the fluctuating nature of the flame base, especially by considering the fact that the fluctuations in the flame base do not undergo an organized and predictable trend. Thus, its cause cannot be attributed to the organized flow structures; instead it indicates the presence of turbulence in the proximity of a flame base [118, 122, 123]. Langman *et al* [16] believed that the "well-established" differences in the turbulent source flow propagate to the far-field (far downstream) and consequently influence the flame. They believed that both the boundary-layer thickness of the discharging jet and the exit velocity profiles are the controlling parameters in the development and growth of large-scale structures.

These studies also advanced our understanding of the stability of an axisymmetric free jet flame (the most conventional type of a turbulent diffusion flame). For example, it is well established that the flame liftoff height, H_l, of a pure jet flame above several diameters from the nozzle varies linearly with the fuel jet velocity, U_{jet}, (e.g., [9, 114, 124–126]). Closer to the nozzle exit, however, the flame liftoff height departs slightly from the linear correlation with the fuel jet exit velocity [9, 116, 127, 128]. In many practical combustion systems, however, a co-airflow stream is introduced in order to increase the efficiency of the combustion process [129], shorten the flame length and reduce the residence time for NO_x formation [52]. The stability of a co-flowing jet flame, however, is not studied as extensively as that of free jet flames, yet there have been several studies on a jet flame in the presence of a co-airflow stream (e.g., [112–115, 124–126, 130–133]). It is demonstrated that a co-flowing lifted diffusion flame has higher liftoff height and a reduced blowout velocity (e.g., [126]). Cha and Chung's experimental results [124] revealed that the H_l for a confined diffusion flame was greater than that of a free/single (i.e., without a co-airflow) jet flame. In fact, replacing the fuel jet exit velocity, U_{jet}, in the conventional liftoff height relation for a pure jet flame ($H_l = f(U_{jet}, U_{co}, etc)$ where U_{co} refers to the velocity of coflow stream) by an effective jet velocity, U_{eff}, (a combination of the co-flow and fuel jet velocities) resulted in a more generalized formulation ($H_l = g(U_{eff}, etc)$) for the liftoff height of a co-flowing jet flame [112, 126, 130]. However, there exist some discrepancies with the concept of this correlation. For example, the studies by Muñiz *et al.* [114] and Brown *et al.* [131] reported that within a range of jet and co-flow velocity, increasing the fuel jet exit velocity would result in a reduction in the flame liftoff height, and that the liftoff height becomes insensitive to the fuel jet exit velocity at very high co-flow velocity (e.g., U_{co}> ~2 m/s for ethylene flame, and U_{co}> ~ 0.5 m/s for methane flame in [131]).

The presence of a hysteresis phenomenon in the proximity of flame liftoff, while reducing the jet velocity, was also observed in diffusion flames with coflow. However, recent studies [55, 115, 116] reported the presence of a newly observed aspect of hysteresis phenomenon in a lifted co-flowing flame where a noticeable increase in the liftoff height is observed when decreasing the fuel jet exit velocity (in the range close to the flame liftoff and/or reattachment velocity). This led either to an abrupt reattachment of the flame [55, 115, 116] or blowout of the flame at high co-flow velocity. Within this velocity range, the flame liftoff height did not follow a linear relationship with the effective jet exit velocity.

A review of the literature revealed also discrepancies on the effect of fuel nozzle geometry on the liftoff velocity. For example, Kalghatgi [9] found that the liftoff velocity, U_l, of an axisymmetric jet flame without co-flow is independent of a nozzle's diameter, which was later confirmed by Chung and Lee [134] for a laminar diffusion flame. However, Eickhoff *et al.* [5] showed that while turbulent flame liftoff velocity for a contracting circular nozzle is fairly insensitive to a nozzle diameter, turbulent flame liftoff velocity for a pipe slightly reduces with increasing nozzle diameter. In contrast, Gollahalli *et al.* [7] and Norheim *et al*. [135] showed that liftoff velocity for a contoured circular nozzle decreases with nozzle diameter. Kumar *et al.*, [136] concluded that the proposed stability theories are unable to explain the effect of the fuel jet diameter on the flame liftoff.

The internal geometry of a nozzle also affects the liftoff velocity of diffusion flame [5–7, 16]. For instance, Eickhoff *et al.* [5] found that a contracting circular nozzle has a liftoff velocity larger than that of a pipe nozzle. Langman *et al.* [16] and Iyogun and Birouk [44] showed that liftoff transition for a diffusion flame from a contracted circular nozzle involves necking and holes in the flame close to the nozzle exit as opposed to that of the pipe which undergoes an abrupt liftoff. In fact, the liftoff phenomena is studied quite extensively in the literature [4–7, 16, 137, 138]. Scholefield and Garside [4] attributed the liftoff phenomena to the effect of several factors such as turbulence, thermal diffusion and velocity distribution. However, they could not define the significance of influence of each factor clearly. Eickhoff *et al*. [5] reported that, by increasing the fuel rate, the attached flame from both pipe and nozzle detaches abruptly. They attributed the flame detachment to the interference of small-scale vortical motions/structures (as opposed to large-scale structures) with the reacting layer (flame front). They believed that at the liftoff velocity, U_l, the "inner high frequency vortices", which are superimposed by turbulence, interfere with the reacting region. The diffusion flame is then extinguished at the interference edge as excessive heat is diffused through small-scale turbulence structures. Gollahalli *et al*. [7] reported that the liftoff phenomenon is governed by flow structures and thermal diffusion.

Takahashi and Schmoll [137] classified four different types of lifting criteria based on observation of diffusion flames from axisymmetric nozzles in the presence of co-airflow. Coats and Zhao [6] stated that at liftoff, a transition from laminar regime to turbulence occurs in the combustion flow which is related to changes in the characteristics of the structure of the central fuel jet. They stated that the low-frequency instability dominates the flame in the lower Reynolds number range. However, transition in the main body of the flame suppresses those structures and cause liftoff to precipitate due to the "invasion" of the laminar flame base by turbulence present in the central jet gas [6]. It was also reported that co-airflow exit velocity has an influence on the flame liftoff velocity [30, 125]. For instance, the results presented by Chen *et al.* [125] and Leung and Wierzba [30] on the dependence of U_l on the co-flow velocity were qualitatively different from those of Iyogun *et al.* [88]. This discrepancy might be related to differences that might exist between the set-up arrangements employed in these studies. It can also be attributed to the presence of enclosure in the studies of Chen *et al.* [125] and Leung and Wierzba [30].

Most studies in the literature, as briefly discussed above, are limited to the stability of turbulent diffusion flames issuing from axisymmetric nozzles and only a few studies dealt with flames issuing from asymmetric nozzles. On the other hand, as mentioned in the previous section of this chapter, there is a considerable number of studies on non-reacting (isothermal) flows which demonstrated that non-symmetric (e.g., rectangular, elliptical, etc) fuel nozzles have the potential of inducing a wider range of turbulent structures as opposed to their counterparts' axisymmetric nozzles [18, 65–69]. It was shown that asymmetric nozzles (especially rectangular nozzle) increase air entrainment and hence mixing between the (central) jet and its surrounding ambient (stagnant or co-flow) which can improve the stability limits of the ensuing flame (e.g., [69]). There are several studies on turbulent diffusion flames from asymmetric nozzles [15, 17, 65, 69, 79, 139, 140]. However, only a few of them discussed the stability issue [15, 69, 139]. The study of Luo [140] on rectangular nozzles is limited to studying the vorticity field. The study of Gollahalli *et al.* [139] on elliptical fuel nozzles reported that asymmetric nozzles produce a wider flame stability limits compared to a circular fuel nozzle. Recently, Iyogun and Birouk [15] employed several asymmetric fuel nozzles and reported an enlarged flame stability limit, especially for the rectangular nozzle, compared with that of an axisymmetric nozzle. However, their study was limited to presenting the mean-velocity decay and spread rate profiles of the ensuing jet from smooth contracted nozzles. That is, the effects of the internal geometry of the fuel nozzle and co-airflow velocity were not explored.

2.3. Motivations and objectives

The literature review on the stability of turbulent non-premixed (diffusion) flames demonstrates that there have been several studies on jet flames emerging from conventional axisymmetric fuel nozzles (i.e., pipe or smoothly contracted nozzle). However, a study that investigates the effect of nozzle geometry on the stability of turbulent diffusion flame in a systematic way is still lacking. The literature reviewed above showed also that the effect of co-airflow on flame stability is still not thoroughly understood. Also, as mentioned previously, most studies on coflowing turbulent jets were performed under relatively high U_{co}/U_{jet} conditions (i.e., U_{co}/U_{jet} >> 0.1) within which a stable lifted flame is usually not attainable. Thus, the first part of the present study/thesis attempts to report on this issue. That is, to examine the impact of a circular nozzle's internal geometry and co-airflow strength on some aspects of the stability of co-flowing methane turbulent flame.

The review presented above also shows that there are several studies on turbulent diffusion flames from asymmetric nozzles. However, most of them focused only on determining the concentration of species and temperature fields, and only a few discussed the stability issue [15, 69, 139]. Gollahalli *et al*. [139] studied elliptical fuel nozzles and found that this type of nozzles produce wider flame stability limits compared with its circular counterpart. Luo [140]'s study on rectangular nozzles is also limited to providing the vorticity field. Only recently, Iyogun and Birouk [44] investigated the stability limit of methane flame from several asymmetric nozzles with a fixed internal geometry. Their study, however, did not report on the effect of a nozzle's exit orifice shape combined with its internal geometry on the stability limits of a turbulent diffusion flame. Thus, the present study aims to examine the impact of varying the nozzle exit orifice shape and coflow strength in conjunction with the nozzle internal geometry.

CHAPTER 3
THE EXPERIMENTAL SET-UP

3.1. Test set-up

The experimental test rig employed in this study consists mainly of an interchangeable fuel nozzle and a co-airflow. The fuel nozzle is attached to a central supply pipe which is connected to a supply cylinder of fuel, as shown in Fig. 3.1. The co-airflow is delivered from a laboratory compressed supply line. The flow rates along with the exit cross-sectional areas were used to determine the exit velocities (i.e. bulk velocities) quoted in the present study.

For laser-based velocity measurements, the desired flow rates of air passes through a settling chamber and mixes with incense smoke which is estimated to have an average diameter of approximately 0.3 μm. Published studies demonstrated that incense generates adequate seeding particles capable of tracing the flow instantaneous motion [125]. The seeded airflow leaving the seeding chamber is then conveyed through a central pipe with a diameter of 7.62 mm before exiting through the (fuel) nozzle, which is attached to the central pipe. To ensure a well-developed jet flow in the pipe, the ratio of the length to diameter of the supply pipe (L_p/D_p) is about 135, which is far greater than its corresponding minimum required ratio for a fully developed turbulent flow over the range of Reynolds number attained in the present study [141]. The geometrical specifications of the nozzles tested in the present study are given in Table 3.1. The nozzles, with different internal geometrical parameters, i.e., equivalent diameter, contraction angle, and orifice length to diameter ratio, have two different exit orifice shapes; that is, an axisymmetric circular and an asymmetric rectangular with an aspect ratio (AR) of 2 (shown in Fig. 3.2).

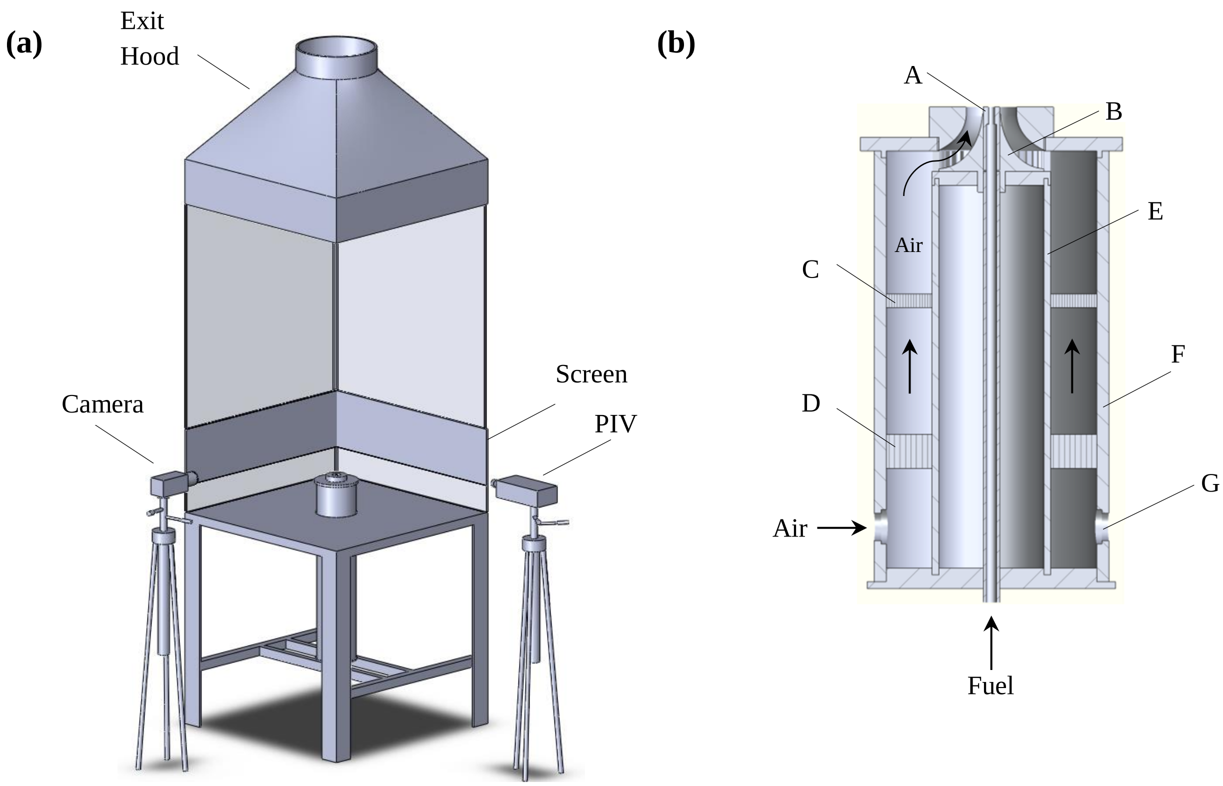

Fig. 3.1 (a) Arrangement of the experimental set-up and position of the PIV and camera, and (b) schematic of the experimental burner A=nozzle, B=nozzle holder, C=fine screen, D=honeycomb, E=inner annulus, F=outer annulus, G=air ports

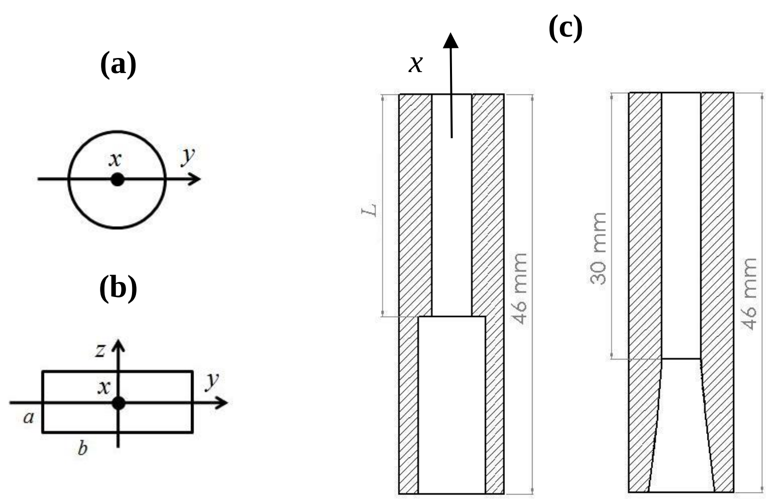

Fig. 3.2 PIV measurements planes of (a) the circular nozzle and (b) the rectangular nozzle, and (c) schematic diagram of the nozzle internal geometry

The selected co-airflow rate, which is supplied to the burner from a laboratory compressed air line, mixes with smoke particles in a seeding chamber, then flows through four equally-spaced tangential ports of the outer annulus, and before discharging into the atmosphere, the air travels through a set of flow conditioning honeycombs and screens as schematically shown in Fig. 3.1. The seeding level of the co-flowing air is controlled by adjusting the fraction of the total airflow rate that bypasses the seeder (the remainder fraction flows through the seeder where it mixes with the seeding particles). The co-airflow discharges into the atmosphere through an annulus with an inside and outside diameter of 14.9 mm and 36.6 mm, respectively.

Table 3.1 Nozzle geometry test matrix

Nozzle Geometry	Experiment #1	Experiment # 2	Experiment # 3
Contraction angle	90 degree	90 degree	90^{o} & Smooth
L/D_e	1	1, 2.6 and 5.6	5.6 and 6.2
D_e (mm)	2, 3 and 4.5	4.5	4.5 and 4.8 (C), 4.7 (R)

C: Circular, R: Rectangular

Dantec Dynamics two-dimensional particle image velocimetry (PIV) was used to characterize the jet flow field. The PIV system consists mainly of a 120 mJ/pulse laser with 532 nm wavelength to illuminate the flow field, and a 12-bit high-resolution digital camera (Dantec Dynamic NanoSense MKIII camera) with a 1024 pixels × 1260 pixels CCD and 12 μm pixel pitch coupled to a 60 mm AF Micro Nikkor lens. The laser sheet was located in the symmetry plane of the jet which allows the PIV measurements to be performed along the jet centerline $x-y$ and $x-z$ orthogonal planes. Instantaneous image pairs of at least 2000 were used to determine the jet flow orthogonal mean velocities, U and V, and their mean fluctuating components (u and v). Figure 3.1 shows the experimental set-up and the arrangement of the laser and camera for the

PIV system. For a given interrogation window size, the laser pulse delay time was determined based on the particle displacement of one quarter of the interrogation width to ensure a good signal-to-noise ratio (Dantec Dynamic PIV Manual). The instantaneous images were processed using 16 pixels × 16 pixels interrogation window with a 50% overlap and adaptive correlation. The adaptive-correlation method is a more modern version of the standard cross-correlation algorithm which utilizes a multi-step Fast Fourier Transform (FFT) cross-correlation to calculate the seeding particle’s average displacement in each interrogation area (http://www.dantecdynamics.com). The Gaussian window function and the low-pass Gaussian filter of Dantec Dynamics FlowManager software were used as input and output filters, respectively, to the correlation algorithm. A moving-average validation technique was used for image processing. The principle of PIV and the error estimation analysis are presented in Appendix A. The analysis of 16 pixels × 16 pixels and 8 pixels × 16 pixels interrogation windows demonstrated that the results were grid independent (see Appendix B).

The flame liftoff height was measured using the same camera of the PIV system. An in-house developed MATLAB code (see Appendix C) was used to analyze flame images and determine the flame base by calculating the number of pixels between the nozzle exit and the flame base. A threshold is applied to separate the background from the real flame image [142]. The MATLAB code assigns each pixel a brightness level between 0 and 256, with 0 being black and 256 being white. The number of pixels between the flame base and the nozzle exit is then multiplied by a pixel height to determine the liftoff height of the flame (the liftoff height, denoted here as H_l, of a typical diffusion flame is shown in Fig. 3.3). The error estimation analysis for liftoff height and velocity measurement is also presented in Appendix A.

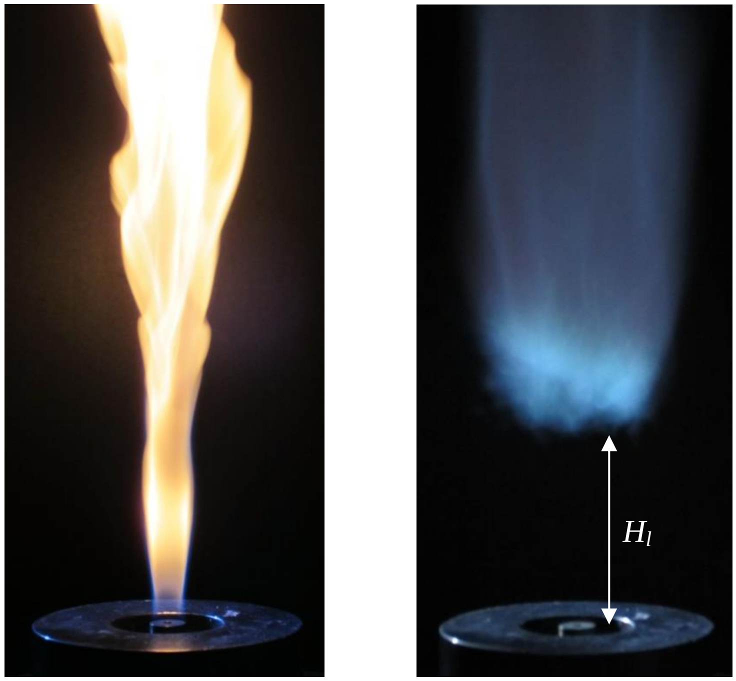

Fig. 3.3 A typical image of an attached flame (left) and lifted flame (right).

3.2. Test conditions

In the present experiment, the test conditions consisted of varying the nozzle's geometry, the fuel jet exit velocity (U_{jet}), and the co-airflow exit velocity (U_{co}). The effect of nozzle geometry is examined as follows. In the first experiment, the parameter being varied was the nozzle orifice equivalent diameter while the other parameters were kept unchanged (experiment #1 of Table 3.1). In the second experiment, the orifice length to diameter ratio (L/D) was varied while keeping all other parameters fixed (experiment #2 of Table 3.1), and in the third experiment, two nozzles having approximately the same exit orifice diameter and length to diameter ratio but with different contraction angle (sudden or smooth). To examine the effect of the exit orifice shape of the nozzle (i.e., a circular or a rectangular exit), the internal geometrical parameters of the nozzles (i.e., equivalent diameter, contraction angle, and orifice length to diameter ratio which are fixed during one experiment) were kept fixed. In the present study, a low-momentum co-airflow stream with a maximum exit velocity of ~2 m/s was employed. Detail of the experimental arrangement and test conditions are given in Table 3.2.

Table 3.2 Test conditions

Orifice diameter, D_e* (mm)	2	3	4.5	4.9 (C) 4.7 (R)**
Contraction angle	90 degree	90 degree	90 degree	Smooth
L/D_e	1	1	1, 2.8 and 5.6	6.2 (C) 6.3 (R)
U_{co} (m/s)	0 – 0.5	0 – 1	0 – 1.65	0 – 1.8
U_{Jet} (m/s)	0 – 42	0 – 55	0 – 80	0 – 100
Re	0 – 5500	0 – 10500	0 – 23000	0 – 31000

* $D_e = \sqrt{4A/\pi}$ where $A = 4ab$ (Fig. 3.2(b)) is the exit area of the rectangular nozzle

** The rectangular nozzle (R) has exit aspect ratio, $AR = b/a = 2$ (Fig. 3.2(b))

CHAPTER 4
RESULTS AND DISCUSSIONS; STABILITY OF TURBULENT DIFFUSION FLAME FROM A CIRCULAR NOZZLE

Results on the effect of the geometry of a circular fuel nozzle, as categorized in Table 3.2, on the liftoff phenomenon of a co-flowing methane turbulent diffusion flame are presented in this chapter. For the measurement of flame stability limits, the parameters presented include the profiles of liftoff velocity (U_l) and flame liftoff height (H_l) as function of coflow velocity (U_{co}). As for the measurement of the velocity field of a turbulent axisymmetric jet (with or without a coflow) mean and turbulent flow quantities presented include axial mean-velocity decay (U_{jet}/U_{cl}), axial and lateral turbulence intensity profiles (u/U_{jet} and v/U_{jet}), and lateral spread of axial mean-velocity ($Y_{1/2}/D$). The chapter is divided into two sections. In the first section, the results on the liftoff phenomenon of an attached flame are presented and discussed using the flow data. The second section reports the results on the liftoff height of a lifted flame being discussed following a similar approach.

4.1. Liftoff velocity

As mentioned in Chapter 2, liftoff velocity (U_l) is referred to a critical fuel jet velocity (U_{jet}) at which an attached diffusion flame lifts off from its burner and stabilizes above it. In this section, results on the effect of the geometry of a circular fuel nozzle, as categorized in Table 3.1 (and shown again here in Fig. 4.1 for comfort), on the liftoff phenomenon of a co-flowing methane turbulent diffusion flame is presented.

Figure 4.2(a) shows that the liftoff velocity increases with co-flow velocity for all nozzle exit diameters. However, the change in the flame liftoff velocity with the co-flow is not the same when changing the nozzle exit diameter. In the absence of a co-flow (i.e., U_{co} = 0 m/s), the liftoff velocity is, in general, greater for the nozzle with the larger diameter. However, the rate of increase in the flame liftoff velocity becomes greater as the nozzle orifice diameter decreases (compare D = 3 mm with D = 4.5 mm). That is, the nozzle with the smaller diameter experiences a jump in the liftoff velocity as the co-flow velocity increases, whereas the flame liftoff velocity for the nozzle with the larger diameter exhibits a slow and steady rise with the co-flow. This figure shows also that the flame blows off earlier (i.e., at a lower co-flow velocity) as the nozzle diameter becomes smaller (blowoff is defined as the extinction of an attached flame (e.g., Leung and Wierzba, [143]), whereas blowout is defined as the extinction of a lifted flame). For instance, the blowoff (due to increasing the fuel jet velocity) occurs at about U_{co} = 0.5 m/s for the 2 mm diameter nozzle, at U_{co} ~ 0.9 m/s for the 3 mm diameter nozzle, and at U_{co} ~ 1.5 m/s for the 4.5 mm diameter nozzle (for each nozzle diameter, beyond the highest co-flow velocity reported in Fig. 4.2(a), increasing fuel jet velocity results in blowing off of the attached flame rather than lifting it off).

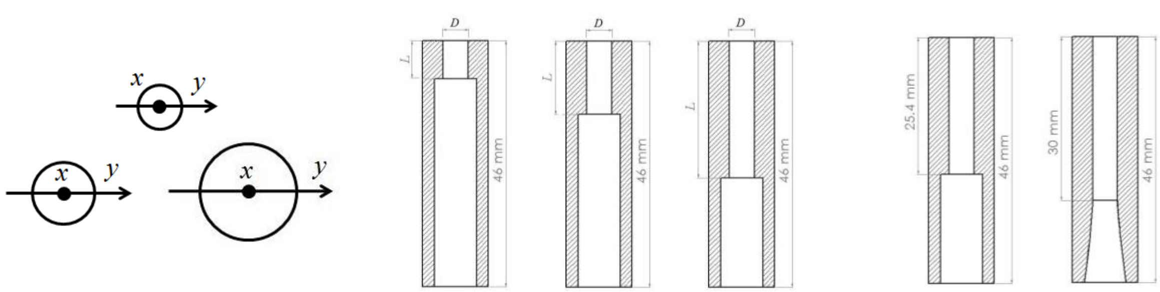

(a) Experiment #1 (b) Experiment #2 (c) Experiment #3

Fig. 4.1 Nozzle geometry test signboard

Figure 4.2(b) presents the methane flame liftoff velocity versus the co-flow exit velocity for various nozzle orifice length to diameter ratios. This figure demonstrates that the flame liftoff velocity is higher for the larger L/D regardless of the co-flow velocity. This figure reveals also that, for each nozzle orifice L/D, the flame liftoff velocity increases with the co-flow velocity until it reaches a maximum beyond which it remains almost unchanged (e.g., for L/D = 1) or exhibits a slow steady decrease (e.g., for L/D = 2.8 and 5.6). This figure indicates also that the difference in the flame liftoff velocity between the different L/D of the nozzle orifice is not so significant at zero co-flow velocity (U_{co} = 0 m/s) but noticeable at any greater co-flow velocity.

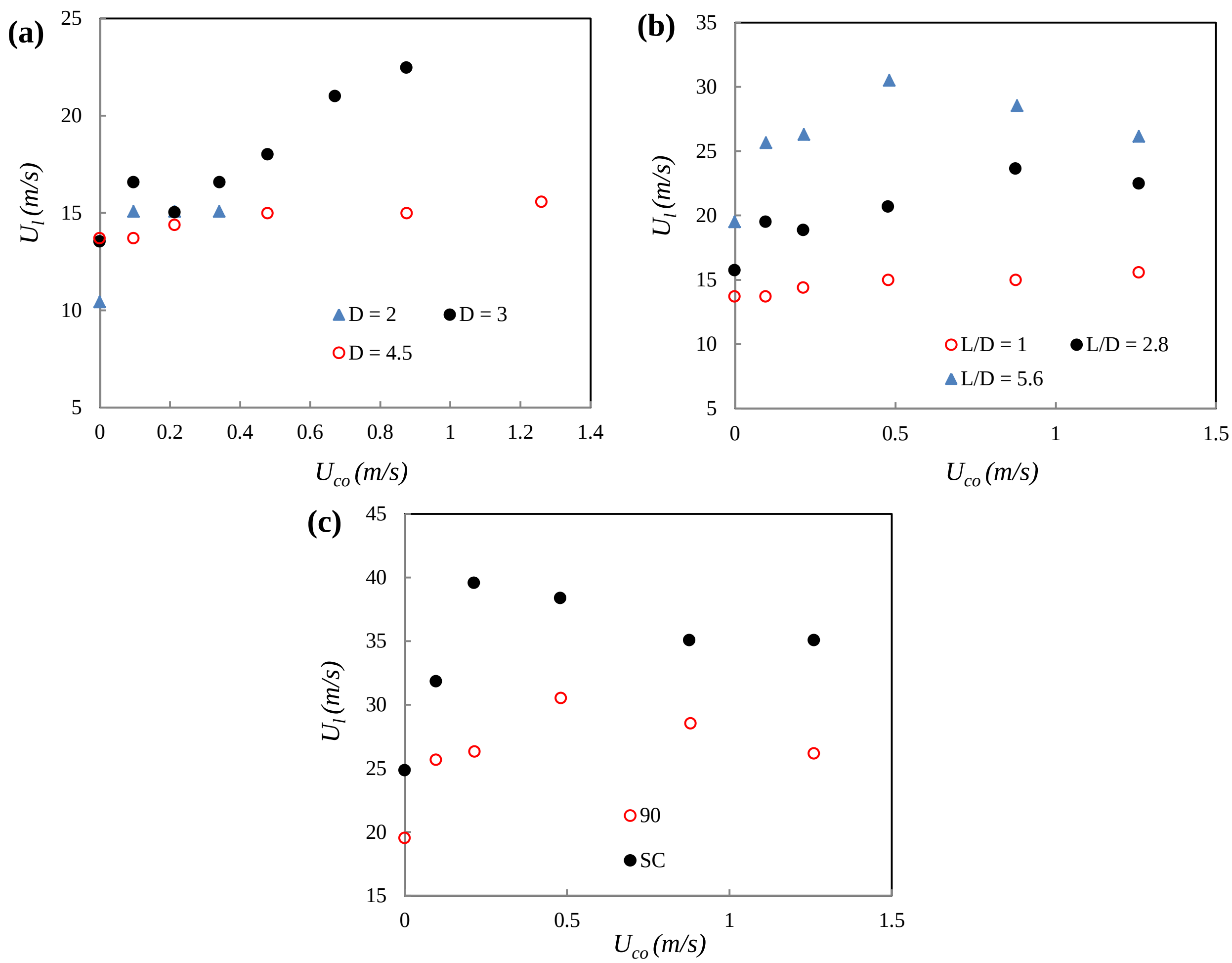

Fig. 4.2 Liftoff velocity versus co-flow velocity for the different nozzle geometries. (a) Effect of nozzle diameter (Experiment #1 in Table 3.1), (b) effect of L/D (Experiment # 2 in Table 3.1), and (c) effect of contraction angle (Experiment #3 in Table 3.1)

Figure 4.2(c) presents the methane flame liftoff velocity versus the co-flow velocity for different nozzle contraction angles. It shows that the circular nozzle having a smooth contraction angle (SC) produces greater liftoff velocity than that of the sudden contraction (90°) nozzle.

Similar to the trend observed in Fig. 4.2(b), Fig. 4.2(c) shows that the liftoff velocity increases with increasing the co-flow velocity until it reaches a maximum beyond which it decreases steadily.

4.1.1. Comparison with literature

The present findings, which revealed that in the absence of a co-airflow (U_{co} = 0 m/s) the liftoff velocity, U_l, is greater for the nozzles with the larger diameter, is in line with the results of Scholefield and Garside [4] but not with the findings of Brown and Roshko [144], Gollahalli *et al*. [7] and Takahashi and Schmoll [137]. Takahashi and Schmoll [137] found that U_l is independent of the nozzle diameter. To the best knowledge of the present author, there is a lack of systematic studies that explored the effect of other geometrical parameters of the circular fuel nozzle on the liftoff velocity such as the ones explored here (i.e., L/D and contraction angle). For example, Scholefield and Garside [4] employed a nozzle with very large L/D (up to one or two orders of magnitude greater than the range explored here) but their focus was not on the issue being addressed in the present paper. In contrast, relatively more experiments have been performed on contoured (or smooth contracting) circular nozzles (e.g., [4, 5, 7, 16, 44, 145]) but no attempt was made to vary the angle. The liftoff velocity of the present circular nozzle with smooth contraction at zero co-flow (i.e., $U_l = 25.0\ \mathrm{m/s}$) agrees with U_l ~ 29 m/s reported by Gollahalli *et al*. [139] for a contoured circular nozzle having a D = 5.5 mm, $U_l \sim$ 28 m/s of Coats and Zhao [6] for a contoured circular nozzle with a D = 5 mm, and with $U_l \sim 23$ m/s of Eickhoff *et al*. [5] for a contoured nozzle with D = 4 mm. This demonstrates that the present results of the contoured nozzle are qualitatively in line with the literature. In fact, the slightly larger values reported by Gollahalli *et al*. [139] and Langman *et al*. [16] can be attributed to their slightly larger diameters. In addition, surprisingly the flame liftoff velocity of the 90-degree contracting-nozzle of the present study with $L/D = 5.6$ (i.e., $U_l = 19.5$ m/s at $U_{co} = 0$) is similar to $U_l \sim 20$ m/s of Langman *et al*. [16] reported for a pipe with a D = 5 mm. Also, the present flame liftoff velocity for the other two 90-degree contracting nozzles (i.e., L/D = 1 and L/D = 2.8) agree with those obtained by Eickhoff *et al*. [5] for a pipe with a similar diameter.

While the liftoff process for the nozzles with 90-degree contraction, regardless of D and L/D, occurs abruptly (not shown here), the flame from the nozzle with smooth contraction exhibits some thinning and necking at several diameters (x/D ~ 4) from the nozzle exit (not shown here) before liftoff. This phenomenon is also revealed in recent published studies (e.g., [6, 16, 44] at zero co-flow). In addition to what was already reported in the literature in this regard, however, the findings of the present study reveal that the occurrence of such a phenomenon is also independent of the co-flow strength. However, the onset of the flame extinction which occurs at x/D ~ 4 appears to disagree with the assumption made by Gollahalli *et al*. [7] that the flow is laminar up to x/D ~ 1 and the flame liftoff occurs in the laminar flow region.

4.1.2. Flow characteristics

To explore the reasons behind the trend exhibited in Fig. 4.2(a-c), details about the corresponding turbulent jet flow field, such as axial and lateral turbulence intensity profiles, and axial mean-velocity decay close to the nozzle exits (i.e., in the near-field region) are provided for all nozzle geometries. These profiles, which are for typical flow conditions prior to the liftoff of the flame (i.e., in the range: $U_{jet} = 10 - 17\ \mathrm{m/s}$), are shown in Figs. 4.3-4.5 for different nozzle geometries (the grid-independence test and validation of the obtained PIV results are presented in Appendix B).

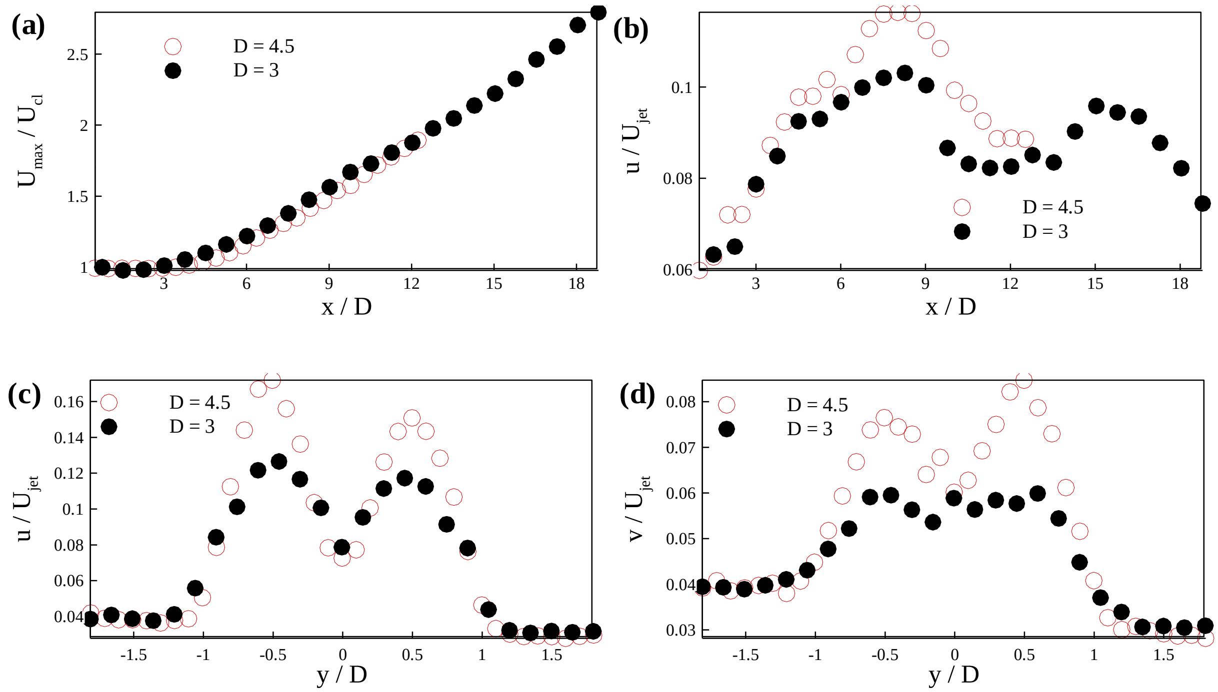

Fig. 4.3 Comparison of the (a) axial mean-velocity decay on the centerline, (b) centerline axial turbulence intensity, (c) lateral distribution of the axial turbulence intensity, and (d) lateral distribution of lateral turbulence intensity at x ~ 10 mm (x/D ~ 2 and x/D ~ 3 for D = 4.5 and D = 3 mm nozzles, respectively) between different nozzle diameters (U_{jet}~17 m/s and U_{co}~0.5 m/s).

Figure 4.3(a) shows that the jet mean-velocity decay is nearly the same for all nozzle diameters (at U_{jet}~ 17 and U_{co}~ 0.5 m/s). This figure shows also that the two jets have approximately the same potential core length (~ $3D$). Figure 4.3(b) shows that the axial component of turbulence intensity (u/U_{jet}) along the nozzle axis is relatively higher for the larger diameter nozzle at x/D > 4. In order to better understand the trend of the axial component of turbulence intensity, shown in Fig. 4.3(b), it was decided to plot the lateral profiles of u/U_{jet} and v/U_{jet} at x ~ 10 mm (i.e., x/D ~ 2–3) in Figs. 4.3(c) and 4.3(d), respectively. These figures show that the turbulence intensity for the larger nozzle is higher in the shear layer zone even though it is slightly smaller in the proximity of the nozzle axis. It is seen, in general, that the turbulence intensity in the near-field region is higher for the nozzle with the larger diameter (see Fig. 4.3(b)-(d)). Figure 4.3(c)-(d) show also that v/U_{jet} is smaller than u/U_{jet} (u/v ~ 2 and 1.3 in the shear layer, and on the centerline, respectively) which indicate that the issuing turbulence jet is clearly anisotropic in the near-field region (which is an indication of the presence of large-scale structures in the near field). However, the lateral distribution and development of u/U_{jet} and v/U_{jet} downstream of the nozzle exit follow a similar trend in agreement with the literature [19].

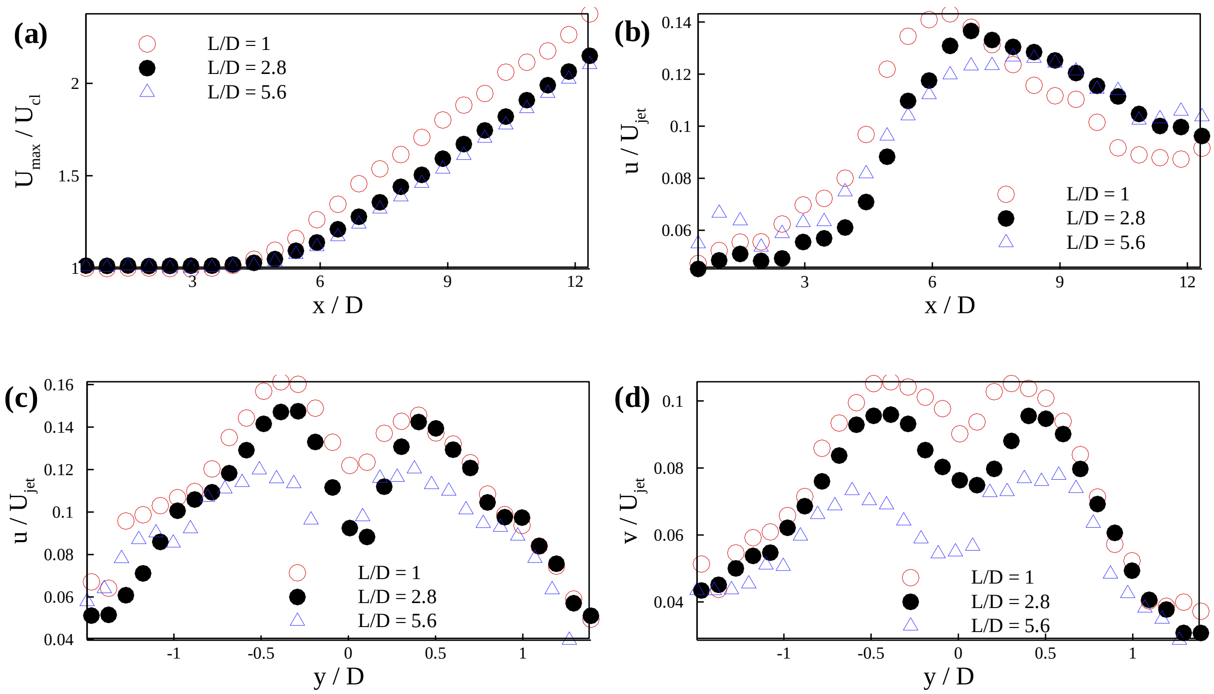

Fig. 4.4 Comparison of the (a) axial mean-velocity decay on the centerline, (b) centerline axial turbulence intensity, (c) lateral distribution of axial turbulence intensity, and (d) lateral distribution of lateral turbulence intensity at x ~ 22 mm (x/D ~ 5) between different nozzle L/D (U_{jet}~10 m/s and U_{co}~0.2 m/s).

Figure 4.4 presents the jet flow characteristics for the nozzle with different L/D. Figure 4.4(a) shows that the axial velocity decay rate is faster for the nozzle with the smaller

L/D. This figure shows also that the nozzle with the smaller L/D has slightly smaller potential core length (~ $4.25D$) compared with that of the nozzles with the larger L/D (~ $4.5D$). The corresponding axial turbulence intensity component along the nozzle axis and its lateral distribution at $x \sim 22$ mm ($x/D \sim 5$), are respectively shown in Figs. 4.4(b) and (c) (the jet and co-flow exit velocities are, respectively, U_{jet} ~ 10 m/s and U_{co} ~ 0.2 m/s). Also, Fig. 4.4(d) shows the radial distribution of the lateral turbulence intensity, v/U_{jet}, at $x \sim 22$ mm ($x/D \sim 5$). Similar to what was previously seen in Fig. 4.3(c-d), v/U_{jet} (Fig. 4.4(c-d)) is clearly smaller than u/U_{jet} (more significantly in the shear layer) which is an indication of the presence of a considerably anisotropic turbulent flow in the near-field region, which in turn suggests the presence of large-scale structures in the jets near field.

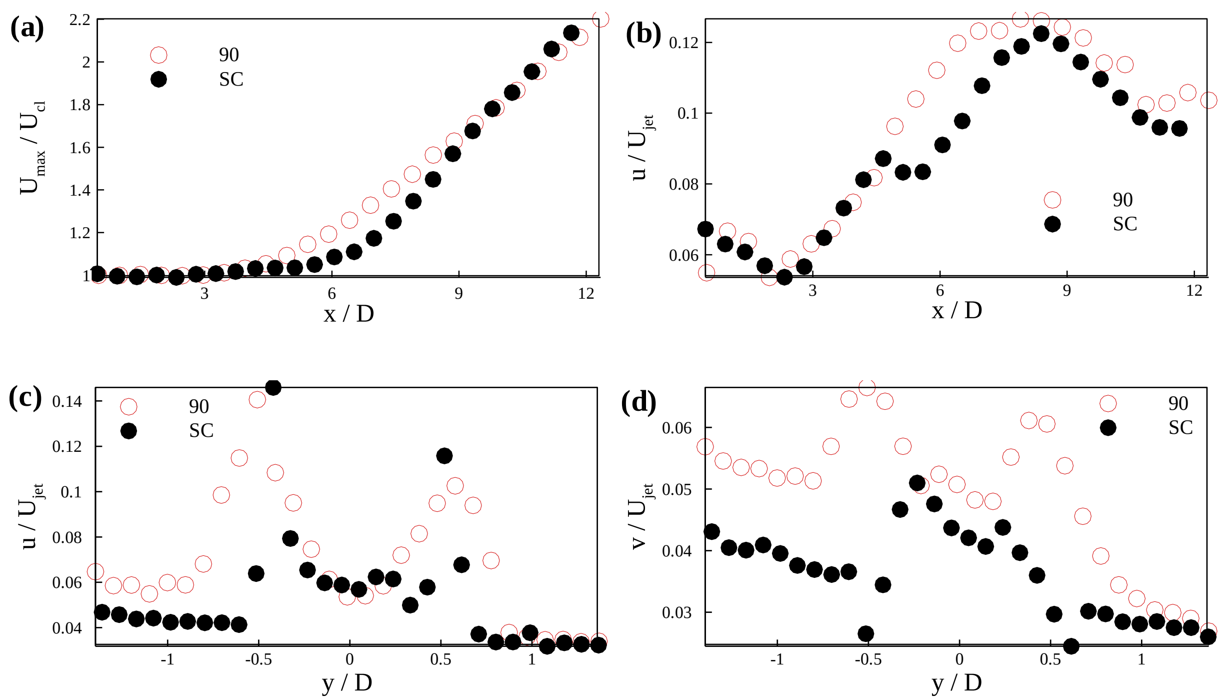

Fig. 4.5 Comparison of (a) axial mean-velocity decay on the centerline, (b) centerline axial turbulence intensity, (c) lateral distribution of axial turbulence intensity, and (d) lateral distribution of lateral turbulence intensity at x ~ 10 mm (x/D ~ 2) between different nozzle contraction angles (U_{jet}~10 m/s and U_{co}~0.2 m/s).

Figure 4.5 presents the effect of the contraction angle of the nozzle on the near-field jet characteristics at typical flow conditions (i.e., U_{jet} ~10 m/s and U_{co} ~ 0.2 m/s). Figure 4.5(a) shows that the axial mean-velocity for the 90-degree contraction nozzle starts decaying earlier compared with the smoothly contracting nozzle. The decay rate (the slope of the curves in Fig. 4.5(a)), however, converges to the same value farther downstream at $x/D > 9$. This figure shows also that the nozzle with the 90-degree contraction has relatively smaller potential core length (~ $4.5D$) than the nozzle with the smooth contraction (~ $5.5D$). The centerline axial turbulence intensity (in the jet near-field, that is, for $x/D < \sim 13$), as seen in Fig. 4.5(b), and its lateral distribution (in Fig. 4.5(c)), as well as the radial distribution of the lateral turbulence intensity (Fig. 4.5(d)), all show in general that the u/U_{jet} and v/U_{jet} are higher for the 90-degree contracting nozzle. Thus, similar to what was seen earlier in Figs. 4.3(c-d) and 4.4(c-d), Fig. 4.5(b-d) confirm the presence of a considerably anisotropic turbulent flow in the near-field region and hence the presence of large-scale structures in the jet near-field.

Figures 4.3-4.5 showed that overall, in the jet near-field, the trend of the variation of the jet near-field decay with the nozzle geometry does not appear to correlate with that of its corresponding turbulence intensity (u/U_{jet} and v/U_{jet}). For instance, while changing the nozzle diameter did not affect the jet near-field decay, a change in the jet near-field turbulence is clearly noticeable. In fact, a correlation seems to exist between the jet near-field turbulence and the corresponding jet flame liftoff velocity presented in Fig. 4.2. That is, the jet that has the highest turbulence intensity in the near-field yields the lowest flame liftoff velocity. For instance, the noticeable difference in the liftoff velocity between the nozzles with $D = 3$ and $D = 4.5$ mm at higher co-flow rates (Fig. 4.2(a)) can be attributed to the important difference in the turbulence intensity between these two nozzles (Fig. 4.3(c-d)). The suggestion that the level of turbulence in the jet near-field has a definite impact on the liftoff (i.e., local quenching) of an attached jet methane flame is supported by the variations in the nozzle geometrical parameters explored in the present study and hence the corresponding level of turbulence. All these variations led to the same conclusion that higher levels of jet near-field turbulence results in a lower flame liftoff velocity regardless of the nozzle geometry.

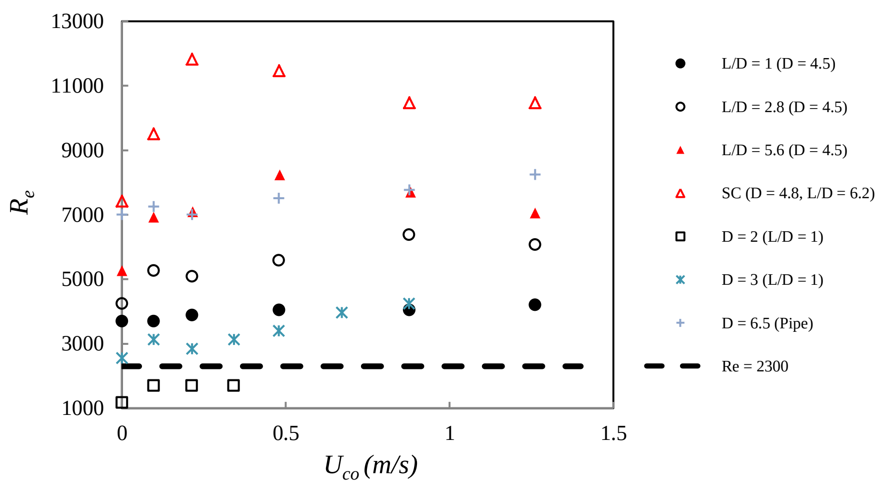

Fig. 4.6 Reynolds number at flame liftoff flow conditions.

4.1.3. Fuel jet exit Reynolds number at liftoff

The exit Reynolds number of the jet issuing from different nozzle geometries employed here is plotted in Fig. 4.6 as a function of the co-flow exit velocity. Reynolds number is defined as $Re = U_{jet} \times D/\upsilon$, where U_{jet} is the exit velocity at the onset of flame liftoff, D is the nozzle exit diameter, and υ is the kinematic viscosity of methane at room temperature. It can be seen that the Reynolds number at the onset of liftoff in all cases, with the exception of the nozzle with the smallest exit orifice diameter, is greater than $Re = 2300$, which is the upper critical Reynolds number for a laminar pipe flow. The same figure shows also that the Reynolds number upper limit is below $Re \sim 10{,}000$, which corresponds to a fully-turbulent pipe flow. Therefore, it is believed that the flow at the onset of flame liftoff is in the transient regime. This information reinforces the suggestion that all the nozzle geometries tested here produce a semi-turbulent (transient turbulent) to turbulent flow regime, which thus reinforces the theory which suggests a strong relationship between the jet near-field turbulence and its corresponding flame liftoff phenomenon.

4.1.4. Discussion

Eickhoff *et al*. [5] reported that, by increasing the fuel rate, the attached flame from either a pipe or a nozzle detaches abruptly. They attributed the flame detachment to the interference of a small-scale vortical motion with the flame front. They believe that at the liftoff velocity, U_l, the inner high frequency vortices, which are superimposed by turbulence, interfere with the flame front. The diffusion flame is then quenched at the interference point as a result of excessive heat diffusion by small scale turbulence structures.

Coats and Zhao [6] found a “pronounced necking” of the outer layer in the region of the transition to liftoff for flame issuing from the nozzle with smooth contraction. Such a structure was also later reported in the literature (e.g., [16, 44]) which is also in agreement with the findings of the present study. Coats and Zhao [6] stated that transition from laminar regime to turbulent combusting flow engaged with changes in the characteristics and structure of the fuel jet occurs at liftoff. They stated that the low-frequency instability dominates the flame in the lower Reynolds number range. However, transition in the main body of the flame suppresses those structures and causes liftoff to precipitate due to the invasion of the laminar flame leading edge by turbulent structures that is generated in the central gaseous jet [6].

The findings of the present study, which demonstrate that the increase in the nozzle exit turbulence level precipitated the occurrence of flame liftoff, is in agreement with the proposed theories of Eickhoff *et al*. [5] and Coats and Zhao [6]. Especially, Coats and Zhao [6] who showed that the effect of turbulence on the stability of the attached diffusion flame was obvious when transition to liftoff in the burner tube was delayed by flow smoothening of the issuing jet from the nozzle. In fact, they associated the transition in the tube jet flame to the pipe-flow turbulence. On the other hand, the transition in the nozzle jet flame was attributed to the "breakdown" of the inner coherent vortices generated at the end of the potential core and so ultimately by the instabilities in the jet shear region. Moreover, their liftoff velocity of the SC was found to be higher than that of the pipe (U_l = 18 m/s for the pipe and U_l = 24 m/s for the SC). These results are in a good agreement with the findings of the present study.

Figure 4.5(b) can be used, as an example, to illustrate the presence of flow structures near the exit of the 90-degree contracted and smooth contracted nozzles. That is, by looking farther away from the nozzle exit on the centerline, the turbulence intensity undergoes local maxima. This maxima and its preceding quick rise occurs closer to the exit in the 90-degree contracted nozzle compared with that of the smooth contracted nozzle. Thus, the observation of the pronounced lobbed structure in the flame from the smooth contracted nozzle can be attributed to smaller turbulence intensity closer to the nozzle exit and that the presence of the local maxima is delayed farther downstream of the smooth contracted nozzle. Therefore, this figure along with the aforementioned discussion explains why the liftoff velocity for the smooth contracted nozzle is higher compared with that of the 90-degree contracted nozzle.

The turbulence intensity profiles previously presented in Fig. 4.4(b) show similar trend about the effect of L/D. That is, according to this figure, increasing L/D via extending the nozzle contracted orifice induces some changes in the turbulence of the emerging jet. In fact, it is seen that the turbulence intensity decreases and its sharp rise is retarded which can justify why the nozzle with the higher L/D produces a higher liftoff velocity.

On the other hand, there is more controversy in the literature over the effect of the nozzle diameter on the flame liftoff velocity. For instance, while Scholefield and Garside [4] reported greater liftoff velocities for nozzles with larger diameter, Gollahalli *et al*. [7] found a small decrease in U_l with nozzle diameter. Other studies reported that the liftoff velocity was independent of the diameter (e.g., [137]). The present results showed that the effect of nozzle diameter on the flame liftoff somehow depends on the strength of the co-flow velocity. At zero co-flow, for instance, Fig. 4.2(a) shows that the liftoff velocity is slightly higher for the nozzle with larger diameter. However, this trend is reversed as the co-flow exit velocity is increased. The profiles of the turbulence intensity in the jet near-field (Fig. 4.3(b-d)) show that the nozzle with the larger diameter has clearly higher turbulence intensity in the shear layer zone where the diffusion flame supposedly takes place.

It can be concluded that the invasion of laminar flame base by turbulent structures, characterized in the present study by turbulence intensity in the vicinity of the nozzle exit, is the controlling parameter of the detachment process of a diffusion flame. In other words, the liftoff velocity is expected to be higher for a nozzle that produces a jet flow with a lower exit turbulence.

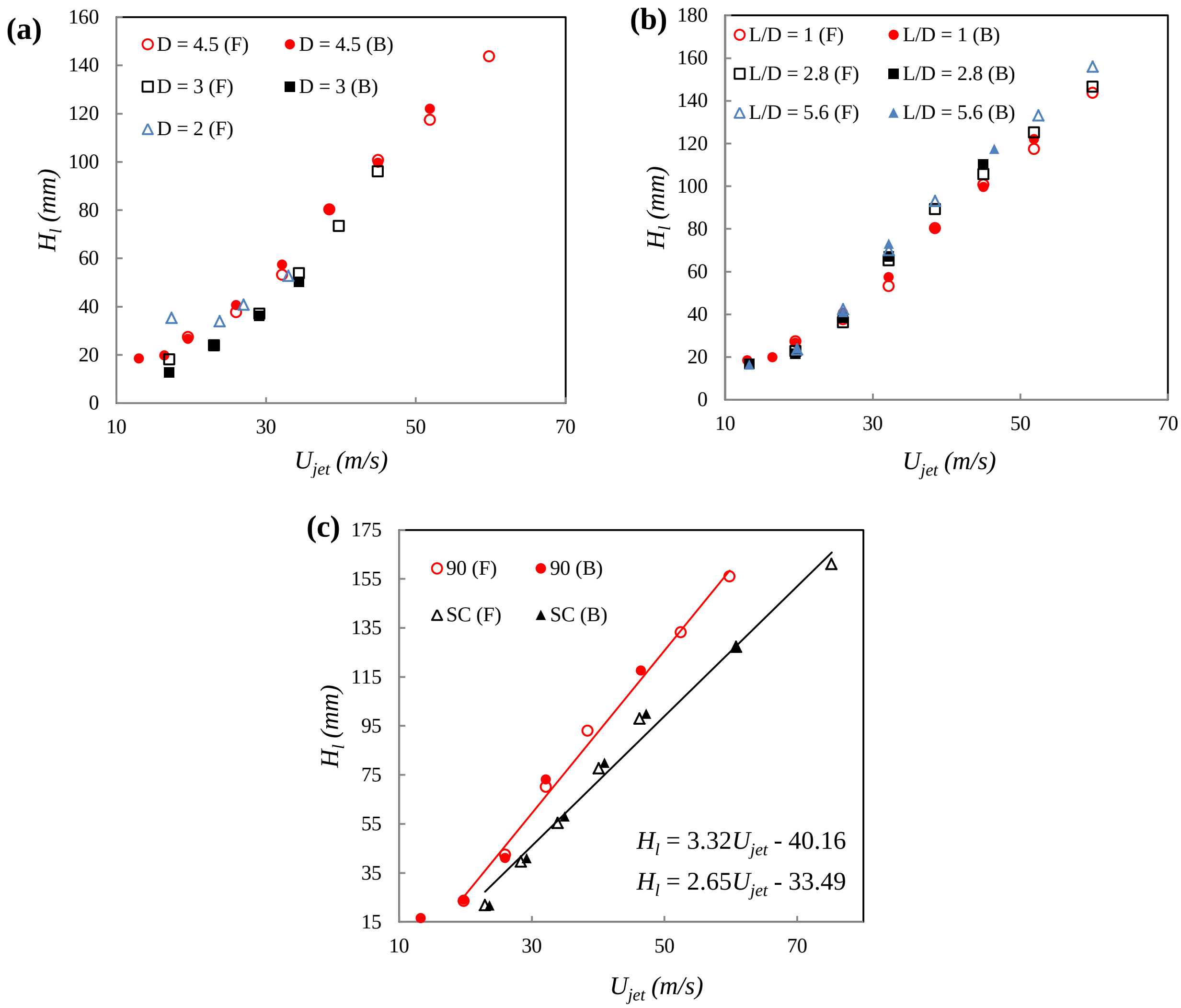

Fig. 4.7 Liftoff height versus jet fuel exit velocity for methane jet flame with zero co-flow for (a) different nozzle diameters, (b) different nozzle L/D, and (c) different nozzle contraction angle.

4.2. Liftoff height

4.2.1. Zero co-flow flame

Figure 4.7(a-c) presents the liftoff height for the nozzle geometries tested here versus the fuel jet exit velocity for zero co-flow exit velocity (F: forward profiles, shown by hollow symbols, were obtained by increasing the jet velocity; and B: backward profiles, shown by filled symbols, were obtained by decreasing the jet velocity). Figure 4.7(a) shows that the flame liftoff height of the $D = 3\ mm$ nozzle orifice is slightly lower than that of the larger orifice ($D = 4.5\ mm$), and that such a small difference diminishes with increasing the fuel jet exit velocity. Figure 4.7(b) shows that increasing the nozzle L/D results in a marginal rise in the flame height. In contrast, Fig. 4.7(c) shows that the liftoff height for the nozzle with the smooth contraction is clearly smaller than that of the nozzle with 90-degree contraction. A common trend shown in Fig. 4.7(a-c), however, is that with the exception of the very low range of fuel jet exit velocity (just above U_l), the flame liftoff height increases linearly with the fuel jet exit velocity for all nozzle geometries tested here. Moreover, Fig. 4.7(a-c) show that the liftoff height for the backward profiles nearly collapse on the forward profiles.

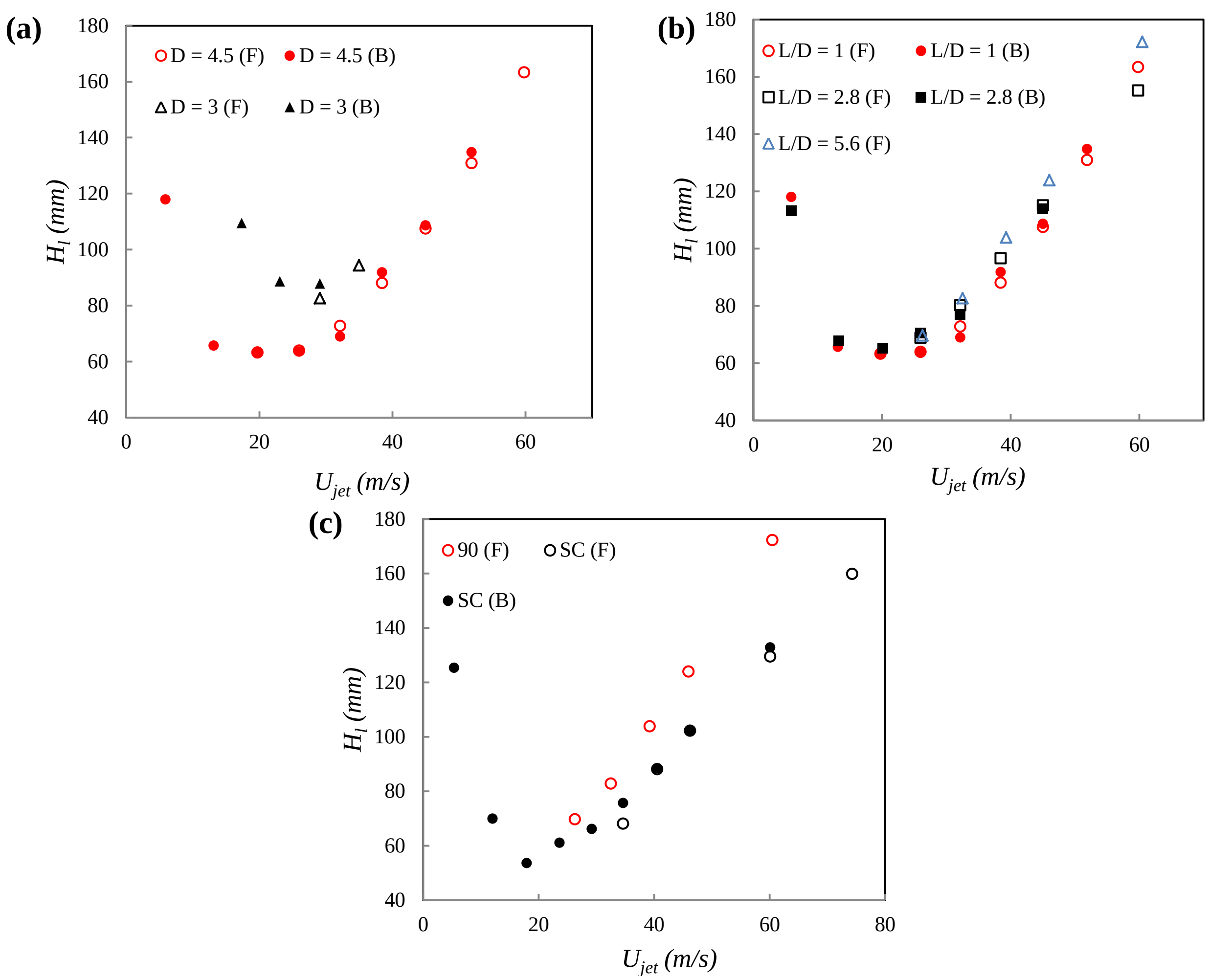

Fig. 4.8 Liftoff height versus jet fuel exit velocity for methane jet flame with $U_{co}\sim 0.9$ m/s for (a) different nozzle diameters, (b) different nozzle L/D, and (c) different nozzle contraction angles.

4.2.2. Co-flowing flame

The liftoff height for a lifted flame with U_{co}~0.9 m/s is shown in Fig. 4.8. Figure 4.8(a) shows that, unlike what was observed in a flame with $U_{co} = 0$ (Fig. 4.7(a)), the flame height of the smaller orifice is greater than that of the larger orifice nozzle. However, a lifted flame from a 3 mm diameter nozzle cannot be maintained as it blows out at relatively lower jet exit velocity compared with the larger nozzle diameter. Specifically, no stable lifted flame for the smallest exit orifice (D = 2 mm) at co-flow U_{co} ~ 0.9 m/s was observed; instead the attached flame blows off immediately after its detachment from the burner/nozzle. Nonetheless, the nozzle diameter does not appear to affect the trend of the flame liftoff once it becomes linearly varying with the fuel jet exit velocity.

The effect of L/D on the flame height, shown in Fig. 4.8(b), is similar to what was previously seen in Fig. 4.7(b); that is, larger L/D produces marginally greater flame liftoff height. Figure 4.8(c), on the other hand, shows that the liftoff height has similar trend to that observed in Fig. 4.7(c) with the exception of the backward profile at very low fuel jet exit velocity. Figure 4.9, which is for U_{co}~ 1.25 m/s, reveals similar trends to those seen in Fig. 4.8 for U_{co} ~ 0.9 m/s (no data for the nozzle diameter was presented in Fig. 4.9 because no stable flame at U_{co} ~ 1.25m/s can be established for D < ~ 4 mm). A distinction between the liftoff height of a co-flowing flame (Fig. 4.8) and that of a simple jet (zero co-flow) flame (Fig. 4.7) is that, regardless of the nozzle geometry, the liftoff height for a co-flowing flame rises drastically with a decrease in the fuel flow rate (i.e., exit jet velocity) to the limit of the reattachment/blowout which is characterized by the non-linear variation of the flame liftoff height, which is almost unnoticeable in Fig. 4.7 at low U_{jet}. It is important to mention that this phenomenon manifests only with the backward profiles where the fuel jet exit velocity can reach to relatively small values prior to the flame reattachment or blow-off.

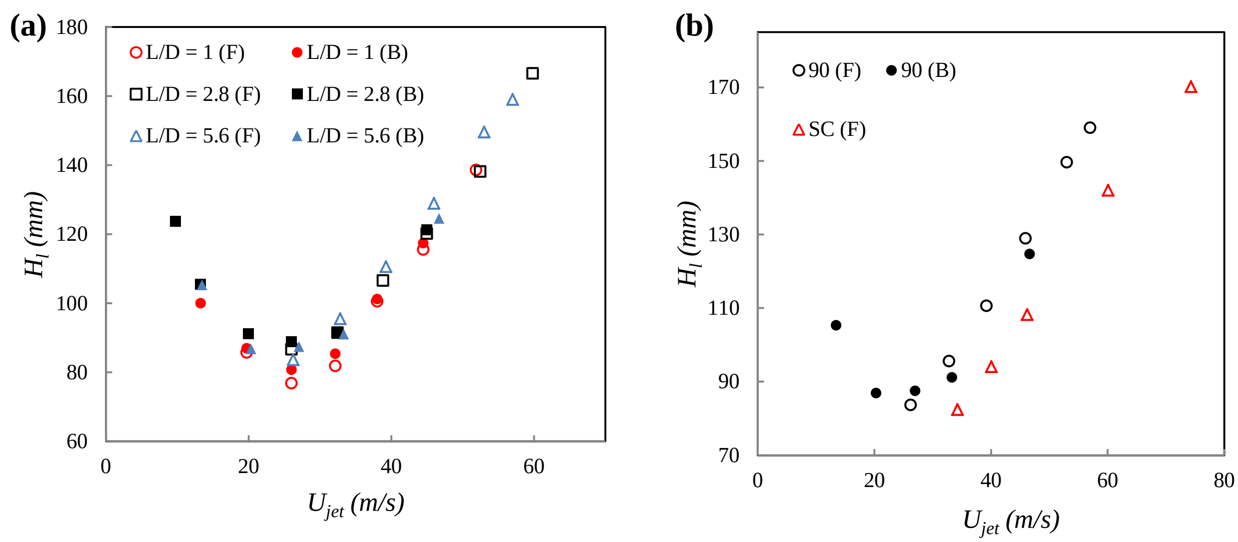

Fig. 4.9 Liftoff height versus jet fuel exit velocity for methane jet flame with $U_{co}\sim 1.25\ m/s$ for (a) different nozzle diameters, (b) different nozzle L/D, and (c) different nozzle contraction angles.

4.2.3. Comparison with published results

Several theories/correlations were reported on the flame liftoff height (e.g., [8–11, 113, 114, 146]). The majority of the lifted flame theories/correlations mentioned above (especially those of Kalghatgi [9] and Broadwell [11]) successfully predict the linear trend (but to less extent the magnitude of the liftoff height) of the present liftoff height data. However, none of these theories/correlations is able to describe the flame liftoff height in the range of jet exit velocity closer to the flame liftoff velocity where the liftoff height varies non-linearly with the jet exit velocity (Appendix B). Note that these proposed theories/correlations were developed for a simple fuel nozzle geometry. Published experimental studies showed that fuel nozzle geometrical parameters (e.g., contraction angle, contraction length, nozzle lip thickness, etc) can affect differently the flame liftoff height [30]. For instance, the experimental results of Eickhoff *et al.*

[5] showed that the flame liftoff height, H_l, depends slightly on the shape and diameter of a nozzle. Coats and Zhao [6], on the other hand, found that the H_l profile is similar between a tube and a smooth contracted nozzle which does not agree with other published studies (e.g., [5, 16, 44]). Langman *et al*. [16] predicted a step-change in H_l of a flame from smooth contracted nozzle which is also not in agreement with the literature. These discrepancies may well be attributed to the differences in the internal geometry of a fuel nozzle which, in turn, could result in different exit flow characteristics. Indeed, the present experimental study clearly demonstrated that the flame liftoff height can be significantly affected by the geometry of a fuel nozzle. The present results revealed that while both the nozzle diameter and its L/D showed only marginal effect especially when it varies linearly with the jet exit velocity, the nozzle orifice contraction angle affected noticeably the flame liftoff height.

The Schlieren photographs of a lifted flame reported by Eickhoff *et al*. [5] showed that there is a fluctuating pattern upstream of the flame base, indicating the importance of turbulence intensity and the intermittent character of the fine scale structures which can support the concept of premixed combustion. Coats and Zhao [6], on the other hand, showed evidence of a "cellular-type" structure. They believed that lifted flame remains sensitive to the jet initial conditions up to a considerable distance from the burner (~ $10D$) and concluded that theories based on assumption of flame propagation within fully-developed turbulent flow regime cannot always accurately explain lifted flames characteristics in the near-burner region. This may justify the non-linear variation of the flame liftoff height with the jet velocity in the proximity of flame liftoff event (see Figs. 4.8 and 4.9). Coats and Zhao [6] concluded that the reaction zone is located away enough from the jet shear layer zone, which does not appear to explain the fluctuating nature of the flame base, especially by considering the fact that the fluctuations in the flame base shown for the 90-degree contraction nozzle with D = 4.5 mm and L/D = 1 in Fig. 4.10 (as an example for the nozzles used in the present study) do not undergo an organized and predictable trend [127]. Thus, its cause cannot be attributed to the organized flow structures; instead it indicates the presence of turbulence in the proximity of the flame base. Langman *et al*. [16] believed that the well-established differences in the turbulent source flow propagate far downstream of the jet and consequently influence the flame. They believed that both the shear layer thickness of the exiting jet along with its exit velocity profile play a dominant influence on the growth and development of the large-scale coherent structures. The present results also showed that the influence of the nozzle geometry on the flame, via changes in the jet exit mean and turbulent velocity profiles, does not affect only the flame stability parameters in the near-field region (such as the flame liftoff process), but also extends to the far-field region where the liftoff height is comparable to the flame length. Overall, a comparison of the present results with published findings revealed the following. (a) There is a linear relationship between the liftoff height and the fuel jet exit velocity as suggested by the correlation of Kalghatgi [9] which reinforces the belief of the premixed theory for the flame base above a certain height from the burner (or nozzle). (b) The intermittency in the oscillations of the location of the flame base confirms the presence of turbulent mixing in the upstream of the flame leading edge. (c) The non-linear behaviour of the flame liftoff height (close to the nozzle exit) does not support the premixed theory, however, it agrees with the findings of Coats and Zhao [6] in that the role of organized flow structures on the liftoff height might be prominent close to the nozzle exit.

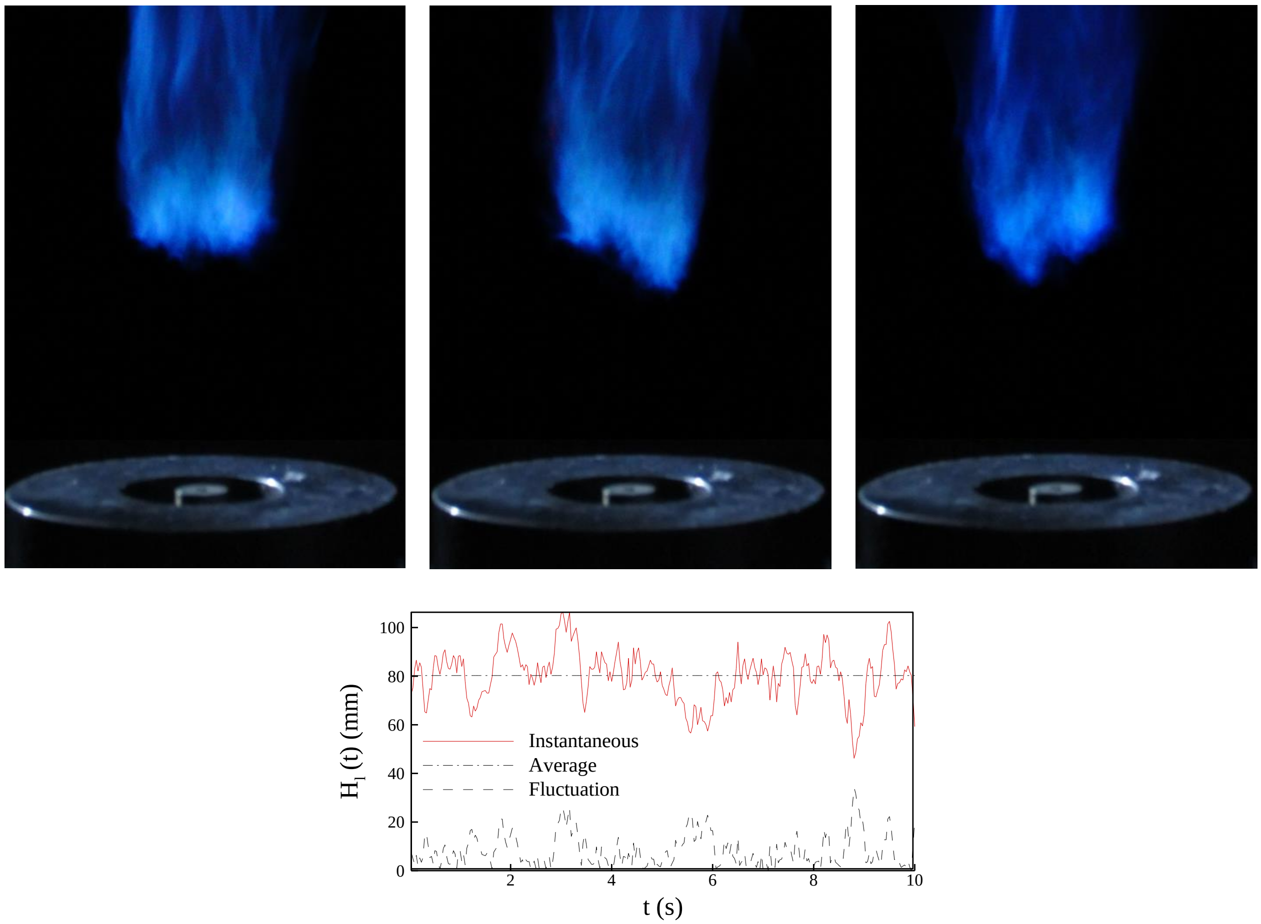

Fig. 4.10 Lifted flame at three different instances (top), and the flame height temporal history (bottom) from 90-degree nozzle with D = 4.5 mm and L/D = 1 (U_{jet} ~ 40 m/s and U_{co} = 0 m/s).

4.2.4. Jet flow characteristics

To shed more light on the behaviour of the flame liftoff height in relation to the nozzle geometries explored here, the development of the corresponding jet flow characteristics downstream of the nozzle were investigated (Figs. 4.11, 4.12, and 4.13). These jet characteristics include the axial mean-velocity decay and jet spread rate (in the near-field region), and the turbulence intensity profiles at the nozzle exit as well as on the jet centerline for a typical flow condition pertaining to lifted flames.

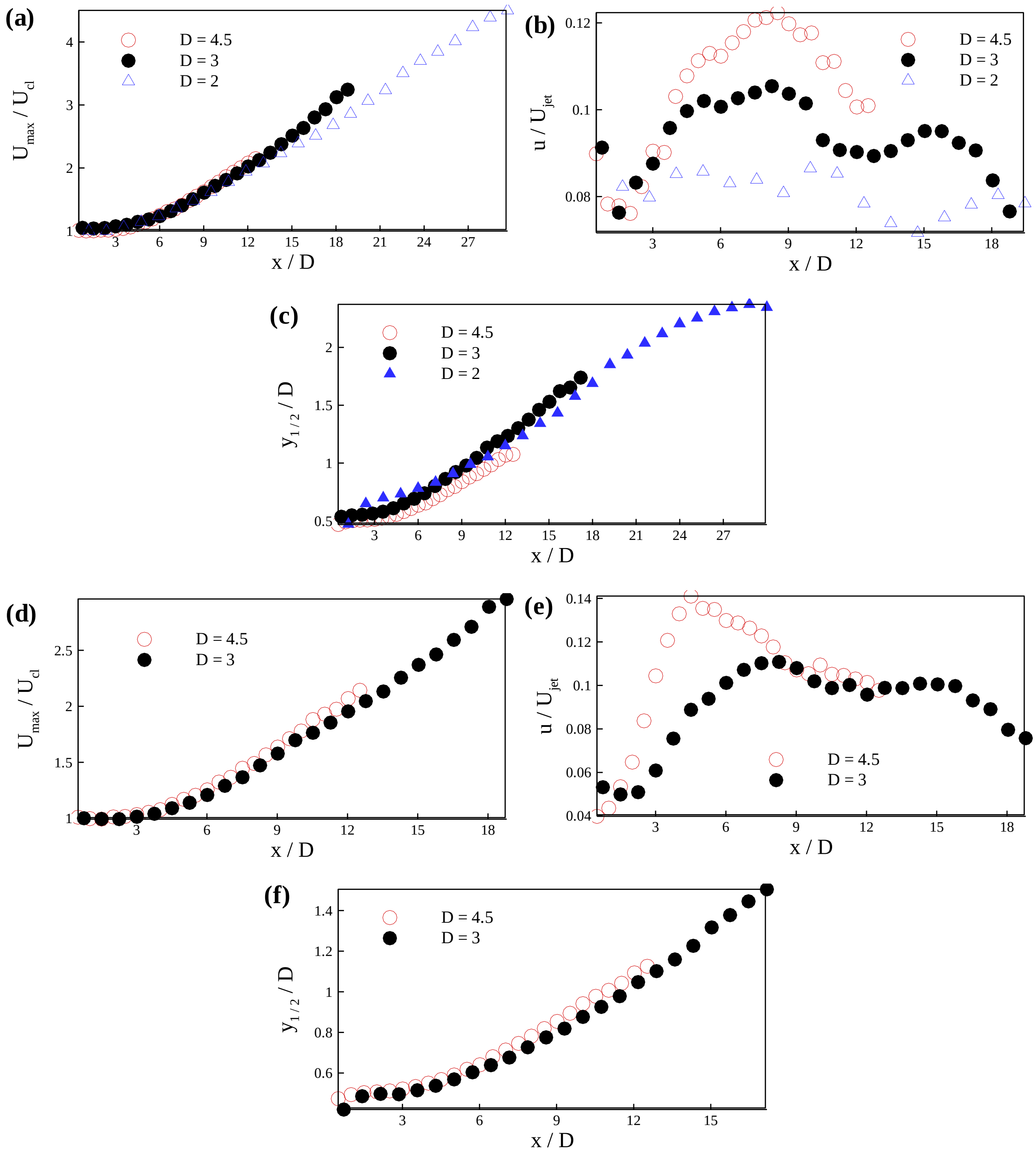

Fig. 4.11 Comparison of the (a) axial mean-velocity decay on the centerline, (b) centerline axial turbulence intensity, (c) lateral spread of the axial mean-velocity of turbulent jet issuing from different nozzle diameters with U_{co}~ 0.2 m/s; and (d) axial mean-velocity decay on the centerline, (e) centerline axial turbulence intensity, (f) lateral spread of the axial mean-velocity of a turbulent jet with U_{co}~ 0.5 m/s ($U_{jet} = 30 - 40$ m/s).

The jet decay and turbulence intensity at U_{co}~ 0.2 m/s along the nozzle axis are presented for different nozzle diameters (Experiment #1 of Table 3.1) in Figs. 4.11(a) and (b). The jet decay (Fig. 4.11(a)) is fairly similar (so as the potential core's length) between the nozzles with different diameters in the near-field region up to x/D ~15; however, beyond x/D = 15 the smallest nozzle exhibits lower decay rate. Figure 4.11(b) shows that the axial component of turbulence intensity (u/U_{jet}) along the nozzle axis is relatively smaller for the nozzle with larger diameter (i.e., the nozzle with $D = 4.5$ mm) close to the nozzle exit ($x/D < \sim 3$), but becomes the greater farther downstream (i.e., for $x/D > \sim 4$). On the other hand, Fig. 4.11(c) shows that the lateral spread of the jet mean-velocity is slightly lower for the nozzle with the larger diameter. Similar profiles are presented in Fig. 4.11(d-f) for the jet with a U_{co}~ 0.5 m/s. The jet decay (Fig. 4.11(d)) is still fairly similar between the nozzles with different diameters especially in the near-field region up to x/D ~10. Figure 4.11(e) clearly shows that the axial component of turbulence intensity (u/U_{jet}) along the nozzle axis is higher for the nozzle with D = 4.5 mm. Figure 4.11(f) shows that the lateral spread of the jet mean-velocity is slightly higher for the nozzle with the larger diameter, unlike the trend previously shown in Fig. 4.11(c) for the jet with U_{co}~ 0.2 m/s.

Figure 4.11(a-c), which present the jet flow characteristics for a weak co-flow (nearly zero-coflow), reveal that the nozzle which has a relatively lower liftoff height, i.e., the nozzle with $D = 3$ mm, has correspondingly the highest jet spread rate. In addition, the corresponding centerline axial turbulence intensity is higher for the nozzle with $D = 3$ mm close to the nozzle exit, and then becomes higher for the nozzle with $D = 4.5$ mm for x/D > 4. The axial mean-velocity decay rate (and also the potential core's length), however, does not show any correlation with the flame liftoff height (e.g., both nozzle diameters 3 mm and 4.5 mm have nearly identical jet decay rate and potential core's length). Figure 4.11(d-f), which present the jet flow characteristics for U_{co} ~ 0.5 m/s, show that the nozzle which has the highest jet spread and decay rate and turbulence intensity (D = 4.5 mm) has also lower liftoff height (Fig. 4.8(a)). These results suggest that the nozzle diameter that produces higher jet spread rate and turbulence ahead of the flame base generally results in a lower liftoff height.

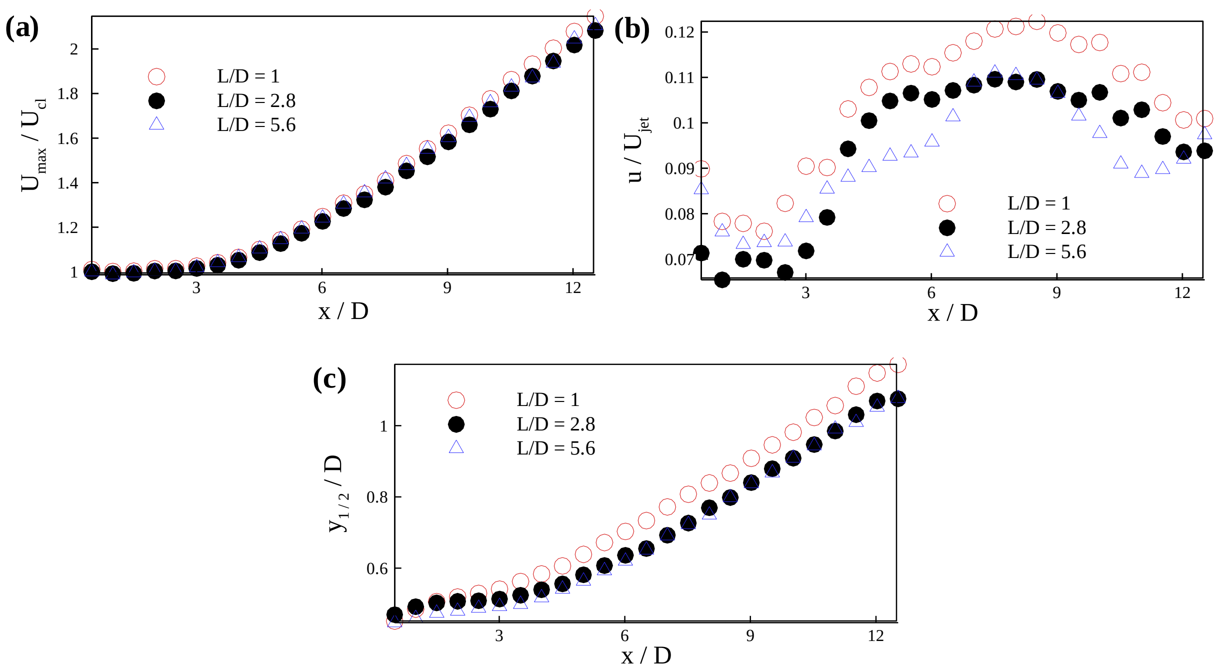

Fig. 4.12 Comparison of the (a) axial mean-velocity decay on the centerline, (b) centerline axial turbulence intensity, (c) lateral spread of the axial mean-velocity of turbulent jet issuing from different nozzle L/D with U_{co} ~ 0.2 m/s (U_{jet}~ 30 m/s).

The flow characteristics for the nozzles of Experiment #2 (i.e., the nozzle with different L/D) are presented in Fig. 4.12(a-c) for the jet with U_{co}~ 0.2 m/s. Figure 4.12(a), for example, shows that the axial mean-velocity decay (and also the potential core's length) does not change noticeably with L/D. The axial turbulence intensity (u/U_{jet}) along the nozzle axis, which is shown in Fig. 4.12(b), is higher for the nozzle having the smallest L/D; however, further increase in L/D (from 2.8 to 5.6) shows no significant difference. Similarly, the jet spread, which is shown in Fig. 4.12(c), is larger for the nozzle with the smallest L/D but almost unchanged between L/D = 2.8 and 5.6.

Examining the jet flow characteristics presented in Fig. 4.12(a-c) for a weak co-flow or nearly zero-co-flow and the corresponding flame liftoff height presented in Fig. 4.8(b) reveals that the nozzle which produces the lower liftoff height has the highest spread and turbulence intensity. Thus, these findings suggest that the jet axial mean-velocity decay rate and its potential core's length (unchanged with L/D) do not appear to have a correlation with the flame liftoff height. However, it is seen that the nozzle which produces higher jet spread rate yields lower flame liftoff height. In addition, the flame liftoff height is lower when the turbulence intensity downstream of the nozzle exit and ahead of the flame base is higher. These results demonstrate clearly that higher jet spread rate and turbulence intensity result in a lower flame liftoff height.

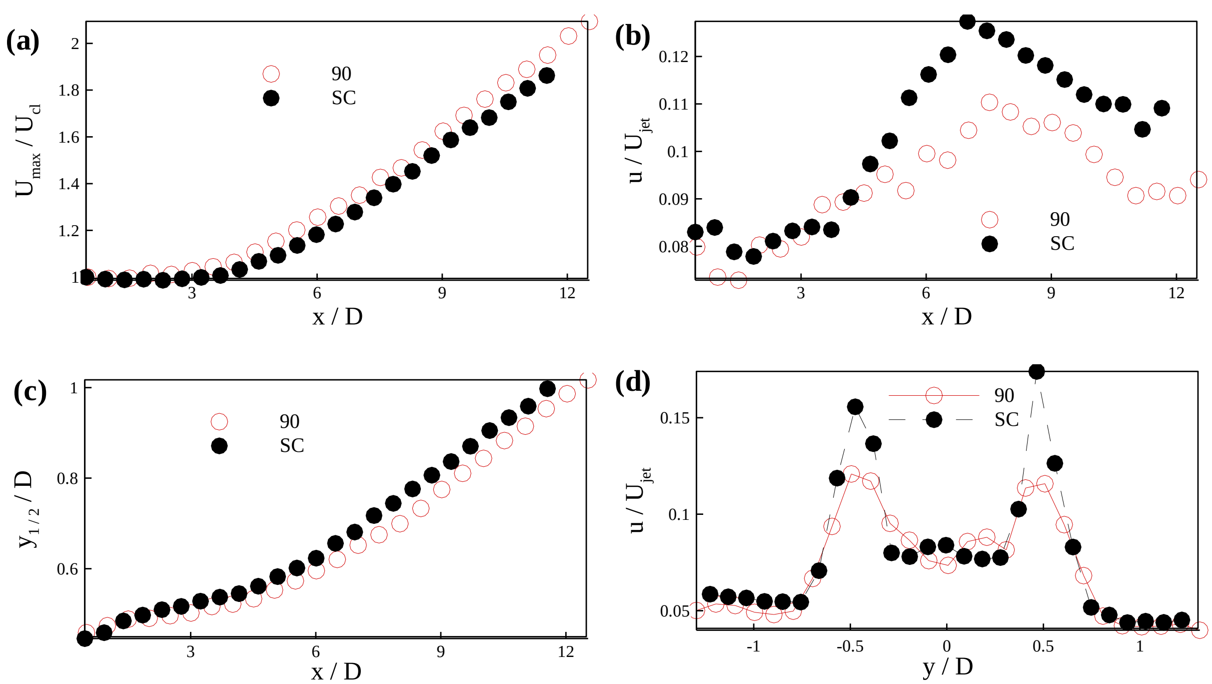

Fig. 4.13 Comparison of the (a) axial velocity decay, (b) centerline axial turbulence intensity, (c) lateral spread of the axial mean-velocity of turbulent jet issuing from different nozzle contraction angles, and (d) lateral distribution of axial turbulent intensity of a turbulent jet issuing from different nozzle contraction angles with U_{co} ~ 0.5 m/s (U_{jet}~30 m/s).

Figure 4.13(a) presents the profile of the jet axial mean-velocity decay along the jet centerline for the two nozzles with different contraction angles (Experiment #3 of Table 3.1) at $U_{co} \sim$ 0.5 m/s. It can be seen from this figure that the jet axial mean-velocity decay rate is nearly the same for both nozzle geometries (the same applies to the jet's potential core length). However, the axial turbulence intensity component (u/U_{jet}), shown in Fig. 4.13(b), is higher for the nozzle with smooth contraction (SC). The jet lateral spread of the mean-velocity, shown in Fig. 4.13(c), is relatively higher for the nozzle with smooth contraction which agrees with the experimental results of Langman *et al*. [16] who obtained higher spread rate for the smooth contraction nozzle compared with that of a pipe jet. In addition, Fig. 4.13(d) shows that the radial profile of the axial turbulence intensity close to the nozzle exit (x/D ~ 1) is nearly comparable between the two nozzles in the centerline of the jet but higher for the smoothly contracting nozzle in the shear layer. This is why this jet spreads faster and hence results in a lower flame liftoff height. To better further understand this behaviour, the exit velocity profile for both nozzles of Experiment #3 (see Table 3.1) is presented in Fig. 4.14. This figure reveals that while the smooth contracted nozzle produces a nearly top-hat velocity profile, the jet velocity profile of the 90-degree contracted nozzle is more similar to a fully-developed pipe flow. The fact that the exit velocity profile of the 90-degree contracted angle nozzle is similar to that of a pipe is consistent with the present flame results. For instance, the flame liftoff velocity of the 90-degree contracted nozzle is comparable to that of the pipe reported in the literature. In addition, the sharper velocity gradient (and correspondingly the more turbulent shear stress – shown in the next chapter) in the shear-layer of the smooth contracted nozzle explains why the velocity spreads faster laterally for this nozzle geometry. On the other hand, because the velocity gradients are very weak in the proximity of the axis of symmetry of the smooth contracted nozzle (and consequently the turbulent shear stress), it is expected that there is no significant influence of the shear-layer on the jet axial parameters such as the axial mean-velocity decay and turbulence intensity on the axis close to nozzle exit. This can explain why the angle does not significantly affect the flow characteristics along the axis, especially in the near-field region of the turbulent jet.

The turbulence intensity profiles presented in Figs. 4.11(b), 4.12(b) and 4.13(b) reveal that the jet turbulence intensity exhibits a rapid increase downstream of the nozzle exit up to x/D ~ 7 to 9, which is an indication of the production of turbulent kinetic energy close to nozzle exit [147]. This production of turbulence kinetic energy is a sign of the development of large scale structures in the flow [19]. These structures have prominent effect on the stability (especially liftoff height) of a lifted flame. Farther downstream of the nozzle, however, the jet attains the self-similar profile of a turbulent jet as suggested by the turbulence intensity profiles (Figs. 4.11(b), 4.12(b) and 4.13(b)). These profiles show that farther downstream of the nozzle (x/D $>$ ~10) the turbulence intensity drops and adopts a trend of a more developed turbulent flow.

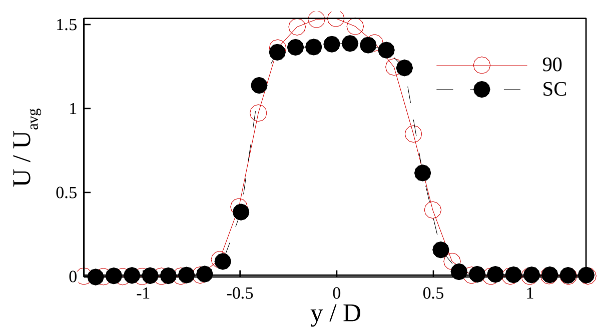

Fig. 4.14 Comparison of the exit mean-velocity profile between different nozzle contraction angles (U_{jet}~30 m/s, U_{co}~0.2 m/s).

4.2.5. Discussion

What is implied from the flame liftoff height profiles (shown in Figs. 4.7, 4.8 and 4.9) and the corresponding jet flow characteristics (shown in Figs. 4.11, 4.12, 4.13 and 4.14) is presented in the following. It is revealed that the jet axial mean-velocity decay showed, in general, no correlation with the flame liftoff height when varying the nozzle geometry including the diameter, L/D and contraction angle (the same applies to the jet's potential core length). On the other hand, the present results revealed consistently that the jet mean-velocity lateral spread showed a good correlation with the flame liftoff height. That is, a jet with faster spread rate results in a lower flame liftoff height.

The finding that the jet axial mean-velocity decay did not correlate with the flame liftoff height is in agreement with the results of Iyogun and Birouk [44] who reported that in the jet near-field region, the centerline mean-velocity decay of the pipe jet and that of the contracted circular jet were nearly identical. In addition, Mi *et al*. [42, 47], Langman *et al*. [16] and Iyogun and Birouk [44] showed that the jet spread rate was higher for the circular nozzle with smooth contraction compared with that of the pipe which also supports the findings of the present study. The flame liftoff height measurements of the smooth contracted nozzle and pipe in the literature (e.g., [16, 44]) also demonstrated that, in general, the liftoff height is smaller for the nozzle that has higher spread rate close to the nozzle exit. The higher jet spread rate is an indication of increased jet entrainment, and hence improved mixing. Therefore, it is believed that the flame liftoff height, as shown in the previous figures, might be governed primarily by local mixing rate, which is indicated by the jet spreading rates.

Furthermore, the results presented above showed that the turbulence intensity level in the near-field region (believed to be in the proximity of the flame leading edge) is higher for the nozzle which yields a lower liftoff height. The premixed theory of Kalghatgi [9] assumes that liftoff height is controlled by turbulent flame speed/burning velocity, and that the flame base propagation speed is proportional to the square root of the turbulence intensity [9]. This implies that when the turbulence intensity level in the flow upstream of the flame base goes up, the propagation speed of the flame base increases, as well. Since this speed balances the upcoming mixture velocity at the flame leading edge/front, it is believed that an increase in turbulence intensity results in an increase in the turbulent propagation speed of the flame, which, in turn, stabilizes the flame base at a lower height. The present findings support this theory, and is in agreement with the conclusion of Lawn [31] in that the premixed theory provides reasonable predictions of the liftoff height for H_l/D > ~20, whereas the instabilities due to large eddies/structures become dominant for lower flame liftoff heights in the presence of hysteresis.

CHAPTER 5
RESULTS AND DISCUSSIONS; EFFECT OF EXIT GEOMETRY OF A NOZZLE ON THE STABILITY OF TURBULENT DIFFUSION FLAME

Results on the effect of the internal geometry (diameter, contraction length L/D, and contraction angle) of a circular fuel nozzle on liftoff phenomena were presented and discussed in Chapter 4. In this chapter, however, to investigate the effect of the fuel nozzle exit geometry on the liftoff phenomena, results of a rectangular nozzle with AR = 2 having internal geometrical parameters similar to that of the circular nozzle (as presented in Table 3.1) are presented and discussed in comparison with that of the circular nozzles given in the previous chapter. Similar to that in Chapter 4, liftoff velocity (U_l) and flame liftoff height (H_l) are presented as function of coflow velocity (U_{co}). For the measurement of the velocity field, however, the profiles of non-dimensional Reynolds shear-stresses are also presented, in addition to the parameters presented in the previous chapter (i.e., axial mean-velocity decay U_{jet}/U_{cl}, axial and lateral turbulence intensity profiles u/U_{jet} and v/U_{jet}, and lateral and spanwise spread of axial mean-velocity $Y_{1/2}/D$ and $Z_{1/2}/D$). This chapter is divided into three sections. In the first section, the effect of internal geometry parameters (diameter, contraction length L/D, and contraction angle) on the liftoff phenomena of the rectangular nozzle are briefly discussed. In the second and third sections, however, the results on the effect of orifice exit geometry on the liftoff phenomena are presented and discussed.

5.1. Effect of the internal geometry of a rectangular nozzle on liftoff phenomena

In this section, the conclusions drawn from the obtained results on the effect of the internal geometry of a rectangular nozzle on the flame liftoff phenomena (following an investigation similar to that undertaken for a circular nozzle in Chapter 4) are presented without bringing detailed results to keep the main text concise. However, details including the estimation of the rectangular jet flow entrainment, and the flame liftoff results and flow characteristics can be found respectively in Appendices D and E.

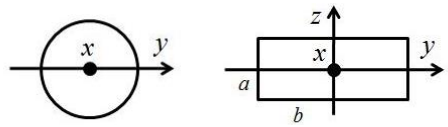

Fig. 5.1 Nozzle exit geometry test, circular nozzle (left), and rectangular nozzle (AR = 2) (right)

The rectangular nozzle exit orifice aspect ratio is equal to 2. The experimental results showed that, similar to the conclusions reached for the circular nozzle flame, the level of turbulence in the jet near-field region of the rectangular jet has also a definite impact on the liftoff phenomena. That is, the rectangular nozzle with higher L/D or the nozzle with smooth contraction which generates higher levels of jet near-field turbulence also maintained an attached flame within higher fuel jet velocity range. In addition, it is found that a rectangular jet which spreads faster in the minor plane and generates higher near-field turbulence (e.g., the rectangular nozzle with lower L/D or the nozzle with smooth contraction) would result in a flame base sitting closer to the nozzle. The results consistently showed that the jet development on the minor plane accompanied by greater spread rates and high turbulence levels have a dominant role on jet entrainment/mixing and hence the stabilization of the flame base downstream of the nozzle. The effect of diameter on liftoff phenomena and flow characteristics was found to be a function of the strength of co-flow, however.

5.2. Effect of the nozzle exit geometry on liftoff velocity

In this section, results on the effect of fuel nozzle exit geometry (i.e., the rectangular nozzle with AR = 2 in comparison with the circular nozzle) on the liftoff phenomena as described in Chapter 3 (Tables 3.1 and 3.2) and shown again here in Fig. 5.1 (for comfort) are presented.

Figure 5.2(a) shows that the flame liftoff velocity increases with co-flow velocity for both circular and rectangular nozzles with D_e = 3 mm and L/D_e = 1. The increase rate is, however, faster for the circular nozzle where the flame liftoff velocity of the circular nozzle is relatively smaller than that of the rectangular nozzle at a low co-flow and then becomes higher for $U_{co}> \sim$ 0.6 m/s. Figure 5.2(b) shows that the flame liftoff velocity, which increases with the co-flow, is very much the same for both, circular and rectangular, nozzles with D_e = 4.5 mm and L/D_e = 1. Figure 5.2(c) presents the flame liftoff velocity variation with the co-flow exit velocity for both, circular and rectangular, nozzles with D_e = 4.5 mm and L/D_e = 2.8. This figure shows that the flame liftoff velocity, which increases slightly with the co-flow velocity up to U_{co} ~ 0.9 m/s beyond which it remains almost unchanged, is noticeably higher for the circular nozzle. Figure 5.2(d) shows that for the same nozzles presented in Fig. 5.2(c) but with an increased L/D_e (= 5.6), the flame liftoff height of the circular nozzle becomes significantly higher than that of the rectangular nozzle. This figure reveals also that the flame liftoff velocity increases with the co-flow velocity until it reaches a maximum at U_{co}~ 0.5 beyond which it exhibits a slow steady decrease. Finally, Fig. 5.2(e) presents the methane flame liftoff velocity versus the co-flow velocity for both, circular and the rectangular, nozzles with a smoothly contracted internal geometry (where D_e ~ 4.8 mm and L/D_e ~ 6.2). The figure shows that the smoothly contracted circular nozzle (SC) has a considerably larger flame liftoff velocity than that of the smoothly contracted rectangular nozzle. The same figure shows also that the liftoff velocity of both, the circular and rectangular, nozzles increases with the co-flow until it reaches a peak (at U_{co}~ 0.2 m/s for the circular nozzle, and U_{co}~ 0.1 m/s for the rectangular nozzle) after which it drops gradually with further increase in the co-flow exit velocity.

A comparison between Figs. 5.2(a) and (b) shows that the flame blows off earlier (i.e., at a smaller co-flow velocity) as the nozzle diameter becomes smaller. The blowoff occurs at U_{co} ~ 0.9 m/s for the 3 mm diameter nozzle but at U_{co} ~ 1.3 m/s for the 4.5 mm diameter nozzle regardless of the exit orifice geometry. Figure 5.2 shows also that the difference in the flame liftoff velocity between the circular and the rectangular nozzle is not significant at zero co-flow exit velocity (for the nozzles with $D_e > 3$ mm) but noticeable at any higher co-flow velocity. Figure 5.2 demonstrates also that the trend of the liftoff velocity dependence on the co-flow velocity (i.e., whether or not the liftoff velocity increases/decreases with co-flow velocity or remains unchanged) is more a function of the nozzle internal geometry rather than the exit orifice shape. However, the exit orifice geometry affects the magnitude of the liftoff velocity without changing the trend of its dependence on co-flow. For instance, Fig. 5.2(a-c) show that the difference in the flame liftoff velocity between the circular and the rectangular nozzle becomes more significant for the nozzle with greater L/D_e (Fig. 5.2(a-c)), and it becomes even more noticeable by increasing the length of the contracted section of the nozzles to L/D_e ~ 6.2 (Fig. 5.2(e)). However, the emphasis of this chapter is on the effect of a nozzle exit orifice shape (i.e., a circular exit or a rectangular exit with AR = 2) on the stability of a turbulent diffusion methane flame, and therefore further details on the effect of the internal geometry of a nozzle (e.g., equivalent diameter, L/D_e and contraction angle) on the stability of a turbulent diffusion methane flame can be found elsewhere (e.g., [148], Chapter 3 and Appendix E).

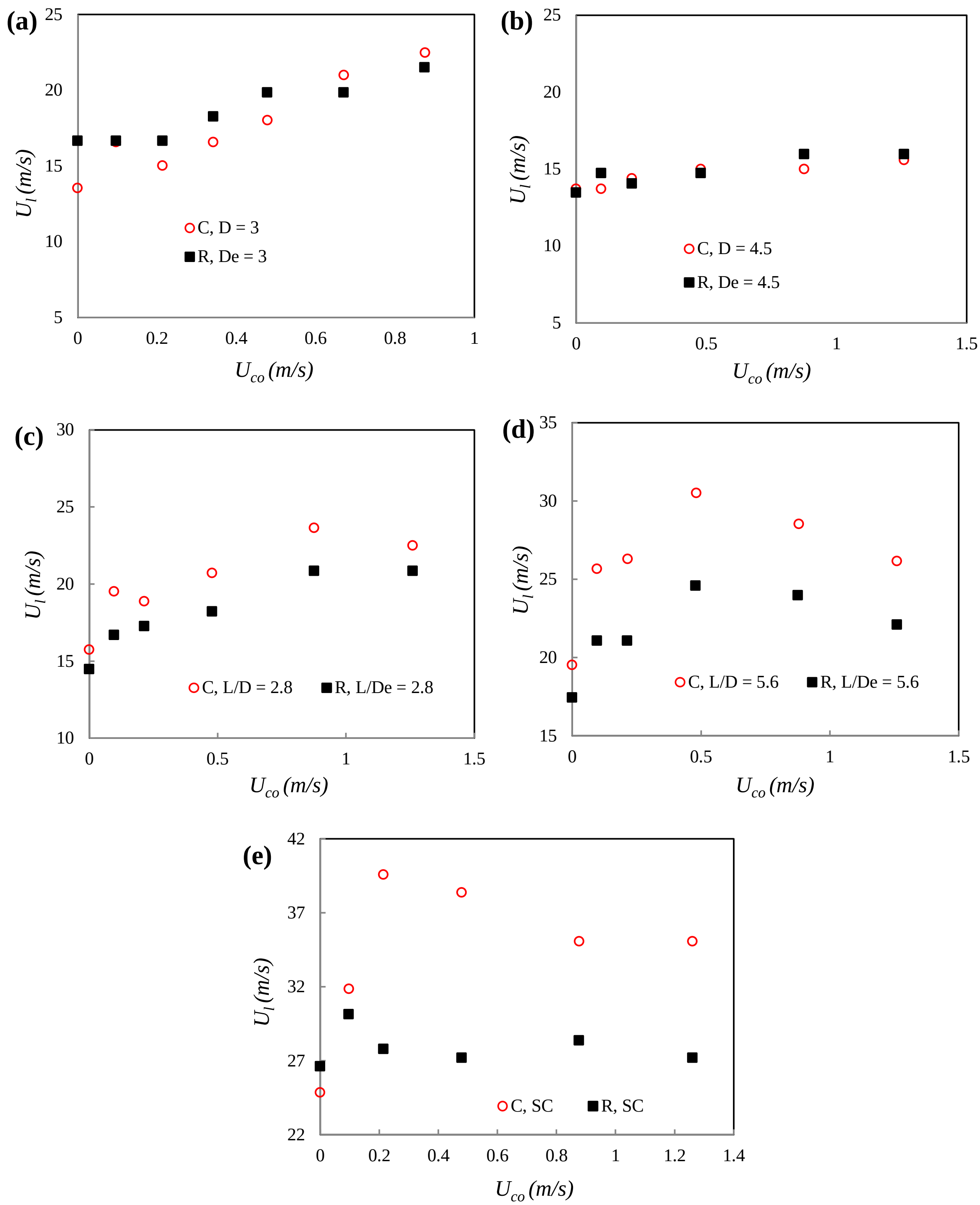

Fig. 5.2 Comparison of the liftoff velocity as a function of the co-flow velocity between the circular and rectangular nozzle exit orifice with (a) D_e = 3 mm and L/D_e = 1, (b) D_e = 4.5 mm and L/D_e = 1, (c) D_e = 4.5 mm and L/D_e = 2.8, (d) D_e = 4.5 mm and L/D_e = 5.6, and (e) D_e = 4.8 mm and L/D_e = 6.2

5.2.1. Flow characteristics

To help understand the reasons behind the trends exhibited in Fig. 5.2(a-e), details about the flow characteristics of the corresponding turbulent jets, such as the axial and lateral development of turbulence intensity profiles, axial mean-velocity decay, and lateral distribution of turbulent shear stress close to the nozzle exits (i.e., in the jet near-field region) are provided for all nozzle geometries. These profiles, which are for typical flow conditions just prior to the liftoff of the flame (i.e., in the range $U_{jet} = 10 - 17\ \mathrm{m/s}$), are shown in Figs. 5.3-5.7 for different nozzle geometries.

Figure 5.3 shows the flow characteristics of the circular and rectangular nozzles with D_e = 3 mm and L/D_e = 1. Figure 5.3(a) shows that the axial mean-velocity decay rate (at U_{jet}~ 17 and U_{co}~ 0.2 m/s) is almost the same for both (circular and rectangular) nozzles. This figure shows also that the two jets have nearly the same potential core's length (~ $3D$). Figure 5.3(b) shows that the axial component of turbulence intensity (u/U_{jet}) along the nozzle axis/centerline is relatively larger for the circular nozzle. However, the lateral profiles of u/U_{jet} at x/D_e ~ 3, which are plotted in Figs. 5.3(c) and (d), respectively, on the major and minor planes, demonstrate that the turbulence intensity for the circular nozzle is higher than that for the rectangular nozzle on the major plane, whereas it is nearly the same between the two nozzles on the minor plane, except in the vicinity of the centerline. A comparison of the lateral profiles of the normalized turbulent shear-stress ($< uv >/U_{cl}^2$) between the circular nozzle and rectangular nozzle is shown in Fig. 5.3(e) on the major axis and in Fig. 5.3(f) on the minor axis at x/D_e ~ 3. These figures clearly demonstrate that $< uv >/U_{cl}^2$ amplitude is fairly similar between the circular and rectangular nozzles on the major axis (Fig. 5.3(e)). However, $< uv >/U_{cl}^2$ and its rate of the lateral gradient (i.e., $d(< uv >/U_{cl}^2)/dz$) is clearly higher for the rectangular nozzle on the minor axis (Fig. 5.3(f)). The Reynolds shear stress signifies the transfer rate of flow momentum through a unit area prependicular to the streamwise (x) direction [19]. From Figs. 5.3(e) and (f), it is clear that this transfer rate is noticeably greater for the rectangular nozzle along the minor axis (compared with its counterpart circular nozzle).

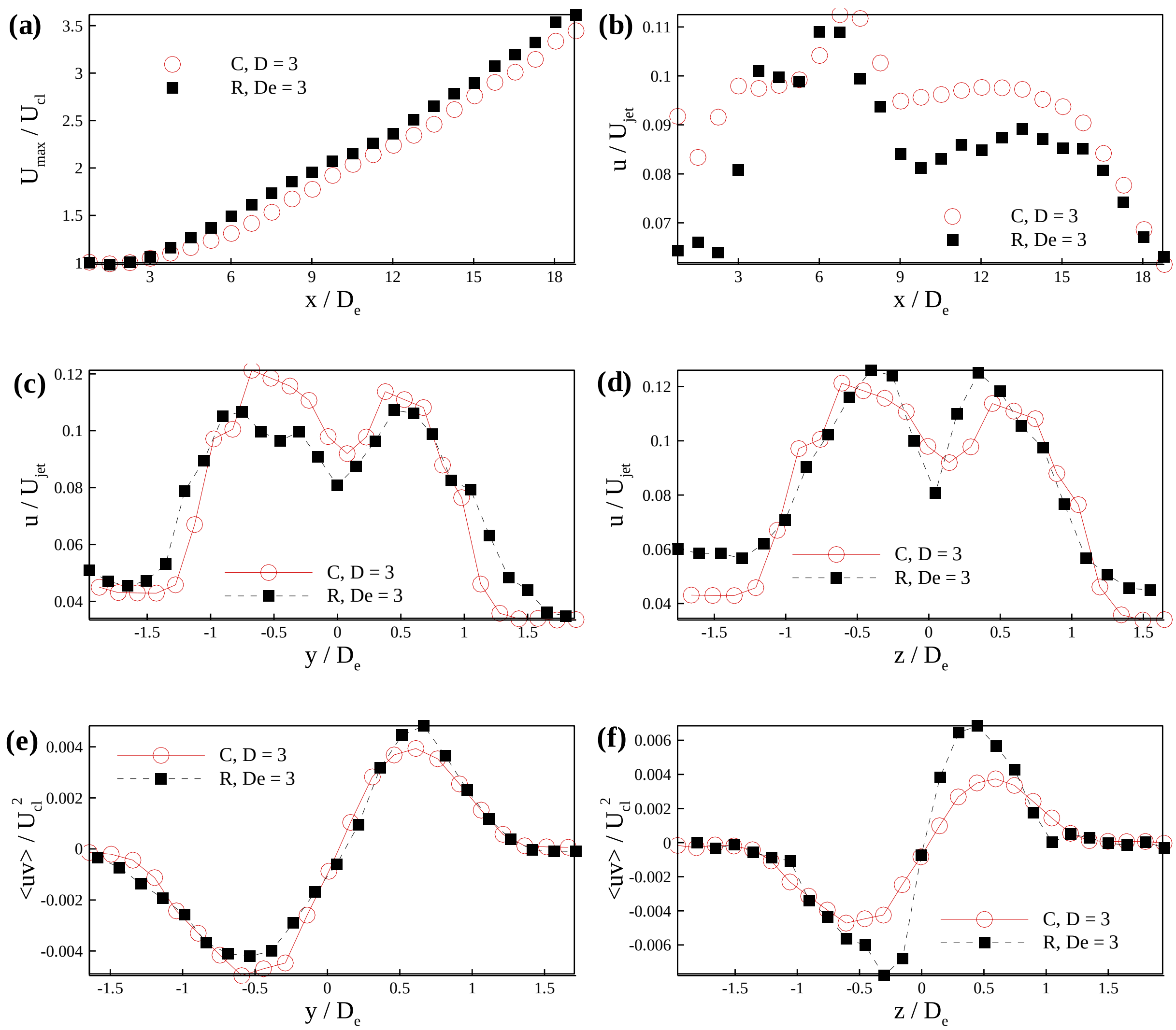

Fig. 5.3 Comparison of the (a) axial mean-velocity decay on the centerline, (b) centerline axial turbulence intensity, (c) lateral distribution of the axial turbulence intensity on the major axis, (d) lateral distribution of axial turbulence intensity on the minor axis, (e) lateral distribution of the normalized turbulent shear-stress on the major axis, and (f) lateral distribution of the normalized turbulent shear-stress on the minor axis at x/D_e ~ 3 between different nozzle's orifice exit geometry (circular and rectangular) with D_e = 3 mm and L/D_e = 1 (U_{jet}~17 m/s and U_{co}~0.2 m/s).

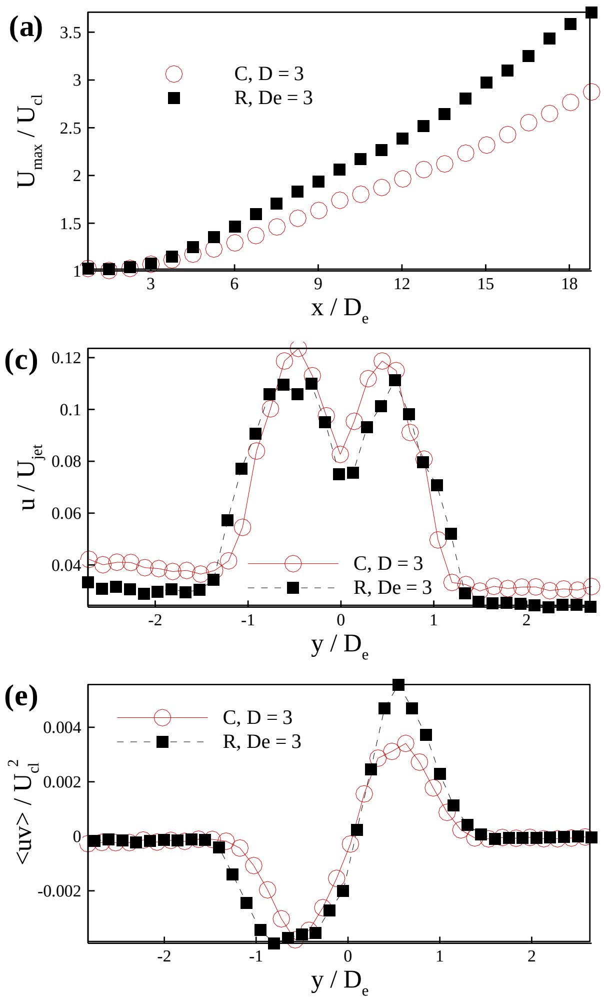

Fig. 5.4 Comparison of the (a) axial mean-velocity decay on the centerline, (b) centerline axial turbulence intensity, (c) lateral distribution of the axial turbulence intensity on the major axis, (d) lateral distribution of axial turbulence intensity on the minor axis, (e) lateral distribution of the normalized turbulent shear-stress on the major axis, and (f) lateral distribution of the normalized turbulent shear-stress on the minor axis at x/D_e ~ 3 between different nozzle's orifice exit geometry (circular and rectangular) with D_e = 3 mm and L/D_e = 1 (U_{jet}~17 m/s and U_{co}~0.5 m/s).

The experimental findings, shown in Fig. 5.4, revealed also that the presence of a stronger co-flow (i.e., U_{co} ~ 0.5 m/s) does not change significantly the trend observed in Fig. 5.3. That is, in comparison with that of the circular nozzle, the rectangular nozzle generates higher axial mean-velocity decay (but fairly the same potential core's length) (Fig. 5.4(a)), and lower turbulence intensity on the centerline (Fig. 5.4(b)) and also on the major axis (Fig. 5.4(c)).

However, the lateral turbulence intensity profiles on the minor axis show that the rectangular nozzle generates slightly higher turbulence intensity in the shear-layer (Fig. 5.4(d)). The lateral profiles of $< uv >/U_{cl}^2$ are also qualitatively similar to that of Fig. 5.3(e-f), except that $< uv > /U_{cl}^2$ on the major axis of the rectangular nozzle is also higher than that of the circular nozzle.

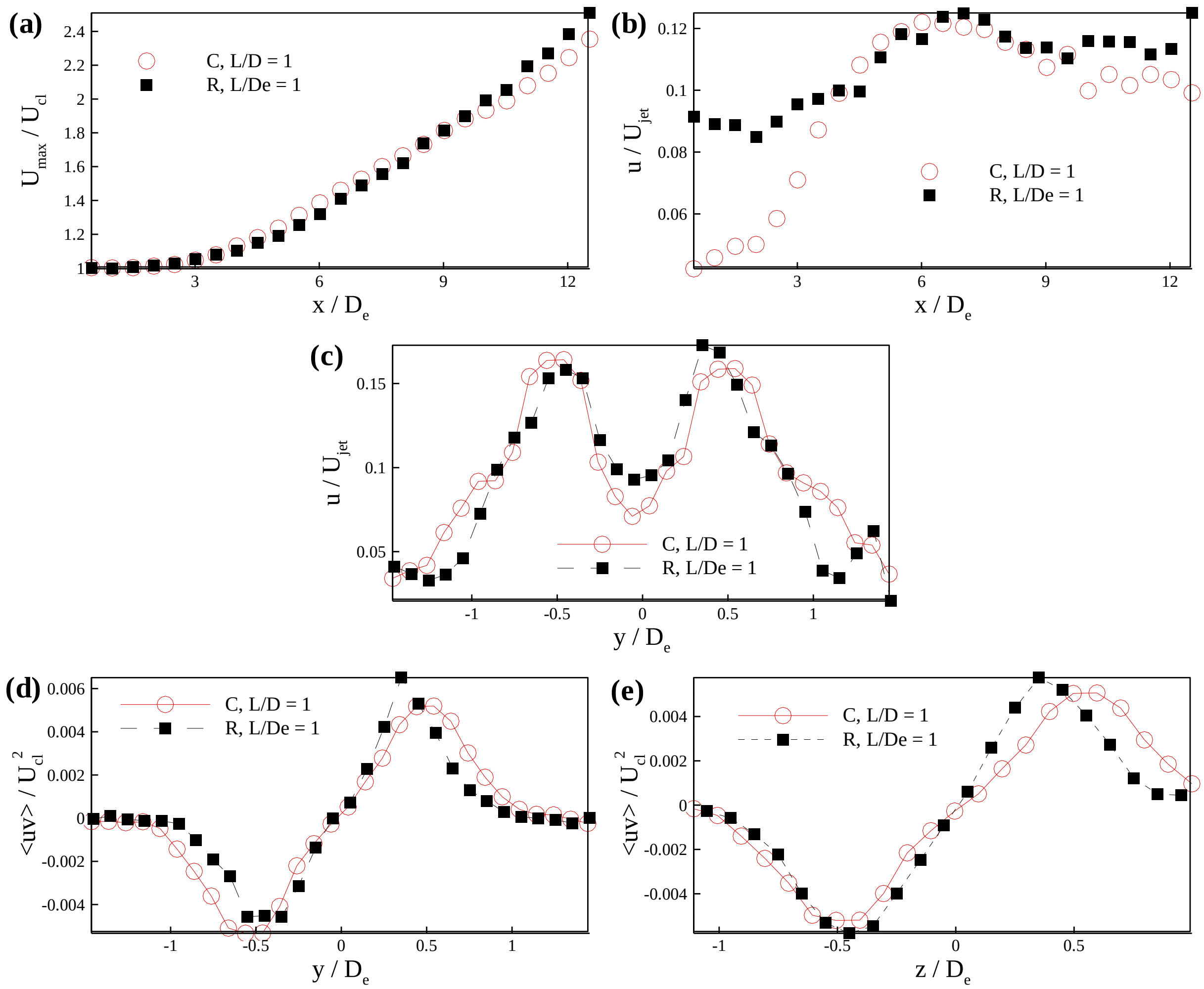

Fig. 5.5 Comparison of the (a) axial mean-velocity decay on the centerline, (b) centerline axial turbulence intensity, (c) lateral distribution of the axial turbulence intensity on the major axis, (d) lateral distribution of the normalized turbulent shear-stress on the major axis, and (e) lateral distribution of the normalized turbulent shear-stress on the minor axis at x/D_e ~ 3 between different nozzle's orifice exit geometry (circular and rectangular) with D_e = 4.5 mm and L/D_e = 1 (U_{jet}~17 m/s and U_{co}~0.2 m/s).

Figure 5.5 presents the jet flow characteristics for the circular and rectangular nozzles with D_e = 4.5 mm and L/D_e = 1. Figure 5.5(a) shows that the axial mean-velocity decay rate is fairly the same between the circular and rectangular nozzles up to x/D_e ~ 8 beyond which it becomes slightly higher for the rectangular nozzle (the same applies to the jet's potential core length). The corresponding axial turbulence intensity component on the jet centerline and its lateral profiles (along the major axis of the rectangular nozzle) at x/D_e ~ 3, which are, respectively, presented in Figs. 5.5(b) and (c), clearly show that u/U_{jet} is relatively higher for the rectangular nozzle close to nozzle exit (up to x/D_e ~ 4), and becomes very much the same between the two nozzles farther downstream. Figure 5.5(c) shows that, except in the vicinity of the centerline (y/D_e ~ $\pm$0.3), both the circular and rectangular nozzles generate fairly the same levels of turbulence intensity. Figure 5.5(d-e) show that the lateral profiles of the $< uv >/U_{cl}^2$ for the rectangular nozzle on the major and minor axes is slightly higher than that of the circular nozzle. Figure 5.5(d) demonstrates that the $< uv >/U_{cl}^2$ has similar amplitude of the lateral gradient between the circular and rectangular nozzles on the major axis, whereas Fig. 5.5(e) shows that although the magnitude of the normalized turbulent shear-stress ($< uv >/U_{cl}^2$) is very similar between the two nozzles, the rate of change is higher for the rectangular jet.

Figure 5.6 presents the jet flow characteristics for the circular and rectangular nozzles with different D_e = 4.5 mm and L/D_e = 2.8. Figure 5.6(a) shows that the axial mean-velocity decay rate is slightly higher for the rectangular nozzle. This figure shows also that the rectangular nozzle has slightly smaller potential core length (< $3D$) compared with that of the circular nozzle (~ $3D$). The corresponding axial turbulence intensity component in the jet centerline, shown in Fig. 5.6(b), is also higher for the rectangular nozzle up to x/D_e ~ 4 beyond which it becomes nearly the same between the two nozzles. The lateral profiles of u/U_{jet} (along the major axis of the rectangular nozzle) at x/D_e ~ 3, as exhibited in Fig. 5.6(c), show that it is higher for the rectangular nozzle in the vicinity of the centerline and on the outer side of the shear-layer, but fairly the same between the two nozzles elsewhere. The turbulence intensity profiles along the minor axis of the rectangular nozzle in comparison with that of the circular nozzle demonstrated similar trend. Figure 5.6(d-e) show that the circular nozzle generates a normalized turbulent shear-stress with similar amplitude but higher lateral gradient in comparison with that of the rectangular nozzle on the major axis. The trend on the minor axis, however, is clearly the opposite. That is, both magnitude of the normalized turbulent shear-stress and its lateral gradient are higher on the minor axis of the rectangular nozzle. Similar conclusions were obtained when looking at the flow characteristics profiles for the nozzles with D_e = 4.5 mm and L/D_e = 5.6 (not shown here but can be found in Appendix E).

Figure 5.7 presents the effect of the fuel nozzle exit orifice shape for a nozzle with a smoothly contracted section on the jet near-field characteristics at the typical conditions (i.e., U_{jet} ~17 m/s and U_{co} ~ 0.2 m/s). Figure 5.7(a) shows that the axial mean-velocity decay rate is clearly higher for the rectangular nozzle. This figure shows also that the circular nozzle with smooth contraction has clearly larger potential core length (~ $4D$) compared with that of the rectangular nozzle having the same internal geometry (~ 2.25D_e). The reduction of the potential core length of the rectangular nozzle in comparison with that of the circular one is an indication of the increase of the mixing rate of the rectangular jet [17, 149]. Similarly, the centerline axial turbulence intensity (in the near field, i.e., for x/D_e < ~6), as seen in Fig. 5.7(b), and its lateral distribution (at x/D_e ~3 in Fig. 5.7(c)) are also clearly higher for the rectangular nozzle. Figure 5.7(d) shows that $< uv >/U_{cl}^2$ is slightly higher along the major axis of the rectangular nozzle; however, the two nozzles exhibit similar lateral gradient. The present experimental findings (Appendix E) revealed also that increasing the co-flow velocity does not change the trend observed in Fig. 5.7.

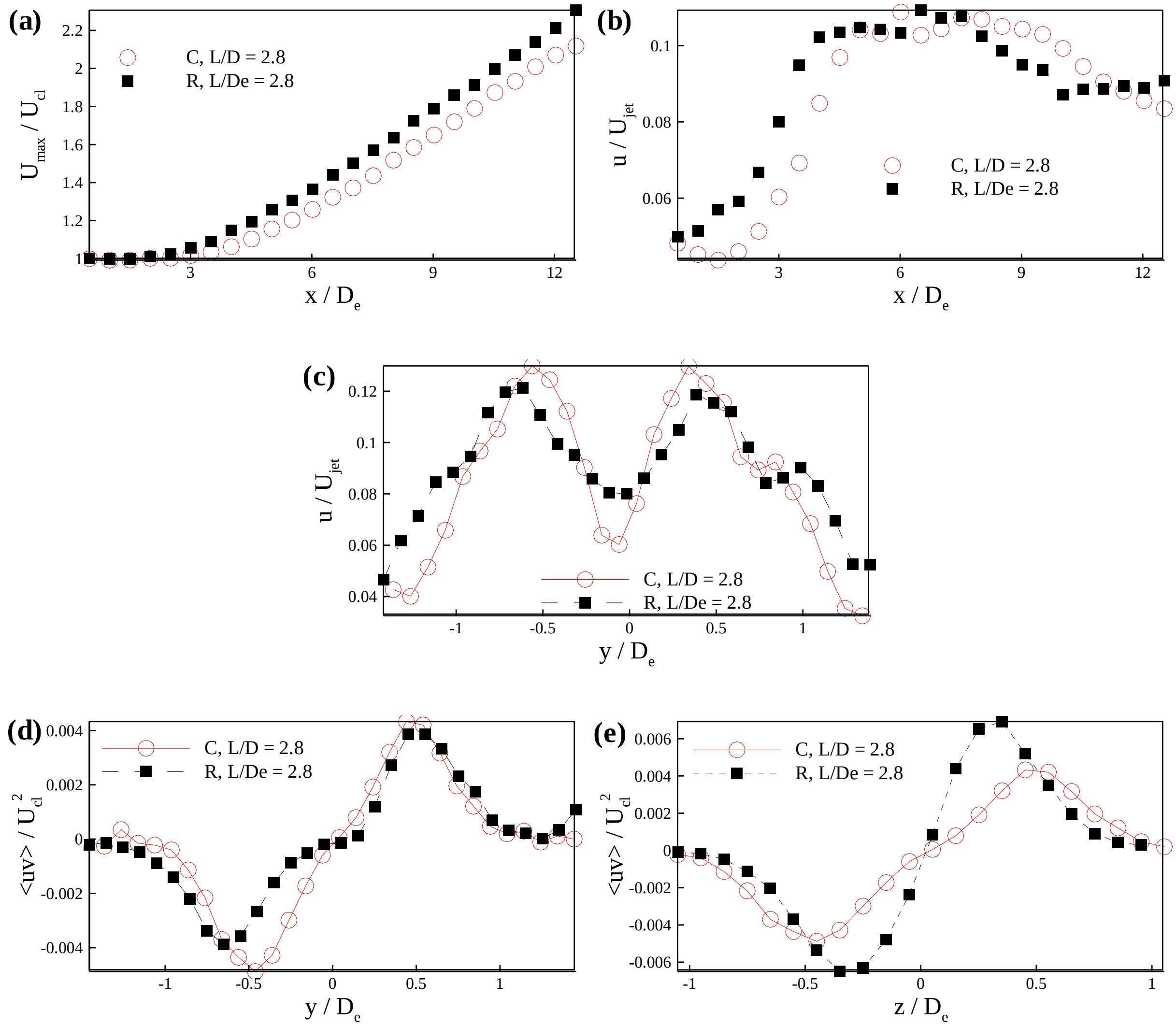

Fig. 5.6 Comparison of the (a) axial mean-velocity decay on the centerline, (b) centerline axial turbulence intensity, (c) lateral distribution of the axial turbulence intensity on the major axis, (d) lateral distribution of the normalized turbulent shear-stress on the major axis, and (e) lateral distribution of the normalized turbulent shear-stress on the minor axis at x/D_e ~ 3 between different nozzle's exit orifice geometry (circular and rectangular) with D_e = 4.5 mm and L/D_e = 2.8 (U_{jet}~17 m/s and U_{co}~0.2 m/s).

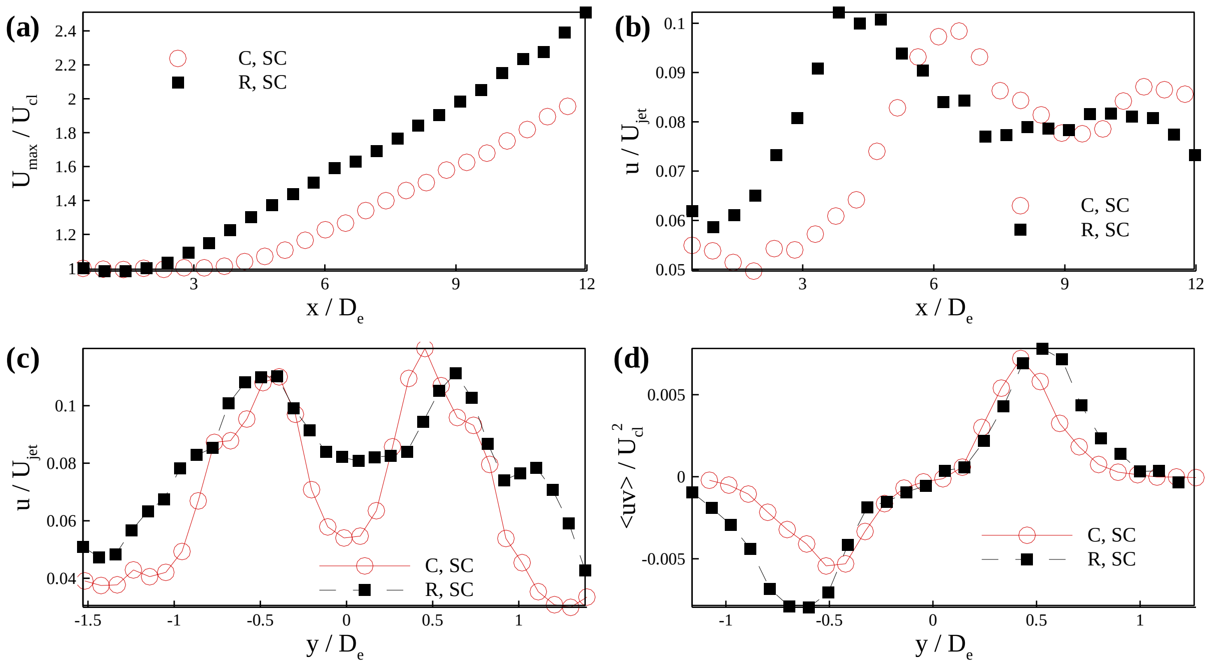

Fig. 5.7 Comparison of the (a) axial mean-velocity decay on the centerline, (b) centerline axial turbulence intensity, (c) lateral distribution of the axial turbulence intensity on the major axis, and (d) lateral distribution of the normalized turbulent shear-stress on the major axis at x/D_e ~ 3 between different nozzle's exit orifice geometry (circular and rectangular) with smooth contraction (U_{jet}~17 m/s and U_{co}~0.2 m/s).

5.2.2. Discussion

Figures 5.3-5.7 showed that overall, in the jet near-field, a rectangular nozzle has higher axial mean-velocity decay rate than a circular nozzle regardless of the internal geometry (i.e., D_e, L/D_e or the contraction angle). These figures showed also that, with the exception of the nozzle with D_e= 3 mm and L/D_e = 1, the rectangular nozzle has higher centerline turbulence intensity. The rectangular nozzle with D_e= 4.5 mm and L/D_e = 1 which has higher centerline turbulence intensity up to x/D_e ~ 4, generated nearly similar turbulence intensity to that of the circular nozzle when moving slightly away from the centerline. As a result, a correlation seems also to exist between the turbulence intensity (u/U_{jet}) profiles and the corresponding flame liftoff velocity of the nozzles with different exit geometries (i.e., the circular and the rectangular nozzle) presented in Fig. 5.2. That is, the higher the jet near-field turbulence intensity, the lower the flame liftoff velocity. For instance, the considerable difference between the liftoff velocity of the circular and rectangular nozzles with smooth contraction (i.e., at U_{co} > ~ 0.2 m/s in Fig. 5.2(e)) can be attributed to the difference in the turbulence intensity between these two nozzles (see Fig. 5.7(b-c)). In fact, such reasoning is also valid for the nozzles with the smaller diameter (i.e., $D_e = 3$ mm in Fig. 5.2(a)). That is, the circular nozzle, which has higher turbulence intensity in the near-field according to Fig. 5.3(b-c), also has lower flame liftoff velocity (Fig. 5.2(a)). The different trends between the nozzles with smaller diameter (D_e = 3 mm) and larger diameter (D_e = 4.5 mm and greater) might be attributed to the impact of the nozzle lip thickness [30] on the flow (i.e., the so-called bluff-body effect) which is more significant for the nozzles with a smaller diameter (considering that all nozzle geometries employed in the present study have the same external geometry).

These findings further confirm the conclusion (reached in Chapter 4) that higher levels of jet near-field turbulence results in a lower flame liftoff velocity regardless of the nozzle geometry. Figures 5.3-5.7 show also that the lateral gradient of the normalized turbulent shear-stress ($< uv >/U_{cl}^2$) comply with the above conclusion. That is, in general, the higher the lateral gradient of the normalized turbulent shear-stress ($< uv >/U_{cl}^2$), the lower the flame liftoff velocity.

It was shown that the jet's Reynolds number at the nozzle exit at liftoff in all cases is greater than $Re = 2300$ (in Chapter 4 and Appendix E, i.e., regardless of the nozzle exit orifice geometry), which is the upper critical Reynolds number for a laminar pipe flow and below $Re \sim 10000$, which corresponds to a fully-turbulent pipe flow. This information confirms the suggestion that all nozzle geometries tested here produce a turbulent or a semi-turbulent (transient turbulent) flow regime, which thus approve the theory that suggests a strong relationship between a jet's turbulence and its corresponding flame liftoff.

It was shown that the flame of the smoothly contracted (circular or rectangular) nozzle exhibits a pronounced necking due to the advent of discontinuities and holes shortly before the occurrence of its liftoff. This was not the case for the flame for a 90-degree contracted nozzle where the attached flame experiences an abrupt liftoff. This suggests that the mode of quenching at liftoff is more dominantly dependent on the internal geometry of a nozzle but not on its exit orifice shape, and/or co-flow velocity. Further details about the detachment transition of an attached flame from its burner can be found elsewhere [15, 16, 148].

It was pointed out in Chapter 4 that previous studies showed the importance of high-frequency flow structures in quenching a diffusion flame. It was reported that the transition from laminar to turbulent flame associated with changes in the structure of the central gas jet occurs at liftoff which suppresses the low-frequency instabilities (which are dominant in the attached flame at the lower Reynolds number range) and hence cause liftoff to precipitate due to the invasion of the laminar flame base by turbulence present in the central fuel jet [5–7]. Especially, Coats and Zhao [6] were able to show that transition in the burner tube (i.e., a pipe) was delayed by smoothing the incoming flow from the nozzle (with a smooth contraction) which marked the effect of turbulence on the stability of the attached flame. In this section, it was also shown that the increase in the jet turbulence intensity level close to the nozzle exit precipitated the occurrence of flame liftoff (regardless of the nozzle exit orifice geometry) which is in agreement with the conclusion of Coats and Zhao [6] and confirms our findings previously presented in Chapter 4.

The centerline turbulence intensity profiles presented above (Figs. 5.3(b)–5.7(b)) can be used to illustrate the importance of flow structures in the jet flow near-field on the stability of a diffusion flame. That is, the rapid increase of the jet turbulence intensity downstream of the nozzle exit (up to x/D ~ 5 to 10) indicates the production of turbulent kinetic energy close to nozzle exit which is a sign of the advent of large scale structures in the flow [19]. These structures have a prominent effect on the stability of a lifted flame [5, 6, 28]. Farther downstream of the nozzle, however, the turbulence intensity drops and adopts a trend of a more developed turbulent flow. These figures show also that, downstream of the nozzle exit on the centerline, the turbulence intensity is, in general, higher for the rectangular nozzle, with the exception of the small diameter nozzle (D_e= 3 mm) for which the opposite scenario is observed. Therefore, in line with the aforementioned discussed literature, these figures may explain why the corresponding liftoff velocity for the rectangular nozzle is, in general, lower compared with that of its counterpart's circular nozzle. However, the inconsistency in the flow characteristics between the two nozzles (D_e = 3 mm and $D_e \geq$ 4.5 mm) might be attributed to the effect of the nozzle's lip thickness on the flow. The lip thickness is larger for the smaller diameter (D_e = 3 mm) since all the nozzles employed in the present study have the same external geometry.

Overall, the present results demonstrated that the level of turbulence intensity in the vicinity of the nozzle exit is the controlling parameter of the flame detachment process from the nozzle. In fact, the present study consistently showed that the liftoff velocity is higher for the fuel nozzle that produces lower turbulence level in the jet near-field flow which is in agreement with the theory of Coats and Zhao [6] in that the flame liftoff is a result of the invasion of laminar flame base by turbulent structures.

5.3. Effect of the nozzle exit geometry on liftoff height

Figure 5.8(a-e) presents the flame liftoff height for the nozzle geometries tested here versus the fuel jet exit velocity for zero co-flow velocity (F: forward profiles, were obtained by increasing the jet velocity; and B: backward profiles, were obtained by decreasing the jet velocity).

Figure 5.8(a) shows that the flame liftoff height of $D = 3$ mm circular nozzle, in the absence of a co-flow, is slightly smaller than that of the rectangular nozzle having the same equivalent diameter and L/D_e (i.e., = 1). Figure 5.8(b) shows that increasing the nozzle diameter from $D_e = 3$ mm (Fig. 5.8(a)) to $D_e = 4.5$ mm (Fig. 5.8(b)) results in an opposite scenario. That is, the liftoff height of the rectangular nozzle with $L/D_e = 1$ and $D_e = 4.5$ mm is slightly smaller than that of the circular nozzle with the same L/D and exit area. Figures 5.8(c) and (d) also exhibit a similar scenario. That is, the rectangular nozzle lifted flame is slightly lower than that of the circular nozzle. Such a trend is found to be independent of L/D_e; however, the difference between the liftoff heights of the circular and rectangular nozzles slightly increases with increasing L/D_e. Also, Fig. 5.8(e) shows that the rectangular nozzle with smooth contraction has a liftoff height which is clearly smaller than that of the circular nozzle having similar internal geometry. This agrees with Fig. 5.8(d) in that the liftoff height difference between the circular and rectangular nozzles with a longer contraction section ratio (i.e., L/D_e) is, in general, more significant.

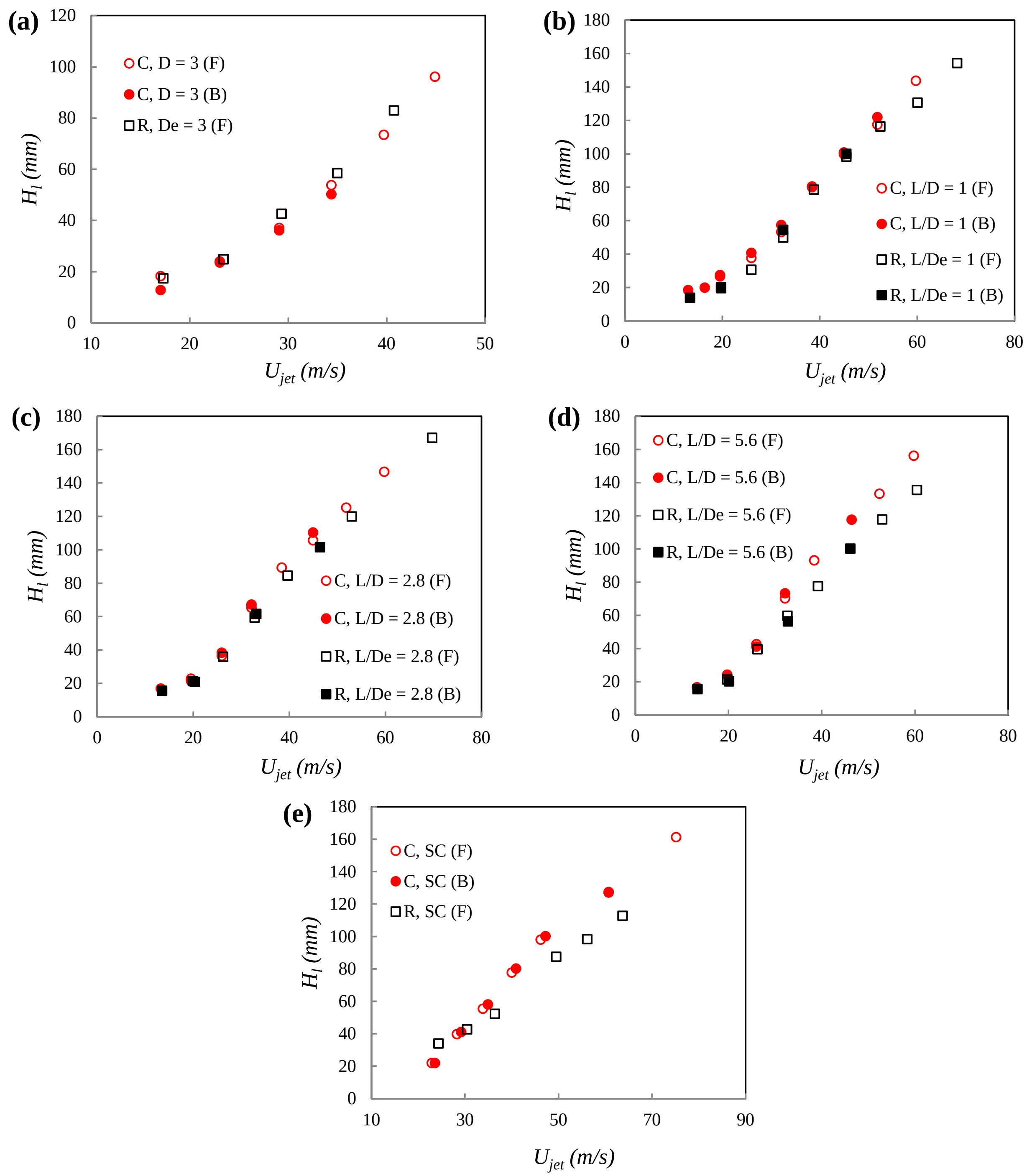

Fig. 5.8 Flame liftoff height versus jet fuel exit velocity at zero co-flow for nozzles with different nozzle's orifice exit geometry having (a) D_e = 3 mm and L/D_e = 1, (b) D_e = 4.5 mm and L/D_e = 1, (c) D_e = 4.5 mm and L/D_e = 2.8, (d) D_e = 4.5 mm and L/D_e = 5.6, and (e) D_e = 4.8 mm and L/D_e = 6.2.

A common trend observed in Fig. 5.8(a-e) is that the liftoff height of the circular and the rectangular nozzles (having the same internal geometry) at low fuel jet velocity are fairly similar, but the difference between the liftoff height profiles increases with increasing the fuel jet velocity. Another common trend is that at zero co-flow velocity, with the exception of the very low range of fuel jet exit velocity (just above U_l), the flame liftoff height for both (circular and rectangular) nozzles (with different internal geometries), increases linearly with the fuel jet exit velocity. However, the increase in the slope is, in general, slightly slower for the rectangular nozzle. The liftoff height for the backward profiles approximately collapse onto that of the forward profiles closer to U_l (independent of the nozzle exit orifice geometry). Below U_l, however, a slower but continuous reduction in the liftoff height was observed followed by an abrupt attachment of the flame onto the nozzle at the reattachment velocity, U_r, in agreement with the literature (e.g., [4, 7, 150]). It should be reminded that details on the effect of the internal geometry of a nozzle (e.g., equivalent diameter, L/D_e and contraction angle) on the liftoff height of a turbulent diffusion methane flame are reported in Chapter 4 and Appendix E.

The liftoff height of a lifted jet flame in the presence of a co-flow, U_{co}~0.9 m/s, is shown in Fig. 5.9. In contrast with what was observed in Fig. 5.8(a) (the liftoff height of the circular nozzle is slightly smaller than that of the rectangular nozzle for a pure flame), Fig. 5.9(a) shows that in the presence of a moderate co-flow, there is no noticeable difference in the flame height between the circular and the rectangular nozzle having $D_e = 3$ mm and $L/D_e = 1$. However, the co-flowing lifted flame (Fig. 5.9(a)) blows out at a relatively lower jet exit velocity in comparison with the pure jet flame (Fig. 5.8(a)). The liftoff height profiles for the nozzles with $D_e = 3$ mm and L/D_e = 1 (Figs. 5.8(a) and (b)), overall, show that the exit orifice shape of the nozzle (i.e., axisymmetric circular or asymmetric rectangular) does not noticeably affect the liftoff height of the lifted methane flame.

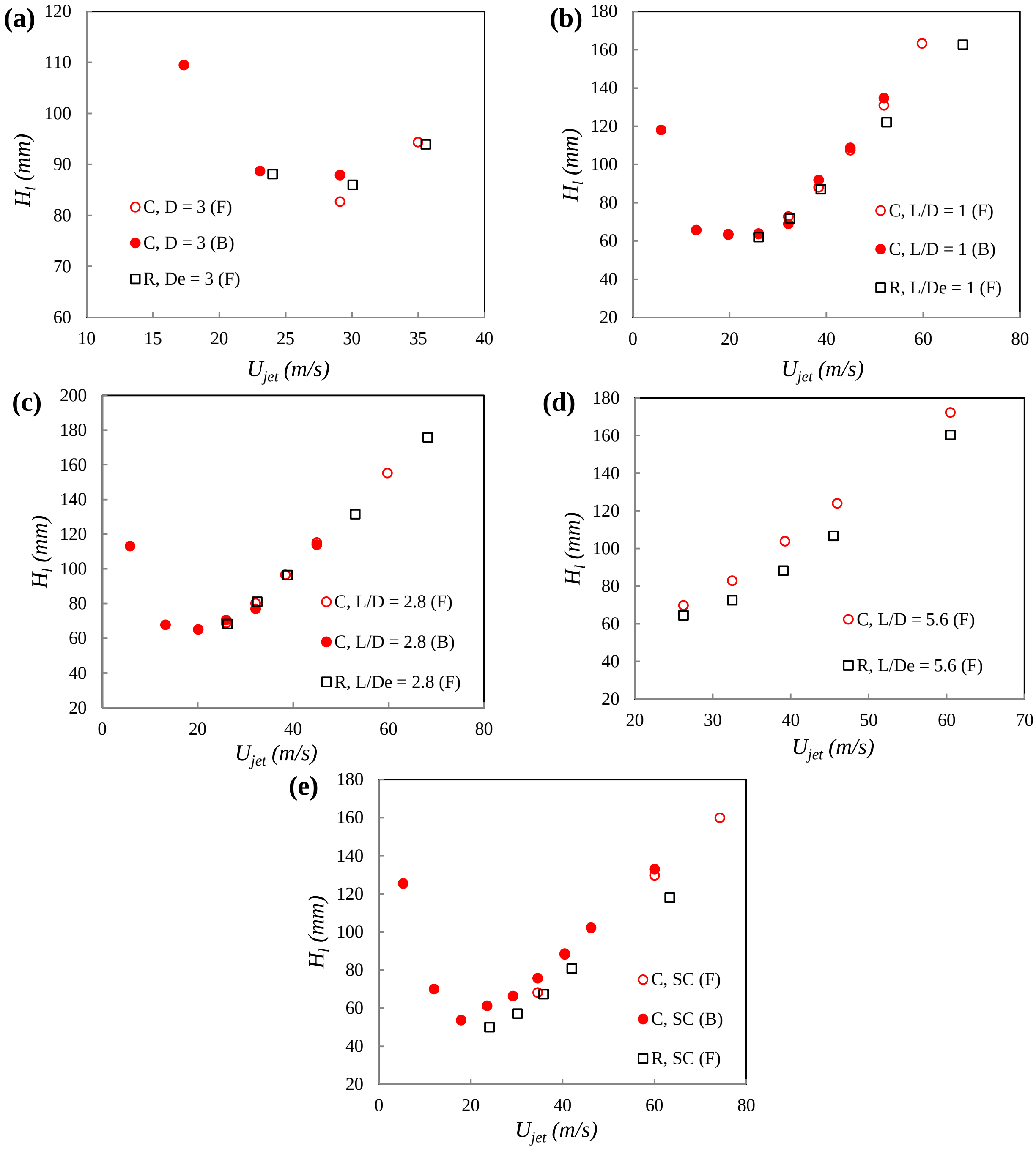

Fig. 5.9 Liftoff height versus jet fuel exit velocity at $U_{co} \sim 0.9\ m/s$ for different nozzle's exit orifice geometry having (a) D_e = 3 mm and L/D_e = 1, (b) D_e = 4.5 mm and L/D_e = 1, (c) D_e = 4.5 mm and L/D_e = 2.8, (d) D_e = 4.5 mm and L/D_e = 5.6, and (e) D_e = 4.8 mm and L/D_e = 6.2.

The effect of the nozzle exit orifice shape on the flame liftoff height in the presence of co-flow, shown in Fig. 5.9(b-e) for the nozzle with larger exit orifice ($D_e > 3$), is similar to what was previously seen in Fig. 5.8(b-e) for non-coflowing methane flame. That is, generally, the circular nozzle produces greater liftoff heights.

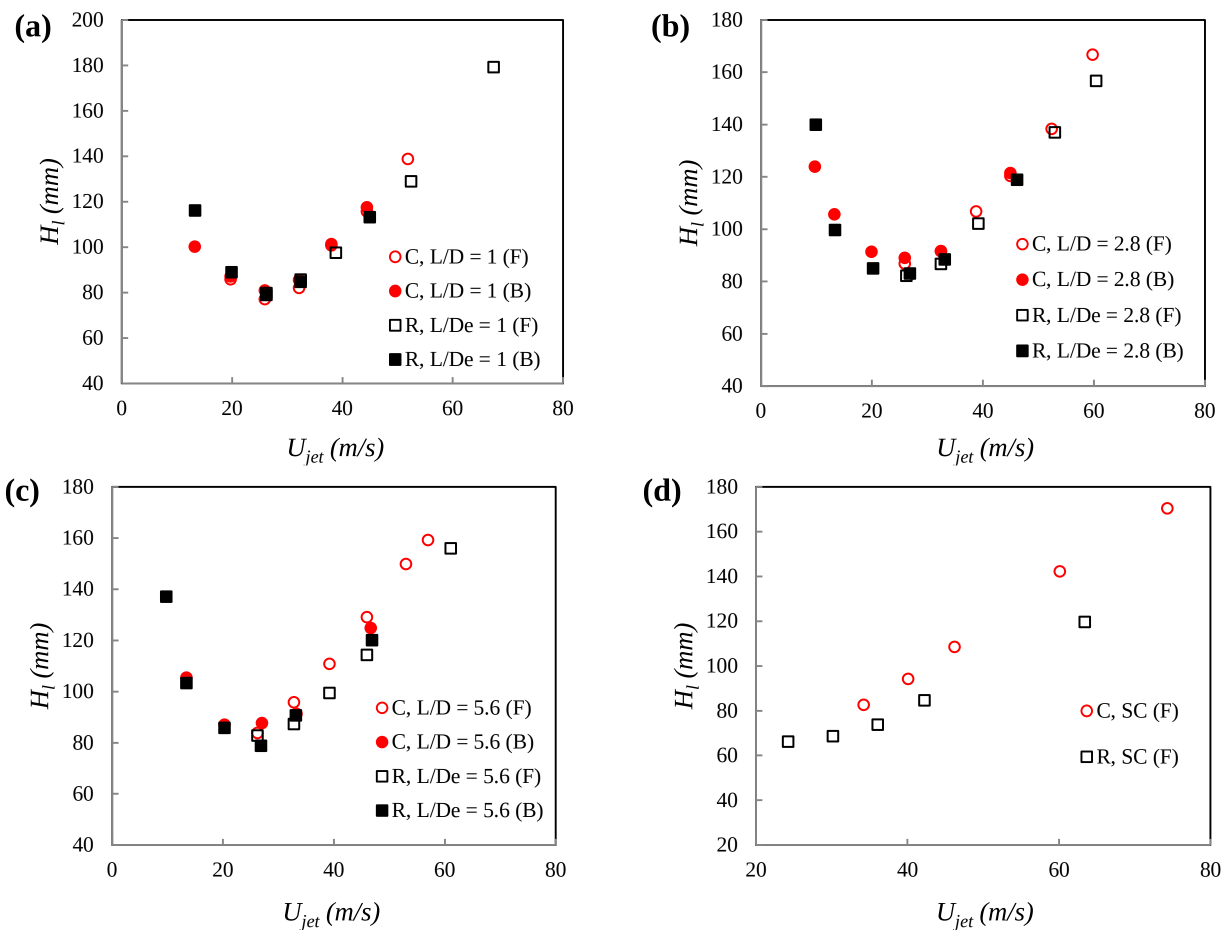

Fig. 5.10 Liftoff height versus jet fuel exit velocity for methane jet flame with $U_{co} \sim 1.25\ m/s$ for different nozzle's orifice exit geomtery having (a) D_e = 4.5 mm and L/D_e = 1, (b) D_e = 4.5 mm and L/D_e = 2.8, (c) D_e = 4.5 mm and L/D_e = 5.6, and (d) D_e = 4.8 mm and L/D_e = 6.2.

Figure 5.10, which is for a relatively higher co-flow, U_{co} ~ 1.25 m/s, reveals similar trends to those seen in Fig. 5.9 (no data reported for the nozzles with $D_e = 3$ mm because no stable lifted flame at U_{co} ~ 1.25 m/s can be established for $D_e <\sim 4$ mm). That is, in general, the rectangular nozzle has lower flame liftoff height. A distinction between the flame liftoff height in Fig. 5.10 (with a noticeable co-flow) and that of a pure-jet (zero co-flow) flame (Fig. 5.8), is that regardless of the geometry (i.e., the exit orifice shape and/or the internal contraction), the flame liftoff height for a co-flowing flame increases drastically with reducing the fuel flow rate to the limit of the flame reattachment/blowout characterized by the non-linear behavior of the flame liftoff height, which is almost unnoticeable in Fig. 5.8 at low U_{jet}. It is also seen from Fig. 5.10(a-d) that there is no consistent correlation between the exit orifice geometry of a nozzle and the flame liftoff height in the non-linear section of the backward profiles. Therefore, overall, it is concluded that the liftoff height at low fuel jet velocity (i.e., at the proximity of liftoff phenomena) is not primarily affected by nozzle exit geometry.

5.3.1. Flow characteristics

To shed more light on the behaviour of the flame liftoff height in relation to the nozzle exit geometries explored here (Figs. 5.8-5.10), the development of the corresponding jet flow characteristics downstream of the nozzle exit were investigated (Figs. 5.11-5.14). These jet characteristics include the axial mean-velocity decay and jet spread rate (in the jet near-field region), the turbulence intensity profiles at certain distances downstream of the nozzle (in the near-field region) as well as on the jet centerline, and lateral profiles of the normalized turbulent shear-stress for typical flow conditions pertaining to lifted flame.

The jet centerline decay and axial turbulence intensity profiles at U_{co}~ 0.2 m/s are presented for the circular and rectangular nozzles with D_e= 3 mm and L/D_e = 1 in Figs. 5.11(a) and (b), respectively. The jet decay rate is higher for the rectangular nozzle (Fig. 5.11(a)) though its decay rate slows down after x/D_e ~ 11. Similarly, Fig. 5.11(b) shows that the axial component of turbulence intensity (u/U_{jet}) along the jet centerline is higher for the rectangular nozzle up to x/D_e ~ 11, and becomes lower farther downstream. The potential core's length is found also to be smaller (see Fig. 5.11(a)) for the rectangular jet (~ $3D$) than that of the circular one (~ $4D$).

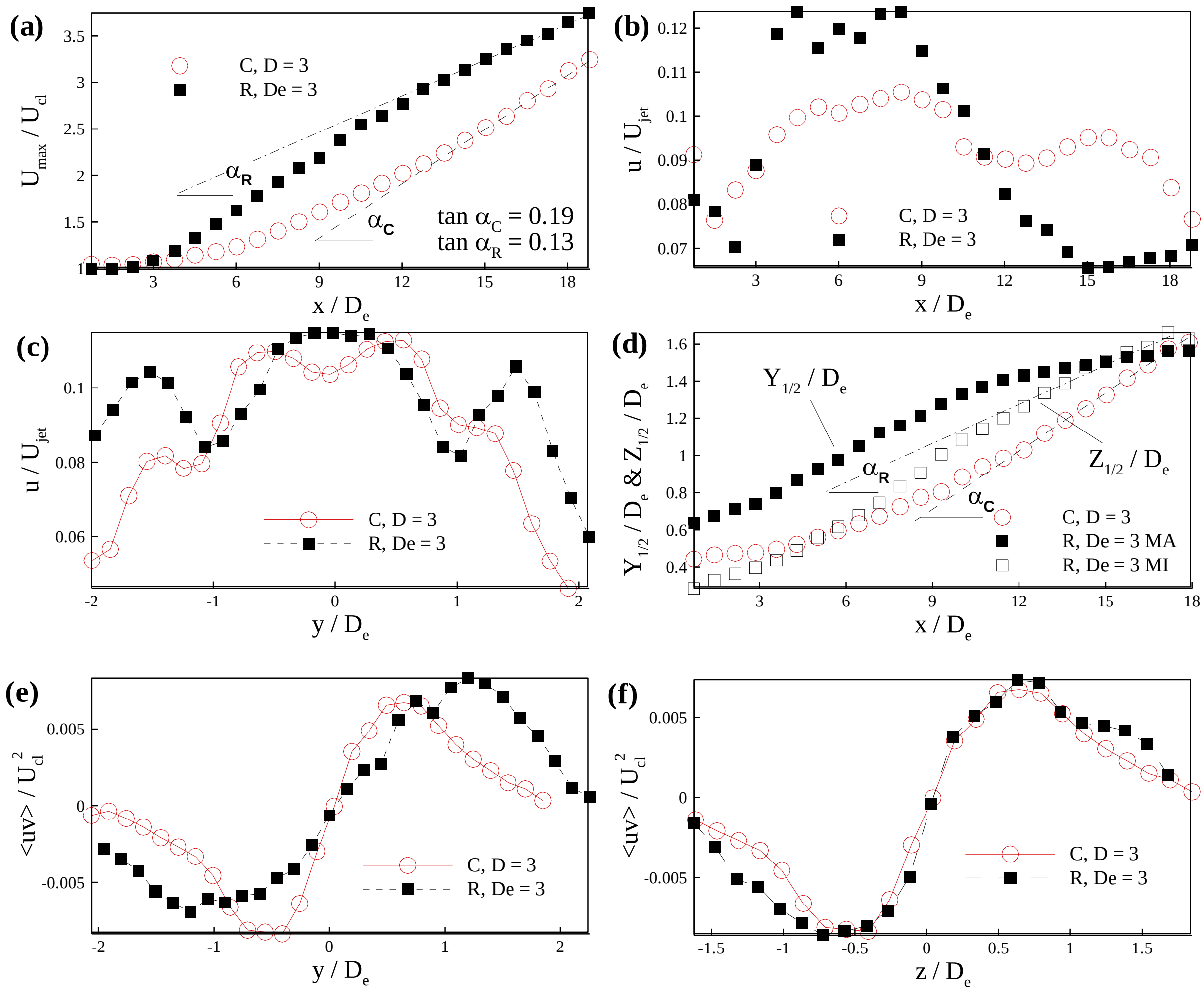

Fig. 5.11 Comparison of the (a) axial mean-velocity decay on the centerline, (b) centerline axial turbulence intensity, (c) lateral distribution of the axial turbulence intensity on the major axis, (d) axial development of axial mean-velocity spread, (e) lateral distribution of the normalized turbulent shear-stress on the major axis, and (f) lateral distribution of the normalized turbulent shear-stress on the minor axis at x/D_e ~ 6 between different nozzle's orifice exit geometry (circular and rectangular) with D_e = 3 mm and L/D_e = 1 (U_{jet}~$30-40$ m/s and U_{co}~0.2 m/s). Hereafter MA: major plane, and MI: minor plane

Figure 5.11(c) shows that although the turbulence intensity, u/U_{jet}, for the circular nozzle in the proximity of centerline in the near-field (x/D_e ~ 6) is smaller than that of the rectangular nozzle along the major axis, it is greater for the circular nozzle in the inner shear-layer (~ 0.5 < $|y/D_e|$ < ~1; i.e., at the interface of the central jet and co-flow). However, the turbulence intensity in the outer shear-layer region (~ 1.25 < $|y/D_e|$; i.e., at the interface of the co-flow stream and the quiescent surrounding) for the rectangular nozzle is overall higher than that of the circular nozzle which shows that the lateral extension of the shear layer on the major axis of the rectangular nozzle at this location downstream of the nozzle exit (i.e., x/D_e ~ 6) is greater than that of the circular nozzle. This can be seen more clearly in Fig. 5.11(d) in which the jet spread is shown. Figure 5.11(d) shows that the jet spread (i.e., the velocity half width) on the major axis for the rectangular nozzle is considerably higher than that along the minor axis of the rectangular nozzle and also that of the circular nozzle up to x/D_e ~ 15. However, the jet spread rate (the slope of spread profiles shown in Fig. 5.11(d)) is the highest along the minor axis of the rectangular nozzle (up to x/D_e~ 11) followed by that of the circular nozzle and the lowest along the major axis of the rectangular nozzle. This indicates that the development of a rectangular jet prevails/predominates along its minor axis (as described in details in Appendix F). In fact, it was demonstrated that the local ambient fluid entrainment rate into a central jet is proportional not only to the mean-velocity lateral spread, but also to its growth (Appendix D). Beyond x/D_e ~ 11 (in Fig. 5.11(d)), however, the circular nozzle's mean-velocity lateral spread rate surpasses the rectangular ones (along both minor and major axes). This is consistent with the development of the turbulence intensity downstream of the nozzles exit (shown in Fig. 5.11(b)) at x/D_e > ~ 11, that is the rectangular nozzle which has faster spread on the minor axis (and faster centerline mean-velocity decay (Fig. 5.11(a)) compared with that of the circular nozzle (Fig. 5.11(d)), has also higher near-field turbulence intensity (Fig. 5.11(b)). Correspondingly, downstream of the nozzles exit, past x/D_e ~ 11, the circular nozzle for which the mean-velocity lateral spread rate (and centerline mean-velocity decay rate (Fig. 5.11(a)) surpasses that of the rectangular nozzle (especially on the minor axis shown in Fig. 5.11(d)), also induces higher turbulence intensity in this region (i.e., x/D_e > ~ 11).

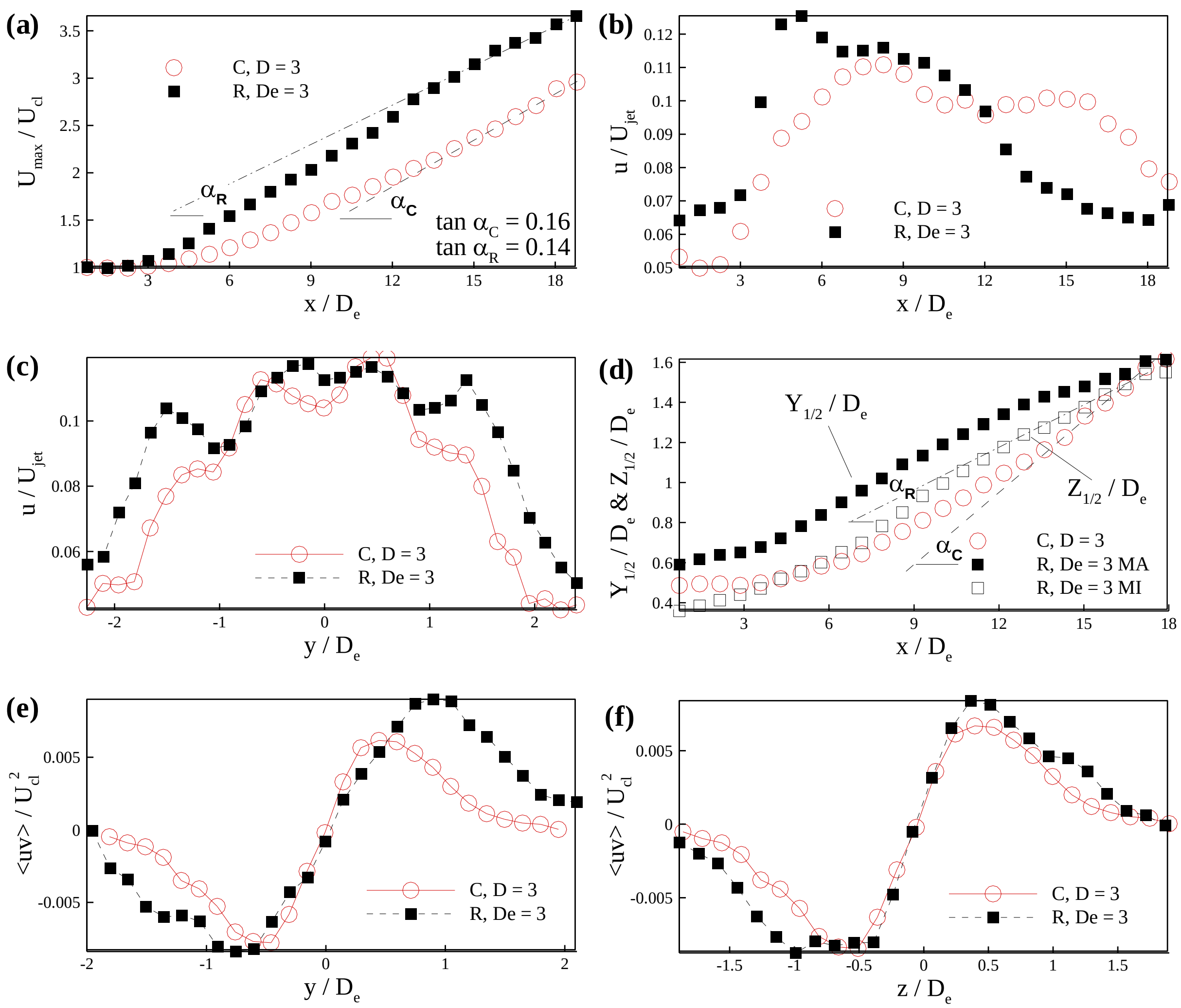

Fig. 5.12 Comparison of the (a) axial mean-velocity decay on the centerline, (b) centerline axial turbulence intensity, (c) lateral distribution of the axial turbulence intensity on the major axis, (d) axial development of axial mean-velocity spread, (e) lateral distribution of the normalized turbulent shear-stress on the major axis, and (f) lateral distribution of the normalized turbulent shear-stress on the minor axis at x/D_e ~ 6 between different nozzle's orifice exit geometry (circular and rectangular) with D_e = 3 mm and L/D_e = 1 (U_{jet}~$30 - 40$ m/s and U_{co}~0.5 m/s).

This finding is consistent with the conclusion of Nathan *et al.* [13] and Akbarzadeh *et al.* [94] who reported that the nozzle which generates higher turbulence intensity and therefore higher flow entrainment close to the nozzle exit in the near-field region (especially those which employ asymmetric geometries or those with self-exciting flow elements without an external force), also entrains less ambient fluid and generates lower turbulence intensity farther downstream in the far-field region. The normalized turbulent shear-stress profiles are shown in Figs. 5.11(e) and (f), along the major and minor axes. The $< uv >/U_{cl}^2$ profiles shown for the major (in Fig. 5.11(e)) and minor (in Fig. 5.11(f)) axes of the rectangular nozzle along with that of the circular nozzle reveal fairly similar magnitude. However, its radial gradient along the major axis in the proximity of the centerline is clearly lower for the rectangular nozzle, but only slightly higher on the minor axis of the rectangular nozzle compared with the circular nozzle. Thus, it is seen that the higher normalized turbulent shear-stress gradient for the rectangular nozzle along the minor axis corroborates well with its higher spread compared with that of the circular nozzle and the rectangular nozzle on the major axis. This suggest that the Reynolds shear stress along the minor axis of the rectangular nozzle represents the mean rate of transfer of the lateral component of the linear momentum (i.e., in z-direction) through a unit area normal to the streamwise direction [19].

The jet characteristics, shown in Fig. 5.12(a-f) for U_{co}~ 0.5 m/s, have in general similar trends to those observed in Fig. 5.11(a-f). However, the difference in the centerline axial turbulence intensity (u/U_{jet}) between the rectangular and circular nozzles is less significant (compared with Fig. 5.11(b) for a lifted flame with a weaker co-flow; i.e., U_{co} ~ 0.2 m/s). Similarly, the jet spread on the major and minor axes of the rectangular nozzle are closer to that of the circular nozzle (with U_{co}~0.5 m/s) in Fig. 5.12(d) in comparison with Fig. 5.11(d) (for

U_{co}~0.2 m/s). Correspondingly, $< uv >/U_{cl}^2$ gradient in the vicinity of the centerline, for a lifted flame with a stronger co-flow (Fig. 5.12(e-f)), is nearly identical for the two nozzles; however, the rectangular nozzle has higher shear stress than its counterpart circular nozzle. Therefore, overall, it can be concluded that increasing the co-flow exit velocity makes the difference between the flow characteristics of the circular and that of the rectangular nozzles to be less noticeable. This can be more clearly seen in Figs. 5.12(b) and (e) in which the difference between the turbulence intensity of the circular and rectangular nozzles on the centerline (Fig. 5.12(b)), and also the difference between the lateral gradients of the turbulent shear stress (Fig. 5.12(e)), become less significant. Also, the difference in turbulence intensity, u/U_{jet} in the inner shear-layer region (i.e., ~ 0.5 < $|y/D_e|$ < ~1, at interface of the jet and co-flow) is less noticeable between the two nozzles at U_{co}~ 0.5 m/s.

The jet flow characteristics for the circular and rectangular nozzles with D_e= 4.5 mm and L/D_e= 1 are presented in Fig. 5.13(a-e) at U_{co} ~ 0.2 m/s. Figure 5.13(a), for example, shows that the axial mean-velocity decay for the rectangular nozzle is only slightly higher than that for the circular nozzle. The potential core's length is also nearly the same between the two jets (~ $3D$). The axial turbulence intensity (u/U_{jet}) along the centerline, which is shown in Fig. 5.13(b), also is higher for the rectangular nozzle. The radial profiles of the axial turbulence intensity shown in Fig. 5.13(c) at x/D_e ~ 6 reveal that although the turbulence intensity for the rectangular nozzle is smaller than that of the circular nozzle in the proximity of the centerline, it is greater for the rectangular nozzle in the shear-layer. Figure 5.13(d) shows that the jet spread rate on the minor axis of the rectangular nozzle is the highest, followed by the spread rate of the circular nozzle which is fairly similar to the spread rate of the rectangular nozzle on the major axis for x/D_e > ~ 4. Figure 5.13(e-f) show that the $< uv >/U_{cl}^2$ amplitude is higher for the circular nozzle compared with that of the rectangular nozzle. However, the gradient of $< uv >/U_{cl}^2$ is fairly the same between the rectangular nozzle on the major axis and that of the circular nozzle, whereas the gradient of the normalized turbulent shear-stress on the minor axis of the rectangular nozzle is clearly higher than that of the circular nozzle as shown in Fig. 5.13(f). The jet flow profiles for higher co-flow (U_{co}> 0.2 m/s) revealed similar findings to those in Fig. 5.13(a-e) (Appendix E).

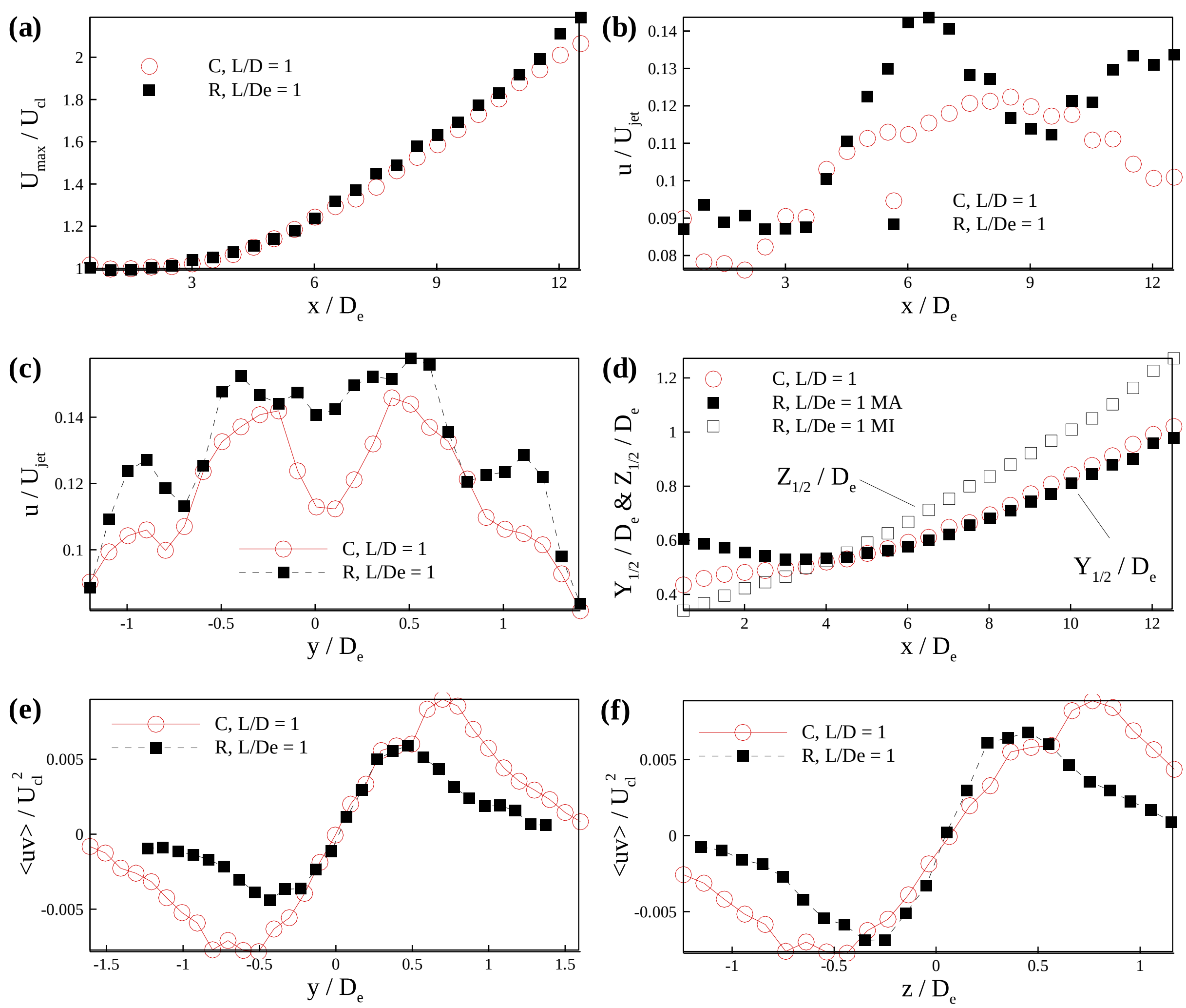

Fig. 5.13 Comparison of the (a) axial mean-velocity decay on the centerline, (b) centerline axial turbulence intensity, (c) lateral distribution of the axial turbulence intensity on the major axis, (d) axial development of axial mean-velocity spread, (e) lateral distribution of the normalized turbulent shear-stress on the major axis, and (f) lateral distribution of the normalized turbulent shear-stress on the minor axis at x/D_e ~ 6 between different nozzle's orifice exit geometry (circular and rectangular) with D_e = 4.5 mm and L/D_e = 1 (U_{jet}~30 m/s and U_{co}~0.2 m/s).

Figure 5.14(a) presents the profiles of the axial mean-velocity decay along the jet centerline for the two nozzles with different exit orifice shapes having a smoothly contracted section (U_{co} ~ 0.2 m/s). It can be seen from this figure that the jet axial mean-velocity decay is clearly higher for the rectangular nozzle; however, the decay rate (the slope) becomes closer to each other between the nozzles beyond x/D_e ~ 6. The potential core's length is found also to be considerably smaller for the rectangular jet (~ $1.5D$) compared with that of the circular one (~ $3D$). The axial turbulence intensity component (u/U_{jet}) on the centerline, shown in Fig. 5.14(b), is also clearly higher for the rectangular nozzle up to x/D_e ~ 6, beyond which it drops and gradually converges to a similar value for both nozzles farther downstream. The higher decay rate of the rectangular nozzle at x/D_e < 6 (Fig. 5.14(a)) corroborates with its clearly greater turbulence intensity in the same region (x/D_e < 6) as shown in Fig. 5.14(b). Figure 5.14(c) which shows the lateral profiles of the axial turbulence intensity at x/D_e ~ 6 reveals that, overall on average, the u/U_{jet} is slightly higher for the rectangular nozzle in the shear-layer. Figure 5.14(d) shows that the initial jet spread is higher along the major axis of the rectangular nozzle followed by that of the circular nozzle and then along the minor axis of the rectangular nozzle. However, the jet spreads faster (compare the slope of the velocity half width) on the minor axis of the rectangular nozzle. Figure 5.14(e) reveals that although the amplitude of $< uv >/U_{cl}^2$ is relatively higher for the rectangular nozzle on the major axis compared with that of the circular nozzle, its gradient in the vicinity of the centerline (at x/D_e ~ 6) is considerably weaker than that of the circular nozzle. Figure 5.14(f) shows that both, the amplitude of $< uv > /U_{cl}^2$ and its gradient, are considerably higher along the minor axis of the rectangular nozzle compared with those of the circular nozzle. This is why the rectangular jet has a faster spread (along the minor axis in Fig. 5.14(d)) compared with the circular nozzle. Increasing the co-flow strength, i.e., U_{co} ~ 0.5 m/s and U_{co} ~ 1.25 m/s, revealed similar trends to the jet flow characteristics with weaker co-flow (Fig. 5.14).

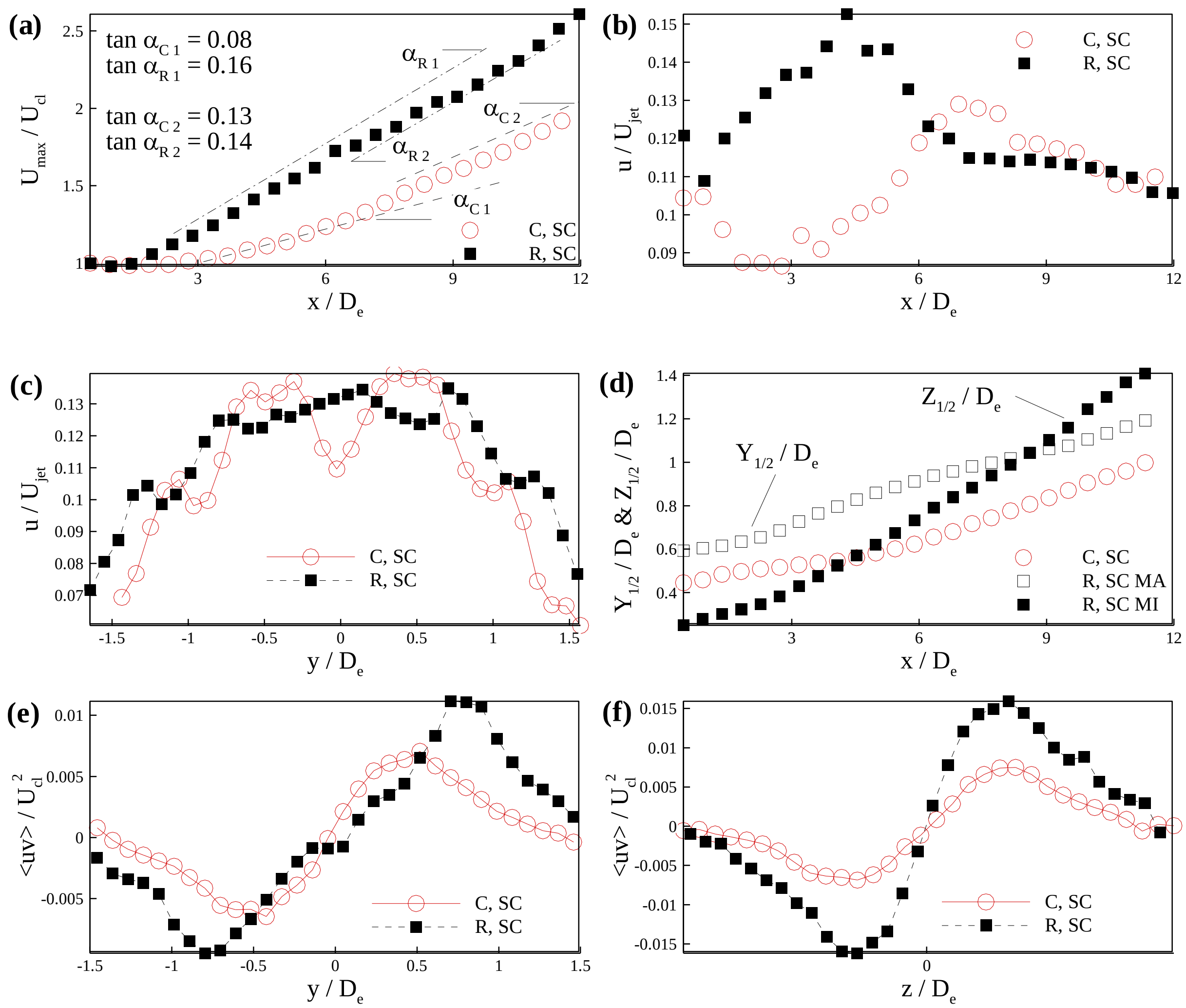

Fig. 5.14 Comparison of the (a) axial mean-velocity decay on the centerline, (b) centerline axial turbulence intensity, (c) lateral distribution of the axial turbulence intensity on the major axis, (d) axial development of axial mean-velocity spread, (e) lateral distribution of the normalized turbulent shear-stress on the major axis, and (f) lateral distribution of the normalized turbulent shear-stress on the minor axis at x/D_e ~ 6 between different nozzle's orifice exit geometry (circular and rectangular) with smooth contraction (U_{jet}~30 m/s and U_{co}~0.2 m/s).

A careful examination of the jet flow characteristics presented in Fig. 5.14 for a weak co-flow and the corresponding flame liftoff height presented in Figs. 5.8(e), 5.9(e) and 5.10(d) reveal that the rectangular nozzle with smooth contraction, which produces lower flame liftoff height than that of the circular nozzle having a similar contraction, has also the highest spread rate on the minor axis, mean-velocity decay and turbulence intensity ahead of the flame base. These results suggest that the rectangular jet which spreads faster and generates higher turbulence intensity upstream of the flame base results in a lower flame liftoff height.

5.3.2. Discussion

Liftoff height figures showed that the flame liftoff height in the range of jet exit velocity close to the liftoff or reattachment varies non-linearly with the jet exit velocity. Therefore, this phenomenon appears not to be associated with the nozzle exit orifice shape but probably with the jet and co-flow characteristics. The available liftoff height stability theories/correlations are obtained for a simple circular turbulent diffusion flame via assuming a developed turbulent unburned mixture ahead of the flame base (e.g., [8–11, 146, 151]). Thus, none of these theories/correlations is able to describe the non-linear behavior of liftoff height.

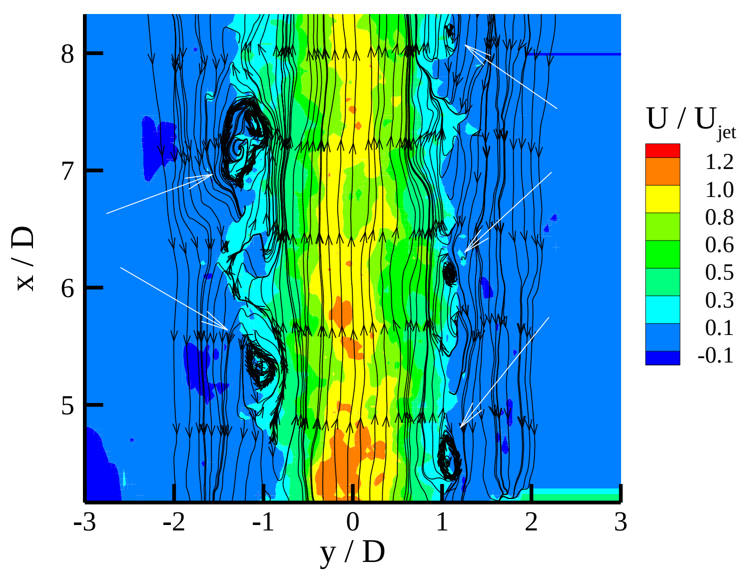

Fig. 5.15 Instantaneous streamlines on the jet central plane of the circular nozzle with smooth contraction (U_{jet}~30 m/s and U_{co}~0.5 m/s).

In the previous chapter, it was shown that geometrical parameters (e.g., diameter, contraction angle, contraction length, nozzle lip thickness, etc) of a circular fuel nozzle can affect differently the flame liftoff height [5, 6, 16, 138]. A review of published experimental studies in this area was reported in Chapters 2 and 4 of the present study, as well. Published literature about the liftoff height of the rectangular nozzle is, however, only limited to the study of Iyogun and Birouk [138].

The present experimental study clearly demonstrated that the flame liftoff height is considerably affected by the exit geometry of a fuel nozzle. Published literature (e.g., [5, 6, 9, 16, 138, 148]) revealed already the presence of a fluctuating turbulence pattern upstream of the flame base which is an indication of the importance of turbulence intensity and the intermittent character of the fine scale structures which can support the concept of premixed combustion. On the other hand, it was also observed that a lifted flame remains sensitive to the initial conditions up to a considerable height above the burner (~ $10D_e$), indicating the importance of cellular-type structure close to the nozzle exit. In fact, the centerline turbulence intensity profiles presented in this study revealed that the jet turbulence intensity exhibits a rapid increase downstream of the nozzle exit up to x/D_e ~ 5 to 10, which is an indication of the production of turbulent kinetic energy close to nozzle exit. This production of turbulence kinetic energy is a sign of the development of large scale structures in the flow [19]. Figure 5.15 shows the instantaneous streamlines (solid lines) projected on the normalized axial mean-velocity (U/U_{jet}) contours for the circular nozzle with smooth contraction. This typical figure is a confirmation of the presence of large-scale structures [32, 152] in the jet near-field (~4 < x/D_e < ~8). Figure 5.15 reveals also a non-symmetric trend in these large-scale structures in spite of the axisymmetry of the nozzle geometry which indicates the complex nature of these turbulent flow structures. These flow structures are responsible for entraining large mass of ambient fluid into the fuel jet and, therefore, have prominent effect on the stability (especially liftoff height) of a lifted flame. Farther downstream of the nozzle, however, the jet attains the self-similar profile of a turbulent jet as suggested by the centerline turbulence intensity profiles. The centerline turbulence intensity profiles show also that farther downstream of the nozzle ($x/D\ >$ ~10) the turbulence intensity drops and adopts the trend of a more developed turbulent flow. Therefore, the lifted flame stability models which assume a fully developed turbulent flow upstream the flame front may not be able to provide very accurate description of a lifted flame in the near-burner region [6].

Overall, the results of the liftoff height of the circular and rectangular nozzle examined in the present study revealed the following. (a) Both the circular and rectangular flames followed the linear relationship of the liftoff height with the fuel jet exit velocity beyond x/D_e ~ 10-20. This may reinforce the premixed theory for the flame base above a certain height from the burner. The intermittency in the oscillations of the location of the flame base (shown in Chapter 4) is independent of the nozzle exit orifice shape and confirms the presence of turbulent mixing in the upstream of the flame leading edge. (b) Close to the nozzle exit (i.e., at x/D_e < ~ 10), the flame liftoff height is fairly similar between the circular and rectangular nozzles. In Chapter 4, it was, however, shown that in this region, downstream of the jet, only the diameter of a nozzle and its lip thickness have an impact on the flame liftoff height. Therefore, this demonstrates that, in this region, the flame is affected more by the diameter and thickness of a nozzle rather than by the asymmetry at the orifice exit (e.g., the presence of corners) and its internal contraction geometry. The non-linear behaviour of the flame liftoff height (close to the nozzle exit) does not support the premixed theory. This agrees with the findings of Coats and Zhao [6] that the role of the organized flow structures on the liftoff height might be prominent close to the nozzle exit and therefore the liftoff height is more dependent on the nozzle diameter and/or nozzle lip thickness (which generates large flow structures in the flow) but fairly independent of the nozzle exit orifice shape (e.g., the corners of a rectangular nozzle which generates small structures).

Further discussion of the relationship between the jet flow characteristics (in Figs. 5.11-5.14) and the corresponding flame liftoff height (Figs. 5.8-5.10) is presented in the following. First, the jet characteristics revealed that the axial mean-velocity decay was higher for the rectangular nozzles showing, in general, a consistent correlation with the flame liftoff height when varying the nozzle exit orifice shape. The results presented in Chapter 4 (also in Appendix E) showed that when varying the nozzle internal contraction geometry but keeping the same exit orifice shape, the axial mean-velocity decay did not show a consistent correlation with the flame liftoff height. Published literature reported also a weak correlation between the flame liftoff height and the corresponding jet centerline decay of a circular nozzle having different internal contractions (e.g., [16, 138]). A discussion of this issue was reported in Chapter 4. Nonetheless, the present results revealed that the effect of the geometry/asymmetry of the fuel nozzle exit orifice is more considerable than the effect of its internal geometry on the jet centerline axial mean-velocity decay.

However, the results presented in Chapter 4 revealed consistently that the jet mean-velocity lateral spread has a good correlation with the flame liftoff height. That is, a circular jet with faster spread rate results in a lower flame liftoff height. In this chapter, however, it was demonstrated that the jet spreading rate on the minor axis of a rectangular nozzle correlates well with the flame liftoff height regardless of the internal contraction geometry of the nozzle. That is, a rectangular jet having faster spreading rate along the minor axis has also a lower flame liftoff height.

It was shown that, for the same nozzle geometry with a rectangular exit orifice having an aspect ratio 2, the spreading of the jet near-field (downstream the nozzle) is higher along the nozzle major plane (up to axis-switching point) (Appendix E). The jet spreading along the minor axis, however, becomes higher past the axis switching flow location which is an indication of a faster growth of the jet spreading on the minor plan. An estimation of the jet local entrainment rate into the central jet in the near-field was shown to be proportional to the jet spread, $R_{1/2}$ (for the circular nozzle, or = $Y_{1/2}$ on the major axis and = $Z_{1/2}$ on the minor axis of the rectangular nozzle), and its local change (gradient) in the streamwise (axial) direction ($d\,R_{1/2}/d\,x$) (Appendix D). It was shown also that this quantity (the jet flow local entrainment rate) along the minor plane of a rectangular nozzle overtakes that along the major plane (Appendix E). Thus, it led to the belief that the stabilization of the flame base (and hence liftoff height) may be governed primarily by the local mixing rate, which, according to our results prevails, in general, in a rectangular nozzle. For instance, Fig. 5.8(a) shows that the liftoff height, in the absence of a co-flow, is slightly smaller for the circular nozzle with D = 3 mm and L/D = 1 than that of the rectangular nozzle with the same equivalent diameter and L/D_e. It can be shown that the circular jet entrainment ahead of the flame base is slightly higher than that on the minor and major plane of the rectangular nozzle having the same equivalent diameter and contraction length (Appendix E). In addition, Fig. 5.9(a) shows that the liftoff height, in the presence of a moderate co-flow, is nearly the same between the circular nozzle with D = 3 mm and L/D = 1 and the rectangular nozzle with the same equivalent diameter and L/D_e. On the other hand, the corresponding jet characteristics at $U_{co}\sim$ 0.5 m/s (Appendix E) showed that the jet entrainment ahead of the flame base is fairly similar between the circular nozzle and the minor axis of the rectangular nozzle. The local entrainment rate calculated for the rest of the rectangular nozzles tested in the present study (can be found in Appendix E) indicates that the entrainment rate from the minor axis of the rectangular nozzles is, in general, greater than that of the circular nozzle which agrees well with the corresponding liftoff height profiles shown in Figs. 5.8 – 5.10, which show that the flame liftoff height of the rectangular orifice is in general less than that of the circular orifice nozzle. To shed more light on the development of the turbulent rectangular jet along the minor plane, the contours of the normalized turbulent kinetic energy $((u^2+v^2)/U_{jet}^2)$ are provided on the centerline plan of the circular nozzle with smooth contraction in Fig. 5.16(a) and the rectangular nozzle with smooth contraction on the major and minor planes, respectively in Figs. 5.16(b) and (c). It can be seen in these figures that the peak of the jet normalized turbulent kinetic energy occurs in the shear-layer between the jet and co-flow just behind the nozzle's lip. Farther downstream, the turbulent kinetic energy shifts outwards as the jet spreads. This trend is fairly similar for both, the circular nozzle (Fig. 5.16(a)) and rectangular nozzle on the major axis (Fig. 5.16(b)) with the exception that the length of the potential core (inferred from the axial location at which the shear-layer growing from the nozzle lip merge together) is noticeably lower for the rectangular nozzle. This might justify why the flame of the rectangular nozzle with smooth contraction lifts off from the burner at a considerably lower fuel jet velocity and sits closer to the burner compared with that of the circular nozzle with smooth contraction (Fig. 5.2(e)). In contrast with the trend of development of turbulence on the plane of symmetry of the circular nozzle and the major symmetric plane of the rectangular nozzle (Fig. 5.16(a-b)), the normalized turbulent kinetic energy undergoes another local maxima of $(u^2+v^2)/U_{jet}^2$ on the minor symmetric plane of the rectangular nozzle with smooth contraction (shown by white arrows in

Fig. 5.16(c)). This indicates a higher ambient fluid entrainment into the central jet via the minor plane of the rectangular nozzle compared with its major plane (further results on the development of the circular/rectangular jet can be found in Appendix F).

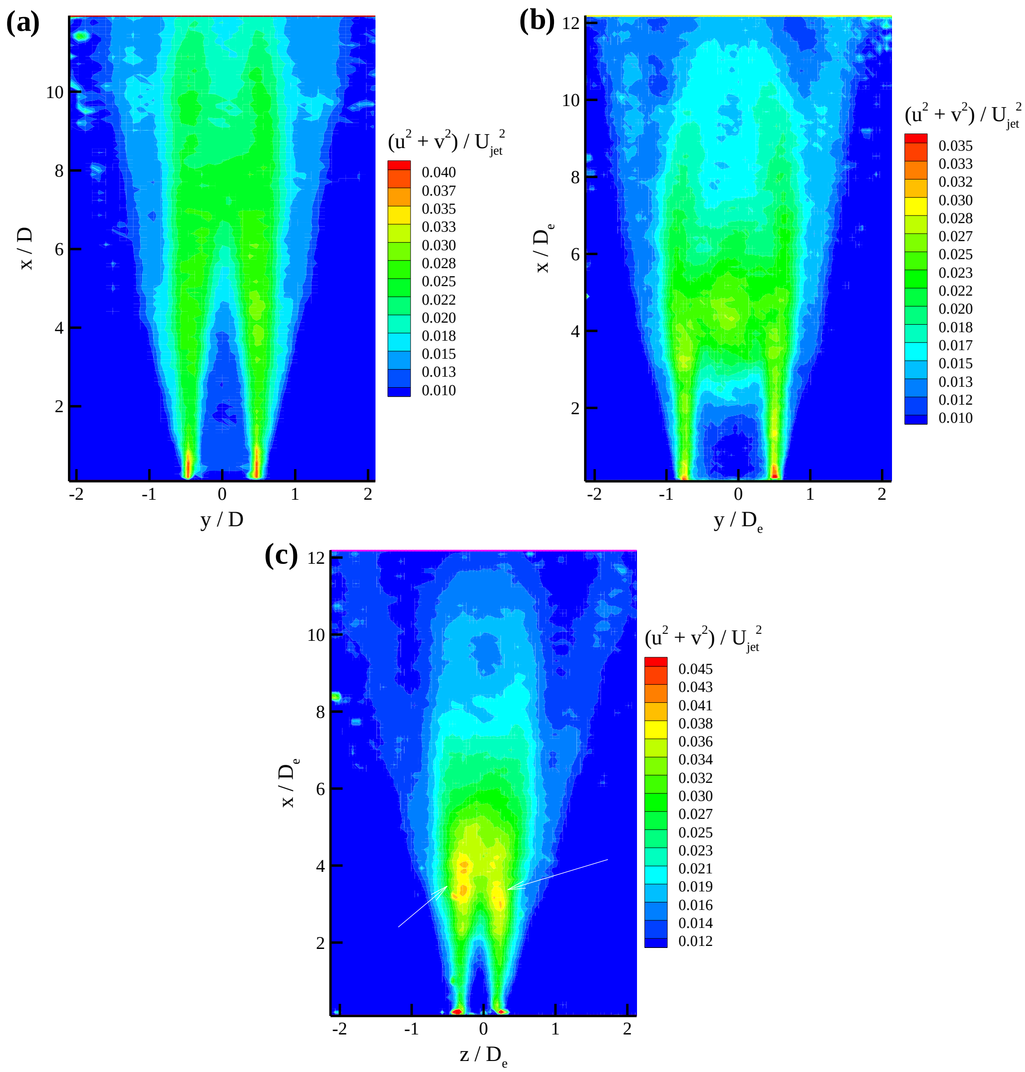

Fig. 5.16 Contours of the normalized mean turbulent kinetic energy ($(u^2+v^2)/U_{jet}^2$) on (a) the symmetric plane of the circular nozzle with smooth contraction, and (b) the major and (c) the minor plane of the rectangular nozzle with smooth contraction (U_{jet}~30 m/s and U_{co}~0.5 m/s).

Furthermore, the flow characteristics presented above showed that the turbulence intensity level in the near-field region (i.e., believed to be in the proximity of the flame leading edge) is higher for the nozzles which have lower liftoff height (in general, the rectangular nozzles). The premixed theory of Kalghatgi [9] assumes that the liftoff is controlled by the turbulent burning velocity, and that the flame base propagation speed is proportional to the square root of the turbulence intensity. This implies that when the local turbulence intensity ahead of the flame base increases, the propagation speed of the flame base also increases. Since this speed balances the upcoming mixture velocity at the flame leading edge/front, it is believed that an increase in turbulence intensity results in an increase in the turbulent propagation speed of the flame which in turn stabilizes the flame base at a lower height. This agrees with the conclusion of Dahm *et al.* [153] who reported that local molecular mixing rate has dominant control on the flame liftoff height.

CHAPTER 6
CONCLUSIONS AND RECOMMENDATIONS FOR FUTURE WORK

6.1. Effect of nozzle internal geometry on the liftoff

The internal geometry of a circular nozzle was found to affect the flame stability limits. The flame liftoff velocity was found to increase with the nozzle's L/D. In addition, the flame liftoff velocity for the smooth contracted circular nozzle was found to be significantly higher than that of the same nozzle but having a sudden contraction. However, the effect of the nozzle diameter on the flame liftoff velocity was found to depend on the co-flow strength. The results consistently showed that the higher turbulence intensity (i.e., the velocity fluctuations in the jet near-field) is an indication of the presence of relatively more turbulent flow structures which are believed to accelerate the onset of the liftoff of an attached flame. The results revealed that the flame liftoff height does not change noticeably with either the nozzle diameter or L/D. However, the nozzle with a smooth contraction has lower liftoff height than that of its counterpart 90-degree contracted nozzle. The jet flow characteristics revealed that there is a consistent interplay between the flame liftoff height and the corresponding jet spread rate and turbulence level. That is, a lower flame liftoff height is a result of an increased jet spread rate and turbulence level. This led to believe that higher jet spread rate and turbulence result in increased flame propagation speed which makes it possible for a flame to stabilize at a relatively lower height from the nozzle.

The experimental results of a rectangular nozzle (with aspect ratio of 2) having internal geometry similar to that of the circular nozzle mentioned above confirmed the above conclusions. That is, it was found that the flame liftoff velocity increases with the nozzle L/D_e but decrease with D_e. Also, the liftoff velocity of the smooth contracted rectangular nozzle was found to be higher than that with a sudden contraction. The results confirmed the conclusion that the higher turbulence intensity (i.e., the velocity fluctuations in the jet near-field), which is an indication of the presence of relatively more turbulent flow structures, accelerates the onset of the liftoff of an attached flame. The jet flow characteristics revealed also that there exists a consistent interplay between the flame liftoff height and the jet spreading rate along the minor axis of the rectangular nozzle. That is, a lower jet flame liftoff height results from an increased jet spreading rate along the minor plane of the rectangular nozzle and jet turbulence level.

6.2. Effect of nozzle exit orifice shape on the liftoff

The shape of the exit orifice of a fuel nozzle was also found to affect the flame stability limits. This was assessed by comparing the flame stability and the corresponding turbulent flow characteristics between a circular and a rectangular nozzle with the same internal geometry. For instance, the flame liftoff velocity was found to be, in general, smaller for a rectangular nozzle. The extent of the role of the orifice exit shape on the flame stability was, however, found to be affected by the internal geometry. For example, the nozzle with the shortest L/D_e has a marginal effect on the flame liftoff height, which is also dependent on the co-flow strength for the nozzle with the smaller diameter. However, the results revealed that the rectangular nozzle which, in general, has lower liftoff velocity, also produces higher turbulence intensity in the jet near-field as an indication of the presence of relatively more turbulent flow structures induced by this nozzle's geometry. These structures are believed to accelerate the onset of the liftoff of an attached flame.

The results showed that the rectangular nozzle, in general, results in a liftoff height lower than that of its circular counterpart. Similarly, the effect of the exit orifice asymmetry of a nozzle on the flame liftoff height was found to be less predominant than that of its internal geometry when L/D_e is short. Also, the effect of the exit orifice asymmetry on the flame liftoff height was found to depend on the co-flow velocity for smaller nozzle diameter. The jet flow characteristics revealed the existence of a strong relationship between the flame liftoff height and the corresponding jet spread rate. That is, in general, the rectangular nozzle has a faster jet spread (on the minor axis) and higher turbulence intensity upstream of the flame base.

Overall, it can be concluded that replacing a circular by a rectangular nozzle can improve the stability limits of turbulent non-premixed methane flame by accelerating the liftoff of an attached flame (i.e., better flame characteristics) and decreasing the liftoff height (enlarging the flame stability range). However, the extent of such an improvement is found to depend upon the nozzle internal geometry.

6.3. Recommendations for future work

The present study brought additional understanding on the effect of fuel nozzle geometry on the stability of a turbulent diffusion methane flame. The results demonstrated clearly that the flow near-field characteristics have a clear effect on the flame stability parameters. However, additional work is needed to develop quantitative relationships between the flame stability limits and the flow characteristics of a turbulent coflowing jet. To do so, the following suggestions are proposed:

- A wider range of nozzle diameter, contraction angle and orifice to length ratio will need to be tested in order to develop a quantitative relationship/correlation between the flame stability and jet flow characteristics.
- It would be interesting to test rectangular nozzles with an aspect ratio (AR) greater than 2. It is believed that its flow characteristics and consequently flame stability will be affected.

- The lip thickness which might play a role similar to that of the bluff body for a flame is also expected to affect the flame stability. However, since all nozzles employed in the present study have an identical external geometry, the lip thickness varied with the nozzle diameter. Therefore, it is recommended to design and test a set of nozzles with different lip thickness but having the same diameter. Similarly, it is recommended to investigate changing the nozzle diameter and keeping the lip thickness fixed.

- The arrangement of the fuel nozzle and co-airflow (e.g., the ratio of the coflow area to the nozzle area) might have an impact on the stability of turbulent diffusion flame. In the present study, however, the area of the coflow was fixed. Therefore, further examination of this parameter may reveal if there is dependency of the flame liftoff.

BIBLIOGRAPHY

1. Lyons, K.M.: Toward an understanding of the stabilization mechanisms of lifted turbulent jet flames: Experiments. Prog. Energy Combust. Sci. 33, 211–231 (2007).

2. Peters, N.: Turbulent combustion. Cambridge university press (2000).

3. Pitts, W.: Assessment of theories for the behavior and blowout of lifted turbulent jet diffusion flames. Symp. Combust. (1989).

4. Scholefield, D.A., Garside, J.E.: The structure and stability of diffusion flames. Symp. Combust. 3, 102–110 (1949).

5. Eickhoff, H., Lenze, B., Leuckel, W.: Experimental investigation on the stabilization mechanism of jet diffusion flames. Symp. Combust. 20, 311–318 (1985).

6. Coats, C.M., Zhao, H.: Transition and stability of turbulent jet diffusion flames. Symp. Combust. 22, 685–692 (1989).

7. Gollahalli, S.R., Savaş, Ö., Huang, R.F., Rodriquez Azara, J.L.: Structure of attached and lifted gas jet flames in hysteresis region. Symp. Combust. 21, 1463–1471 (1988).

8. Vanquickenborne, L., Tiggelen, A. Van: The stabilization mechanism of lifted diffusion flames. Combust. Flame. 10, 59–69 (1966).

9. Kalghatgi, G.T.: Lift-off heights and visible lengths of vertical turbulent jet diffusion flames in still sir. Combust. Sci. Technol. 41, 17–29 (1984).

10. Peters, N., Williams, F.F.A.: Liftoff characteristics of turbulent jet diffusion flames. AIAA J. 21, 423–429 (1983).

11. Broadwell, J.E.J.J.E., Dahm, W.W.J.A., Mungal, M.G.: Blowout of turbulent diffusion flames. Symp. Combust. 20, 303–310 (1985).

12. Broadwell, J., Breidenthal, R.: A simple model of mixing and chemical reaction in a turbulent shear layer. J. Fluid Mech. (1982).

13. Nathan, G.J., Mi, J., Alwahabi, Z.T., Newbold, G.J.R., Nobes, D.S.: Impacts of a jet's exit flow pattern on mixing and combustion performance. Prog. Energy Combust. Sci. 32, 496–538 (2006).

14. Moore, J.D., Kuo, K.K.: Effect of Switching Methane/Oxygen Reactants in a Coaxial Injector on the Stability of Non-Premixed Flames. Combust. Sci. Technol. 180, 401–417 (2008).

15. Iyogun, C.O., Birouk, M.: Stability of a turbulent jet methane flame issuing from an asymmetrical nozzles with sudden expansion. Combust. Sci. Technol. 181, 1–17 (2008).

16. Langman, A.S., Nathan, G.J., Mi, J., Ashman, P.J.: The influence of geometric nozzle profile on the global properties of a turbulent diffusion flame. Proc. Combust. Inst. 31, 1599–1607 (2007).

17. Gutmark, E.J., Grinstein, F.F.: Flow control with noncircular jets 1. Annu. Rev. Fluid Mech. 31, 239–272 (1999).

18. Pollard, A., Marsters, G., Quinn, W.: Measurements in a turbulent rectangular free jet. Symp. Turbul. Shear Flows, 4 th, Karlsruhe, West Ger. (1984).

19. Quinn, W.R.: Experimental study of the near field and transition region of a free jet issuing from a sharp-edged elliptic orifice plate. Eur. J. Mech. - B/Fluids. 26, 583–614 (2007).

20. Pitts, W.: Importance of isothermal mixing processes to the understanding of lift-off and blowout of turbulent jet diffusion flames. Combust. Flame. (1989).

21. Su, L.K., Sun, O.S., Mungal, M.G.: Experimental investigation of stabilization mechanisms in turbulent, lifted jet diffusion flames. Combust. Flame. 144, 494–512 (2006).

22. Hinze, J.: Turbulence: An introduction to its mechanisms and theory. Mcfirau Hill, New York. (1959).

23. Corrsin, S., Kistler, A.L., Corrsin, B.S., Tab, D.: Free-stream boundaries of turbulent flows. Natl. Advis. Comm. Aeronaut. (1955).

24. Wygnanski, I., Fiedler, H.: Some measurements in the self-preserving jet. J. Fluid Mech. 38, 577 (1969).

25. Hussein, H.: Velocity measurements in a high-Reynolds-number, momentum-conserving, axisymmetric, turbulent jet. J. Fluid Mech. 258, 31–75 (1994).

26. Quinn, W.R., Pollard, A., Marsters, G.F.: O “saddle-backed” velocity distributions in a three-dimensional turbulent free jet. 16th Fluid and Plasma Dynamics Conference. AIAA, Danvers, MA, USA (1983).

27. Grandmaison, E., Pollard, A., Ng, S.: Scalar mixing in a free, turbulent rectangular jet. Int. J. Heat Mass Transf. 34, 2653–2662 (1991).

28. McCraw, J.L., Moore, N.J., Lyons, K.M.: Observations on Upstream Flame Propagation in the Ignition of Hydrocarbon Jets. Flow, Turbul. Combust. 79, 83–97 (2007).

29. Lyons, K.M., Watson, K. a., Carter, C.D., Donbar, J.M.: Upstream Islands of Flame in Lifted-Jet Partially Premixed Combustion. Combust. Sci. Technol. 179, 1029–1037 (2007).

30. Leung, T., Wierzba, I.: The effect of co-flow stream velocity on turbulent non-premixed jet flame stability. Proc. Combust. Inst. 32, 1671–1678 (2009).

31. Lawn, C.J.: Lifted flames on fuel jets in co-flowing air. Prog. Energy Combust. Sci. 35, 1–30 (2009).

32. Mi, J., Kalt, P., Nathan, G.J., Wong, C.Y.: PIV measurements of a turbulent jet issuing from round sharp-edged plate. Exp. Fluids. 42, 625–637 (2007).

33. Hussain, A.: Coherent structures and turbulence. J. Fluid Mech. 173, 303–356 (1986).

34. Grinstein, F.F.: Vortex dynamics and entrainment in rectangular free jets. J. Fluid Mech. 437, 69–101 (2001).

35. Boersma, B.J., Brethouwer, G., Nieuwstadt, F.T.M.: A numerical investigation on the effect of the inflow conditions on the self-similar region of a round jet. Phys. Fluids. 10, 899 (1998).

36. Baker, C.B.: An analysis of the turbulent buoyant jet: a thesis in aerospace engineering, (1980).

37. Seif, A.: Higher order closure model for turbulent jets. Diss. Abstr. Int. Part B Sci. Eng. 42, 1982 (1982).

38. Lehmann, B.: Laser-doppler measurements in a turbulent free jet. (1986).

39. Bruun, H.H.: Hot-wire anemometry: principles and signal analysis. Meas. Sci. Technol. 7, (1996).

40. Panchapakesan, N., Lumley, J.: Turbulence measurements in axisymmetric jets of air and helium. Part 1. Air jet. J. Fluid Mech. 246, 197–223 (1993).

41. George, W.: The self-preservation of turbulent flows and its relation to initial conditions and coherent structures. Adv. Turbul. (1989).

42. Mi, J., Nathan, G.J., Nobes, D.S.: Mixing characteristics of axisymmetric free jets from a contoured nozzle, an orifice plate and a pipe. Trans. ASME. J. Fluids Eng. 123, 878–883 (2001).

43. Xu, G., Antonia, R.: Effect of different initial conditions on a turbulent round free jet. Exp. Fluids. 33, 677–683 (2002).

44. Iyogun, C.O., Birouk, M.: Effect of fuel nozzle geometry on the stability of a turbulent jet methane flame. Combust. Sci. Technol. 181, 2186–2209 (2008).

45. Antonia, R. a., Zhao, Q.: Effect of initial conditions on a circular jet. Exp. Fluids. 31, 319–323 (2001).

46. Xu, G., Antonia, R.: Effect of initial conditions on the temperature field of a turbulent round free jet. Int. Commun. heat mass Transf. 29, 1057–1068 (2002).

47. Mi, J., Nobes, D., Nathan, G.: Influence of jet exit conditions on the passive scalar field of an axisymmetric free jet. J. Fluid Mech. 432, 91–125 (2001).

48. Ashforth-Frost, S., Jambunathan, K.: Effect of nozzle geometry and semi-confinement on the potential core of a turbulent axisymmetric free jet. Int. Commun. Heat Mass Transf. 23, 155–162 (1996).

49. Sadr, R., Klewicki, J.C.: An experimental investigation of the near-field flow development in coaxial jets. Phys. Fluids. 15, 1233 (2003).

50. Warda, H. a., Kassab, S.Z., Elshorbagy, K. a., Elsaadawy, E. a.: An experimental investigation of the near-field region of a free turbulent coaxial jet using LDA. Flow Meas. Instrum. 10, 15–26 (1999).

51. Williams, T., Ali, M., Anderson, J.: Noise and flow characteristics of coaxial jets. J. Mech. Eng. 11, 133–142 (1969).

52. Feikema, D., Chen, R.R.-H., Driscoll, J.F.J.: Blowout of nonpremixed flames: maximum coaxial air velocities achievable, with and without swirl. Combust. Flame. 86, 347–358 (1991).

53. Nickels, T., Perry, A.: An experimental and theoretical study of the turbulent coflowing jet. J. Fluid Mech. 309, 157–182 (1996).

54. Briones, A.M., Aggarwal, S.K., Katta, V.R.: A numerical investigation of flame liftoff, stabilization, and blowout. Phys. Fluids. 18, 043603 (2006).

55. Terry, S.D., Lyons, K.M.: Low Reynolds Number Turbulent Lifted Flames in High Co-Flow. Combust. Sci. Technol. 177, 2091–2112 (2005).

56. Forstall W., J., Shapiro, A.H.: Momentum and mass transfer in coaxial gas jets. Am. Soc. Mech. Eng. -- Trans. -- J. Appl. Mech. 18, 219–220 (1951).

57. Champagne, F., Wygnanski, I.: An experimental investigation of coaxial turbulent jets. Int. J. Heat Mass Transf. 14, 1445–1464 (1971).

58. Ko, N., Kwan, A.: The initial region of subsonic coaxial jets. J. Fluid Mech. 73, 305–332 (1976).

59. Kwan, A., Ko, N.: The initial region of subsonic coaxial jets. Part 2. J. Fluid Mech. 82, 273–287 (1977).

60. Dahm, W., Frieler, C., Tryggvason, G.: Vortex structure and dynamics in the near field of a coaxial jet. J. Fluid Mech. 241, 371–402 (1992).

61. Buresti, G., Petagna, P., Talamelli, A.: Experimental investigation on the turbulent near-field of coaxial jets. Exp. Therm. fluid Sci. 17, 18–26 (1998).

62. Warda, H. a., Kassab, S.Z., Elshorbagy, K. a., Elsaadawy, E. a.: An experimental investigation of the near-field region of free turbulent round central and annular jets. Flow Meas. Instrum. 10, 1–14 (1999).

63. Warda, H. a., Kassab, S.Z., Elshorbagy, K. a., Elsaadawy, E. a.: Influence of the magnitude of the two initial velocities on the flow field of a coaxial turbulent jet. Flow Meas. Instrum. 12, 29–35 (2001).

64. Buresti, G., Talamelli, A., Petagna, P.: Experimental characterization of the velocity field of a coaxial jet configuration. Exp. Therm. fluid Sci. 9, 135–146 (1994).

65. Gutmark, E., Schadow, K.C., Parr, T.P.: Noncircular jets in combustion systems. Exp. …. 7, 248–258 (1989).

66. Schadow, K.C., Gutmark, E., Parr, D.M., Wilson, K.J.: Selective control of flow coherence in triangular jets. Exp. Fluids. 6, 129–135 (1988).

67. Quinn, W.R.: Turbulent free jet flows issuing from sharp-edged rectangular slots: the influence of slot aspect ratio. Exp. Therm. fluid Sci. 5, 203–215 (1992).

68. Quinn, W.R.: Measurements in the near flow field of an isosceles triangular turbulent free jet. Exp. Fluids. 39, 111–126 (2005).

69. Iyogun, C.O., Birouk, M.: Effect of Sudden Expansion on Entrainment and Spreading Rates of a Jet Issuing from Asymmetric Nozzles. Flow, Turbul. Combust. 82, 287–315 (2009).

70. Quinn, W., Militzer, J.: Experimental and numerical study of a turbulent free square jet. Phys. fluids. (1988).

71. Mi, J., Nathan, G., Luxton, R.: Mixing characteristics of a flapping jet from a self-exciting nozzle. Flow, Turbul. Combust. 1–23 (2001).

72. Nastase, I., Meslem, A., Gervais, P.: Primary and secondary vortical structures contribution in the entrainment of low Reynolds number jet flows. Exp. Fluids. 44, 1027–1033 (2008).

73. Zaman, K.: Axis switching and spreading of an asymmetric jet: the role of coherent structure dynamics. J. Fluid Mech. 316, 1–27 (1996).

74. Reeder, M.F., Zaman, K.B.M.Q.: Impact of tab location relative to the nozzle exit on jet distortion. AIAA J. 34, 197–199 (1996).

75. Hu, H., Saga, T., Kobayashi, T., Taniguchi, N.: Research on the vortical and turbulent structures in the lobed jet flow using laser induced fluorescence and particle image velocimetry techniques. Meas. Sci. Technol. 11, 698–711 (2000).

76. Ho, C.M., Gutmark, E.: Vortex induction and mass entrainment in a small-aspect-ratio elliptic jet. J. Fluid Mech. 179, 383–405 (1987).

77. Gutmark, E., Schadow, K.C., Parr, T.P., Hanson-Parr, D.M., Wilson, K.J.: Noncircular jets in combustion systems. Exp. Fluids. 7, 248–258 (1989).

78. Gutmark, E., Schadow, K., Wilson, K.: Noncircular jet dynamics in supersonic combustion. J. Propuls. Power. 5, 529–533 (1989).

79. Gutmark, E., Schadow, K.C., Wilson, K.J.: Subsonic and supersonic combustion using noncircular injectors. J. Propuls. Power. 7, 240–249 (1991).

80. Sau, A.: Vortex dynamics and mass entrainment in a rectangular channel with a suddenly expanded and contracted part. Phys. Fluids. 14, 3280 (2002).

81. Sau, A.: Generation of streamwise vortices in square sudden-expansion flows. Phys. Rev. E. 69, 1–10 (2004).

82. Miller, R., Madnia, C., Givi, P.: Numerical simulation of non-circular jets. Comput. Fluids. 24, (1995).

83. Wilson, R., Demuren, A.: Numerical Simulation of Turbulent Jets with Rectangular Cross-Section. ICASE Rep. No. 97-1, NASA CR-201642. (1997).

84. Hold, A.E.H., Simpson, B.A.F.: Simulations of high-aspect-ratio jets. 359, 343–359 (2002).

85. Rembold, B., Adams, N. a., Kleiser, L.: Direct numerical simulation of a transitional rectangular jet. Int. J. Heat Fluid Flow. 23, 547–553 (2002).

86. Grinstein, F., Young, T., Gutmark, E.: Flow dynamics in a swirl combustor. J. Turbul. 3, (2002).

87. Gutmark, E., Parr, T., Grinstein, F.: Near field dynamics of subsonic free square jets. A computational and experimental study. Phys. Fluids. 7, 1483–1497 (1995).

88. Iyogun, C.O., Birouk, M., Kozinski, J. a.: Experimental investigation of the effect of fuel nozzle geometry on the stability of a swirling non-premixed methane flame. Fuel. 90, 1416–1423 (2011).

89. Grandmaison, E., Zettler, N.: Turbulent mixing in coflowing plane jets. Can. J. Chem. Eng. 67, 889–897 (1989).

90. Zaman, K.B.M.Q.: Spreading characteristics of compressible jets from nozzles of various geometries. J. Fluid Mech. 383, 197–228 (1999).

91. Zaman, K., Steffen, C., Reddy, D.: Entrainment and spreading characteristics of jets from asymmetric nozzles. 28th AIAA Fluid Dyn. Conf. 4th AIAA. (1997).

92. Quinn, W.R.: Passive near-field mixing enhancement in rectangular jet flows. AIAA J. 29, 515–519 (1991).

93. Faghani, E., Saemi, S.D., Maddahian, R., Farhanieh, B.: On the effect of inflow conditions in simulation of a turbulent round jet. Arch. Appl. Mech. 81, 1439–1453 (2010).

94. Akbarzadeh, M., Birouk, M., Sarh, B.: Numerical simulation of a turbulent free jet issuing from a rectangular nozzle. Comput. Therm. Sci. 4, 1–22 (2012).

95. Mi, J., Nathan, G.J., Luxton, R.E.: Centreline mixing characteristics of jets from nine differently shaped nozzles. Exp. Fluids. 28, 93–94 (2000).

96. Riopelle, G., Stubley, G., Strong, A.: Numerical study of the influence of the ambient pressure field on free plane turbulent vertical jets and plumes. Numer. Heat Transf. Part A. 26, 272–286 (1994).

97. Abramovich, G.: On the deformation of the rectangular turbulent jet cross-section. Int. J. Heat Mass Transf. 25, 1885–1894 (1982).

98. Quinn, W.: Streamwise evolution of a square jet cross section. AIAA J. (1992).

99. Quinn, W.R.: Turbulent mixing in a free jet issuing from a low aspect ratio contoured rectangular nozzle. Aeronaut. J. 99, 337–342 (1995).

100. Lozanova, M., Stankov, P.: Experimental investigation on the similarity of a 3D rectangular turbulent jet. Exp. Fluids. 24, (1998).

101. Mi, J., Deo, R.C., Nathan, G.J.: Characterization of turbulent jets from high-aspect-ratio rectangular nozzles. Phys. Fluids. 17, 068102 (2005).

102. Deo, R.C., Mi, J., Nathan, G.J.: The influence of nozzle aspect ratio on plane jets. Exp. Therm. Fluid Sci. 31, 825–838 (2007).

103. McGuirk, J.J., Rodi, W.: The calculation of three-dimensional turbulent free jets. Turbulent Shear Flows I. pp. 71–83. Springer-Verlag, Univ. of Karlsruhe, Karlsruhe, West Germany BT (1979).

104. Zhu, J., Shih, T.: Computation of confined coflow jets with three turbulence models. Int. J. Numer. methods fluids. 19, 939–956 (1994).

105. Berg, J.R., Ormiston, S.J., Soliman, H.M.: Prediction of the flow structure in a turbulent rectangular free jet. Int. Commun. Heat Mass Transf. 33, 552–563 (2006).

106. McCormick, D.C., Bennett Jr., J.C.: Vortical and turbulent structure of a lobed mixer free shear layer. AIAA J. 32, 1852–1859 (1993).

107. Belovich, V.M., Samimy, M., Reeder, M.F.: Dual stream axisymmetric mixing in the presence of axial vorticity. J. Propuls. power. 12, 178–185 (1996).

108. Ahuja, K.K., Brown, W.H.: Shear flow control by mechanical tabs. AIAA, 2nd Shear Flow Conference (1989).

109. Zaman, K.B.M.Q., Reeder, M.F., Samimy, M.: Control of an axisymmetric jet using vortex generators. Phys. Fluids. 6, 778 (1994).

110. Reeder, M.F., Samimy, M.: The evolution of a jet with vortex-generating tabs: real-time visualization and quantitative measurements. J. Fluid Mech. 311, 73–118 (1996).

111. Foss, J.K., Zaman, K.B.M.Q.: Large- and small-scale vortical motions in a shear layer perturbed by tabs. J. Fluid Mech. 382, 307–329 (1999).

112. Kalghatgi, G.G.T.: Blow-out stability of gaseous jet diffusion flames Part II: Effect of cross wind. Combust. Sci. Technol. 26, 241–244 (1981).

113. Dahm, W.J.A., Dibble, R.W.: Coflowing turbulent jet diffusion flame blowout. Symp. Combust. 22, 801–808 (1989).

114. Muñiz, L., Mungal, M.G.: Instantaneous flame-stabilization velocities in lifted-jet diffusion flames. Combust. Flame. 111, 16–31 (1997).

115. Terry, S.D., Lyons, K.M.: Turbulent lifted flames in the hysteresis regime and the effects of coflow. J. Energy Resour. Technol. 128, 319 (2006).

116. Moore, N.J., Terry, S.D., Lyons, K.M.: Flame hysteresis effects in methane jet flames in air-coflow. J. Energy Resour. Technol. 133, 1–5 (2011).

117. Watson, K., Lyons, K., Donbar, J., Carter, C.: Observations on the leading edge in lifted flame stabilization. Combust. Flame. 2180, 10–13 (1999).

118. Schefer, R., Namazian, M., Kelly, J.: Stabilization of lifted turbulent-jet flames. Combust. Flame. 99, 75–86 (1994).

119. Domingo, P., Vervisch, L., Veynante, D.: Large-eddy simulation of a lifted methane jet flame in a vitiated coflow. Combust. Flame. 152, 415–432 (2008).

120. Buckmaster, J.: Edge-flames. Prog. Energy Combust. Sci. 28, 435–475 (2002).

121. Ruetsch, G.R., Vervisch, L., Liñán, a.: Effects of heat release on triple flames. Phys. Fluids. 7, 1447 (1995).

122. Kelman, J.B., Eltobaji, a. J., Masri, a. R.: Laser Imaging in the Stabilisation Region of Turbulent Lifted Flames. Combust. Sci. Technol. 135, 117–134 (1998).

123. Schefer, R., Namazian, M., Kelly, J.: Structural characteristics of lifted turbulent-jet flames. Symp. Combust. 22, 833–842 (1989).

124. Cha, M.S., Chung, S.H.: Characteristics of lifted flames in nonpremixed turbulent confined jets. Symp. Combust. 26, 121–128 (1996).

125. Chen, Y., Chang, C., Pan, K.-L., Yang, J.-T.: Flame Lift-off and Stabilization Mechanisms of Nonpremixed Jet Flames on a Bluff-body Burner. Combust. Flame. 115, 51–65 (1998).

126. Montgomery, C.J., Kaplan, C.R., Oran, E.S.: The effect of coflow velocity on a lifted methane-air jet diffusion flame. Symp. Combust. 27, 1175–1182 (1998).

127. Moore, N.J., Lyons, K.M.: Leading-Edge Flame Fluctuations in Lifted Turbulent Flames. Combust. Sci. Technol. 182, 777–793 (2010).

128. Wu, Y., Lu, Y., Al-Rahbi, I.S., Kalghatgi, G.T.: Prediction of the liftoff, blowout and blowoff stability limits of pure hydrogen and hydrogen/hydrocarbon mixture jet flames. Int. J. Hydrogen Energy. 34, 5940–5945 (2009).

129. Briones, a, Mukhopadhyay, a, Aggarwal, S.: Analysis of entropy generation in hydrogen-enriched methane–air propagating triple flames. Int. J. Hydrogen Energy. 34, 1074–1083 (2009).

130. Kalghatgi, G.T.: The visible shape and size of a turbulent hydrocarbon jet diffusion flame in a cross-wind. Combust. Flame. 52, 91–106 (1983).

131. Brown, C.D., Watson, K.A., Lyons, K.M.: Studies on lifted jet flames in coflow: the stabilization mechanism in the near- and far-fields. Flow, Turbul. Combust. 62, 249–273 (1999).

132. Chen, M., Herrmann, M., Peters, N.: Flamelet modeling of lifted turbulent methane/air and propane/air jet diffusion flames. Proc. Combust. Inst. 28, 167–174 (2000).

133. Kim, K.N., Won, S.H., Chung, S.H.: Characteristics of turbulent lifted flames in coflow jets with initial temperature variation. Proc. Combust. Inst. 31, 1591–1598 (2007).

134. Chung, S.H., Lee, B.J.: On the characteristics of laminar lifted flames in a nonpremixed jet. Combust. Flame. 86, 62–72 (1991).

135. Norheim, B.: Lift-off of methane jet flames in O2/CO2 atmospheres, (2009).

136. Kumar, S., Paul, P., Mukunda, H.: Prediction of flame liftoff height of diffusion/partially premixed jet flames and modeling of mild combustion burners. Combust. Sci. Technol. 179, 2219–2253 (2007).

137. Takahashi, F., Schmoll, W.J.: Lifting criteria of jet diffusion flames. Symp. Combust. 23, 677–683 (1991).

138. Iyogun, C.O., Birouk, M.: On the Stability of a Turbulent Non-Premixed Methane Flame. Combust. Sci. Technol. 181, 1443–1463 (2009).

139. Gollahalli, S.R., Khanna, T., Prabhu, N.: Diffusion flames of gas jets issued from circular and elliptic nozzles. Combust. Sci. Technol. 86, 267–288 (1992).

140. Luo, K.H.: Axis switching in turbulent buoyant diffusion flames. Proc. Combust. Inst. 30, 603–610 (2005).

141. Kays, W.M., Crawford, M.E., Weigand, B.: Convective heat and mass transfer. (2005).

142. Ahmed, S., Mastorakos, E.: Spark ignition of lifted turbulent jet flames. Combust. Flame. 146, 215–231 (2006).

143. Leung, T., Wierzba, I.: The effect of hydrogen addition on biogas non-premixed jet flame stability in a co-flowing air stream. Int. J. Hydrogen Energy. 33, 3856–3862 (2008).

144. Brown, G.L., Roshko, A.: On density effects and large structure in turbulent mixing layers. J. Fluid Mech. 64, 775–816 (1974).

145. Savas, O., Gollahalli, S.R.: Flow structure in near-nozzle region of gas jet flames. AIAA J. 24, 1137–1140 (1986).

146. Upatnieks, A., Driscoll, J.F., Rasmussen, C.C., Ceccio, S.L.: Liftoff of turbulent jet flames—assessment of edge flame and other concepts using cinema-PIV. Combust. Flame. 138, 259–272 (2004).

147. Yu, H., Girimaji, S.S.: Near-field turbulent simulations of rectangular jets using lattice Boltzmann method. Phys. Fluids. 17, 125106 (2005).

148. Akbarzadeh, M., Birouk, M.: Liftoff of a co-flowing non-premixed turbulent methane flame: effect of the internal geometrical parameters of a circular fuel nozzle. Combust. Sci. Technol. 185, 1–23 (2013).

149. Imine, B., Imine, O., Abidat, M., Liazid, a.: Study of non-reactive isothermal turbulent asymmetric jet with variable density. Comput. Mech. 38, 151–162 (2005).

150. Terry, S.D.: On flame stability in the hysteresis regime in co-flow. PhD thesis, North Carolina State Univ. (2005).

151. Watson, K. a., Lyons, K.M., Donbar, J.M., Carter, C.D.: On scalar dissipation and partially premixed flame propagation. Combust. Sci. Technol. 175, 649–664 (2003).

152. Agrawal, A., Prasad, A.K.: Organizational modes of large-scale vortices in an axisymmetric turbulent jet. Flow, Turbul. Combust. 68, 359–377 (2002).

153. Dahm, W.J.A., Maymant, A.G.: Blowout limits of turbulent jet diffusion flames for arbitrary source conditions. AIAA J. 28, 1157–1162 (1990).

154. Willert, C., Gharib, M.: A new video technique to capture images generated by a smoke-wire. Exp. Fluids. 1988–1989 (1989).

155. Westerweel, J.: Fundamentals of digital particle image velocimetry. Meas. Sci. Technol. 8, 1379 (1999).

156. Willert, C., Gharib, M.: Digital particle image velocimetry. Exp. Fluids. 193, 181–193 (1991).

157. Raffel, M., Willert, C., Kompenhans, J.: Particle image velocimetry: a practical guide. Springer (1998).

158. Ji, X., Le Bihan, O., Ramalho, O., Mandin, C., D'Anna, B., Martinon, L., Nicolas, M., Bard, D., Pairon, J.-C.: Characterization of particles emitted by incense burning in an experimental house. Indoor Air. 20, 147–58 (2010).

159. Keane, R., Adrian, R.: Optimization of particle image velocimeters. I. Double pulsed systems. Meas. Sci. Technol. 1404, 1202–1215 (1990).

160. Coleman, H., Steele, W.: Engineering application of experimental uncertainty analysis. AIAA J. 33, (1995).

161. Rabinowitz, P., Richter, N.: New error coefficients for estimating quadrature errors for analytic functions. Math. Comp. 24, 561–570 (1970).

162. Rabinowicz, E.: An introduction to experimentation. Addison-Wesley Publishing Company (1970).

163. Holman, J., Gajda, W.: Experimental methods for engineers. McGraw Hill Inc., New York. (1994).

164. Iyogun, C.O.: Effect of nozzle geometry on the stability of a turbulent jet flame with and without swirling co-flow. PhD thesis, Univ. Manitoba. (2009).

165. Donnerhack, S., Peters, N.: Stabilization heights in lifted methane-air jet diffusion flames diluted with nitrogen. Combust. Sci. Technol. 41, 101–108 (1984).

166. Shah, M.K., Agelinchaab, M., Tachie, M.F.: Influence of PIV interrogation area on turbulent statistics up to 4th order moments in smooth and rough wall turbulent flows. Exp. Therm. Fluid Sci. 32, 725–747 (2008).

167. Singh, G.: Entrainment and mixing studies for a variable density confined jet. Numer. Heat Transf. Part A Appl. 37–41 (1999).

168. Richards, C.D., Pitts, W.M.: Global density effects on the self-preservation behaviour of turbulent free jets. J. Fluid Mech. 254, 417–435 (1993).

APPENDIX A

PRINCIPLE OF PIV AND ERROR ESTIMATION ANALYSIS

A.1 An overview of the principle of PIV

Particle image velocimetry (PIV) is an optical method for flow instantaneous velocity measurements. PIV is categorized as a non-intrusive velocity measurement technique.

The fluid is seeded with tracer particles and illuminated by a dual pulsed laser separated by a time delay. Frequency doubled neodymium-yttrium-aluminum-garnet (Nd:YAG) lasers are frequently employed for PIV lasers for the reason that these systems deliver monochromatic laser light with high-intensity illumination. The seeding particles which trace the flow motion needs to be sufficiently small so as to follow the flow successfully but also sufficiently large in order to provide enough scattered light to be captured by the camera. The tracer particles need to have sufficiently good light scattering property to guarantee that they can be detected by the CCD sensor, as well [154]. In addition, the seeding/tracer particles must be distributed homogeneously in the flow [155]. The light scattered by the particles are recorded on two separate images which comprise an image pair. The motion of the seeding particles is used to calculate the velocity field of the flow being studied. For this purpose, each image is divided into grid cells called interrogation areas, and for each interrogation area, the local displacement vector of the particles between the first and second image of each image pair (having a time delay) is determined via cross-correlation algorithm (adaptive correlation in the present study). The seeding density might be different depending on the PIV method employed. However, it is shown that for obtaining a “high valid detection probability”, the “particle image density” should be greater than 5 particles per interrogation area [156].

For sufficiently small particles, it is assumed that seeding particles will faithfully and successfully follow the flow motions. The "tracing quality" (i.e., how successfully the tracer particles follow the flow) is represented by the Stokes' equation for the "settling velocity", v_s, and the "response time", t_r, of the particles as the following [157],

$$v_s = \frac{(\rho_p - \rho_{air}) g d_p^2}{18\mu_{air}}$$

$$t_r = \rho_p \frac{d_p^2}{18\mu_{air}}$$

Using Stokes' equation, the settling velocity of the particles was found to be 2.83×10^{-6} m/s. A comparison of this velocity with the results presented in Chapters 4 and 5 demonstrates that the settling velocity is considerably smaller than the axial mean-velocities measured in the present study. In addition, the response time which is obtained to be 2.89×10^{-7} s is very small compared with the sampling times used in this study (~ 135 s). This demonstrates that incense generates adequate seeding particles capable of tracing the flow's instantaneous motion [125, 158].

The preference of the PIV to other flow measurements techniques (such as pitot tube, hot-wire anemometry, Laser Doppler Velocimetry (LDV)) is that PIV produces two dimensional vector fields (that is, by performing the cross-correlation algorithm for each and every interrogation area (each having an image pair), a velocity vector field over the entire domain is obtained), whereas the other measurement techniques provide the velocity at a point. Such capability makes it possible to resolve the flow structures and calculate the different terms in the transport equations. The disadvantage of PIV, on the other hand, is the huge data storage requirement that consequently affect its spatial and temporal resolutions in comparison with that of hotwire and LDA.

Typical PIV set-up consists of a camera (commonly a CCD digital camera), laser sheet, seeding/tracer particles and a synchronizer that externally triggers and control the laser and camera. Finally, PIV software is used to perform post-processing of images. A schematic diagram of a typical PIV arrangement is given in Fig. A.1. In order to obtain highly accurate results from PIV measurements, the interrogation areas must be sufficiently large so as to accommodate enough particles. On the other hand, the interrogation area must be small enough so that one vector can predict the velocity field. Therefore, there must be a compromise between these limits [159]. In addition, the particle image size should be approximately two pixels which is another limit on the particle size and/or magnification factor [157].

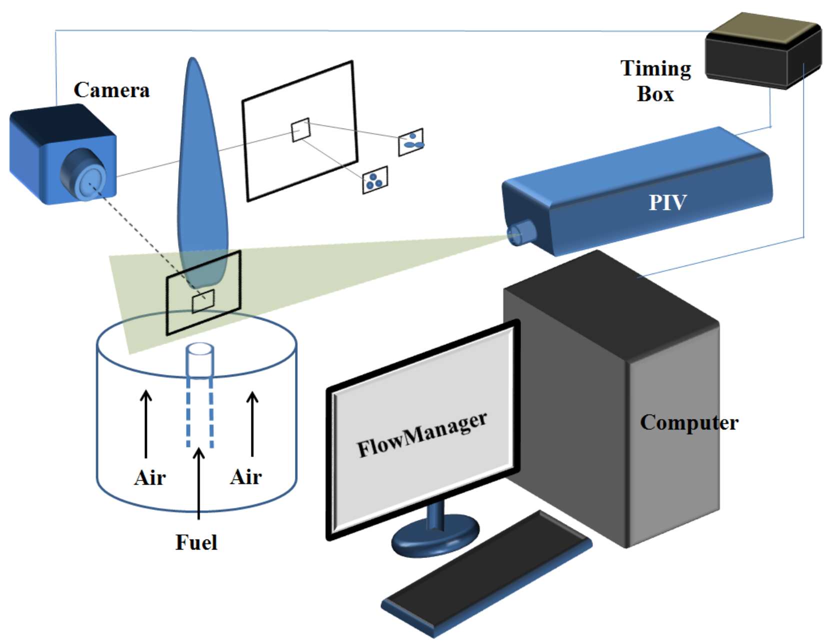

Fig. A.1 A schematic diagram of a typical PIV arrangement

A.2 Estimation of error in PIV measurements and uncertainty analysis

In this section, a summary of measurements errors associated with PIV technique and the measurement uncertainty analysis are presented. According to Coleman and Steele [160], for a given measurement system, the uncertainty E_V in a measured variable, $V(X_1, X_2, \ldots, X_i, \ldots, X_n)$, is defined as,

$$E_V^2 = B_V^2 + P_V^2 \qquad (1)$$

where X_i is independent variable and V (dependent variable) can be expressed solely as a function of X_i. B_V and P_V are, respectively, biased error and precision error of the dependent variable V due to uncertainties in the determination of the independent variable (X_i). The biased error, B_V, can be determined as follows [160]:

$$B_V = \sum \alpha_{X_i}^2 B_{X_i}^2 \qquad (2)$$

where α_{X_i}, the sensitivity coefficient, is defined as,

$$\alpha_{X_i} = \frac{\partial V}{\partial X_i} \qquad (3)$$

For instance, the instantaneous streamwise velocity component measured in each interrogation area, U, is obtained by the following equation,

$$U = \Delta s / M \Delta t \qquad (4)$$

where, M is the magnification factor and Δt is the time interval between the two laser pulses. Also, Δs is the streamwise component of the particles displacement in the interrogation area which is obtained from the statistical analysis. The sensitivity coefficients will be as follows,

$$\alpha_{\Delta s} = \frac{\partial U}{\partial \Delta s} = \frac{1}{M \Delta t},\ \alpha_M = \frac{\partial U}{\partial M} = -\frac{\Delta s}{M^2 \Delta t},\ \text{and}\ \alpha_{\Delta t} = \frac{\partial U}{\partial M} = -\frac{\Delta s}{M \Delta t^2}. \qquad (5)$$

For determining the precision error, the method outlined by Rabinowicz [161, 162] and Holman [163] is used. That is, the precision error, P_V, is given by

$$P_V = t\sigma/\sqrt{N} \qquad (6)$$

where σ is the standard deviation of V of a sample N (i.e., $\sigma = \sqrt{\frac{\sum_1^N (V_i - \bar{V})^2}{N}}$), and t is equal to 2 for a 95 % confidence level; with $\bar{V}$ is equal to $\frac{1}{N}\sum_1^N V_i$.

In the present study, the uncertainties in the measurement of mean velocity, turbulence intensities and Reynolds/turbulent shear-stresses are, respectively, estimated to be ±4.5 %, ±7.5 % and ±9.5 %. As an example, details of the error analysis for the streamwise instantaneous velocity component, U, (i.e., B_U and P_U) at a selective point (x/D_e = 9.0 on the centerline of the turbulent jet from the circular nozzle with smooth contraction) are given in the following. The biased error (and also the properties of this point) are given in Table A.1. The biased uncertainties of Δs, Δt and M (respectively, $B_{\Delta s}$, $B_{\Delta t}$ and B_M) are obtained from the manufacturer's specifications catalogue.

Table A.1 Bias error of the axial mean-velocity, U, on the centerline (y = 0) of the circular nozzle with smooth contraction at x/D_e = 9.0 (U = 2.39E+01) (U_{jet} ~ 30 m/s, U_{co} ~ 0.5 m/s).

Variable (X_i)	Magnitude	α_{X_i}	B_{X_i}	$(\alpha_{X_i} B_{X_i})^2$
Δs (pix)	4.44E+00	5.38E+00	1.27E-02	4.66E-03
Δt (s)	1.00E-05	-2.39E+06	1.00E-07	5.70E-02
M (pix/m)	1.86E+04	-1.55E-03	2.00E-01	9.66E-08

B_U = 2.48E-01 and, therefore, the biased error (B_U/U) is equal to 1.04E+00 %.

For determining the precision error, 5000 instantaneous images were captured, and divided into 10 sets of 500 images per set. The axial mean-velocity, U, was calculated for each set in order to obtain the 10 different values of U for each grid location. The average value of U and its standard deviation at y = 0 and x/D_e = 9.0 were estimated to be 2.39E+01 and 1.24 %, respectively. From Eqn. (6), this results in a precision error of about P_U = 0.78 %. Therefore, the total error in the axial mean-velocity is (Eqn. (1)) $E_U = \sqrt{B_U^2 + P_U^2}$ = 1.30 %.

A.3 Estimation of uncertainty in the measurement of the flame liftoff height

The biased error is mainly due to camera's resolution, calibration, etc. However, since determining these uncertainties is difficult, the error analysis in determining the flame liftoff height is limited to calculating the precision error [164]. The error analysis for the liftoff height was performed for the various test conditions. In the present study, the uncertainties in the liftoff height were estimated to be ±2.5 %.

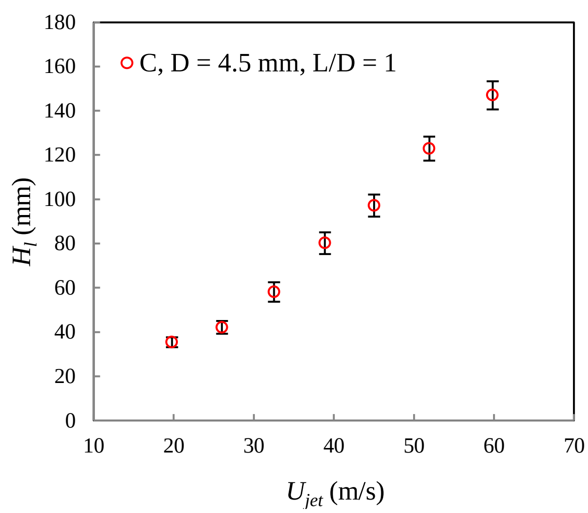

Fig. A.2 Liftoff height profile versus jet velocity for the circular nozzle with D = 4.5 mm and L/D = 1 (U_{co}~ 0.2 m/s); the uncertainty analysis

As an example, in the following, the corresponding calculations (following the same procedure explained in the previous section) for the precision error in the liftoff height, P_{H_l}, is estimated for $N = 300$ images of a lifted flame from the 90-degree contracted circular nozzle with D = 4.5 mm and $L/D = 1$ at U_{jet}~60 m/s and U_{co}~0.2 m/s (having the highest standard deviation as shown in Fig. A.2). Also, t is assumed to be equal to 2 for a 95 % confidence level [163].

$$P_{H_l} = t\sigma/\sqrt{N}$$

$$P_{H_l} = \frac{2\times12.675}{\sqrt{300}} = 1.46 \text{ mm}$$

For this flame with U_{jet}~60 m/s and U_{co} ~ 0.2 m/s and liftoff height of 146.98 mm, the precision error is $P_{H_l} = \frac{1.46}{146.98} = 0.99$ %.

A.4 Estimation of uncertainty in the measurement of the liftoff velocity

The flowmeters (air and methane rotameters) were calibrated using venturi meters. For a few points, PIV was also served to check the accuracy of the flowmeters (Appendix C). The manufacturer's calibrations were provided in tabular format, while the glass tube of the rotameters was linearly scaled by the manufacturer. In the working ranges, the calibrations of the rotameters were typically within 2% of the manufacturer's values; therefore, the manufacturer's calibration values were used in the data analysis.

In the present study, the uncertainties in the liftoff velocity were estimated to be in the range ±7.5 %. As an example, the error analysis is presented in the following for the circular nozzle with D = 4.5 mm and L/D = 2.8. As can be seen from the liftoff velocity profile shown in Fig. A.3, the highest uncertainty exists in the liftoff velocity at U_{co}~ 0.1. Therefore, the error analysis is shown only for this point. The flowmeter's biased error at this fuel jet velocity (U_{jet}= 18.36 m/s) is about 3.5%. The corresponding calculations for the precision error in the liftoff velocity, P_{U_l}, is estimated for $N = 10$ readings from the flow meter at liftoff (at U_{co}~ 0.1). The standard deviation was estimated to be 4.5 % of the average value (U_{jet}= 18.36 m/s). The t is assumed to be equal to 2 for a 95 % confidence level [163]. From Eqn. (6), this results in a precision error of about P_U = 2.85 %. Therefore, the total error in the axial mean-velocity is (Eqn. (1)) $E_U = \sqrt{B_U^2 + P_U^2}$ = 5.33 %.

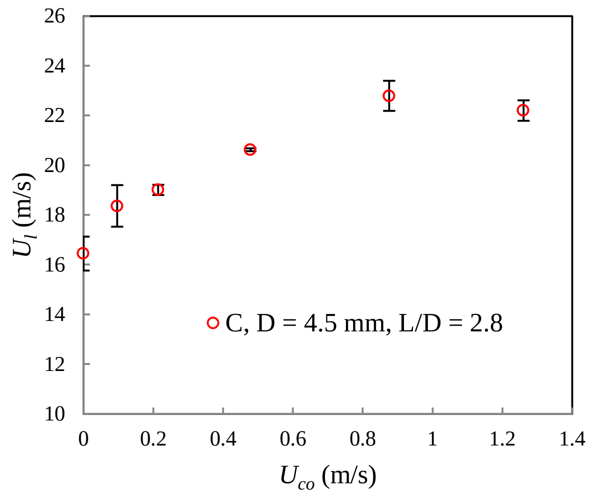

Fig. A.3 Liftoff velocity profile versus coflow velocity for the circular nozzle with D = 4.5 mm and L/D = 2.8; the uncertainty analysis

APPENDIX B

VALIDATION AND GRID INDEPENDENCE TEST

In this appendix, the flame liftoff height of the circular nozzle with smooth contraction (as an example of the nozzle geometries tested in the present study) is compared with the experimental results and well-known liftoff height correlations of the literature as shown in Fig. B.1. The axial mean-velocity decay for the same nozzle (i.e., the circular nozzle with smooth contraction) is also compared with that of the literature in Fig. B.2. A good agreement is found between the present PIV results and the LDV results from the literature [69]. In addition, the average velocity obtained from PIV measurements (almost at the nozzle exit) is compared with that obtained from the flow meter. Also, the effect of the interrogation size on the PIV measurements is investigated. The latter is done by using different interrogation-area sizes to process the PIV images. For this purpose, a 8×16 interrogation area is employed for processing the PIV images in order to compare its result with the 16×16 used for processing the PIV results presented in Chapters 4 and 5.

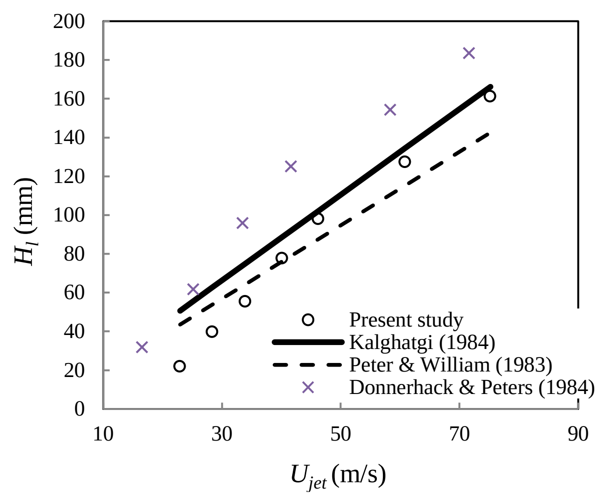

Fig. B.1 Liftoff height profile of the flame from the circular nozzle with smooth contraction as function of U_{jet} (U_{co} = 0) in comparison with the literature [9, 10, 165]

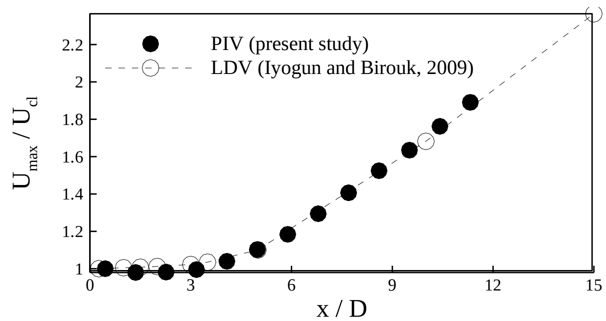

Fig. B.2 Axial mean-velocity decay for the circular nozzle with smooth contraction in comparison with the LDV results in the literature [69]

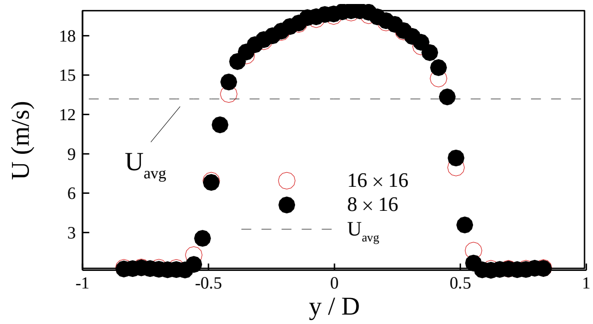

Fig. B.3 Average axial mean-velocity, U_{avg}, (almost at the nozzle exit) obtained from the PIV measurement for pipe nozzle with D = 6.5 mm ($U_{avg} = \frac{4}{\pi D^2}\int_0^{D/2} U 2\pi r dr$)

The difference between the average velocities for the pipe nozzle obtained from the flowmeter (13.13 m/s) and the PIV results (13.18 m/s, as can be seen in Fig. B.3) is less than 0.5 %. The above results (Figs. B.3, B.4(a) and B.4(c)) demonstrate also that the axial mean-velocity, U, does not change with the size of the interrogation area tested in the present study. In addition, it is seen from Fig. B.4(b) that the RMS velocity, u, is fairly independent of the interrogation area size. Therefore, it is concluded that the size of the interrogation area chosen for processing the PIV images in the present study (i.e., 16×16) satisfies the grid-independence requirements. More details on the effect of interrogation area size and other PIV image processing parameters on mean and turbulent flow variables can be found in the literature [166].

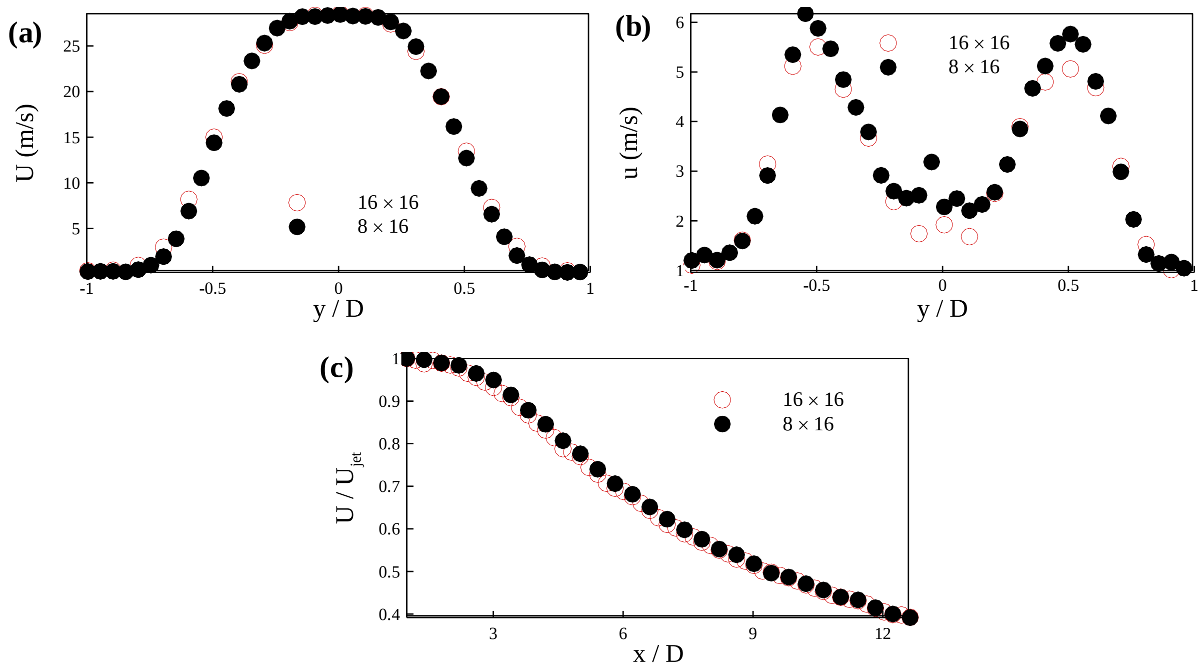

Fig. B.4 Grid independence test. (a) the axial mean-velocity, U, and (b) the RMS velocity, u, and (c) the non-dimensional axial mean-velocity, U/U_{jet}, for the circular nozzle with L/D = 1 and D = 4.5 mm (x/D ~ 1)

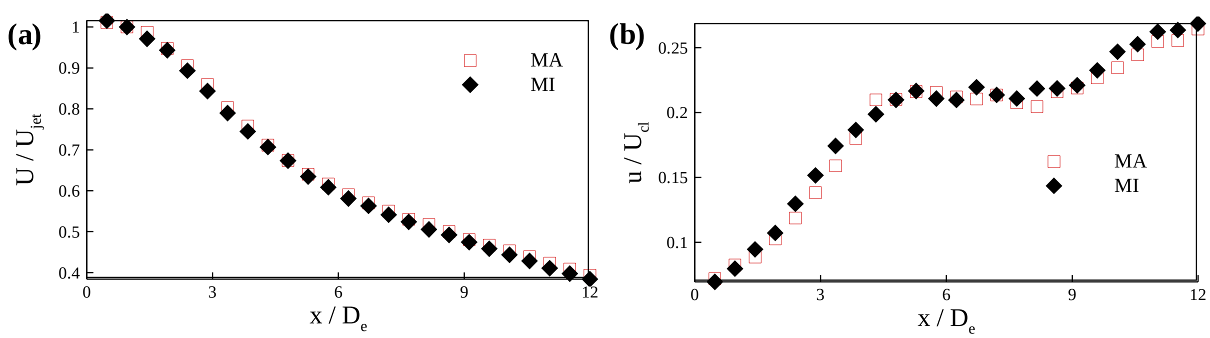

Fig. B.5 Repeatability of the PIV results, (a) non-dimensional axial mean-velocity (U/U_{jet}), and (b) turbulence intensity (u/U_{cl}), on the centerline of the rectangular nozzle with smooth contraction (U_{jet} ~ 30 m/s and U_{co} ~ 0.5 m/s)

Figure B.5 shows the non-dimensional axial mean-velocity (U/U_{jet}) (Fig. B.5(a)) and turbulence intensity (u/U_{cl}) (Fig. B.5(b)) on the centerline of the rectangular nozzle with smooth contraction obtained from the major-plane measurement of the rectangular nozzle in comparison with that of the minor-plane. These results consistently demonstrate that the obtained PIV results are repeatable and that the centerline values are independent of the plane of measurement of the rectangular nozzle.

Finally, the axial mean-velocity decay and turbulence intensity profiles for cold and combusting jet flows on the centerline of the circular nozzle with D = 4.5 mm and L/D = 1 (as an example of the nozzles tested in the present study) are shown in Fig. B.6. These results are in qualitative agreement with that of the literature on turbulent jets with variable densities (e.g., [149, 167, 168]) and agree with the conclusion of Su *et al.*, [21] in that mixing and velocity fields upstream of the flame base evolve consistently with non-reacting jet scaling.

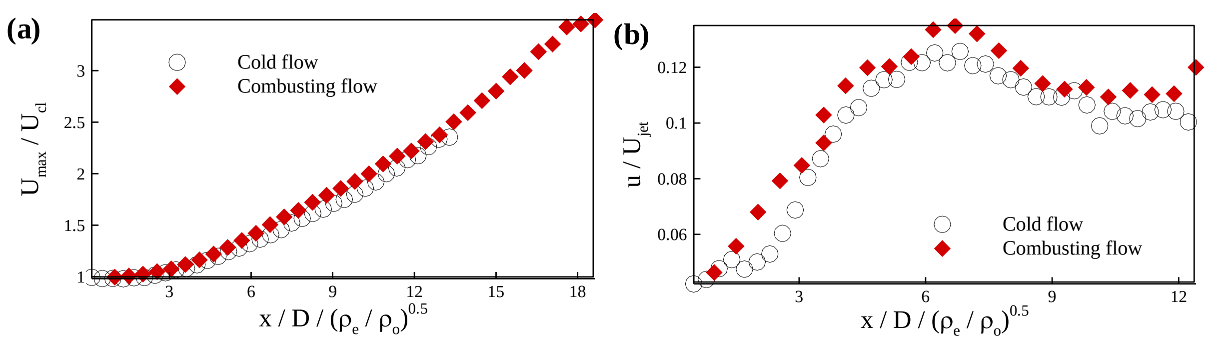

Fig. B.6 (a) Axial mean-velocity decay, and (b) axial turbulence intensity, for the cold and combusting jet flows on the centerline of the circular nozzle with D = 4.5 mm and L/D = 1 (U_{jet}~17 m/s and U_{co}~ 0.5 m/s)

APPENDIX C

MATLAB CODE FOR IMAGE PROCESSING

C.1 Matlab code for determining the flame liftoff height

```
threshold = 28;
threshold = input('threshold = ');
Nozzle_pix = 30;    % Nozzle pix from the figure with higher reselution
yLength = 272;     % The physical length of the image in mm
x_pix = 1280;
y_pix = 1024;
xLength = floor(yLength*x_pix/y_pix);
y_pix2 = 1024;    %y_pix;     % Resized pix size

%Path = 'C:\University Stuff\Projects\EXP\New Images 16 Nov2011';
Max_Files = 201;
n2 = 0;

for (n = 1: Max_Files)

    if (n < 11)
        EndFile = ['00000' num2str(n-1)];
    end
    if (n>10 && n<101)
        EndFile = ['0000' num2str(n-1)];
    end
    if (n>100 && n< 1001)
        EndFile = ['000' num2str(n-1)];
    end
    FileName = ['ImgA' endfile '.tif'];

    clear IMG;
    IMG = imread([FileName],'tiff');
    IMG(IMG<threshold) = 0;
    IMG(IMG>=threshold) = 1;
    IMG = bwareaopen(IMG,1000);
    size(IMG);
    IMGG = IMG(:,:,1);
    [a,b] = size(IMGG);
    m=0;
    clear A;
    i=50;
    [nnn,mmm]=size(IMGG(IMGG(i,round(b/3):round(4*b/5))>0));
    while(mmm==0)
        for j=(b/4):(3*b/4)
            if(IMGG(i,j)>0)
                m=m+1;
                A(m,1)=j;
                A(m,2)=i;
            end
        end
        [nnn,mmm]=size(IMGG(IMGG(i,round(b/3):round(4*b/5))>0));
        i=i+1;
    end
```

```
    if (m>0)
        n2 = n2 + 1;
        B(n2,1) = A(1,1);
        B(n2,2) = A(1,2);
        n3(n2) = n;
    end
end

X_b_pix = mean(B(:,1))
Y_b_pix = mean(B(:,2))
yLength_corr = 1.*(y_pix - Nozzle_pix)/y_pix*yLength;
Y_b_mm = yLength_corr - 1.*(y_pix2 - Y_b_pix)/y_pix2*yLength

fid1 = fopen('FlameHeight.txt', 'wt');
count = fprintf(fid1, '%s', 'H = ');
count = fprintf(fid1, '%8.4f \n', Y_b_mm);
count = fprintf(fid1, '\n %s', 'Average pixel = ');
count = fprintf(fid1, '%5i \n', round(mean(B(:,2))));
count = fprintf(fid1, '\n %s', 'Number of images processed = ');
count = fprintf(fid1, '%5i \n', n2);
fclose(fid1);

Y_b_mm = yLength_corr - 1.*(y_pix2 - B(:,2))/y_pix2*yLength;
fid2 = fopen('FlameHeightSpectrum.txt', 'wt');
R = [(1:n2) ; n3 ; Y_b_mm' ; B(:,2)'];
count = fprintf(fid2, '%5i %5i %12.4f %8i \n', R);
fclose(fid2);
```

C.2 Matlab code for determining the flame front

```
threshold = 12;
Nozzle_pix = 2093;
Nozzle_pixx = 1755;
yLength = 285.; %the physical length of the image in mm
xLength = floor(yLength*356/236);
Folder = 1;

Path = 'C:\University Stuff\Projects\EXP\Monday 13 June\Resized';
if (Folder == 1)
    Path = 'C:\University Stuff\Projects\EXP\Monday 13 June';
end

INIT = 3900;
MaxFiles = 1;
End = INIT + maxFiles;

for (n = 1:maxFiles)

    EndFile = ['DSC0' num2str(n-1+INIT) '-356'];
    if (Folder == 1)
    EndFile = ['DSC0' num2str(n-1+INIT)];
    end
    FileName = [EndFile '.jpg'];
    clear IMG;
```

```
    IMG = imread([Path '\' FileName],'jpg');
    IMG(IMG<threshold) = 0;
    IMG(IMG>=threshold) = 1;
    clear IMG1 IMG2 IMG3;
    IMG1 = IMG(:,:,1);
    IMG2 = IMG(:,:,2);
    IMG3 = IMG(:,:,3);
    size(IMG);
    IMGG = IMG2;
    [a,b] = size(IMGG);
%   ***********************************************************************
    IMGG_EDGE = IMGG;
    for i=2:a-1
        for j=2:b-1
            if (IMGG(i-1,j)>0 && IMGG(i,j-1)>0 && IMGG(i+1,j)>0 &&
IMGG(i,j+1)>0)
                IMGG_EDGE(i,j) = 0;
            end
        end
    end
    IMGG = IMGG_EDGE;
%   ***********************************************************************
for i=1:a
    nnn = [];
    m=0;
    for j=1:b
    if (IMGG(i,j)>0)
        m=m+1;
        nnn(m)=j;
    end
    if (m>2)
        IMGG(i,nnn(m-1))=0;
    end
    end
end
%   ***********************************************************************
    m=0;
    clear A;
    i=1;
    [nnn,mmm]=size(IMGG(IMGG(i,:)>0));
    while(mmm~=0)
        for j=1:b
            if(IMGG(i,j)>0)
                m=m+1;
                A(m,1)=j;
                A(m,2)=i;
            end
        end
        i=i+1;
        [nnn,mmm]=size(IMGG(IMGG(i,:)>0));
    end
    [O,P]=size(A);
    A1 = A(1:2:O,:);
    A2 = A(2:2:O,:);
    [O1,P1] = size(A1);
    [O2,P2] = size(A2);
    A(1:O1,:) = A1(1:O1,:);
```

```
    A(O1+1:O2+O1,:) = A2(O2:-1:1,:);

    [A_nonzero_size,column] = size(IMGG(IMGG>0));
    if (A_nonzero_size==0)
        A = [0 0;0 0];
    end
    [I,J] = max(A);
    B(n,1) = A(J(1,2),1);
    B(n,2) = A(J(1,2),2);
end

X_b_pix = mean(B(:,1))
Y_b_pix = mean(B(:,2))

yLength_corr = 1.*Nozzle_pix/2368.*yLength;
Y_b_mm = yLength_corr - 1.*Y_b_pix/236.*yLength
if (Folder == 1)
    Y_b_mm = yLength_corr - 1.*Y_b_pix/2368.*yLength
end

X_mm = (A(:,1) - 356.*Nozzle_pixx/3568.)*3568./2368.*yLength/356.;
if (Folder == 1)
    X_mm = (A(:,1) - 1.*Nozzle_pixx)./2368.*yLength;
end

Y_mm = yLength_corr - 1.*A(:,2)./236.*yLength;
if (Folder == 1)
    Y_mm = yLength_corr - 1.*A(:,2)./2368.*yLength;
end

[a,b] = size(X_mm);
%   ***********************************************************************
%   Flame size
%   ***********************************************************************
figure(1);
plot(B(:,1),1:maxFiles,'s');
hold on;
plot(mean(B(:,1)),1:maxFiles,'r*');
xlabel('X_b');
ylabel('N');
figure(2);
plot(1:maxFiles,B(:,2),'o');
hold on;
plot(1:maxFiles,mean(B(:,2)),'r*');
xlabel('N');
ylabel('Y_b');
figure(3);
plot(A(:,1),236 - A(:,2),'o');
hold on;
xlabel('Xpix');
ylabel('Ypix');
figure(4);
plot(X_mm,Y_mm,'.');
axis([-150 150 0 300]);
hold on;
xlabel('X (mm)');
```

```
ylabel('Y (mm)');
figure(5);
X_D = X_mm/4.54;
Y_D = Y_mm/4.54;
plot(X_D,Y_D,'.');
axis([-10 10 0 70]);
hold on;
xlabel('X/D_e');
ylabel('Y/D_e');
figure(6);
hold on;
N = 20;
OO = floor(1.*(O1+O2)/N);
np(1:N)=2;
for i=1:N
    I1 = (i-1)*OO+1;
    I2 = i*OO;
    P(i,(1:np(i)+1)) = POLYFIT(X_D(I1:I2),Y_D(I1:I2),np(i));
    Z(I1:I2) = polyval(P(i,(1:np(i)+1)),X_D(I1:I2));
    plot(X_D(I1:I2),Z(I1:I2),'o');
end
```

APPENDIX D

ESTIMATION OF THE JET LOCAL ENTRAINMENT RATE

In this appendix, an analytical relation is developed to estimate the air flow rate entrained into the central jet, i.e., $\dot{V}'(x)$, where $\dot{V}(x)$ is the flow rate of the jet and the entrained co-axial air flow into the jet at x (x is the distance from the nozzle exit). Figure D.1 shows a schematic diagram of the turbulent jet, the corresponding control volume, and the jet parameters.

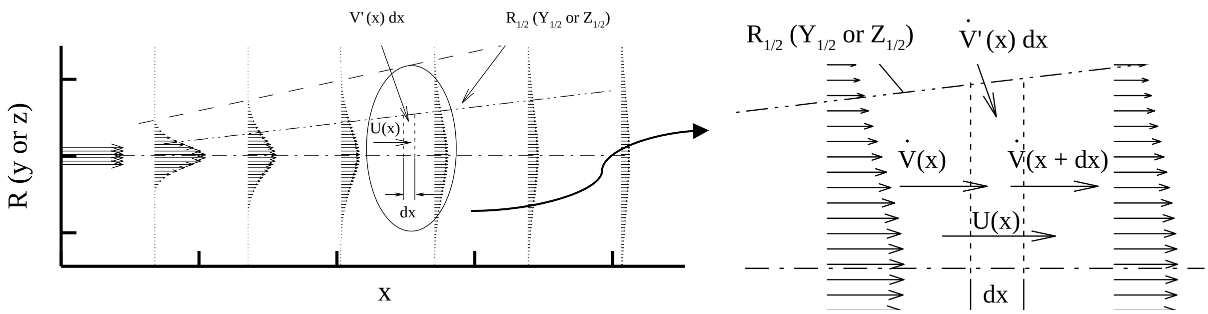

Fig. D.1 Schematic of a turbulent jet

The jet flow rate at *x* is given as

$$\dot{V}(x) = \pi U(x) R_{1/2}^2(x) \qquad (1)$$

and at *x*+*dx* is

$$\dot{V}(x+dx) = \pi U(x+dx) R_{1/2}^2(x+dx) \qquad (2)$$

$R_{1/2}(x)$ is the jet half width at x/D_e which could be $Y_{1/2}(x)$ (the jet's half width on the major plane) or $Z_{1/2}(x)$ (the jet's half width on the minor plane).

From Taylor's series expansion

$$\dot{V}(x+dx) \approx \dot{V}(x) + \dot{V}'(x)\, dx \qquad (3)$$

therefore,

$$\dot{V}(x+dx) = \pi U(x) R_{\frac{1}{2}}^2(x) \ + \pi\left(2U(x) R_{\frac{1}{2}}(x) R_{\frac{1}{2}}^{'}(x) + U'(x) R_{\frac{1}{2}}^2(x)\right) dx \qquad (4)$$

in which $\dot{V}'(x)$ is the co-axial air flow rate entrained into the jet at x which is

$$\dot{V}'(x) = (\dot{V}(x + dx) - \dot{V}(x))/dx \; = \; d\dot{V}(x)/dx \qquad (5)$$

thus,

$$\dot{V}'(x) = \pi(2U(x)R_{\frac{1}{2}}(x)R_{\frac{1}{2}}'(x) + U'(x)R_{\frac{1}{2}}^2(x)) \qquad (6)$$

however, it can be shown that $U'(x)R_{\frac{1}{2}}^2(x)$ is much smaller than $2U(x)R_{\frac{1}{2}}(x)R_{\frac{1}{2}}'(x)$ (or in other words, $U'(x)R(x) \ll 2U(x)R_{\frac{1}{2}}'(x)$) in the turbulent jet flow of the present study, and thus it can be ignored without losing the accuracy in determining $\dot{V}'(x)$. Therefore, Eqn. (6) becomes

$$\dot{V}'(x) = d\dot{V}(x)/dx \approx 2\,\pi\, U(x)R_{\frac{1}{2}}(x)R_{\frac{1}{2}}'(x) \qquad (7)$$

the above equation becomes non-dimensionalized once normalized by the nozzle diameter, D_e, and the jet exit mean-velocity U_{jet}. Thus,

$$\frac{d\dot{V}}{D\times d(\frac{x}{D})} \approx 2\,\pi\,(U_{jet} \times D)\;\frac{U(x)}{U_{jet}}\frac{R_{\frac{1}{2}}(x)}{D}\frac{d(R_{\frac{1}{2}}(x)/D)}{d(\frac{x}{D})} \qquad (8)$$

or,

$$\frac{d\dot{V}}{2\,\pi D^2 U_{jet}\times d(\frac{x}{D})} \approx \left(\frac{U(x)}{U_{jet}}\right)\left(\frac{R_{\frac{1}{2}}(x)}{D}\right)\left(\frac{d(R_{\frac{1}{2}}(x)/D)}{d(\frac{x}{D})}\right) \qquad (9)$$

introducing $\pi D^2 U_{jet}/4$ as $\dot{V}(x = 0)$ which represents the jet flow rate at the nozzle exit (i.e., at $x = 0$), we obtain

$$\frac{d\dot{V}/\dot{V(0)}}{d(\frac{x}{D})} \approx \; 8 \times \left(\frac{U(x)}{U_{jet}}\right)\left(\frac{R_{\frac{1}{2}}(x)}{D}\right)\left(\frac{d(R_{\frac{1}{2}}(x)/D)}{d(\frac{x}{D})}\right) \qquad (10)$$

It should be noted that $U(x)$ is an average axial mean-velocity between U_{cl} (on the centerline velocity) and half velocity ($1/2U_{cl}$) at $R_{1/2}$ (jet's half width). That is, $\frac{1}{2}U_{cl} < U(x) < U_{cl}$. Therefore,

$$\frac{d\dot{V}/V(\dot{0})}{d(\frac{x}{D})} \propto \left(\frac{U_{cl}}{U_{jet}}\right)\left(\frac{R_{\frac{1}{2}}(x)}{D}\right)\left(\frac{d(R_{\frac{1}{2}}(x)/D)}{d(\frac{x}{D})}\right) \qquad (11)$$

Thus, it is obvious that the non-dimensional co-axial flow entrainment rate is proportional to $\frac{U_{cl}}{U_{jet}}$ (jet's reciprocal decay), $\frac{R_{\frac{1}{2}}(x)}{D}$ (non-dimensional jet spread) and $\frac{d(R_{\frac{1}{2}}(x)/D)}{d(\frac{x}{D})}$ (the jet spread rate along the axial direction). However, it is clear that for the same jet, $\frac{U_{cl}}{U_{jet}}$ is the same between the minor and major plane. Therefore, it can be concluded that the non-dimensional co-axial air flow rate entrained into the central jet at the jet's half width (i.e., $\frac{d\dot{V}/V(\dot{0})}{d(\frac{x}{D})}$) is proportional to the the jet spread rate and its derivative in the axial direction:

$$\frac{d\dot{V}/V(\dot{0})}{d(\frac{x}{D})} \propto \left(\frac{R_{\frac{1}{2}}(x)}{D}\right)\left(\frac{d(R_{\frac{1}{2}}(x)/D)}{d(\frac{x}{D})}\right) \qquad (12).$$

The following figures show the profiles of the different terms appeared in obtaining Eqn. (12) for the rectangular nozzle with D_e = 3 mm and L/D_e = 1 (as an example of the rectangular nozzles tested in the present study). Figure D.2(a-b) demonstrates that although the spread is higher for the nozzle's major axis (Fig. D.2(a)), the spread rate (i.e., the slope of profile) is faster along its minor axis (Fig. D.2(b)). Figure D.2(c) shows that in the most part of the nozzle's downstream $d(U_{cl}/U_{jet})/d(x/D_e)$ is significantly smaller than U_{cl}/U_{jet} which therefore demonstrates that the assumption made in obtaining Eqn.(7) from Eqn.(6) is reasonable. Finally, Fig. D.2(d) shows that the non-dimensional co-axial air flow rate entrained into the central jet at the jet's half width (i.e., Eqn.(12)) is higher along the nozzle's minor axis in the most part of the nozzle's downstream.

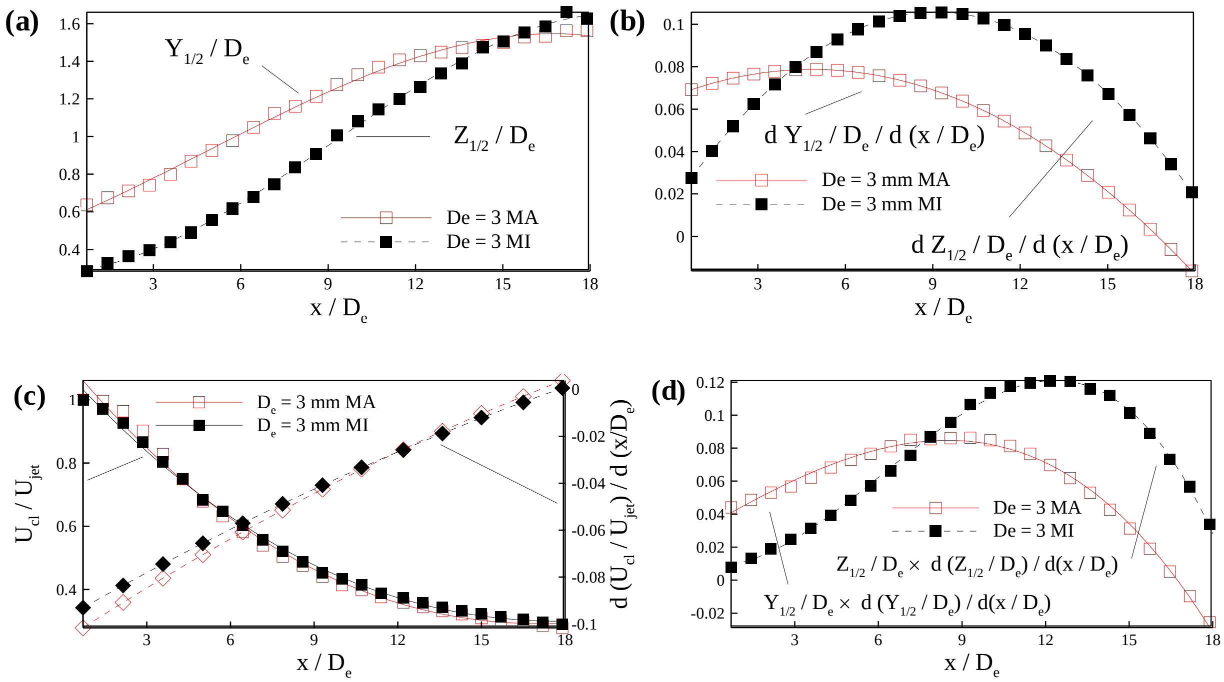

Fig. D.2 Different terms in obtaining Eqn. (12), (a) $Y_{1/2}/D_e$ and $Z_{1/2}/D_e$, (b) $d(Y_{1/2}/D_e)/d(x/D_e)$ and $d(Z_{1/2}/D_e)/d(x/D_e)$, (c) U_{cl}/U_{jet} and $d(U_{cl}/U_{jet})/d(x/D_e)$, and (d) $R_{1/2}(x)\big(d(R_{1/2}(x)/D_e)/d(x/D_e)\big)$.

APPENDIX E

E.1 Part I: effect of the internal geometry of a rectangular nozzle on flame liftoff phenomena and jet characteristics

In this section, detailed results on the effect of the internal geometry of a rectangular nozzle on the flame liftoff, turbulent jet characteristics and its development (which were briefly presented in Chapter 5) are presented below.

E.1.1 Liftoff velocity

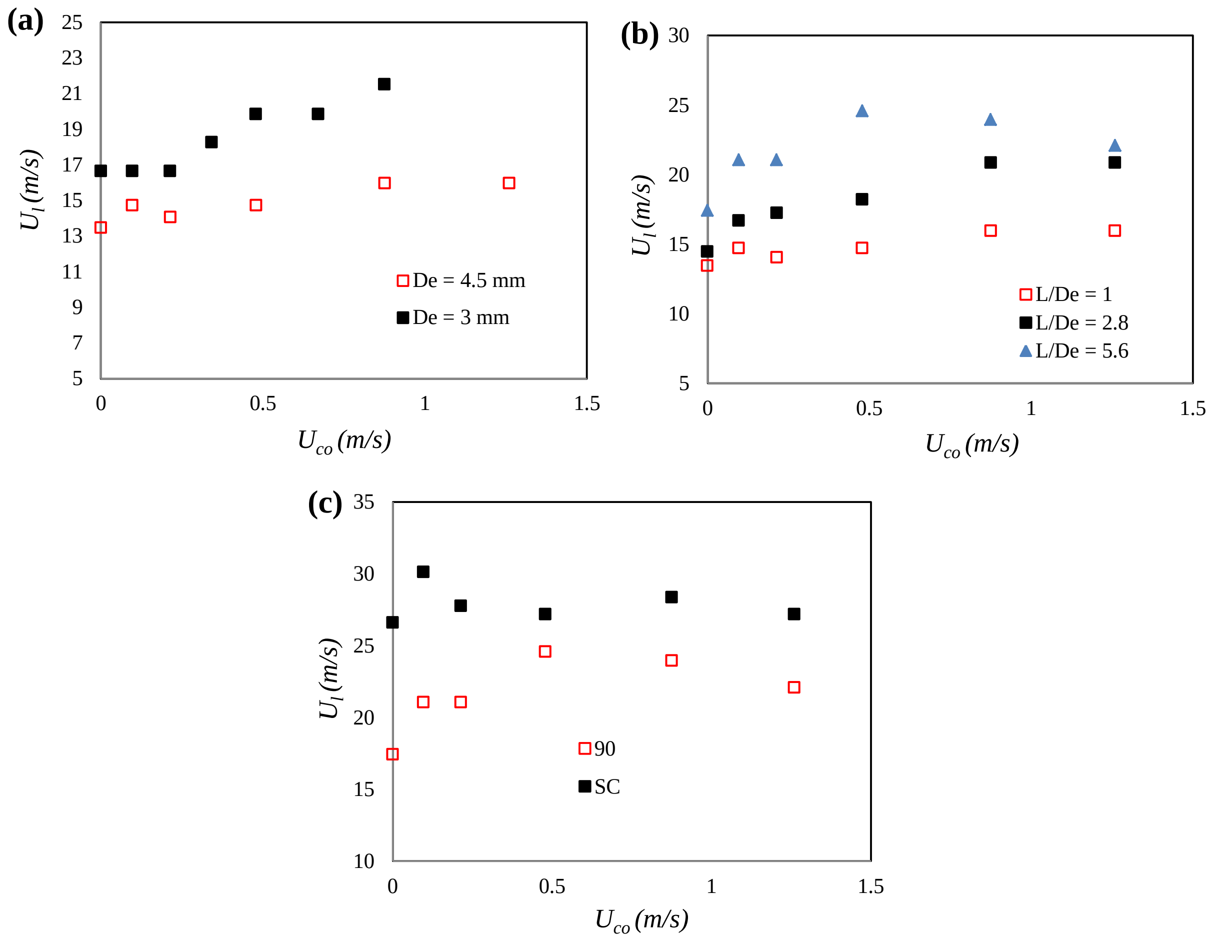

Fig. E.1 Liftoff velocity versus co-flow velocity for the different nozzle geometries. (a) Effect of nozzle equivalent diameter, D_e (Experiment #1 in Table 3.1), (b) effect of L/D_e (Experiment # 2 in Table 3.1), and (c) effect of contraction angle (Experiment #3 in Table 3.1)

Results on the effect of the internal geometry of a rectangular fuel nozzle (see Table 3.2) on the liftoff velocity of a co-flowing methane turbulent diffusion flame are presented in Fig. E.1. This figure shows that for all nozzles the flame liftoff velocity increases slightly with the co-flow exit velocity up to a certain U_{co} beyond which the liftoff velocity profile becomes plateau or decreases slightly. This U_{co} limit (at which the liftoff velocity becomes plateau or start to decrease) decreases by increasing the L/D_e. In fact, this U_{co} is the lowest for the smooth contracting nozzle which has also the highest L/D_e. The nozzle having the smaller diameter experiences a faster increase in the liftoff velocity as the co-flow velocity increases. The figure demonstrates also that the larger the L/D_e is, the higher the flame liftoff regardless of the co-flow velocity. The liftoff velocity is the highest for the rectangular nozzle with smooth contraction which also has the highest L/D_e.

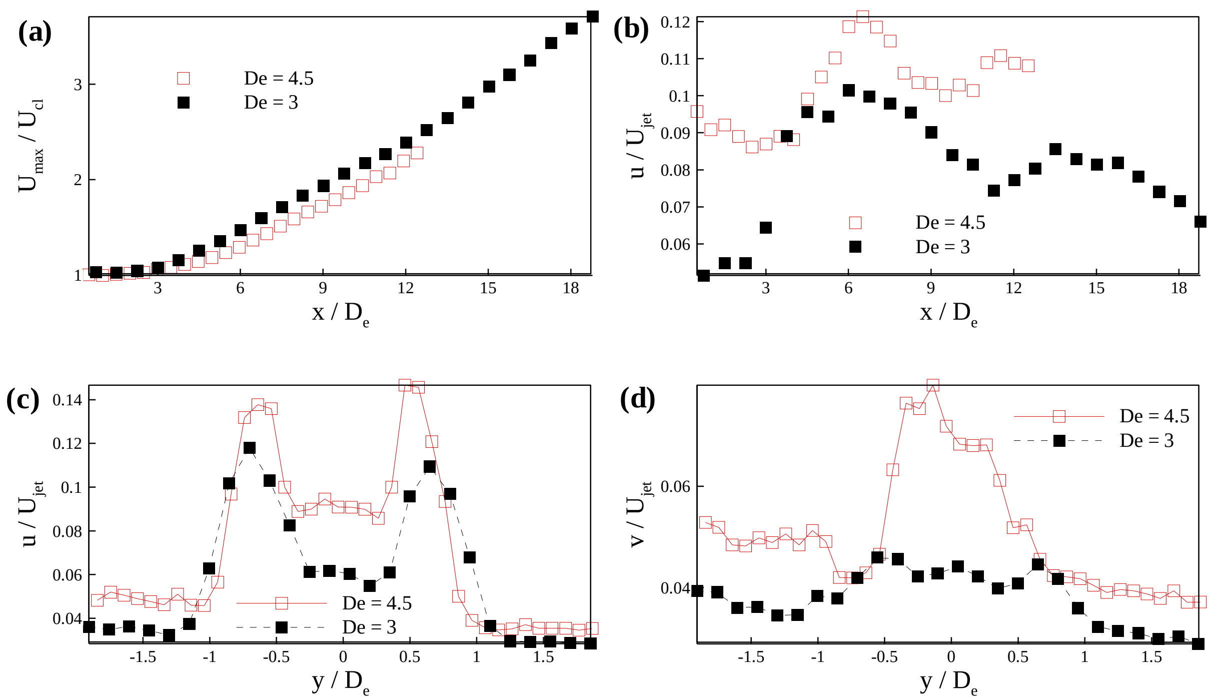

Fig. E.2 Comparison of the (a) axial mean-velocity decay, (b) centerline axial turbulence intensity, (c) radial profile of the axial turbulence intensity, and (d) radial profile of the lateral turbulence intensity at $x/D_e \sim 1-1.5$ (U_{jet}~17 m/s and U_{co}~0.5 m/s) between different nozzle equivalent diameters.

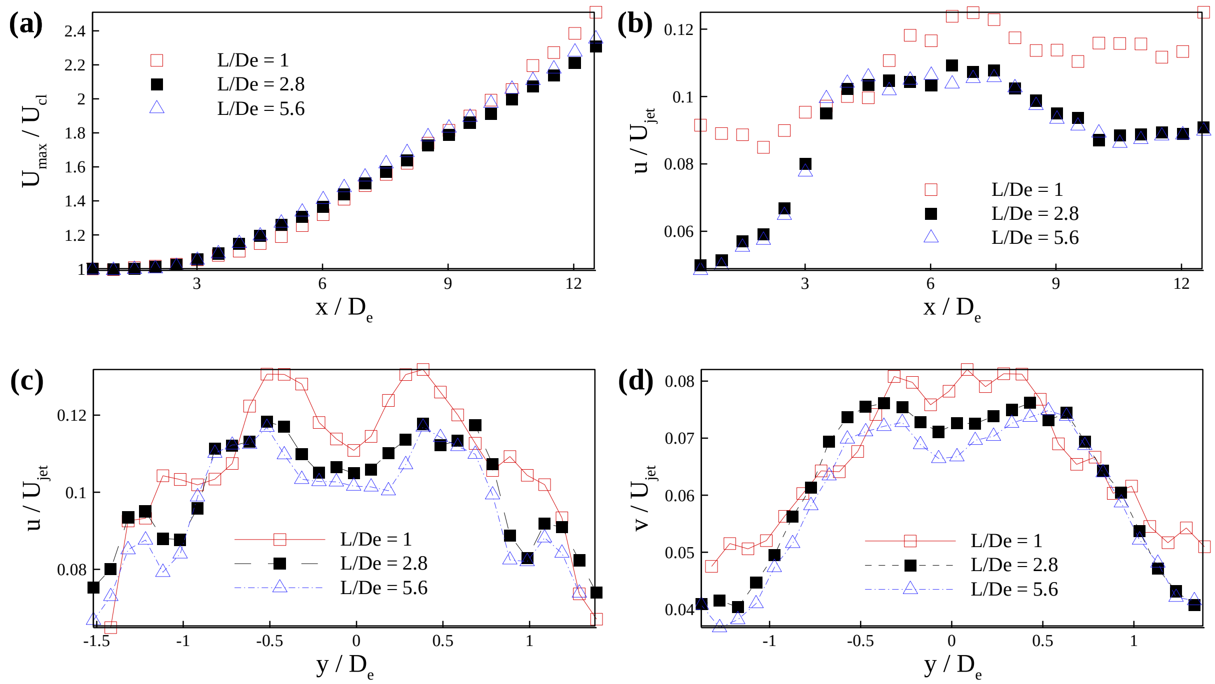

Fig. E.3 Comparison of the (a) axial mean-velocity decay, (b) centerline axial turbulence intensity, (c) radial profile of the longitudinal/axial turbulence intensity, and (d) radial profile of the lateral turbulence intensity at x/D_e~5 (U_{jet}~17 m/s and U_{co}~0.2 m/s) between different nozzle L/D_e.

E.1.1.1 Flow characteristics

Details about the corresponding turbulent jet flow characteristics, such as the axial and lateral development of turbulence intensity profiles, and axial mean-velocity decay close to the nozzle exit (i.e., in the near-field region) are provided for all rectangular nozzles. These profiles, which are for typical flow conditions just prior to the liftoff of the flame (i.e., in the range U_{jet}~ 17 m/s), are shown in Figs. E.2-E.4 for different nozzle geometries.

These figures showed that, overall, in the jet near-field, there is no significant difference between the axial mean-velocity decay rate when changing the nozzle's internal geometry (i.e., D_e, L/D_e or the contraction angle). On the other hand, a correlation seems to exist between the turbulence intensity profiles (u/U_{jet} and v/U_{jet}) and the corresponding flame liftoff velocity presented in Fig. E.1. That is, the higher is the jet near-field turbulence intensity, the lower the flame liftoff velocity. For instance, the noticeable difference between the liftoff velocity of the nozzles with D_e = 3 and D_e = 4.5 mm at higher co-flow rates (Fig. E.1(a)) can be attributed to the important difference in the turbulence intensity between these two nozzles (see Fig. E.2(c-d)).

The flow Reynolds number for the different nozzle internal geometries employed here is plotted in Fig. E.5. It can be seen that the Reynolds number at liftoff in all cases is greater than Re = 2300. The same figure shows also that the Reynolds number at liftoff is below Re ~ 10000.

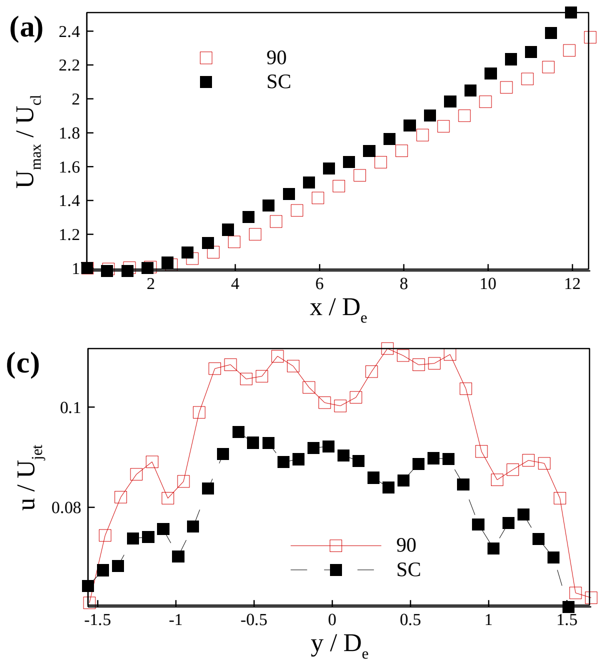

Fig. E.4 Comparison of (a) the axial/longitudinal mean-velocity decay, (b) centerline longitudinal/axial turbulence intensity, (c) radial/lateral profile of the longitudinal/axial turbulence intensity, and (d) radial profile of the lateral turbulence intensity at $x/D_e{\sim}6$ ($U_{jet}{\sim}17$ m/s and $U_{co}{\sim}0.2$ m/s) between different nozzle contraction angles.

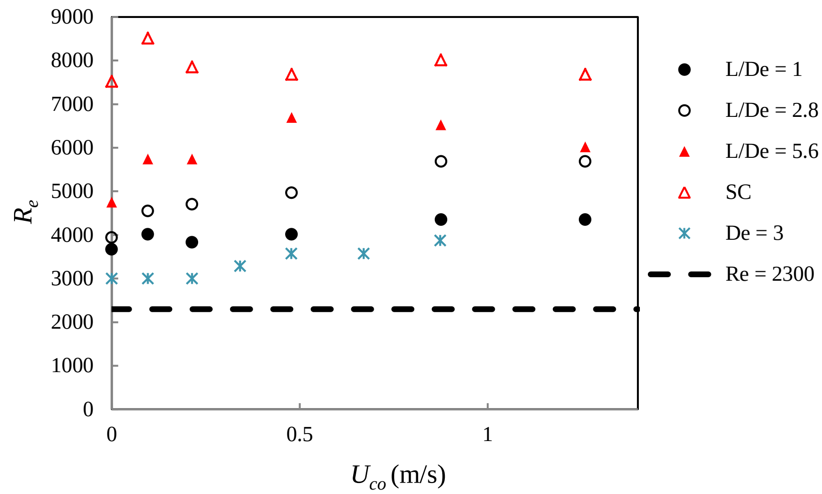

Fig. E.5 Reynolds number at flame liftoff flow conditions.

E.1.2 Liftoff height

Figures E.6-E.9 present the flame liftoff height for the nozzle geometries tested here versus the fuel jet exit velocity (F: forward profiles, were obtained by increasing the jet velocity; and B: backward profiles, were obtained by decreasing the jet velocity). These figures show that the flame liftoff height dependence on the nozzle equivalent diameter, D_e is a function of co-flow strength. It is also shown that increasing the nozzle L/D_e results in unnoticeable rise in the flame liftoff height for a given jet exit velocity. The figures show also that the liftoff height of the nozzle with smooth contraction is noticeably lower than that of the 90-degree nozzle. A distinction between the flame liftoff height of a stronger co-flow (Fig. E.8) and that of a pure-jet (zero co-flow) flame (Fig. E.6) or at moderate co-flow (Fig. E.7), is that, regardless of the geometry, the flame liftoff height for a relatively stronger co-flow rises drastically with reducing the fuel flow rate to the limit of the flame reattachment/blowout. It is important to mention that this phenomenon manifests only with the backward profiles where the jet/fuel exit velocity can reach to relatively small values prior to the flame reattachment/blowout.

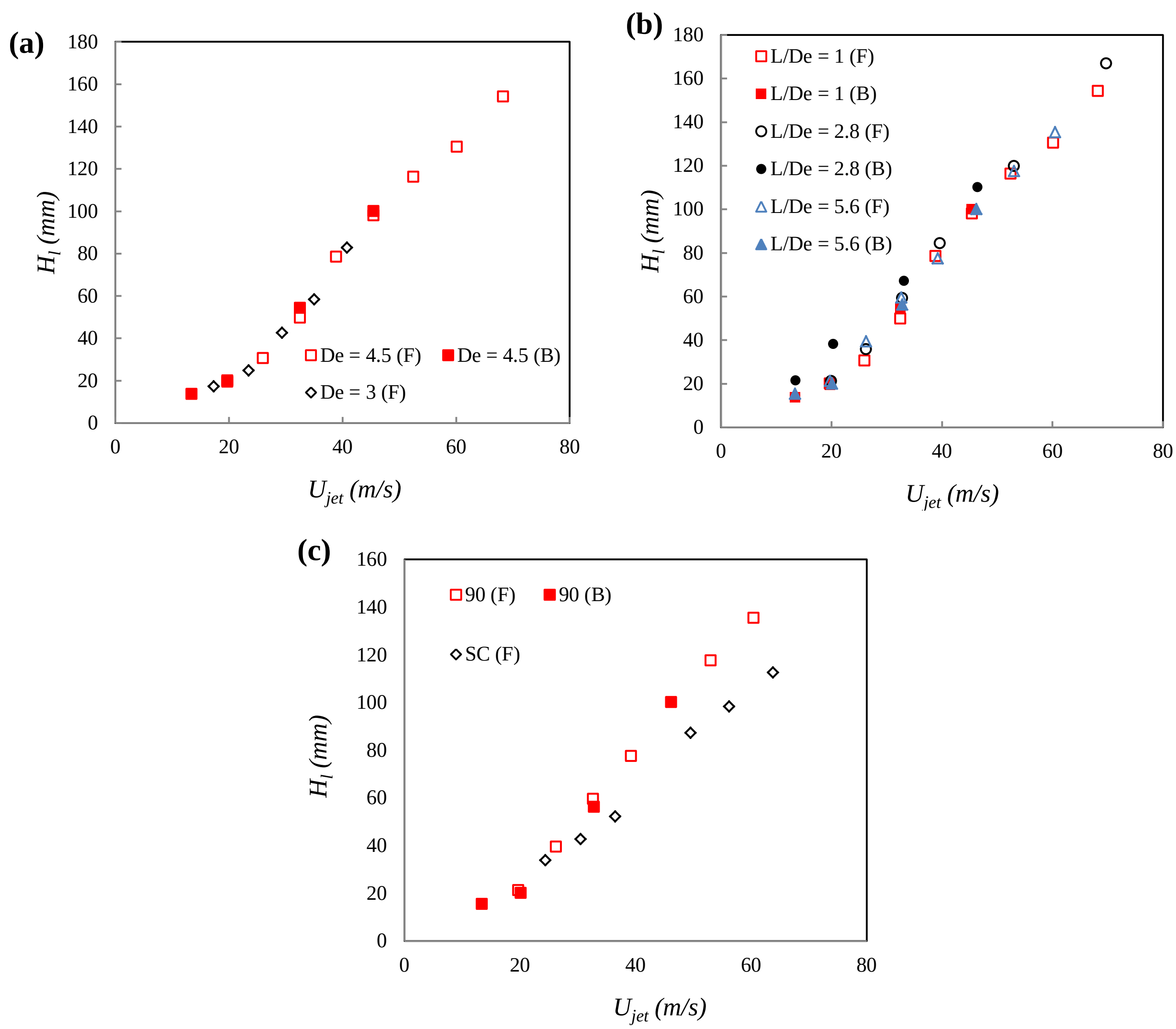

Fig. E.6 Liftoff height versus jet fuel exit velocity for methane jet flame with zero co-flow for (a) different nozzle equivalent diameters, (b) different nozzle L/D_e, and (c) different nozzle contraction angle.

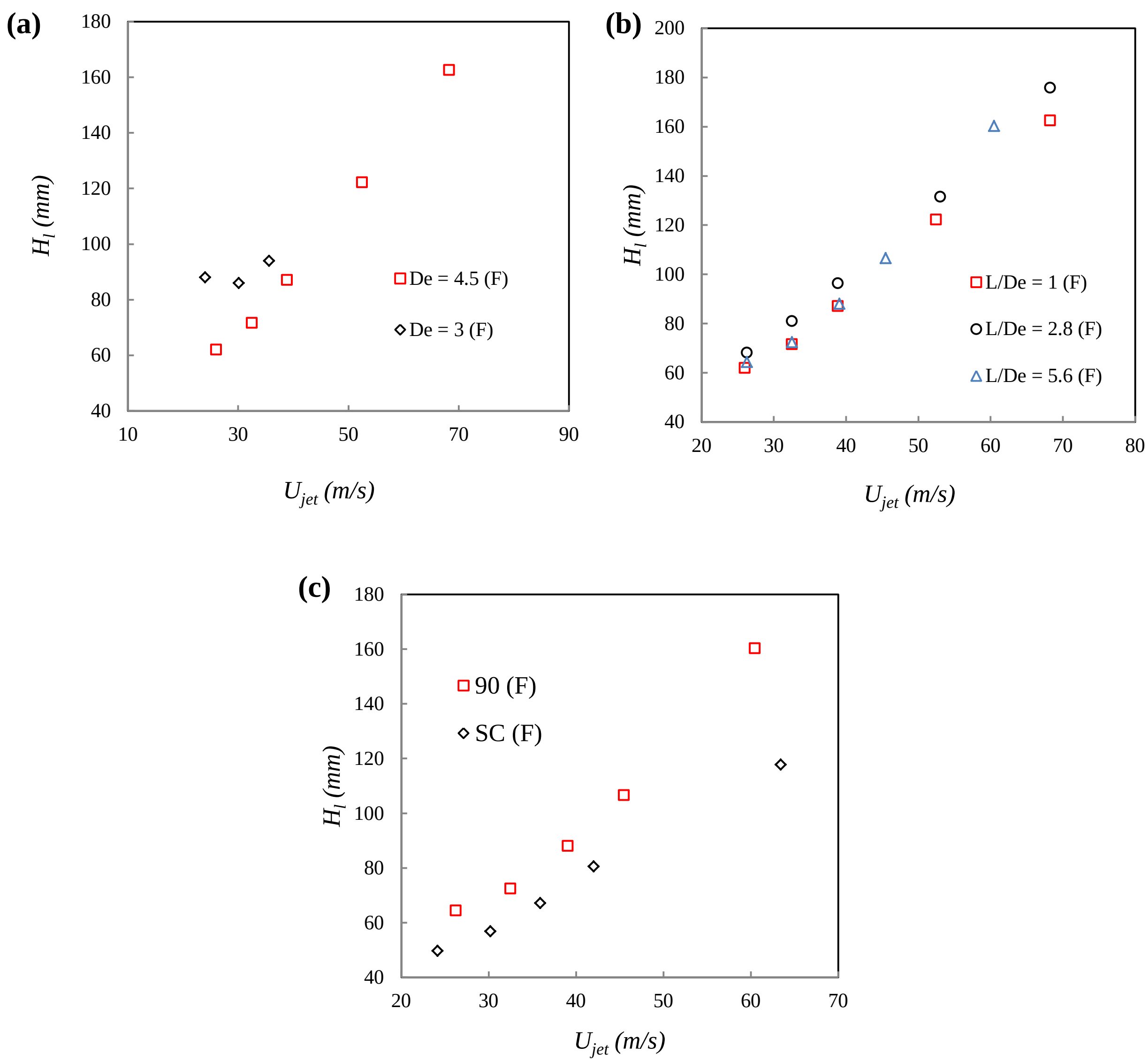

Fig. E.7 Liftoff height versus jet fuel exit velocity for methane jet flame with $U_{co} \sim 0.9\ m/s$ for (a) different nozzle equivalent diameters, (b) different nozzle L/D_e, and (c) different nozzle contraction angles.

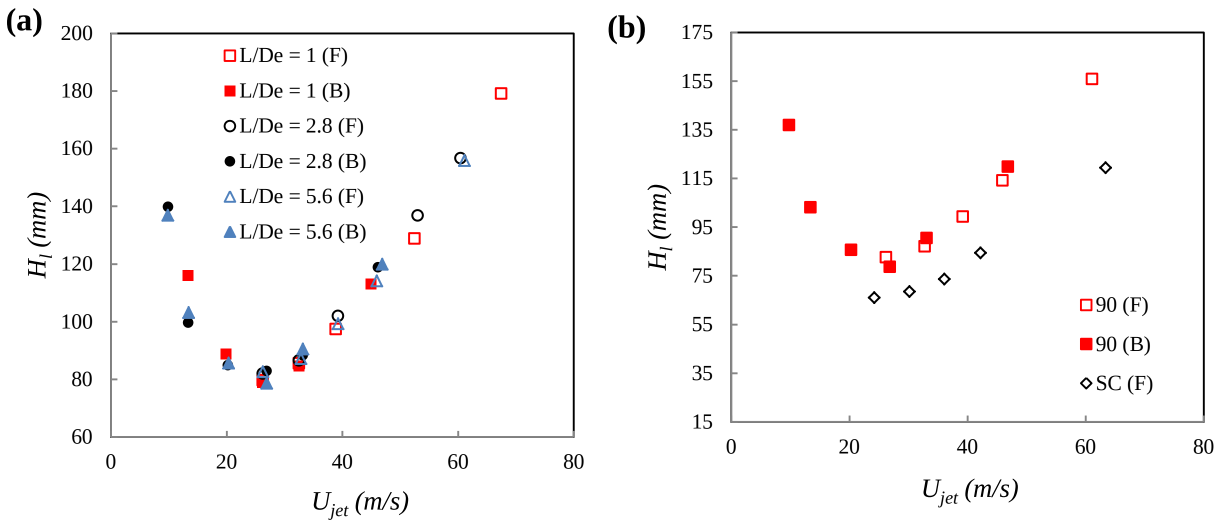

Fig. E.8 Liftoff height versus jet fuel exit velocity for methane jet flame with $U_{co} \sim 1.25\ m/s$ for (a) different nozzle L/D_e, and (b) different nozzle contraction angles.

E.1.2.1 Flow characteristics

The development of the corresponding jet flow characteristics downstream of the nozzle were investigated through Figs. E.9-E.14. These jet characteristics include the axial mean-velocity decay and jet spread rate (in the jet near-field region), and the turbulence intensity profiles at certain distances downstream of the nozzle as well as on the jet centerline for typical flow conditions pertaining to lifted flame.

The jet characteristics revealed that the axial mean-velocity decay showed, in general, no consistent correlation with the flame liftoff height when varying the nozzle geometry including D_e, L/D_e and contraction angle. However, the flow characteristics presented above showed that the turbulence intensity level in the near-field region (i.e., believed to be in the proximity of the flame leading edge) is higher for the nozzles which have lower liftoff height.

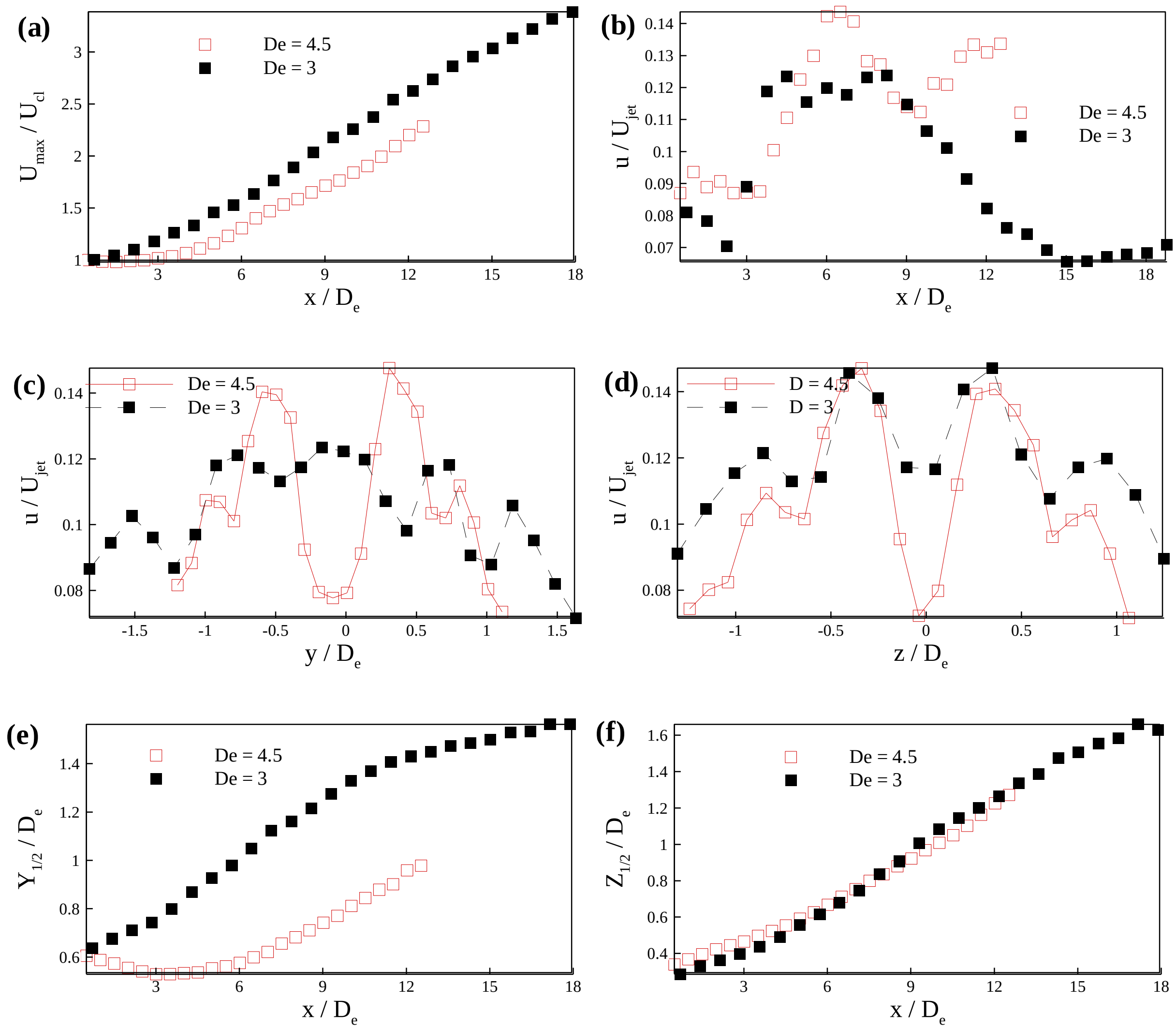

Fig. E.9 Comparison of the (a) longitudinal/axial mean-velocity decay, (b) centerline longitudinal/axial turbulence intensity, (c) radial profile of the axial turbulence intensity on the major axis at $x/D_e{\sim}3-4.5$, (d) radial profile of the longitudinal/axial turbulence intensity on the minor axis at $x/D_e{\sim}3-4.5$, (e) jet spread on the major axis, (f) jet spread on the minor axis issuing from different nozzle equivalent diameters with $U_{co}{\sim}0.2$ m/s and $U_{jet}=30-40$ m/s.

The present results revealed consistently that the jet spreading rate on the minor axis ($Z_{1/2}/D_e$) correlates well with the flame liftoff height for all nozzle geometries. That is, a jet having faster spreading rate along the minor axis will also produce a flame with a lower liftoff height. The results of Chapter 4 on circular nozzle having different internal geometries proved that the nozzle with a higher jet spread rate has also a lower liftoff height. Higher jet spread rate is an indication of increased jet entrainment, and hence improved mixing. As seen in Figs. E.9-E.14 and also reported in the literature [147], the jet spread rate along the major axis of a rectangular nozzle ($Y_{1/2}/D_e$) is different from that along the minor axis ($Z_{1/2}/D_e$). However, as mentioned above only the jet spreading rate along the minor axis showed a good correlation with the flame liftoff height. Thus, the question is why the flame liftoff height has a consistent correlation with the jet spread rate on the minor plane but not on the major plane. An attempt to answer this question is provided in the following.

Figure E.15 shows that, for the same nozzle geometry, the jet spread in the near-field (upstream of the flame base) is higher along the nozzle major plane. The jet spreading along the minor axis, however, becomes higher past the flow axis switching location. The same figure shows faster growth of the jet spreading on the minor plan (these trends agree well with the literature, [19, 76, 147]). An estimation of the jet local entrainment rate, following the procedure described in the Appendix D of the present manuscript, demonstrates that the local flow entrainment rate into the central jet in the near-field, upstream the flame base, is proportional to the jet spread, $R_{1/2}$ (= $Y_{1/2}$ on the major axis or = $Z_{1/2}$ on the minor axis), times its local change (gradient) in the streamwise/axial direction ($d\,R_{1/2}/d\,x$). As shown in Fig. E.16, this quantity (the jet flow local entrainment rate) along the minor plane overtakes that along the major plane for all rectangular nozzles employed in the present study. This finding leads to believe that the stabilization of the flame base (and hence liftoff height) may be governed primarily by the local mixing rate, which, according to the present analysis, prevails along the rectangular nozzle minor plane. For instance, Fig. E.6(a) shows that the liftoff height, in the absence of a co-flow, is almost insensitive to the nozzle equivalent diameter. This agrees with the corresponding jet characteristics at nearly zero-coflow where the jet spread (that is, $Z_{1/2}/D_e$ in Fig. E.9(f), and correspondingly its axial rate, $d\,(Z_{1/2}/D_e)/d\,(x/D_e)$) is fairly the same between the nozzles with different equivalent diameters. In addition, Figs. E.17(a) and (b), which show a comparison of the local entrainment rate on the same plan/axis between different nozzle equivalent diameters at a nearly zero-coflow, reveal that although the flow local entrainment rate along the major axis (Fig. E.17(b)) is different for the two nozzle diameters, it is nearly the same for these nozzle diameters along the minor axis. Moreover, the jet local entrainment is greater on the nozzle minor axis, which is why there is a good correlation between the jet spread on the minor axis and the corresponding flame liftoff height. Figure E.7(a) shows that, at higher co-flow exit velocity, the flame liftoff height of the smaller orifice is noticeably greater than that of the larger orifice nozzle. This is also in agreement with Fig. E.10(f) which shows that both $Z_{1/2}/D_e$ in Fig. E.10(f) and consequently $d\,(Z_{1/2}/D_e)/d\,(x/D_e)$ are relatively higher for the nozzle with the larger diameter.

Figures E.6(b), E.7(b) and E.8(a) show that the liftoff height is only slightly lower for the nozzle with the shortest L/D_e (= 1). This is also in agreement with the results of Figs. E.11(e) and E.12(e) that show that the spread (and correspondingly its axial derivative) is relatively higher for the nozzle with the shortest L/D_e. These figures, on the other hand, predict similar spread for the other two nozzles whose flame liftoff height is also identical. Figures E.17(c) and (d) show that the local entrainment rate on the minor axis is slightly higher for the nozzle with the shortest L/D_e (= 1) but fairly similar between the two other nozzles which agrees with the corresponding liftoff height data shown in Figs. E.6(b), E.7(b) and E.8(c). It is to be noted that the three nozzles (with different L/D_e) have different local jet entrainment rate on the major axis (Fig. E.17(c)); however, this quantity is significantly smaller and hence unimportant in comparison with its counterpart on the minor axis. Finally, the trend of the flame liftoff height shown in Figs. E.6(c), E.7(c) and E.8(b) is in agreement with that shown by the corresponding jet spreading rate. That is, both $Z_{1/2}/D_e$ (see Figs. E.13(f) and E.14(f)) and hence $d\,(Z_{1/2}/D_e)/d\,(x/D_e)$ are higher for the nozzle with smooth contraction. Figures E.17(e-f) confirm the above conclusion. That is, the local entrainment rate on the minor axis is considerably greater than that on the major axis regardless of the nozzle contraction angle, which suggests that the jet mixing is dominant along the minor axis. It also shows that the local entrainment rate on the nozzle minor axis is significantly greater for the nozzle with smooth contraction which is why its corresponding flame liftoff height is lower.

Therefore, the nozzle which exhibits higher jet spread rate on the minor plan/axis and also has a higher turbulence level in the near-field (both of which have impact on local molecular mixing) results in a lifted flame which seats at a lower height from the burner.

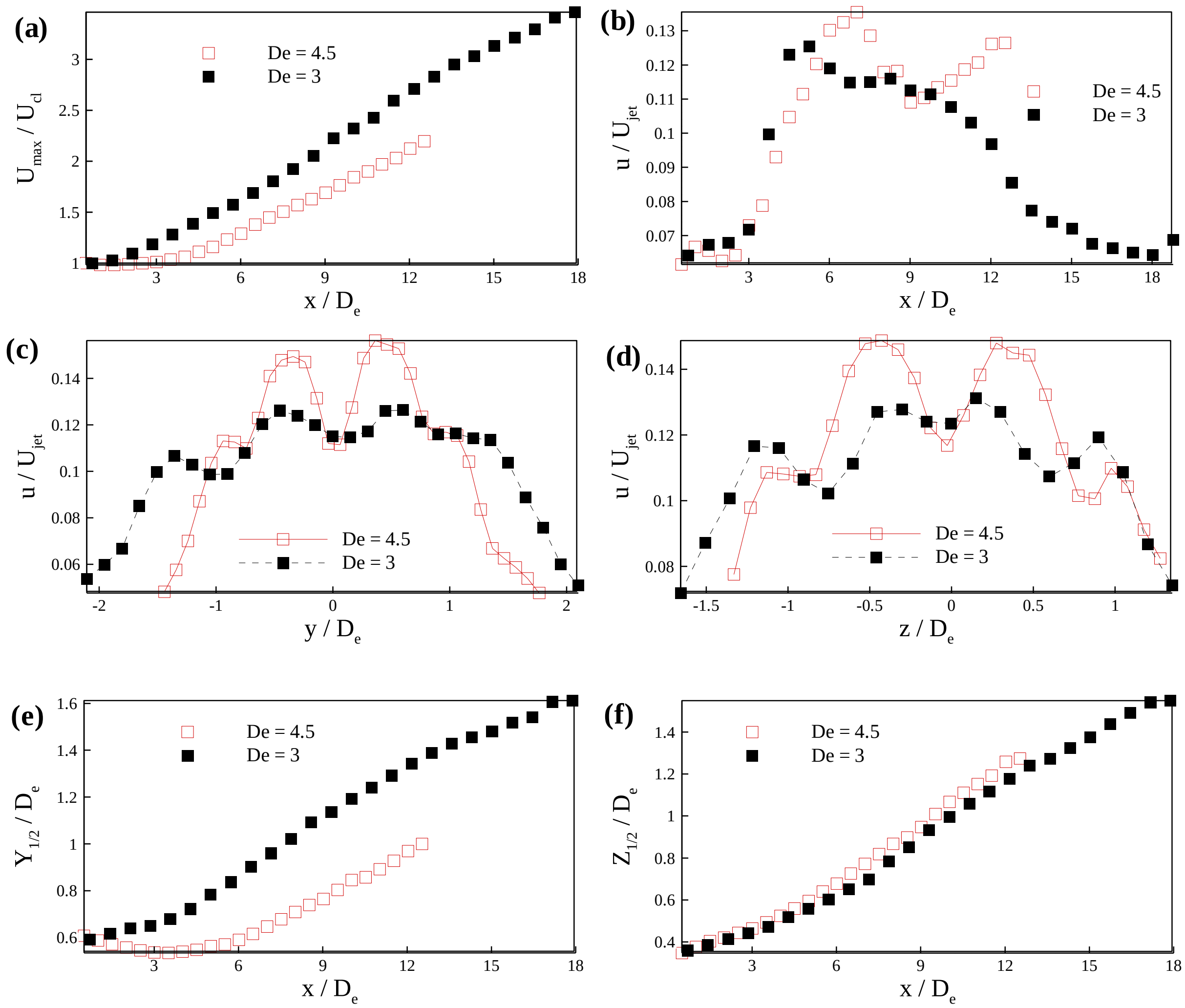

Fig. E.10 Comparison of the (a) longitudinal/axial mean-velocity decay, (b) centerline longitudinal/axial turbulence intensity, (c) radial profile of the longitudinal/axial turbulence intensity on the major axis at $x/D_e \sim 5 - 7.5$, (d) radial profile of the longitudinal/axial turbulence intensity on the minor axis at $x/D_e \sim 5 - 7.5$, (e) jet spread on the major axis, and (f) jet spread on the minor axis issuing from different nozzle equivalent diameters with $U_{co} \sim 0.5$ m/s and $U_{jet} = 30 - 40$ m/s.

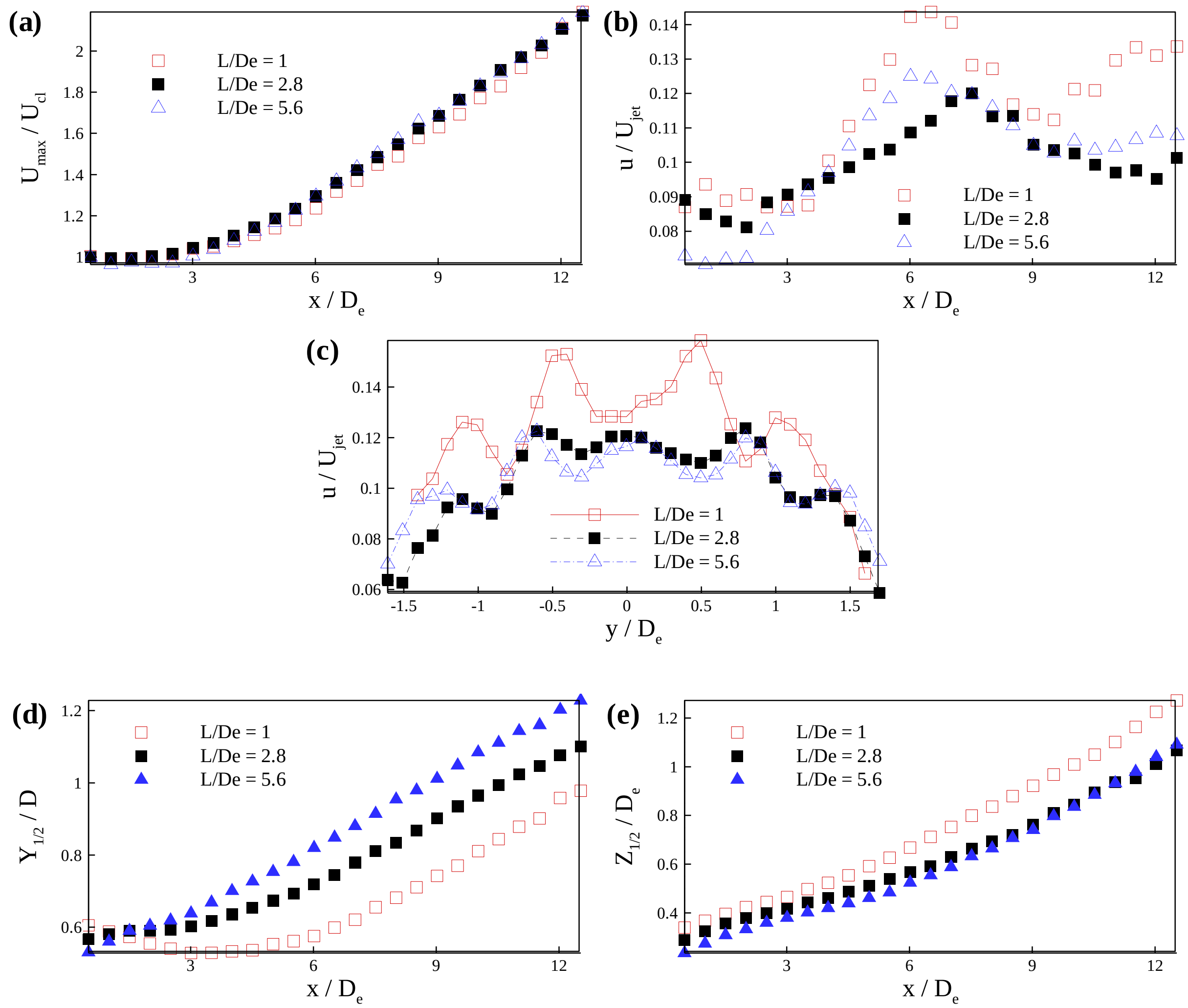

Fig. E.11 Comparison of the (a) longitudinal/axial mean-velocity decay, (b) centerline longitudinal/axial turbulence intensity, (c) radial profile of the longitudinal/axial turbulence intensity on the major axis at $x/D_e \sim 7.5$, (d) jet spread on the major axis, (e) jet spread on the minor axis issuing from different nozzle L/D_e with $U_{co} \sim$ 0.2 m/s and $U_{jet} \sim$ 30 m/s.

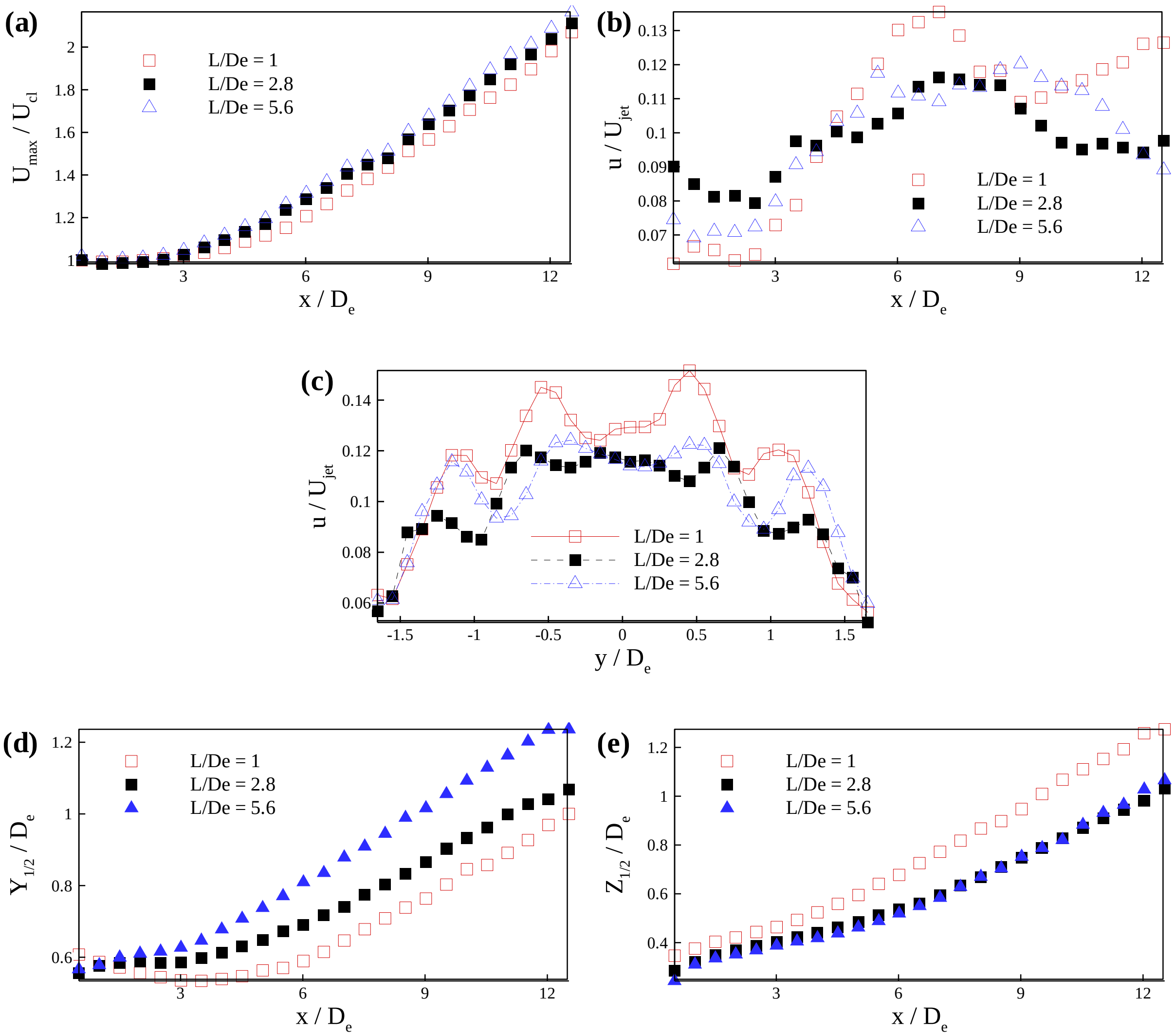

Fig. E.12 Comparison of the (a) longitudinal/axial mean-velocity decay, (b) centerline longitudinal/axial turbulence intensity, (c) radial profile of the longitudinal/axial turbulence intensity on the major axis x/D_e~7.5, (d) jet spread on the major axis, and (e) jet spread on the minor axis issuing from different nozzle L/D_e with U_{co} ~ 0.5 m/s and U_{jet}~ 30 m/s.

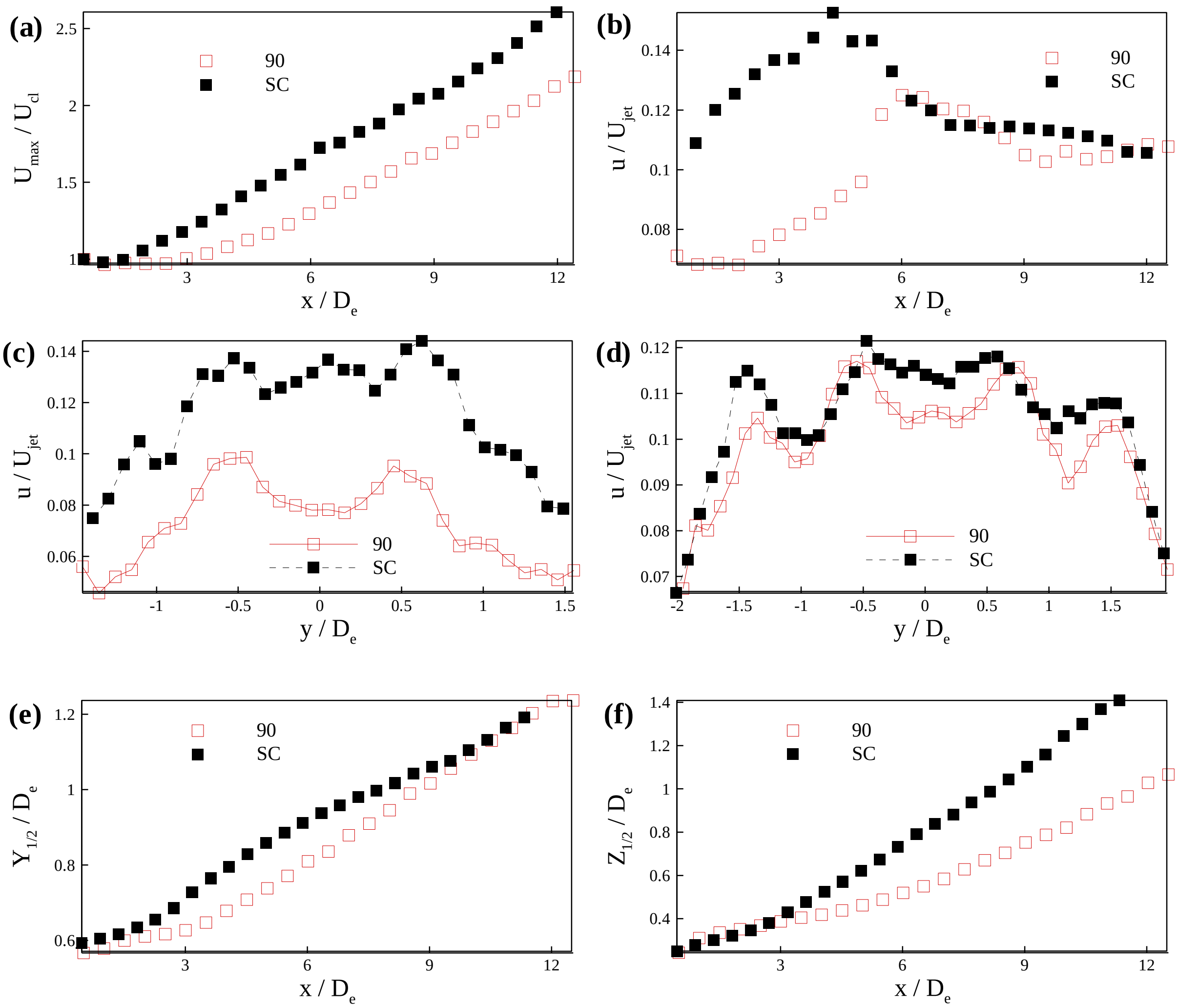

Fig. E.13 Comparison of the (a) longitudinal/axial mean-velocity decay, (b) centerline longitudinal/axial turbulence intensity, (c) radial profile of the longitudinal/axial turbulence intensity on the major axis at $x/D_e{\sim}3$, (d) radial profile of the longitudinal/axial turbulence intensity on the major axis at $x/D_e{\sim}10$, (e) jet spread on the major axis, (f) jet spread on the minor axis issuing from nozzles with different contraction angles with $U_{co}{\sim}0.2$ m/s.

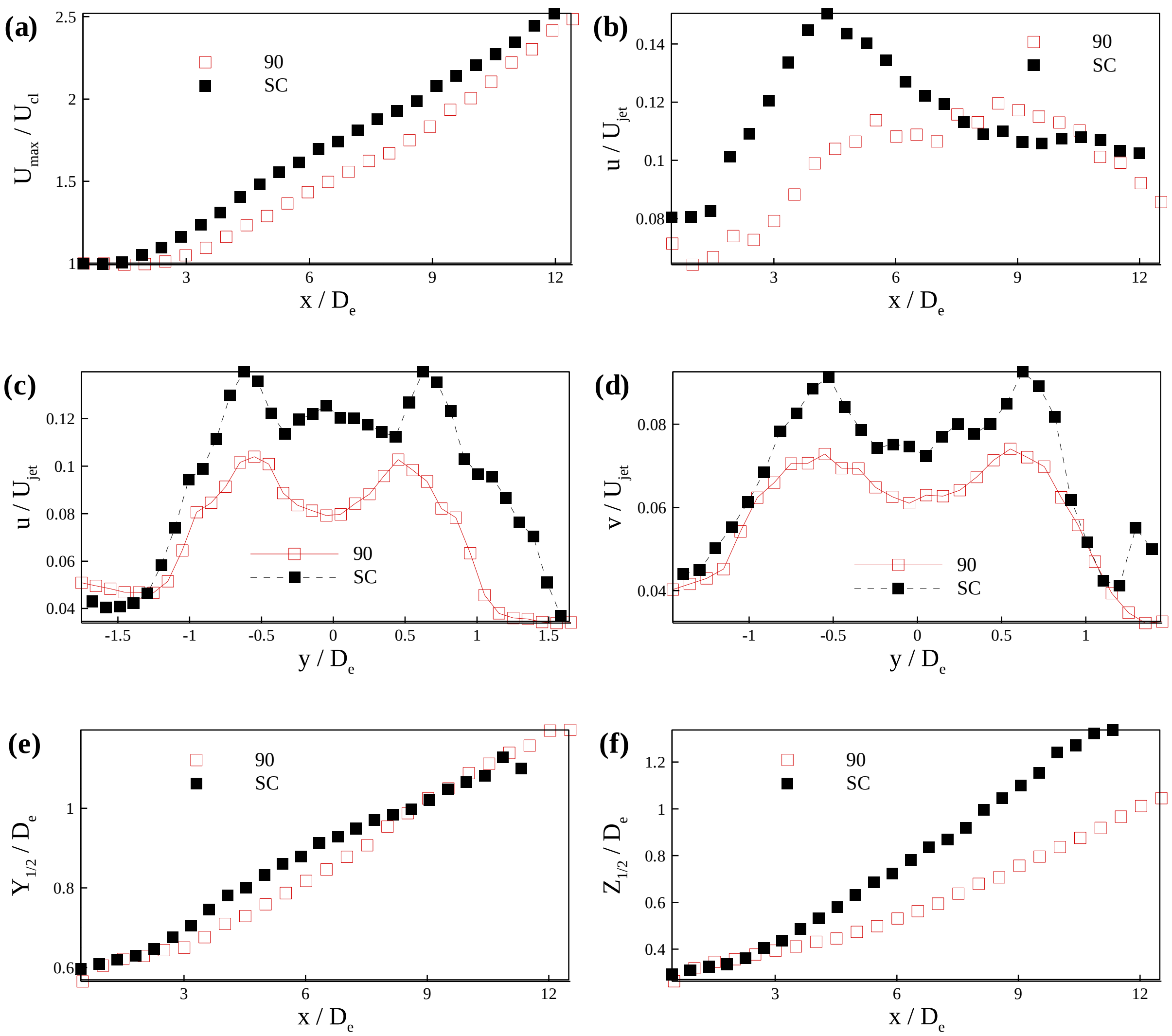

Fig. E.14 Comparison of the (a) the longitudinal/axial mean-velocity decay, (b) centerline longitudinal/axial turbulence intensity, (c) radial profile of the longitudinal/axial turbulence intensity on the major axis at $x/D_e{\sim}3$, (d) radial profile of the lateral turbulence intensity on the major axis at $x/D_e{\sim}3$, (e) jet spread on the major axis, and (f) jet spread on the minor axis issuing from different nozzle contraction angles with $U_{co}{\sim}0.5$ m/s and $U_{jet}{\sim}30$ m/s.

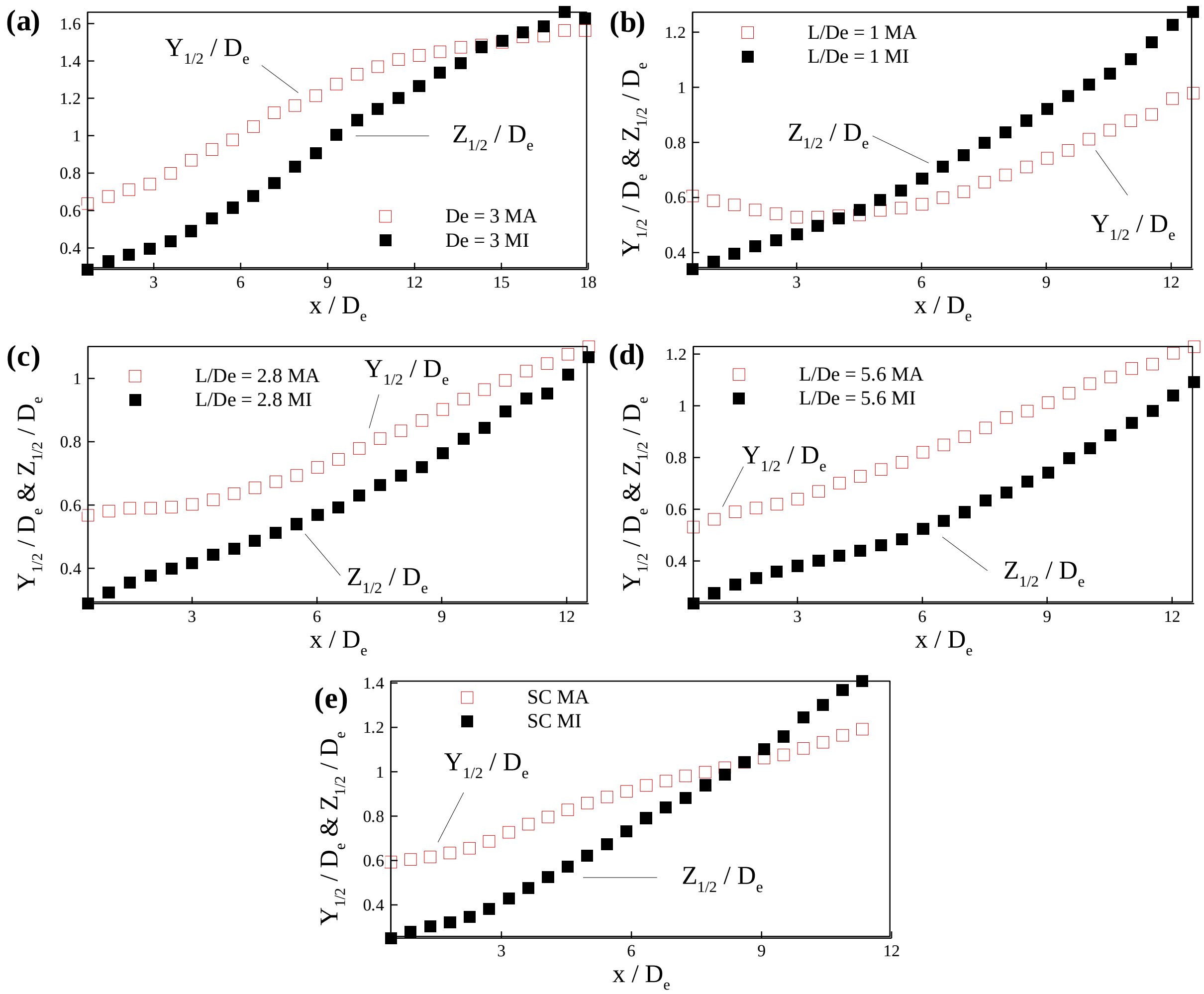

Fig. E.15 Comparison of the jet spread along the major plane (MA), $Y_{1/2}/D_e$ and the minor plane (MI), $Z_{1/2}/D_e$ for a rectangular nozzle with (a) $D_e = 3$ mm, (b) $D_e = 4.5$ mm and $L/D_e = 1$, (c) $D_e = 4.5$ mm and $L/D_e = 2.8$, (d) $D_e = 4.5$ mm and $L/D_e = 5.6$, and (e) smooth contraction angle at U_{co}~0.2 m/s and U_{jet}~30 m/s.

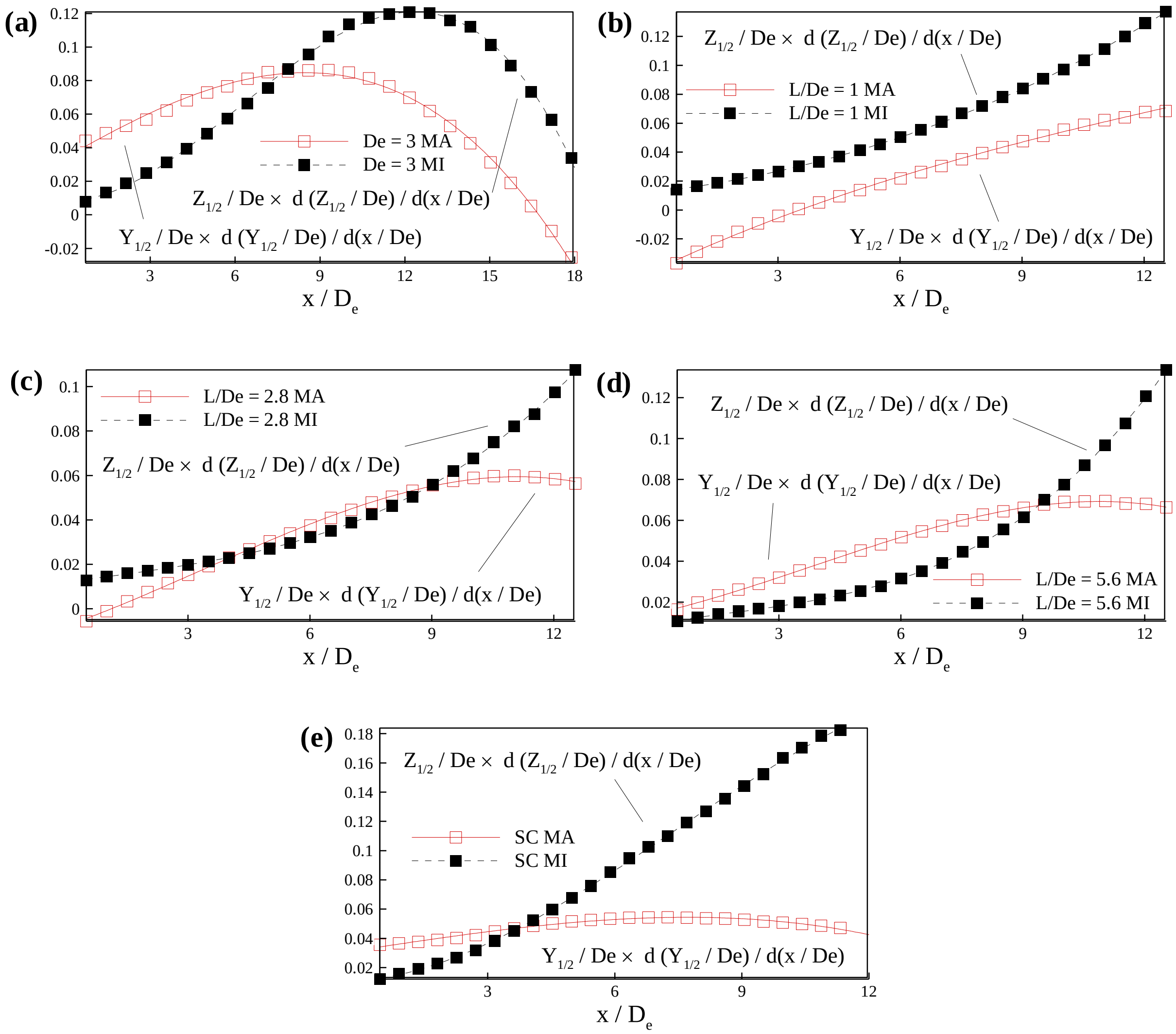

Fig. E.16 Comparison of the flow local entrainment rate between the major plane (MA) and the minor plane (MI) for a rectangular nozzle with (a) $D_e = 3$ mm, (b) $D_e = 4.5$ mm and $L/D_e = 1$, (c) $D_e = 4.5$ mm and $L/D_e = 2.8$, (d) $D_e = 4.5$ mm and $L/D_e = 5.6$, (e) smooth contraction angle at U_{co}~0.2 m/s and U_{jet}~30 m/s.

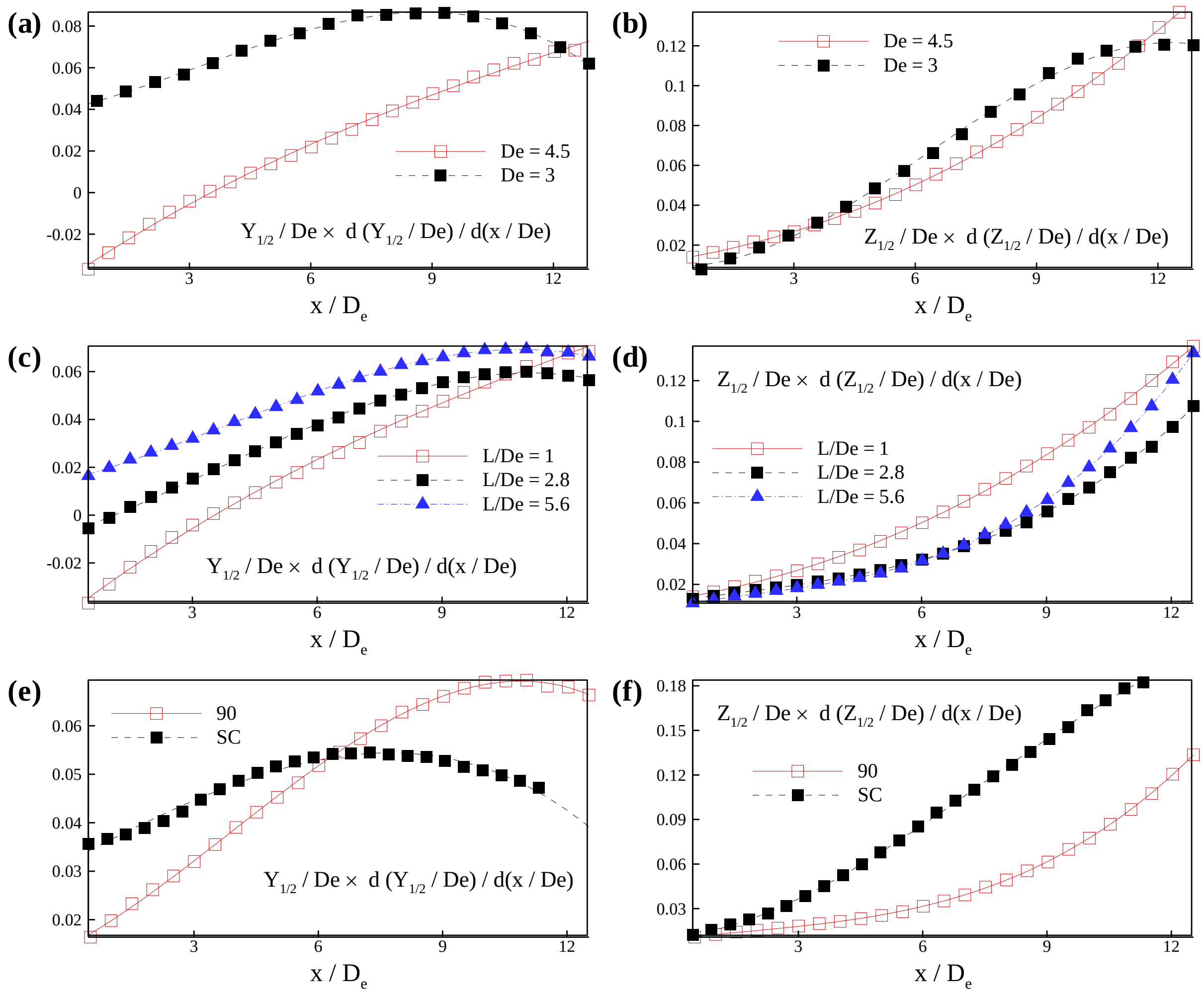

Fig. E.17 The effect of nozzle geometry on the flow local entrainment rate (a) on the major plane and (b) on the minor plane for different D_e, (c) on the major plane and (d) on the minor plane for different L/D_e, and (e) on the major plane and (f) on the minor plane for different contraction angles (all at U_{co}~0.2 m/s and U_{jet}~30 m/s).

E.2 Part II: More results on the effect of the nozzle geometry on jet characteristics

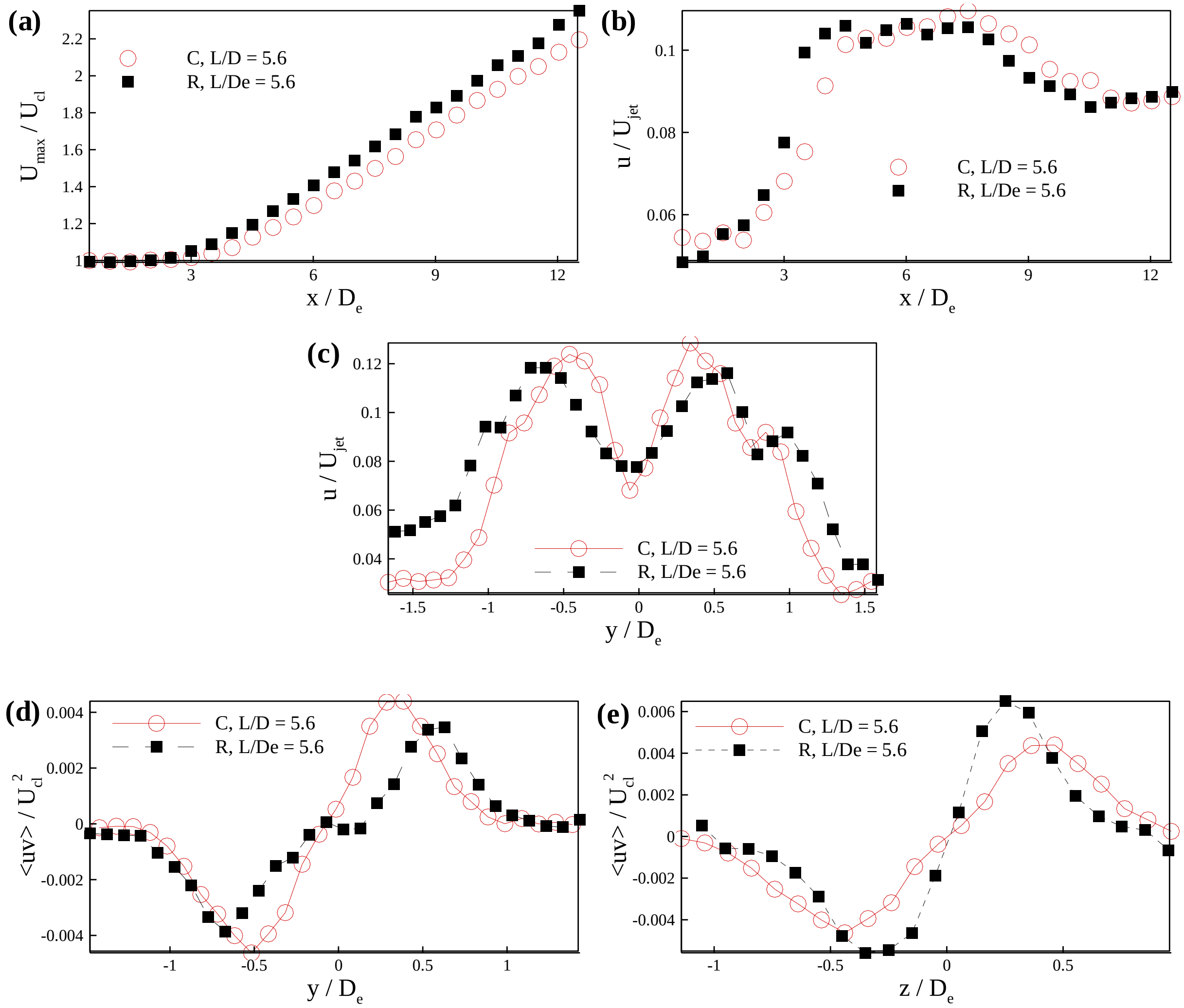

Fig. E.18 Comparison of the (a) axial mean-velocity decay on the centerline, (b) centerline axial turbulence intensity, (c) lateral distribution of the axial turbulence intensity on the major axis, (d) lateral distribution of the normalized turbulent shear-stress on the major axis, and (e) lateral distribution of the normalized turbulent shear-stress on the minor axis at x/D_e ~ 3 between different nozzle exit orifices with D_e = 4.5 mm and L/D_e = 1 (U_{jet}~17 m/s and U_{co}~0.5 m/s).

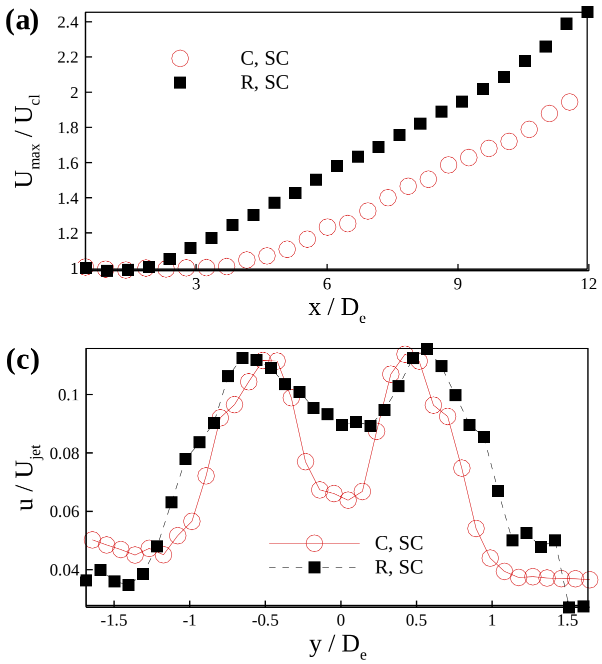

Fig. E.19 Comparison of the (a) axial mean-velocity decay on the centerline, (b) centerline axial turbulence intensity, (c) lateral distribution of the axial turbulence intensity on the major axis, and (d) lateral distribution of the normalized turbulent shear-stress on the major axis at x/D_e ~ 3 between different nozzle exit orifices with smooth contraction (U_{jet}~17 m/s and U_{co}~0.2 m/s).

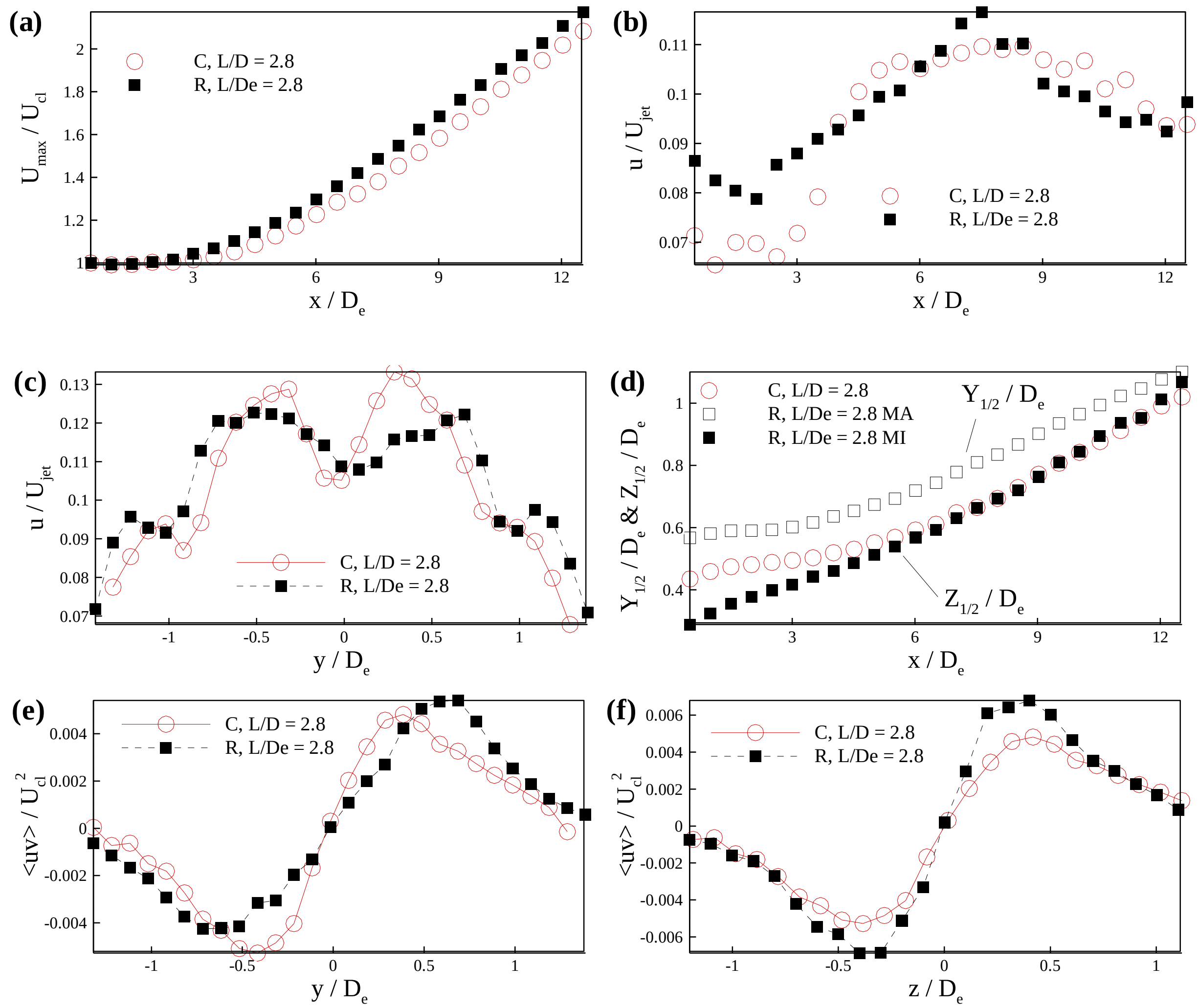

Fig. E.20 Comparison of the (a) axial mean-velocity decay on the centerline, (b) centerline axial turbulence intensity, (c) lateral distribution of the axial turbulence intensity on the major axis, (d) axial development of axial mean-velocity spread, (e) lateral distribution of the normalized turbulent shear-stress on the major axis, and (f) lateral distribution of the normalized turbulent shear-stress on the minor axis at x/D_e ~ 6 between different nozzle exit orifices with D_e = 4.5 mm and L/D_e = 2.8 (U_{jet}~30 m/s and U_{co}~0.2 m/s).

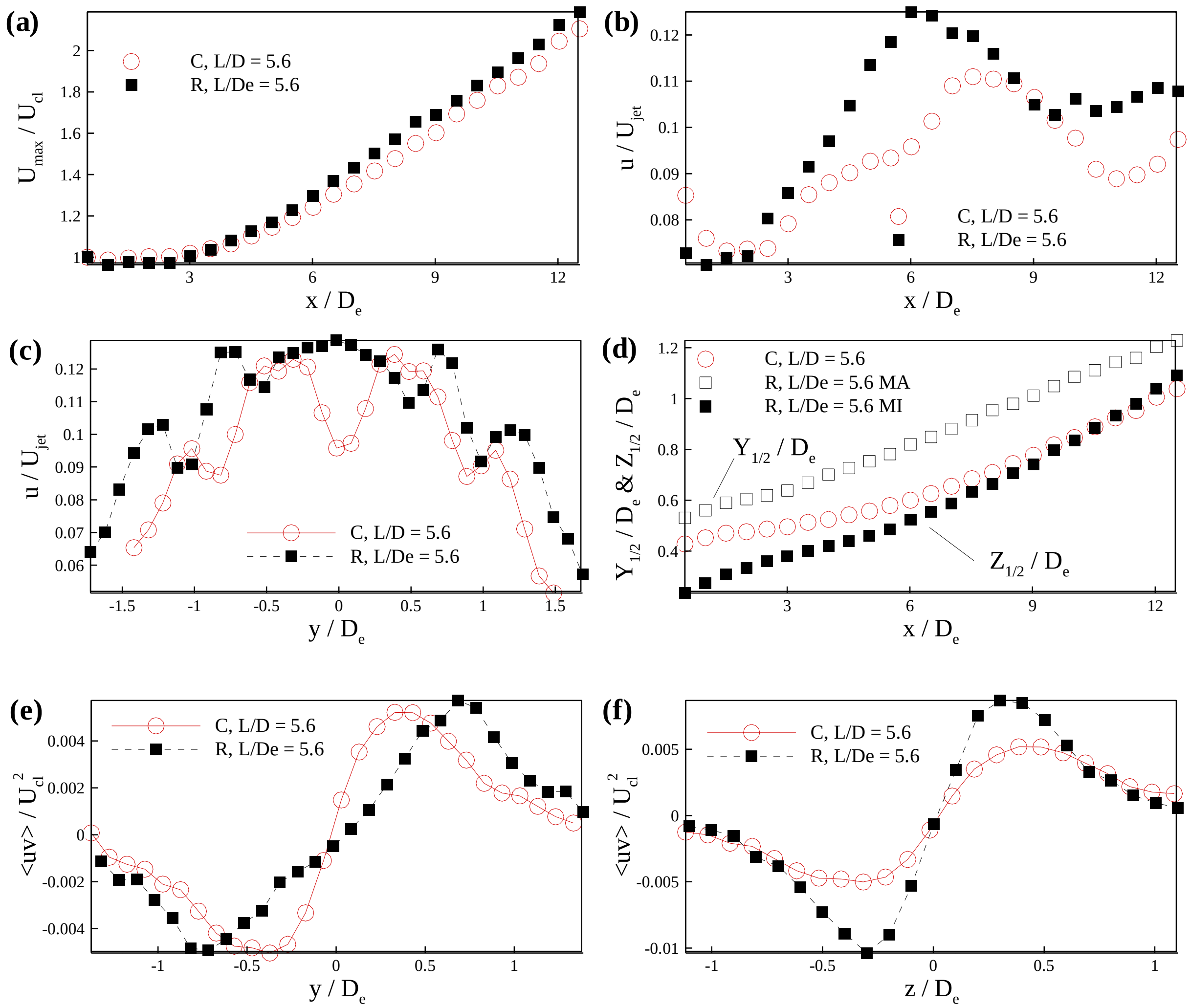

Fig. E.21 Comparison of the (a) axial mean-velocity decay on the centerline, (b) centerline axial turbulence intensity, (c) lateral distribution of the axial turbulence intensity on the major axis, (d) axial development of axial mean-velocity spread, (e) lateral distribution of the normalized turbulent shear-stress on the major axis, and (f) lateral distribution of the normalized turbulent shear-stress on the minor axis at $x/D_e \sim 6$ between different nozzle exit orifices with D_e = 4.5 mm and L/D_e = 5.6 (U_{jet}~30 m/s and U_{co}~0.2 m/s).

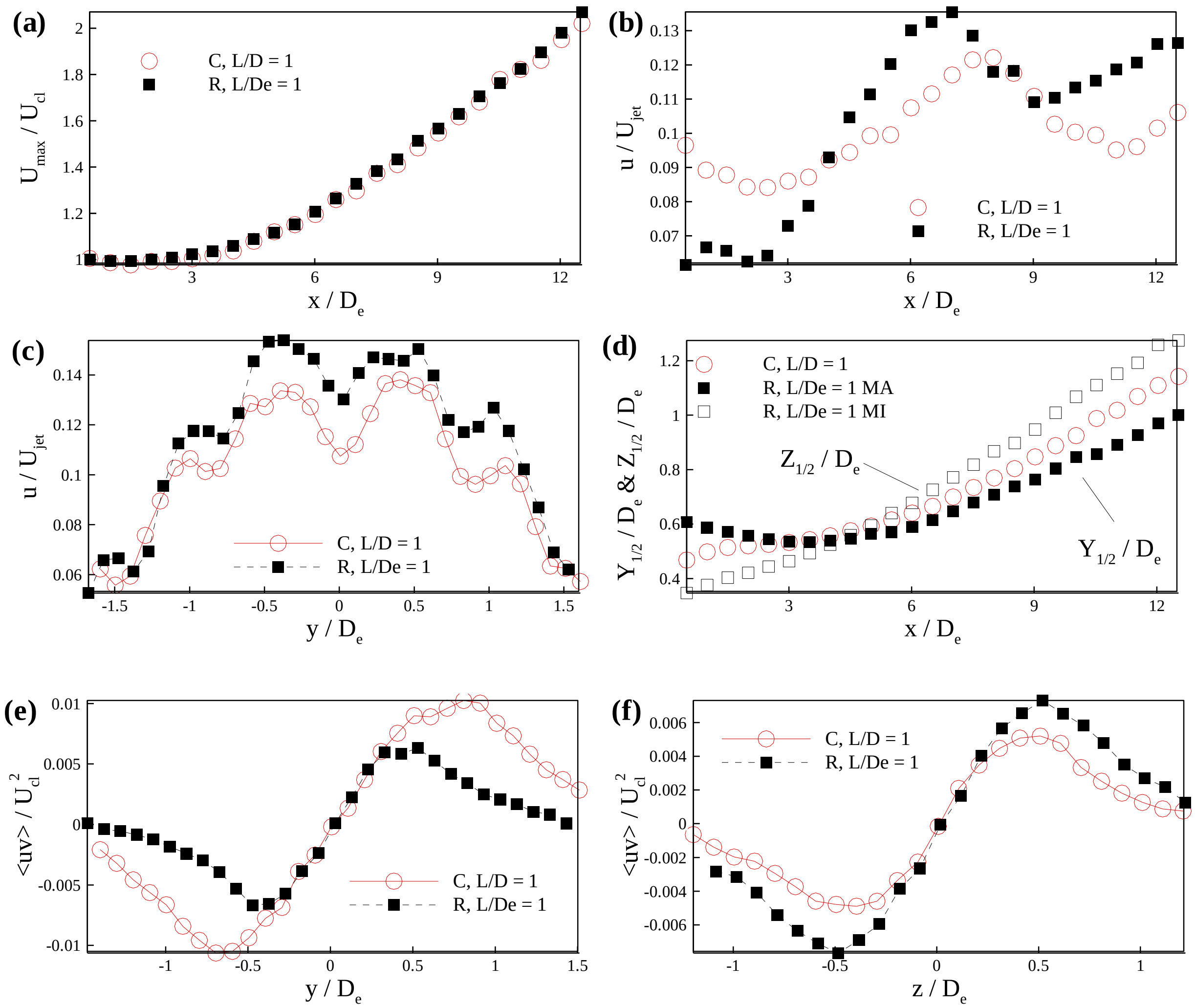

Fig. E.22 Comparison of the (a) axial mean-velocity decay on the centerline, (b) centerline axial turbulence intensity, (c) lateral distribution of the axial turbulence intensity on the major axis, (d) axial development of axial mean-velocity spread, (e) lateral distribution of the normalized turbulent shear-stress on the major axis, and (f) lateral distribution of the normalized turbulent shear-stress on the minor axis at x/D_e ~ 6 between different nozzle exit orifices with D_e = 4.5 mm and L/D_e = 1 (U_{jet}~30 m/s and U_{co}~0.5 m/s).

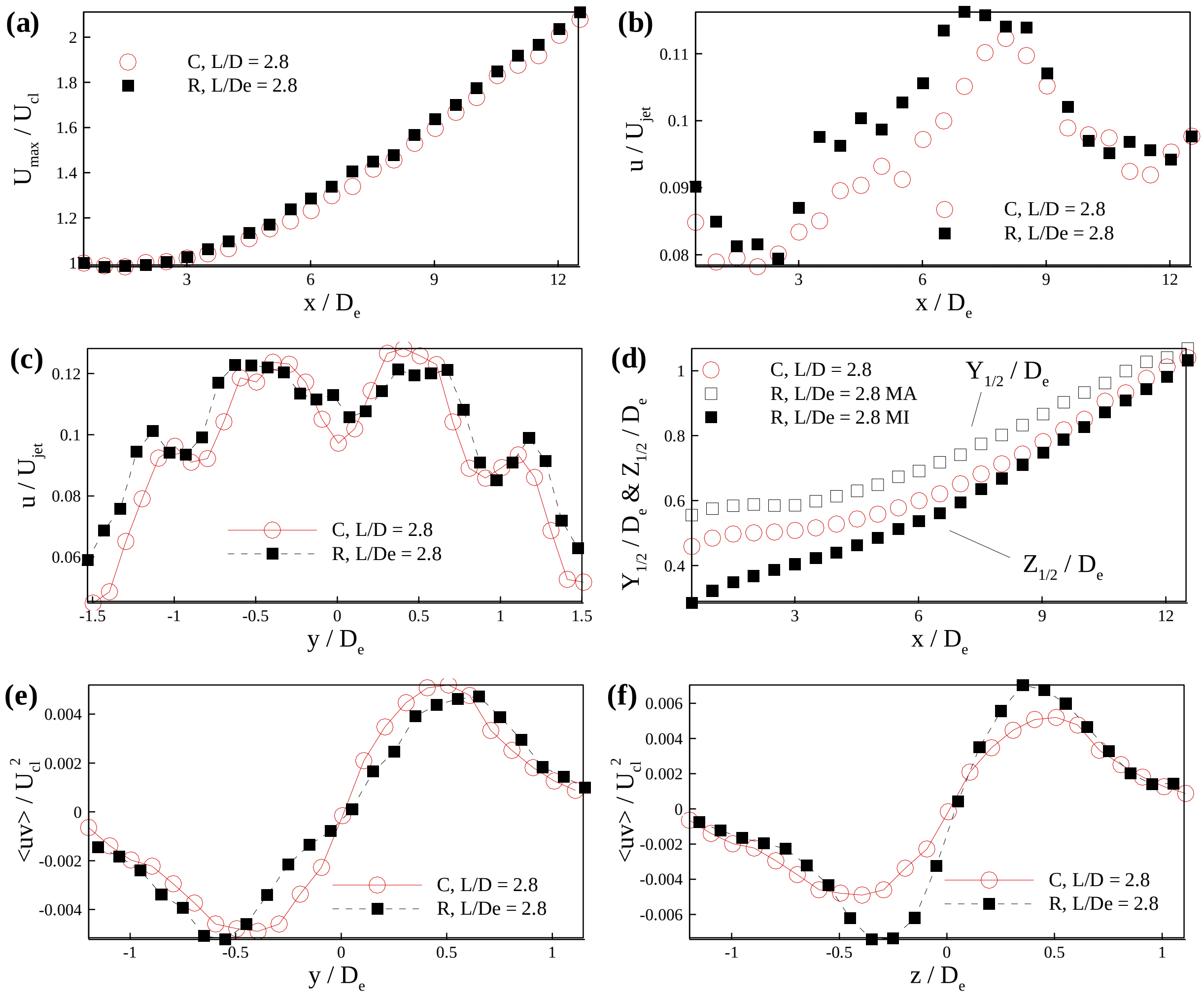

Fig. E.23 Comparison of the (a) axial mean-velocity decay on the centerline, (b) centerline axial turbulence intensity, (c) lateral distribution of the axial turbulence intensity on the major axis, (d) axial development of axial mean-velocity spread, (e) lateral distribution of the normalized turbulent shear-stress on the major axis, and (f) lateral distribution of the normalized turbulent shear-stress on the minor axis at x/D_e ~ 6 between different nozzle exit orifices with D_e = 4.5 mm and L/D_e = 2.8 (U_{jet}~30 m/s and U_{co}~0.5 m/s).

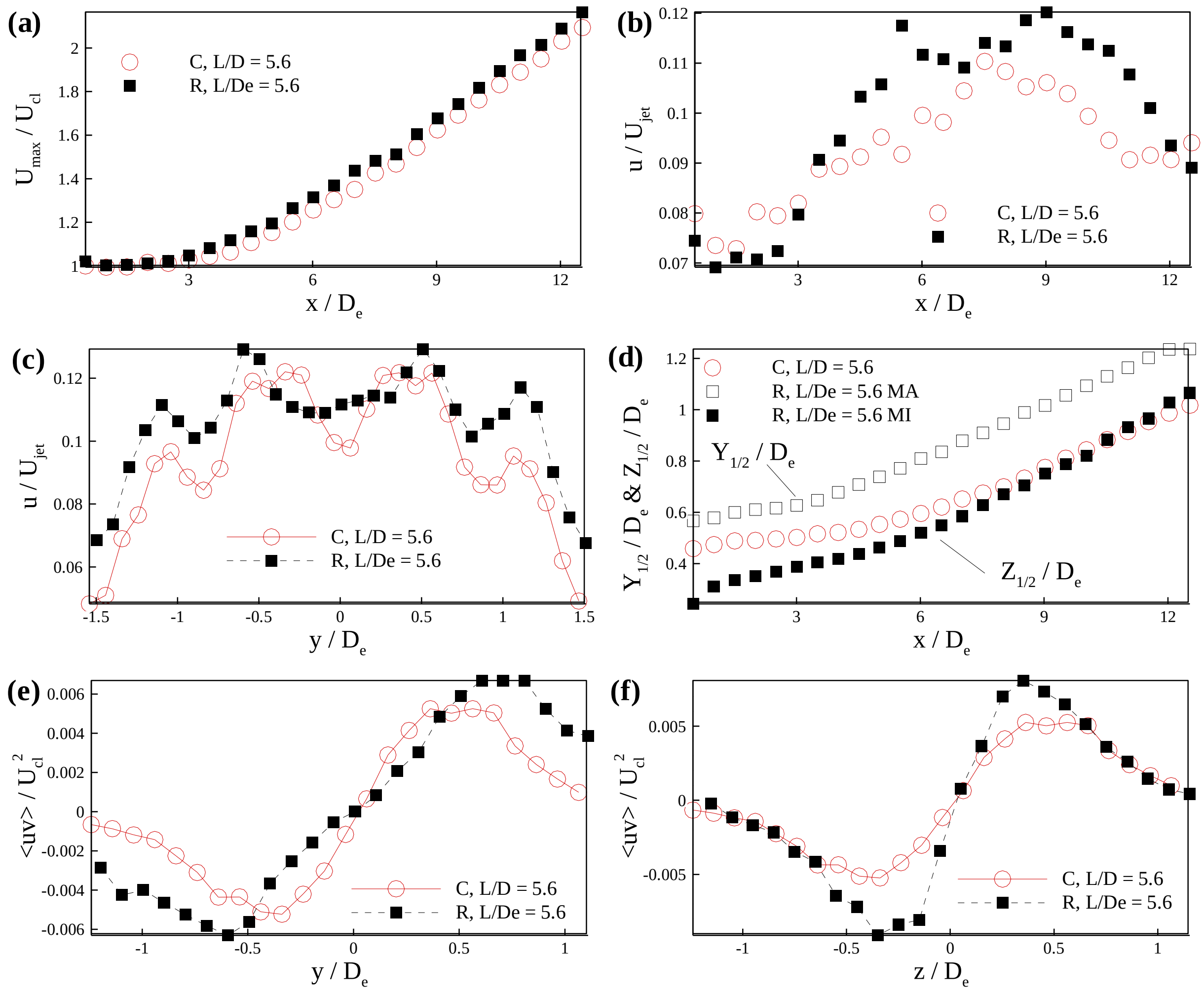

Fig. E.24 Comparison of the (a) axial mean-velocity decay on the centerline, (b) centerline axial turbulence intensity, (c) lateral distribution of the axial turbulence intensity on the major axis, (d) axial development of axial mean-velocity spread, (e) lateral distribution of the normalized turbulent shear-stress on the major axis, and (f) lateral distribution of the normalized turbulent shear-stress on the minor axis at x/D_e ~ 6 between different nozzle exit orifices with D_e = 4.5 mm and L/D_e = 5.6 (U_{jet}~30 m/s and U_{co}~0.5 m/s).

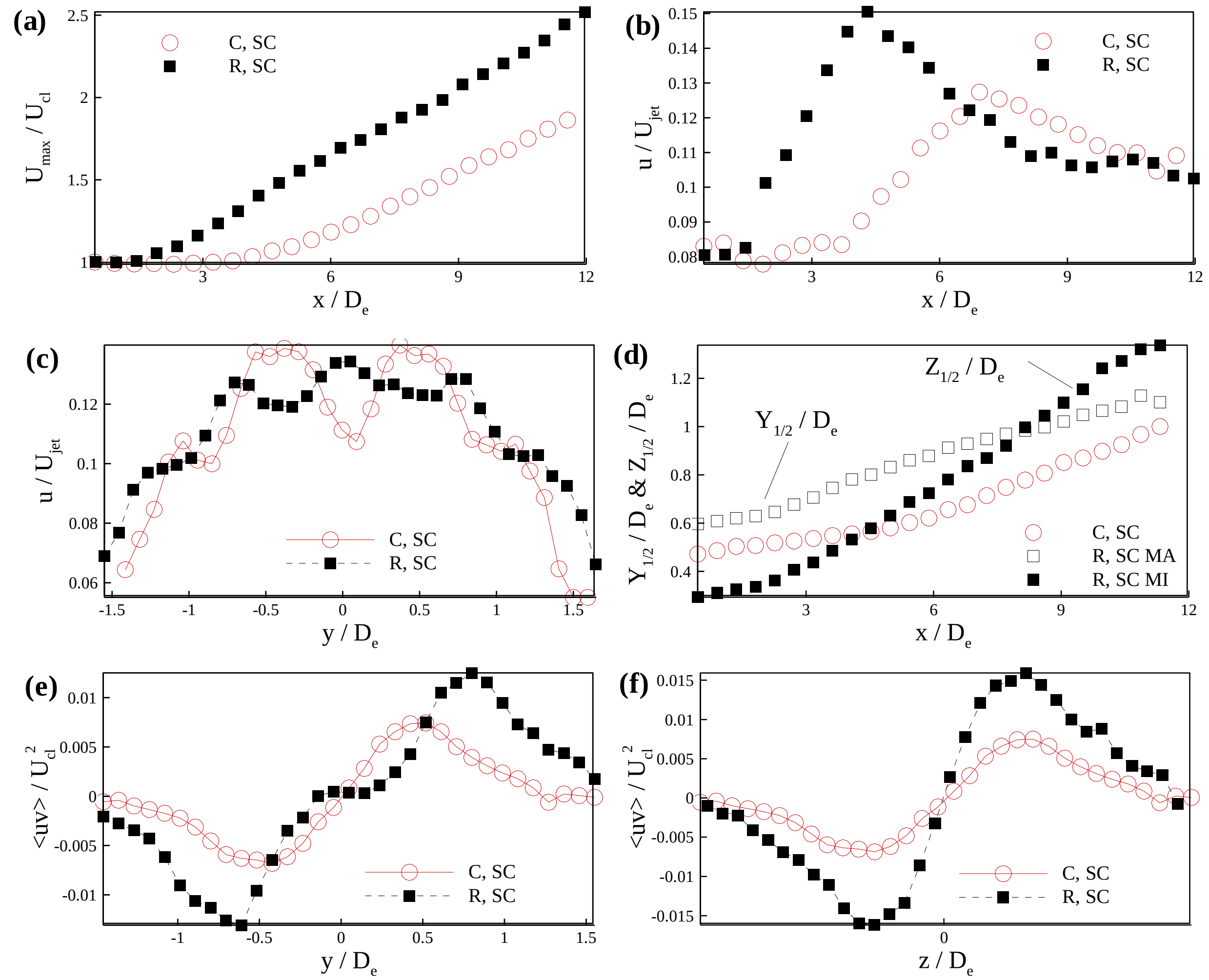

Fig. E.25 Comparison of the (a) axial mean-velocity decay on the centerline, (b) centerline axial turbulence intensity, (c) lateral distribution of the axial turbulence intensity on the major axis, (d) axial development of axial mean-velocity spread, (e) lateral distribution of the normalized turbulent shear-stress on the major axis, and (f) lateral distribution of the normalized turbulent shear-stress on the minor axis at x/D_e ~ 6 between different nozzle exit orifices with smooth contraction (U_{jet}~30 m/s and U_{co}~0.5 m/s).

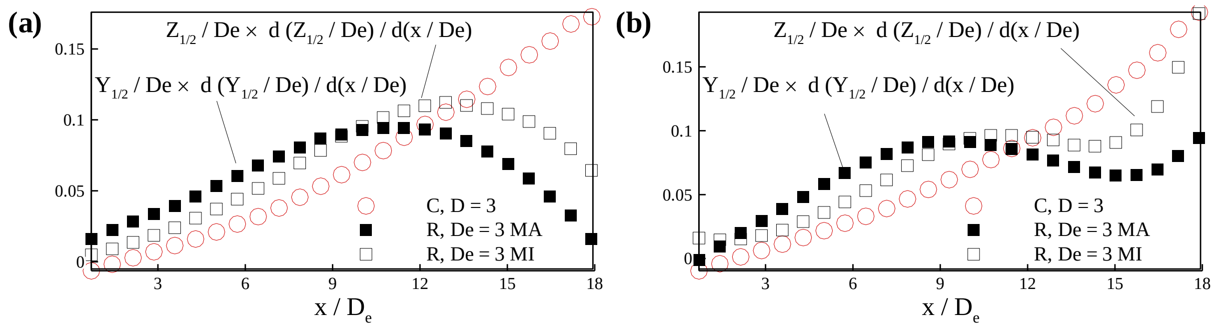

Fig. E.26 Comparison of the local entrainment between the circular and the rectangular nozzles with D_e = 3 mm and L/D_e =1 (a) at U_{co} ~ 0.2 m/s, and (b) at U_{co} ~ 0.5 m/s (U_{jet}~30 m/s).

APPENDIX F

DEVELOPMENT OF A TURBULENT JET

The characterization of the development of a jet issuing from a circular/rectangular nozzle with smooth contraction, as an example of the nozzle geometries used in the present study (details of the nozzle geometry are given in Table 3.1), is presented below.

Figures F.1(a-c) show the flow streamlines on normalized axial mean-velocity (U/U_{jet}) contours. From these figures, it is clearly seen that the rectangular jet which has initially the smallest width on the minor plane (Fig. F.1(c)) also has the highest spread rate downstream of the jet. Figures F.1(a-c) show also that the length of the potential core (the axial location at which the axial mean-velocity remains almost the same with the jet exit velocity) of the circular jet is considerably higher. In addition, these figures show also how most of the co-airflow is entrained into the central jet in the near-field (x/D_e <~ 4).

Figures F.2(a-c) show the non-dimensional axial instantaneous velocity at three different time instances. These figures show the turbulent nature of the jets studied in the present study. Figure F.3 shows the lateral profiles of non-dimensional velocity (U/U_{cl}) versus the non-dimensional lateral coordinate ($y/Y_{1/2}$ and $z/Z_{1/2}$) at different axial locations (x/D_e). This figure demonstrates that the axial mean-velocity, for the circular nozzle (Fig. F.3(a)) and the rectangular nozzle on the minor plane (Fig. F.3(c)), becomes self-similar at x/D_e~ 8, whereas such a similarity does not occur on the major axis of the rectangular nozzle until up to x/D_e ~ 12 (Fig. F.3(b)). This agrees with the spread rate of the examined jets (see Fig. F.1) in that the rectangular jet, which has the lowest spread rate on the major plane, achieves self-similarity farther downstream compared with the circular jet and the rectangular jet on the minor plane.

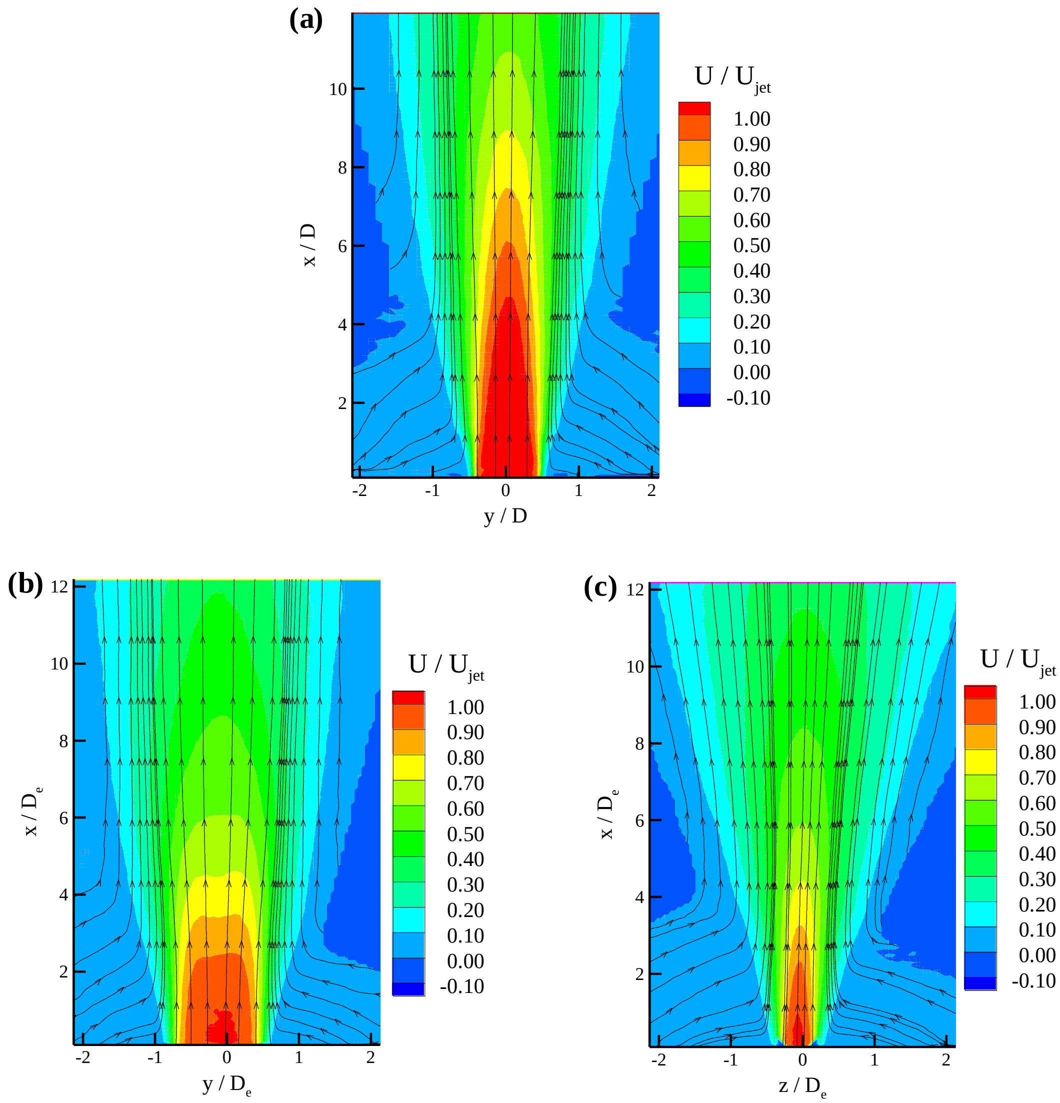

Fig. F.1 Non-dimensional axial mean-velocity (U/U_{jet}) contours for (a) the circular nozzle with SC, (b) the rectangular nozzle with SC on the major axis, and (c) the rectangular nozzle with SC on the minor axis (U_{jet}~ 30 m/s and U_{co}~ 0.5 m/s).

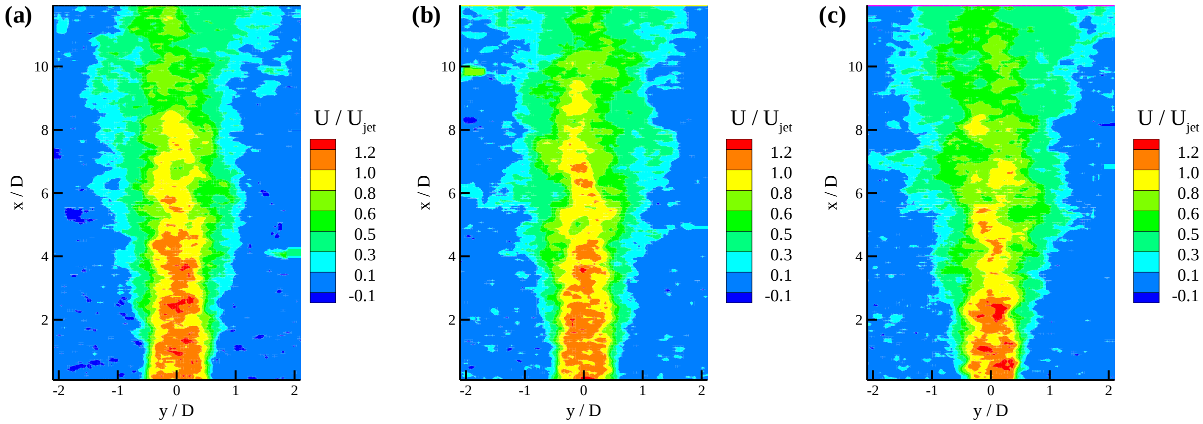

Fig. F.2 Instantaneous non-dimensional axial mean-velocity (U/U_{jet}) contours at three different time instances for the circular nozzle with smooth contraction, at (a) t_1, (b) t_1 + ~6 sec, and (c) t_1 + ~12 sec (U_{jet} ~ 30 m/s and U_{co} ~ 0.5 m/s)

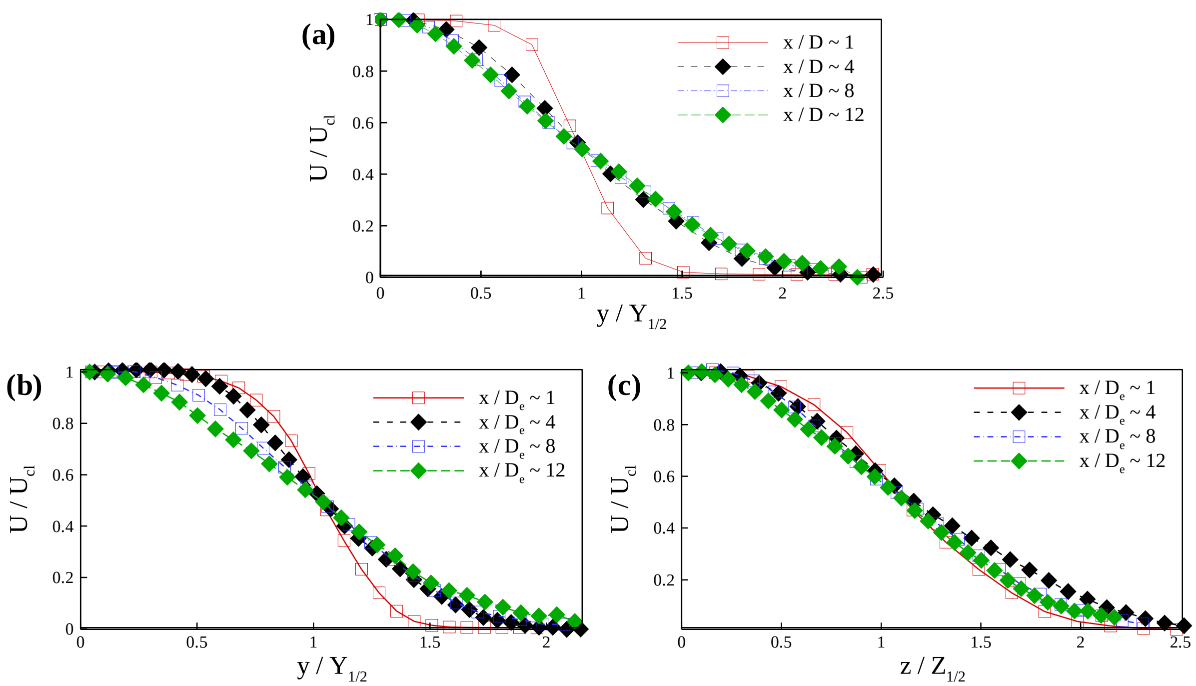

Fig. F.3 Lateral profiles of non-dimensional axial mean-velocity (U/U_{cl}) for (a) the circular nozzle with SC, (b) the rectangular nozzle with SC on the major axis, and (c) the rectangular nozzle with SC on the minor axis, at different axial locations (U_{jet}~ 30 m/s and U_{co}~ 0.5 m/s).

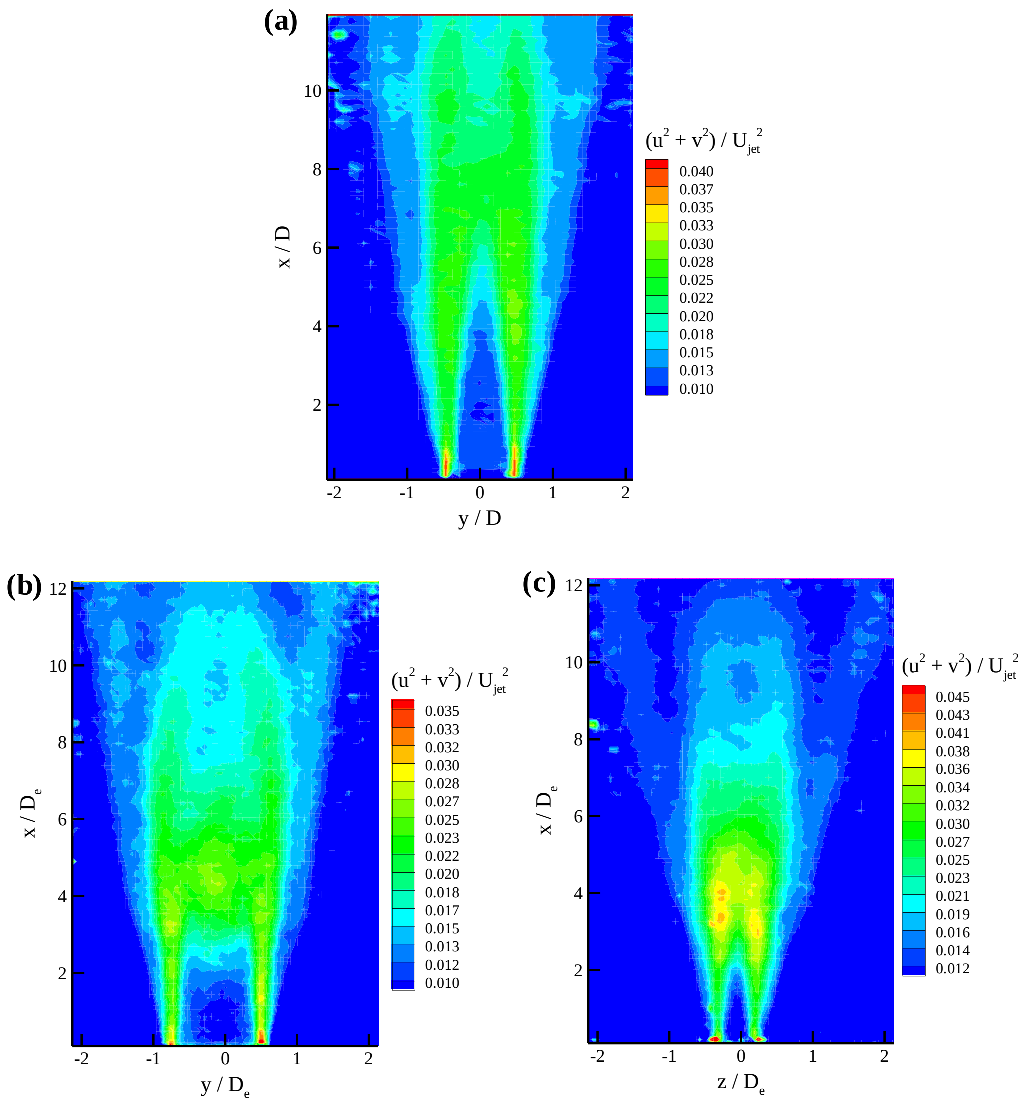

Fig. F.4 Non-dimensional turbulent kinetic energy ($(u^2 + v^2)/U_{jet}^2$) contours for (a) the circular nozzle with SC, (b) the rectangular nozzle with SC on the major axis, and (c) the rectangular nozzle with SC on the minor axis (U_{jet}~ 30 m/s and U_{co}~ 0.5 m/s).

Figure F.4 presents the contours of the normalized turbulent kinetic energy ($(u^2 + v^2)/U_{jet}^2$) for the circular (on the nozzle symmetric plan in Fig. F.4(a)) and the rectangular nozzle with SC (on the major and minor planes, respectively in Figs. F.4(b) and F.4(c)). It can be seen in these figures that the peak of the jet normalized turbulent kinetic energy occurs in the shear-layer between the jet and co-flow just behind the nozzle's lip. Farther downstream, the turbulent kinetic energy shifts outwards as the jet spreads out. This trend is fairly similar for both, the circular nozzle (Fig. F.4(a)) and rectangular nozzle on the major axis (Fig. F.4(b)). In contrast with the trend of development of turbulence on the plane of symmetry of the circular nozzle and the major symmetric plane of the rectangular nozzle (Fig. F.4(a-b)), the normalized turbulent kinetic energy undergoes another local maxima of $(u^2 + v^2)/U_{jet}^2$ on the minor symmetric plane of the rectangular nozzle with smooth contraction (Fig. F.4(c)).

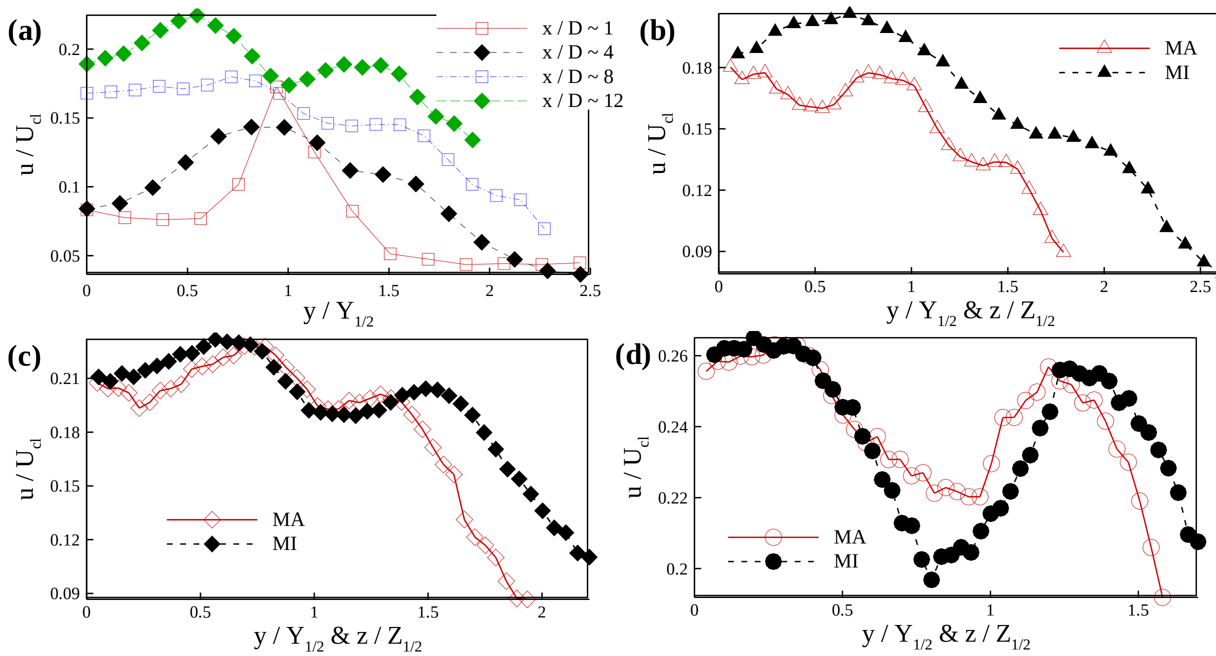

Fig. F.5 Lateral profiles of the axial turbulence intensity (u/U_{cl}) for (a) the circular nozzle with SC at different x/D, and for the rectangular nozzle with SC on the major and minor axes at (b) x/D_e ~ 4, (c) x/D_e ~ 8, and (d) x/D_e ~ 12 (U_{jet}~ 30 m/s and U_{co}~ 0.5 m/s).

The lateral profiles of axial turbulence intensity (u/U_{cl}) are provided for the circular nozzle in Fig. F.5(a) and for the rectangular nozzle in Fig. F.5(b-d). Figure F.5(a) shows that unlike the axial mean-velocity, the turbulence intensity does not become self-similar by x/D~ 12. Figures F.5(b-d) show that by going farther downstream, the lateral distribution of turbulence intensity become more similar between the major and minor axes of the rectangular nozzle.

However, a comparison between the results in Fig. F.5(b-d) shows that the self-similarity of turbulence intensity has neither been observed in the near-filed of the rectangular jet.

The lateral profiles of the non-dimensional turbulent (Reynolds) shear stress ($< uv > / U_{cl}^2$) are provided for the circular nozzle in Fig. F.6(a) at different axial locations, and for the rectangular nozzle through Figs. F.6(b-d) on both major and minor axes. Figure F.6 shows also that similar to the turbulence intensity (u/U_{cl}), $< uv >/U_{cl}^2$ profiles do not become self-similar by x/D~ 12. Figures F.6(b-d) show that by going farther downstream, the lateral distribution of the normalized turbulent shear-stress become more similar between the major and minor axes of the rectangular nozzle. However, no self-similarity of the normalized turbulent shear-stress for the circular/rectangular nozzle is seen up to x/D_e~ 12, either.

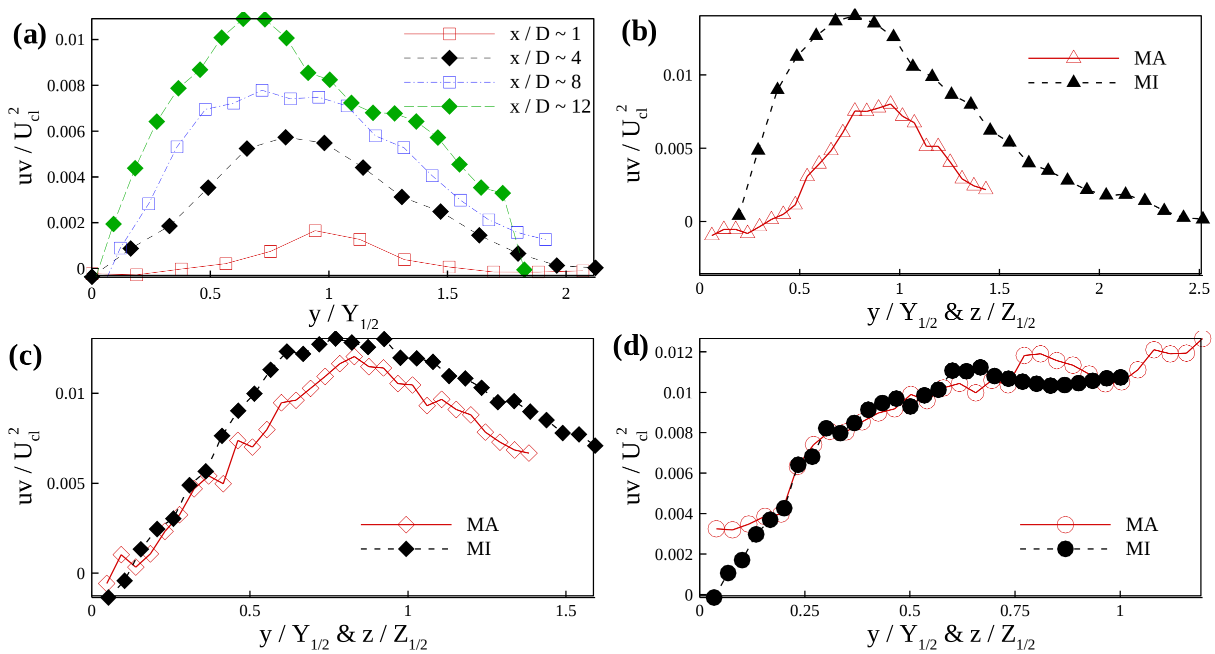

Fig. F.6 Lateral profiles of the non-dimensional Reynolds shear stress (uv/U_{cl}^2) for (a) the circular nozzle at different x/D, and for the rectangular nozzle on both major and minor axes at (b) x/D_e ~ 4, (c) x/D_e ~ 8, and (d) x/D_e ~ 12 (U_{jet}~ 30 m/s and U_{co}~ 0.5 m/s).